
Temperature and Structural Effects on Singlet Fission and Intersystem Crossing in Organic Semiconductor Systems



University of
Sheffield

Eman Mohammed A. Bu Ali

Supervised by Prof. Jenny Clark

The University of Sheffield

Faculty of Science

Department of Physics and Astronomy

*A thesis submitted in partial fulfilment of the requirements for the
degree of Doctor of Philosophy*

May 2025

Abstract

In this thesis, we investigate the fundamental mechanisms that contribute to triplet exciton generation in organic molecular systems, such as singlet fission, triplet-triplet annihilation, and intersystem crossing. We examine the effects of external conditions such as magnetic fields and temperature, as well as internal factors such as molecular structure, on exciton behaviours and triplet generation process.

We initially studied the temperature and magnetic field dependence on photoluminescence of a diF-TES-ADT singlet fission system. We showed, through magnetic field-dependent photoluminescence spectroscopy and a range of different optical and magnetic resonance spectroscopic techniques, that singlet fission to form a weakly bound triplet pair state is highly temperature-dependent in this material. Then, we investigated the photophysical properties of different tetracene derivatives in solution, as well as illustrated the mechanism of triplet formation using excitation wavelength-dependent transient absorption spectroscopy. By providing a comprehensive analysis of the excited state dynamics, we showed excitation-dependent behaviour in a newly synthesized tetracene dimer and some monomers, displaying unique characteristics, along with the detection of ultrafast intersystem crossing triplet formation.

Finally, we investigated the photophysical properties of a new synthesis macrocyclic parallel pentacene dimer. This dimer demonstrated an ultrafast intramolecular singlet fission process and selective generation of the quintet states. It also exhibits the longest room-temperature coherence time of a quintet state, to our knowledge at the time of publication, of 648 ns.

Declaration

The work within this thesis was completed by the author, unless explicitly stated in the text where the work involves collaboration. Throughout, the first person plural ‘we’ is used as in standard scientific convention. This work has never been submitted for a degree at any other institution. Excluding its appendices, this thesis is within the 80 000 word limit.

- Eman Mohammed A. Bu Ali

May 2025

Acknowledgements

I would like to begin by sincerely thanking my supervisor, Prof. Jenny Clark, for her exceptional guidance and support throughout my PhD journey. From the earliest stages of project planning to the final stages of writing my thesis, her invaluable feedback, support, and encouragement have consistently pushed me to stay motivated and pursue success. I have learnt so much from her research approach, scientific discussion, and writing advice. Thank you for creating such a wonderful and collaborative environment in our group.

I also would like to thank my collaborators: Samara Medina at the University of Malaga, Wataru Ishii at Kyushu University, Arnau Bertraninglada, Gabriel Moise, and Claudia Tait at the University of Oxford, and Rachel Kilbride at the University of Sheffield, for their invaluable contributions and for making these projects possible. We carried out successful work that resulted in an achievement I am proud to share with them.

I want to express my sincere thanks to Shuangqing (Simon) for his guidance and assistance in building the magnetic field effect setup, Ravi Kumar for his help in building the nanosecond transient absorption and NOPA setups, and James Pidgeon for his help in operating the nanosecond transient absorption setup and all experimental trainings. Your hands-on help, training sessions, time spent guiding me, and willingness to share your expertise were invaluable. I also thank Dimitri, James, and Mitch for keeping the Chemistry labs running smoothly throughout.

I am also grateful to the Fast Spectroscopy group members: James, Rob, Samara, Daniel, Tom, Ravi, Simon, Rahul, Sayantan, Robbie, and Mitch for their

contributions, whether through experimental work, scientific discussions, or assistance with data analysis. Thank you for making the last few years such an enjoyable experience.

Lastly, I express my deepest appreciation to my husband. Thank you for your endless support throughout this journey and for being beside me, encouraging me to keep going. To my parents, thank you from the bottom of my heart for your unconditional love, support, and encouragement throughout every stage of my life. To my siblings, thank you for all your encouragement and support. To my wonderful kids, thank you for your love, patience, and kindness. Your smiles lightened even the most challenging days. I dedicate this work to all of you.

Funding: Eman M. Bu Ali thanks King Faisal University in Saudi Arabia for her PhD scholarship, and acknowledges support from the Saudi Arabian Cultural Bureau in London. Eman also thanks EPSRC for enabling her research through grants EP/T012455, EP/L022613, and EP/R042802.

Publications

Eman M Bu Ali, Arnau Bertran, Gabriel Moise, Shuangqing Wang, Rachel C. Kilbride, John E. Anthony, Claudia E. Tait, and Jenny Clark. ‘Intersystem crossing out-competes triplet-pair separation from¹(TT) below 270 K in anthradithiophene films’. *Journal of the American Chemical Society* (2025).

Wataru Ishii[†], Masaaki Fuki[†], Eman M. Bu Ali[†], Shunsuke Sato[†], Bhavesh Parmar, Akio Yamauchi, Catherine Helenna Mulyadi, Masanori Uji, Samara Medina Rivero, Go Watanabe, Jenny Clark, Yasuhiro Kobori, and Nobuhiro Yanai. ‘Macrocyclic Parallel Dimer Showing Quantum Coherence of Quintet Multiexcitons at Room Temperature’. *Journal of the American Chemical Society* 146, 37, 25527-25535 (2024).

[†]These authors contributed equally.

Contents

Publications	vii
Contents	ix
1 Introduction	1
2 Theory and Background	7
2.1 Conjugated organic molecules	7
2.2 Electronic properties of an organic conjugated molecule	9
2.3 Excitons	10
2.4 Electron Spin	13
2.4.1 Zeeman Interaction	17
2.4.2 Hyperfine Interaction	19
2.4.3 Interactions of two electron spins	19
2.4.4 Triplet Pair	22
2.4.5 The Spin Hamiltonian	24
2.4.6 Spin Evolution	25
2.5 Photophysical Processes	27
2.5.1 Absorption and Emission	28
2.5.2 Non-Radiative Transitions	34
2.5.3 Exciton-Exciton Annihilation	37
2.6 Singlet Fission and triplet-triplet annihilation	38
2.6.1 The Mechanism	38
2.6.2 Magnetic Field Effects MFE in Singlet Fission	41

2.6.3	Singlet Fission in Acenes	43
3	Materials and Methods	45
3.1	Materials	45
3.1.1	diF-TES-ADT	45
3.1.2	Tetracene dimers and TDA monomer	46
3.1.3	Mono-TIPS tetracene	47
3.1.4	5,12-diphenyltetracene (DPT)	48
3.1.5	5,6,11,12-tetraphenyltetracene (rubrene)	48
3.1.6	Pentacene MPD-1 dimer and PDA monomer	49
3.2	Sample Preparation	49
3.2.1	diF-TES-ADT Films	49
3.2.2	Tetracene dimers and monomers	50
3.2.3	Pentacene MPD-1 dimer and PDA-monomer	51
3.3	Sample Characterisation Techniques	51
3.3.1	Grazing Incidence Wide-Angle X-ray Scattering GIWAX	51
3.3.2	Atomic Force Microscopy AFM	53
3.3.3	Ground-State Absorption	53
3.3.4	Steady-State Photoluminescence PL Measurements	54
3.4	Transient Absorption Spectroscopy	55
3.4.1	Picosecond Transient Absorption Spectroscopy	58
3.4.2	Nanosecond Transient Absorption Spectroscopy	59
3.5	Magnetic Field Effect	62
3.5.1	Temperature-Dependent MFE measurements	63
3.6	Transient Electron Spin Resonance (trESR)	65
3.7	Nutation measurement	67
4	Intersystem crossing out-competes triplet-pair separation from $^1(\text{TT})$ below 270 K in anthradithiophene films	69
4.1	Introduction	70
4.2	Results and discussion	75

4.2.1	Model system	75
4.2.2	Temperature-dependent magnetic field effect reveals the absence of SF below 270 K	78
4.2.3	Transient electron spin resonance (trESR) demonstrates the production of triplet states by ISC at low temperat- ures	82
4.2.4	MFE simulation and kinetic modelling	89
4.3	Conclusion	92
5	The investigation of excitation dependence reveals ultrafast in- tersystem crossing in tetracene dimers	95
5.1	Introduction	96
5.2	Results and discussion	98
5.2.1	Model systems	98
5.2.2	Investigation of singlet fission and triplet formation in tet- racene dimers	103
5.2.3	Excitation wavelength dependence shows high-level inter- system crossing	107
5.3	Conclusion	112
6	Excitation wavelength dependence in tetracene monomers	115
6.1	Introdicton	116
6.2	Results and discussion	118
6.2.1	Model systems	118
6.2.2	Photoluminescence quantum yield (PLQY)	121
6.2.3	Excitation wavelength dependence in mono-TIPS tetracene monomer	122
6.2.4	Excitation wavelength dependence in DPT	124
6.3	Conclusion	132
7	A Macrocyclic Parallel Dimer Showing Quantum Coherence of	

Quintet Multiexcitons at Room Temperature	135
7.1 Introduction	136
7.2 Results and discussion	139
7.2.1 Model system	139
7.2.2 Optical properties of MPD-1 and PDA	143
7.2.3 Transient absorption spectroscopy revealed ultrafast SF in pentacene dimer	145
7.2.4 Continuous-wave transient electron paramagnetic reson- ance measurement of MPD-1	151
7.2.5 Nutation measurement of MPD-1	156
7.3 Conclusion	160
8 Conclusions	161
8.1 Summary	161
8.2 Open Questions and Future Work	163
A Supplementary information for Chapter 4	167
A.1 Morphological Characterization of diF-TES-ADT Films	167
A.2 Steady-State Absorption and Emission	169
A.3 Temperature-Dependent Time-Resolved Photoluminescence Dy- namics	170
A.4 Temperature-Dependent MFE measurements	171
A.5 Simulation and modeling of MFEs	174
A.5.1 Kinetic Modeling of Room Temperature MFE	174
A.5.2 Kinetic Modeling of Temperature-Dependent MFE	176
A.5.3 Fluence-dependent simulation	183
A.6 Transient Electron Spin Resonance	184
A.6.1 trESR measurements on diF-TES-ADT in frozen solution .	184
A.6.2 Spectral signatures for photoinduced paramagnetic states for different formation mechanisms	185
A.6.3 Partial ordering in diF-TES- ADT films	187

A.6.4	Contributions to the trESR spectra	188
A.6.5	Modeling of the trESR time evolution	190
A.6.6	Experimental Procedures and Data Analysis Conducted by Collaborators at the University of Oxford	196
B	Supplementary information for Chapter 5 and 6	199
B.1	Tetracene dimers	199
B.1.1	Molecular weight of DPT-dimers	199
B.1.2	Absorbance spectra of the dimers	200
B.1.3	Absorption spectra of DPT-dimer1: solvent dependency . .	201
B.1.4	calibration curves of DPT-dimer1 in different solvents at different wavelengths	202
B.2	Tetracene monomers and rubrene	203
B.2.1	Molecular weight of the monomers	203
B.2.2	Photoluminescence quantum yield (PLQY) of the monomers	203
B.3	DPT sensitization measurement using different sensitizers.	206
B.4	Excitation wavelength dependence in rubrene	207
B.5	Diffusion-ordered spectroscopy nuclear magnetic resonance (DOSY- NMR) analysis	208
B.5.1	DiPhenyltetracene 7.2 mg in 0.6 ml of toluene	208
B.5.2	DiPhenyltetracene 3.8 mg in 0.6 ml of toluene	211
B.5.3	DiPhenyltetracene 2.2 mg in 0.62 ml of CDCl ₃	213
B.5.4	DiPhenyltetracene 0.82 mg in 0.55 ml of toluene	215
B.5.5	Monomer-dimer fitting using Hill equation	217
C	Supplementary information for Chapter 7	219
C.1	General characterizations conducted at Kyushu University by col- laborators	219
C.2	Crystallography	220
C.3	MD simulations	222

C.4 Steady-state absorption and fluorescence spectra of pentacene dimer and monomer in polystyrene film	223
C.5 Photoluminescence quantum yield (PLQY)	224
C.6 Time-resolved CW-EPR and pulsed EPR measurements	225
C.7 Magnetic field effect measurement	229
References	231

Chapter 1

Introduction

As the global need for cleaner and more sustainable energy continues to grow, solar energy is considered a very promising option. In particular, solar photovoltaics, PV, which facilitate the direct conversion of sunlight into electricity, have played a central role in this transition. Single-junction silicon solar cells dominate the photovoltaic sector.^{1,2} However, the highest efficiency of a silicon solar cell varies from 29% to 33.7%, which is known as the Shockley-Queisser limit.²⁻⁴ In the last two decades, advancements in solar cell technology have enhanced device efficiency slightly from 24% to 26.7%.³ Improvements in device efficiency are gradual and constrained as we approach the Shockley-Queisser limit. Photons with high energy are converted inefficiently, since their extra energy is released as thermal loss before being extracted.⁵ Approximately 33–39% of the power losses are attributable to thermalisation losses.^{1,4} Figure 1.1 illustrates this by dividing the solar spectrum into loss components, where the thermalization is the main loss in the silicon solar cell.⁴

Several approaches for reducing thermalisation losses have been proposed throughout the previous decade. One approach is to explore alternative solar cell materials to silicon, aiming for higher efficiency than the Shockley-Queisser limit of silicon.⁶⁻⁸ Another approach is singlet fission (SF), which enables a single high-energy photon to produce two excitons rather than one. This enhances efficiency by minimizing energy loss and generating more charge carriers. Singlet fission

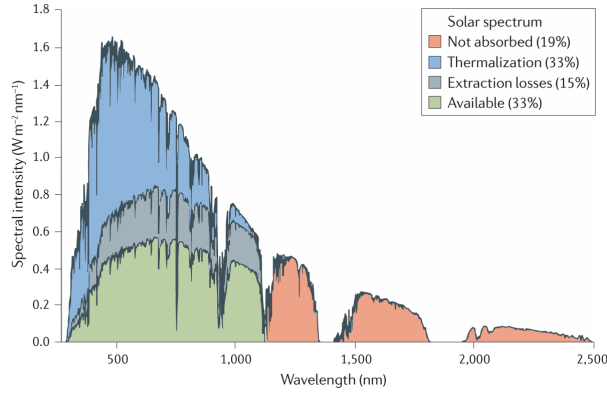


Figure 1.1 – Solar radiation and the Shockley-Queisser limit. Silicon solar cells can capture only 33% of solar radiation (green region). The losses shown in the orange region arise from the inability to absorb photons below the bandgap. The blue region shows the energy lost by thermalisation, as the energy of the absorbed photon is above the bandgap. This figure is obtained from Ref.⁴

may enhance the maximum harvesting efficiency to 35-45%.^{3,4,9} In 1979, Dexter suggested using singlet fission to sensitise a solar cell.¹⁰ However, it is challenging to extract the triplet excitons from singlet fission. Singlet fission not only provides the potential to raise silicon's efficiency limit, but it also reduces the heat load of silicon photovoltaics. Filtering out higher energy photons reduces thermalisation and lowers the operating temperature of the silicon cell. This lowers the costs of providing solar energy by extending the lifetime of the solar cell.¹¹ Despite the current limitations in using singlet fission in photovoltaics, it can significantly enhance the efficiency of silicon solar cells at a feasible cost.

Singlet fission is a carrier multiplication phenomenon that transpires in organic semiconductors. The absorption of a photon in conjugated organic molecules creates electron-hole pairs. This results in the formation of a singlet exciton. The transformation of a spin-0 singlet exciton into double spin-1 triplet excitons is referred to as singlet fission. Triplet-triplet annihilation (TTA) is a photophysical opposite process in which a pair of spin-1 low-energy triplet excitons merge to form a single spin-0 high-energy exciton. In terms of energy, singlet fission is a down-conversion process, where the energy of each exciton is reduced to half its

original value as one exciton splits into two. In contrast, during triplet-triplet annihilation, two excitons combine into one, effectively doubling the energy of the resulting exciton, making it an up-conversion process.

This multiexciton generation process has been studied over the past decade primarily because of its promise to improve solar cell efficiency^{5,12–14}, as one high-energy photon creates two low-energy excited states without losses due to thermalization. SF could also be useful for non-linear optics^{15,16}, OLEDs¹⁷ or even quantum technologies^{18–20} by taking advantage of the fact that a single photon creates a pair of spin-entangled quantum states. However, despite promising results²¹, concrete applications have yet to be realised, in part due to the limited library of materials which undergo singlet fission, none of which is yet ideal¹³. Efficient triplet-triplet annihilation, on the other hand, is preferable for improving the efficiency of organic light emitting diodes (OLEDs)^{22,23} and solar photovoltaics^{24,25}, in addition to biomedical applications²⁶ such as targeted drug delivery and optogenetics^{27,28}. In order to develop these applications, we need to develop a better understanding of singlet fission and triplet-triplet annihilation mechanisms.

Interest in research into SF and TTA dates to the late 1960s.^{29–31} Hence, it predates the discovery of the relationship between solar energy harvesting and singlet fission and triple-triplet annihilation^{32,33}. From a basic physics perspective, these photophysical processes were introduced to investigate interactions between excitonic types and nonradiative transformations. Over the last decade, the recognition that singlet fission and triplet-triplet annihilation potentially permits fundamental improvements in photovoltaics efficiency has led to a significant re-emergence of interest in research in this field^{10,12}. This corresponds with the extensive availability of ultrafast laser systems, which facilitate photophysical processes, especially in relation to singlet fission, which can be detected with unmatched time resolution on femtosecond timescales.^{34,35}

Singlet fission occurs when a photo-excited singlet state S_1 and a ground state singlet state S_0 form an intermediate triplet-pair state known as $^1(TT)$,^{9,36–39}

which by spin evolution, produces a quintet triplet pair state $^5(\text{TT})$. Subsequently, this intermediate triplet pair separates to form a weakly bound triplet pair state ($\text{T}.. \text{T}$), eventually forming two independent triplet excitons. SF is a spin-allowed process, making it sensitive to the spin states involved and the interactions between them. Previous studies have demonstrated that this sensitivity to the spin dynamics makes it highly influenced by external magnetic fields.^{40–42} Therefore, magnetic field effects (MFE) have been used in organic molecules governed by excited state dynamics and spin-dependent phenomena to illustrate singlet fission mechanisms, and to influence their dynamic processes in order to understand the underlying mechanics.^{41,43,44}

Therefore, in Chapter 4, we investigate the temperature and magnetic field-dependence on photoluminescence of a well-characterized anthradithiophene (diF-TES-ADT) singlet fission system.^{37,45} Previous studies based on transient absorption and photoluminescence spectroscopy have suggested that the first step of singlet fission, the generation of $^1(\text{TT})$ is temperature-independent in polycrystalline films of this material.^{37,45} However, in this chapter, we show that magnetic field-dependent photoluminescence spectroscopy reveals that singlet fission to form ($\text{T}.. \text{T}$) is highly temperature-dependent in this material.

In addition to the singlet fission process, in some organic photovoltaic materials, triplet excitons are generated via a direct process known as intersystem crossing (ISC). Some commonly used photovoltaic materials exhibit relatively high ISC yields.⁴⁶ The timescales for ISC are often much slower than those of the corresponding singlet transitions. Nevertheless, examples of ultrafast intersystem crossing are present, although mostly in molecular systems including heavy atoms.⁴⁷ In Chapters 5 and 6, we investigate the rapid intersystem crossing and triplet state formation in tetracene derivatives via excitation-wavelength dependence in picosecond transient absorption spectroscopy. We demonstrate that triplet states are formed by ultrafast intersystem crossing in some tetracene dimers and monomers. The results suggest that ISC is affected by the excitation wavelength, and the triplet yield increases at higher excitation energy.

Tetracenes and pentacenes stand out as the most extensively studied molecules among the various materials investigated for their potential in quantum applications.^{41,48,49} In quantum information science, singlet fission is a promising approach because it can generate spin-entangled quintet triplet pairs by photoexcitation independent of temperature. Achieving quantum coherence at room temperature is challenging, as it requires precise control over the orientation and dynamics of triplet pairs. In Chapter 7, we show that the quantum coherence of quintet multiexcitons can be achieved at room temperature by arranging two pentacene chromophores in parallel and close proximity within a macrocycle. This parallel proximity between adjacent pentacene leads to ultrafast intramolecular singlet fission and selective generation of the quintet states. It also exhibits the longest room-temperature coherence time of the quintet, to our knowledge at the time of publication, of 648 ns. This indicates that the macrocyclic structure is a promising strategy for generating multilevel quantum bits (qubits), whose structure can be strictly defined at the atomic level, and which have a long coherence time, that can be driven at room temperature.

All results chapters are provided after the relevant theoretical background and experimental methodology covered in Chapters 2 and 3, respectively. Finally, in Chapter 8, we conclude by summarizing the key findings of the experimental results, as well as highlighting some critical topics that need further investigation.

Chapter 2

Theory and Background

This chapter presents the fundamental theoretical principles required for understanding the experimental results discussed in the following chapters. These topics include singlet and triplet excitons, their interaction with light, and the mechanisms by which they convert from one state to another. We start by focusing on the interactions between organic molecules and light, along with the excited states produced from these interactions. We demonstrate the interconversion of several excited states, resulting in an extensive range of photophysical behaviours. Finally, we discuss fundamental processes that are essential for this work, such as singlet fission and triplet-triplet annihilation, as well as their use in spectral energy conversion. Most of the information provided in this chapter is from these references^{36,48,50–52}, unless otherwise stated. Additional details and specific points are supported by other references, which are cited accordingly.

2.1 Conjugated organic molecules

Organic molecules refer to molecules that consist of carbon atoms bonded to hydrogen, and also include elements like nitrogen, oxygen, sulphur, and other heteroatoms. Conjugated molecules contain an arrangement of single and double bonds connecting neighbouring carbon atoms. This arrangement facilitates the creation of electronic states that can delocalise over several atoms. The elec-

trons in these states, described in terms of ‘molecular orbitals’, are responsible for several interesting features of conjugated organic materials, particularly their interaction with light.

The unique electronic properties of conjugated systems arise from the delocalisation of π -electrons, which essentially depends on the nature of π -bonds. In these systems, π -bonds are responsible for the extended electronic structure, which affects molecule stability, optical absorption, and conductivity. To fully understand how conjugation works, it is important to illustrate the creation and function of π -bonds in a molecular environment.

Hund’s rules define the electronic structure of carbon atoms as $(1s)^2(2s)^2(2p)^2$. The inner 1s and outer 2s orbits contain pairs of electrons, whereas the 2p orbitals contain the last two electrons. Consequently, the outer shell of carbon consists of four valence electrons. To better explain bonding in carbon-based compounds, we will use the sp^n hybridisation approximation. Hybridised orbitals are atomic orbitals that combine to generate new, equivalent orbitals with specific spatial orientations optimized for bonding, while unhybridised orbitals maintain their original shape and orientation.

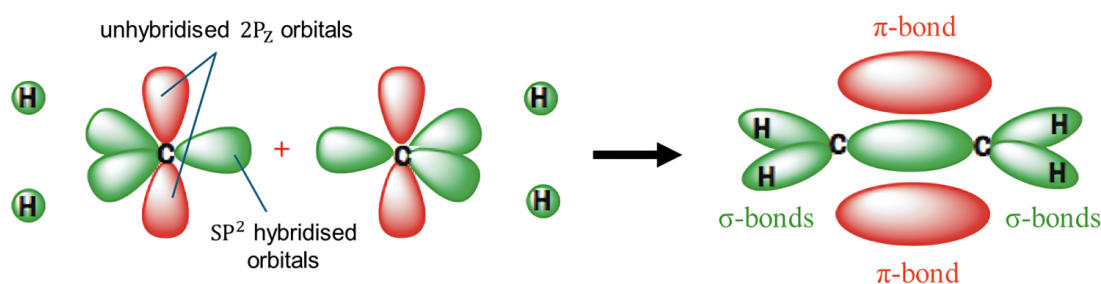


Figure 2.1 – Hybridisation of atomic orbitals. Schematic representation of σ -bond formation from sp^2 hybridised carbon atoms and π -bond production via the overlap of unhybridised p_z -orbitals.

For example, Figure 2.1 demonstrates that the 2s, $2p_x$, and $2p_y$ orbitals combine through hybridization to form three sp^2 orbitals arranged in the xy-plane. One electron is present in each of the sp^2 orbitals. The remaining electron resides in the unhybridized $2p_z$ orbital, oriented perpendicular to the sp^2 plane. The

sp^2 orbitals between the two carbon atoms create a σ -bond through the head-on overlap of sp^2 - sp^2 orbitals. The sideways overlap of unhybridized $2p_z$ orbitals forms π -bonds, enabling conjugation across the molecule. In the π -bond, the electron density is delocalised in areas located above and below the molecular plane. Understanding the nature of atomic bonding is crucial because it helps in the interpretation of molecular structures, which can be investigated and characterised experimentally using spectroscopy.

2.2 Electronic properties of an organic conjugated molecule

Spectroscopy involves examining how matter interacts with electromagnetic radiation, such as light, specifically investigating how matter absorbs or emits energy across various wavelengths. Quantum physics allows us to characterise the energies of target molecules by expressing any system in terms of a wavefunction Ψ , which typically depends on spatial and temporal coordinates. Using the time-independent Schrödinger equation, the electronic characteristics of an organic molecule can be described as

$$H|\Psi\rangle = E|\Psi\rangle. \quad (2.1)$$

A key simplifying assumption is the Born-Oppenheimer approximation, which involves the separation of the behaviour of the electrons and the nuclei. Nuclear motion is much slower than electronic motion due to the large mass difference. As a result, the electronic and nuclear motions can be treated independently. Under this assumption, the total Hamiltonian is separated into three components: an electronic term H_{e-e} arising solely from electrons, a nuclear term H_{n-n} associated with the nuclei, and a mixed electron-nuclear interaction term H_{e-n}

$$H(r, R) = H_{el-el}(r) + H_{nuc-nuc}(R) + H_{el-nuc}(r, R), \quad (2.2)$$

where R and r denote the set of nuclear and electronic coordinates, respectively. H_{el-el} is the electronic term, which can be written as

$$H_{el-el}(r) = \sum_i \frac{\mathbf{p}_i^2}{2m_i} + \frac{1}{2} \sum_{i \neq j} \frac{e^2}{4\pi\epsilon_0 |\mathbf{r}_i - \mathbf{r}_j|}, \quad (2.3)$$

where the first component indicates the electronic kinetic energy of the electrons, while the second term defines the electronic electrostatic potential. The momentum operator for electron i is denoted as \mathbf{p}_i , and m represents the single electron mass. e indicates the elementary charge, and the vacuum permittivity is denoted by ϵ_0 .

Likewise, the nuclear term, $H_{nuc-nuc}$, can be expressed as

$$H_{nuc-nuc}(R) = \sum_\alpha \frac{\mathbf{P}_\alpha^2}{2M_\alpha} + \frac{1}{2} \sum_{\alpha \neq \beta} \frac{Z_\alpha Z_\beta e^2}{4\pi\epsilon_0 |\mathbf{R}_\alpha - \mathbf{R}_\beta|}, \quad (2.4)$$

where the first component indicates the nuclear kinetic energy and the subsequent term is the nuclear electrostatic potential energy. \mathbf{P}_α denotes the momentum operator for nucleus α , M_α represents the mass of nucleus α , and Z_α denotes the proton number of nucleus α . Note that the general form of the momentum operators is $\mathbf{p} = -i\hbar\nabla$, where ∇ is the gradient operator, defined as $\nabla = \left(\frac{\partial}{\partial x}, \frac{\partial}{\partial y}, \frac{\partial}{\partial z} \right)$ in Cartesian coordinates. It acts on a scalar wavefunction to give the spatial rate of change in each dimension.

Finally, the nuclei-electrons Coulomb attraction, H_{el-nuc} , is described as

$$H_{el-nuc}(r, R) = V_{el-nuc}(r, R) = - \sum_{\alpha, i} \frac{Z_\alpha e^2}{4\pi\epsilon_0 |\mathbf{R}_\alpha - \mathbf{r}_i|}. \quad (2.5)$$

2.3 Excitons

In condensed matter physics, the behavior of electrons is described in terms of energy bands, mainly the valence band and the conduction band. These bands determine the electrical conductivity of a material, as seen in Figure 2.2. The energy range separating the valence and conduction bands is a forbidden region,

known as the band gap. In conductors, there is no significant energy gap between the valence and conduction bands. In some metals, these bands even partially overlap, allowing electrons to move freely between them. As a result, the conduction band is partially filled. In insulators, a large energy gap separates the valence band from the conduction band. The valence band is completely filled, leaving the conduction band empty. Semiconductors fall between conductors and insulators, presenting a smaller band gap. Energy is required to break covalent bonds and release free electrons into the conduction band, which typically contains a large number of empty states. At room temperature, some semiconductors have sufficient thermal energy to move some electrons from the valence band into the conduction band, allowing limited electrical conduction.⁵³

When an electron transitions from valence band to the conduction band, a positively charged hole is created in the valence band. The hole in the valence band and the electron in the conduction band are attracted to each other by electrostatic force, resulting in the creation of an electron-hole pair. The bound state of an electron-hole pair is referred to as an exciton.

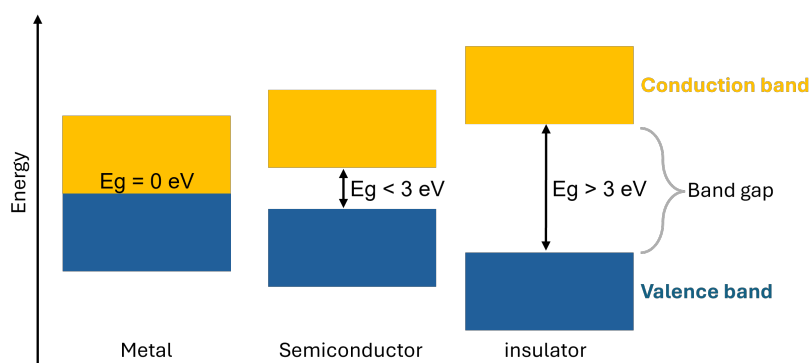


Figure 2.2 – Valence and conduction bands. A schematic diagram of metallic, semiconductor, and insulating materials illustrating the distinct valence and conduction bands associated with each type. The main distinction between these materials lies in the band gap, which is more than 3 eV in insulators, smaller than 3 eV in semiconductors, and negligible in conductors (metals).⁵⁴ This Figure is adapted from Ref.⁵⁵

In molecular orbital theory, exciton is formed when a photon is absorbed and

an electron is promoted from the molecule’s highest occupied molecular orbital (or HOMO) to the lowest unoccupied molecular orbital (or LUMO), leaving behind a positively charged hole in HOMO. This electron-hole pair then interacts through the Coulomb force, forming a bound state, the exciton.

There are three main types of excitons. Wannier-Mott exciton, Frenkel exciton, and charge transfer exciton (Figure 2.3). Wannier-Mott excitons are primarily found in inorganic semiconductors, where the high dielectric constant weakens the electron-hole interaction. This results in weakly bound excitons (~ 10 meV binding energy).⁵⁰ The electron and hole separation is extremely large, ranging from a few hundred up to thousands of Angstroms,⁵⁶ resulting in exciton delocalisation. Conversely, Frenkel excitons can be observed in organic molecules presenting poor dielectric screening of the electron-hole electrostatic attraction. These excitons are tightly bound, with an electron-hole binding energy of around 0.1- 1 eV.^{50,57} This localises the exciton to a single molecule. Finally, charge-transfer (CT) exciton, which is commonly found in organic semiconductors, lies somewhere between the localized Frenkel excitons and delocalised Wannier-Mott excitons. This exciton is relatively localised, with the hole and electron commonly located on nearby molecules, as shown in Figure 2.3.

Exciton binding energy is the energy required to separate an electron and a hole that have formed a bound state (exciton) in a material. It’s related to the bandgap energy, which is the energy required to create a free electron and hole in the material. The exciton binding energy is typically less than the bandgap energy and can be determined by measuring the difference between the transport band gap, which represents the energy of the free electron state, and optical band gap, which corresponds to the exciton energy as the first excitation state.⁵⁸

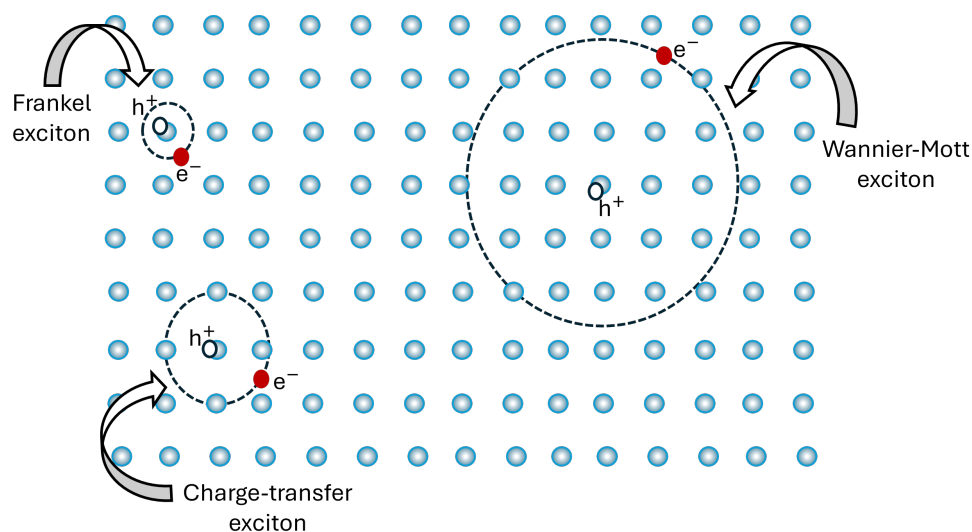


Figure 2.3 – Exciton types. Weakly bound Wannier-Mott excitons with an extremely large distance between the hole and electron. Frenkel excitons are tightly bound and highly localized to a single molecule. Charge-transfer excitons are relatively localized, with the hole and electron commonly located on nearby molecules.⁵⁰

The term ‘exciton’ in this thesis will refer to a Frenkel exciton, unless otherwise indicated, since we are mostly working with conjugated molecules. Excitons are fundamentally two-electron excited states, and due to the nature of electrons as spin $-\frac{1}{2}$ particles, spin is crucial in exciton photophysics.

2.4 Electron Spin

Exciton is an electron-hole bound state, fundamentally involving two particles. It arises due to the Coulomb interaction between the unpaired electron in the LUMO and the hole left behind in the HOMO after photoexcitation. In the ground state, the HOMO is occupied by two electrons, and according to the Pauli exclusion principle[†], both electrons must have different spins. As a result, one electron is spin up, $|\uparrow\rangle_1$, while the other electron is spin down, $|\downarrow\rangle_2$.

[†]Pauli exclusion principle: The total wavefunction (including spin) must be antisymmetric with respect to the interchange of any pair of electrons.⁵¹

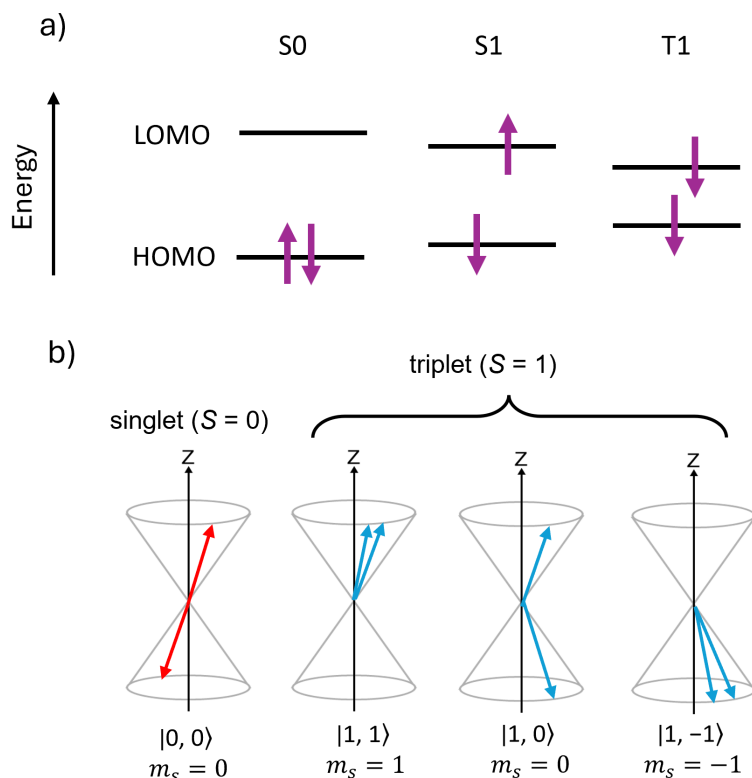


Figure 2.4 – Singlet and triplet excitons. (a) Energy level diagram showing the HOMO and LUMO for the ground state (S_0), singlet exciton (S_1), and triplet exciton (T_1). The relative positions of S_1 and T_1 with respect to S_0 are influenced by Coulomb interaction (exciton binding energy) as well as exchange interaction. (b) Vector diagram of two-electron singlet (red arrows) and triplet (blue arrows) spin states.⁵¹

Upon excitation, one electron moves to the LUMO, placing the electrons in different orbitals, which allows them to have either parallel or antiparallel spins (Fig. 2.4 a). An exciton consists of two electrons, each with two possible spin states, resulting in four possible spin wavefunctions. Figure 2.4 b presents a vector representation of them, where in the antiparallel case (red arrows), the state is known as ‘singlet’, where the total spin angular momentum $S=0$. The three more different arrangements of spins that provide a total spin of $S=1$ are known as ‘triplets’.

It is possible to generate the spin wavefunctions for these two electrons from the products of the spins of one electron, such as $|\uparrow\rangle_1 |\downarrow\rangle_2$. The Spin wavefunc-

tions are the eigenstates of the total spin operator $S^2 = (S_1 + S_2)^2$, which has an eigenvalue of S . Spin wavefunctions must also be eigenstates of the spin operator projection S_z onto the z -axis, which has an eigenvalue of the magnetic spin quantum number m_S . In bra-ket notation, the eigenstates are represented as $|S, m_S\rangle$ and are determined by

$$\textbf{Singlet: } |S\rangle \rightarrow |0, 0\rangle = \frac{1}{\sqrt{2}}(|\uparrow\rangle_1 |\downarrow\rangle_2 - |\downarrow\rangle_1 |\uparrow\rangle_2) \quad (2.6)$$

$$\textbf{Triplets: } |T_+\rangle \rightarrow |1, +1\rangle = |\uparrow\rangle_1 |\uparrow\rangle_2 \quad (2.7)$$

$$|T_0\rangle \rightarrow |1, 0\rangle = \frac{1}{\sqrt{2}}(|\uparrow\rangle_1 |\downarrow\rangle_2 + |\downarrow\rangle_1 |\uparrow\rangle_2) \quad (2.8)$$

$$|T_-\rangle \rightarrow |1, -1\rangle = |\downarrow\rangle_1 |\downarrow\rangle_2. \quad (2.9)$$

We notice that the triplet spin wavefunctions exhibit full symmetry with respect to particle exchange, unlike the antisymmetric singlet spin wavefunction. To explore this, we introduce a particle exchange operator, $P_{1\leftrightarrow 2}$, which simply swaps the labels of two identical particles in a quantum state. For example:⁵⁹

$$P_{1\leftrightarrow 2} |x_1; x_2\rangle = |x_2; x_1\rangle. \quad (2.10)$$

Applying this operator to the singlet spin wavefunction yields an eigenvalue of -1:

$$P_{1\leftrightarrow 2} |0, 0\rangle = \frac{1}{\sqrt{2}} (|\uparrow\rangle_2 |\downarrow\rangle_1 - |\downarrow\rangle_2 |\uparrow\rangle_1) = -|0, 0\rangle. \quad (2.11)$$

This result confirms that the singlet state is antisymmetric under the exchange of the two electrons. It is worth noting that in Equations 2.6 -2.9, the spin wavefunctions are one part of the ‘total’ electron wavefunctions $|\Psi_k\rangle$. The spatial wavefunctions $|\psi_k\rangle$ must also be taken into account. The total wavefunction of two electrons must exhibit antisymmetry under the electrons’ exchange, according to the Pauli exclusion principle. Thus, the singlet spin wavefunction (antisymmetric)

must be coupled to a symmetric spatial wavefunction, whereas the triplet spin wavefunction (symmetric) must be coupled to an antisymmetric spatial wavefunction. Therefore, the spatial wavefunctions for the first and second electrons in $|\phi_a\rangle$ and $|\phi_b\rangle$ orbitals are written as

$$|\psi^{\text{singlet}}\rangle = \frac{1}{\sqrt{2}} (|\phi_a^1\rangle|\phi_b^2\rangle + |\phi_b^1\rangle|\phi_a^2\rangle) \quad \text{symmetric.} \quad (2.12)$$

$$|\psi^{\text{triplet}}\rangle = \frac{1}{\sqrt{2}} (|\phi_a^1\rangle|\phi_b^2\rangle - |\phi_b^1\rangle|\phi_a^2\rangle) \quad \text{anti-symmetric.} \quad (2.13)$$

It is essential to take into account the quantum mechanical dimension. According to the Pauli exclusion principle, two electrons having identical spins cannot reside in the same spatial position. Therefore, the triplet state electrons experience increased repulsion, resulting in a reduction in Coulomb repulsion and a consequent drop in total energy. In contrast, singlet electrons have antiparallel spins, resulting in their being close to each other. This leads to an enhancement of the Coulomb interaction, hence increasing the total energy.

This additional energy change is denoted as the exchange energy J . It serves as a quantum mechanical refinement of the classical Coulomb interaction. Thus, triplet excitons typically have a lower energy level than singlet excitons (Figure 2.4 a), and the singlet and triplet energy splitting is $\Delta E_{\text{S-T}} = 2J$. This energy is usually around 0.7–1.0 eV for a broad variety of conjugated molecules and polymers.⁵¹ The exchange energy can be calculated using the exchange integral defined as:

$$J_{ex} = \iint \phi_a^*(\mathbf{r}_1)\phi_b^*(\mathbf{r}_2)V_{el-el}^{\text{eff}}(\mathbf{r}_1 - \mathbf{r}_2)\phi_b(\mathbf{r}_1)\phi_a(\mathbf{r}_2) d^3\mathbf{r}_1 d^3\mathbf{r}_2, \quad (2.14)$$

where V_{e-e} is the Coulombic interaction potential between the two electrons, and it has no spin dependence.⁶⁰ From Equation 2.14, it is evident that J is influenced by the overlap between $|\phi_a\rangle$ and $|\phi_b\rangle$. Molecules with significant overlap between the HOMO and LUMO tend to exhibit a high energy gap between singlet and triplet excitons, while reduced overlap leads to a smaller singlet–triplet separation. Consequently, the singlet-triplet gap may be adjusted by suitable molecular

design.⁶¹

The presence of separate singlet and triplet states accounts for several interesting physical characteristics of conjugated organic molecules, and the modifiability of the exchange energy has significant implications for singlet exciton fission. The electron spin results in a magnetic moment that may interact with external magnetic fields via Zeeman interaction. The magnetic moment of an electron can also interact with the magnetic moment of nuclear spins via the hyperfine interaction or with other electron spins via dipolar or exchange couplings. These interactions will be discussed below.

2.4.1 Zeeman Interaction

Due to the spin of the electron, a magnetic moment is produced,

$$\hat{\mu} = -g_e\mu_B\hat{S}. \quad (2.15)$$

In this equation, g_e represents the electron g -factor, $\mu_B = \frac{e\hbar}{2m_e}$ denotes the Bohr magneton, which is determined by the electron charge ‘ e ’, and the electron mass is denoted as ‘ m_e ’. The z-axis projection of the spin magnetic moment, $\hat{\mu}_z$, is expressed as

$$\hat{\mu}_z|s, m_s\rangle = -g_e\mu_B m_s|s, m_s\rangle. \quad (2.16)$$

The interaction between an external magnetic field, B , and this magnetic moment is represented in the Hamiltonian equation as follows:

$$\hat{H}_Z = -\hat{\mu} \cdot \mathbf{B} = g_e\mu_B\hat{S} \cdot \mathbf{B}. \quad (2.17)$$

The spin state energy is divided under the influence of a magnetic field, based on its spin projection, m_s . When a magnetic field is applied in the z-direction, spin states with $m_s = 0$ exhibit consistency under the Zeeman interaction. Therefore, their energy remains constant despite the increasing magnetic field. When a strong field is present in the z-direction, $\hat{\mu}$ may be substituted by the z-component of

the spin magnetic moment, $\hat{\mu}_z$. This substitution yields the energy eigenvalues, expressed as $E = g_e \mu_B m_s B_0$, where B_0 is the magnetic field strength. For an electron with $m_s = \pm \frac{1}{2}$, this results in an energy splitting of

$$\Delta E = g_e \mu_B B_0. \quad (2.18)$$

Based on the geometry of the molecule as well as spin-orbit coupling (section 2.5.2), the g -factor could be anisotropic. Therefore, the more general version of the Zeeman interaction consists of the g -tensor, g ,

$$\hat{H}_Z = g \mu_B \cdot \mathbf{B} \cdot \hat{S}. \quad (2.19)$$

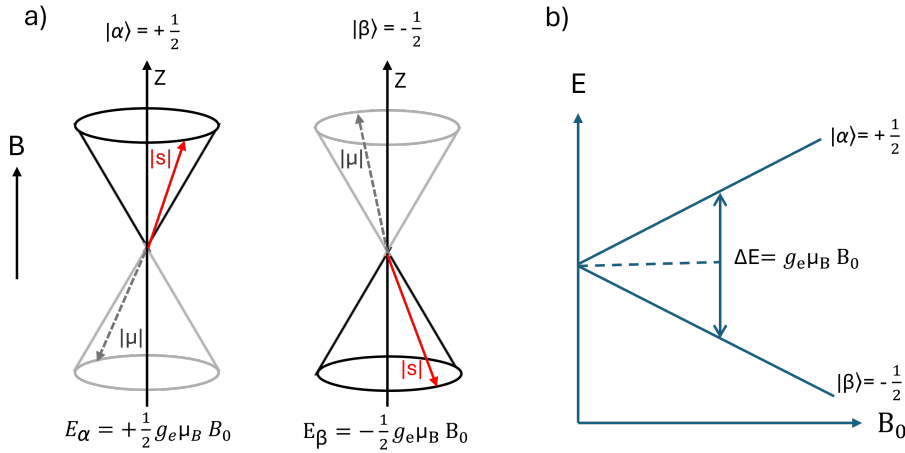


Figure 2.5 – One electron spin. (a) The vector model represents the $|\alpha\rangle$ and $|\beta\rangle$ states. It also represents the magnetic moment, μ (dashed arrow), generated by the spin, which is anti-parallel to the spin vector. (b) Zeeman Interaction occurs when an external magnetic field is applied to a one-electron system. It induces the separation of the degenerate states $|\alpha\rangle$ and $|\beta\rangle$.^{53,62}

When a magnetic field is present, a spin undergoes precession around the field direction at a frequency known as the Larmor frequency, ω_L , defined by,

$$\omega_L = \frac{g_e \mu_B}{\hbar} B_0. \quad (2.20)$$

Spin mixing and relaxation are two processes significantly influenced by Larmor precession. Figure 2.5 presents an overview of the $|\alpha\rangle$ and $|\beta\rangle$ states[†]. In the vector model (Figure 2.5 a), the spins are represented as a cone, along with the magnetic moment, μ , generated by the spins. The energy level splitting caused by the Zeeman interaction is presented in Figure 2.5 b.

2.4.2 Hyperfine Interaction

A hyperfine interaction may arise when electron spins interact with the magnetic moments of nuclear spins. The hyperfine interaction is significantly weaker than the Zeeman interaction. This interaction is significant in the study of spin-correlated radical pairs (anions and cations).^{63,64} Nevertheless, because of its minor impact on the Hamiltonian, it is often disregarded by the singlet fission community. However, the hyperfine interaction affects spin relaxation processes and Larmor precession.^{65,66}

2.4.3 Interactions of two electron spins

When an external magnetic field is applied, the spin states with non-zero spin projection, $|T_+\rangle$ and $|T_-\rangle$, will experience energy separation that increases with the field strength based on Zeeman interaction, as discussed in Section 2.4.1. In addition, due to the interaction between electron spins and the nuclear environment, each spin state will exhibit hyperfine structure. Furthermore, the electron spin will interact with nearby electron spins via electron-electron interactions. This interaction is divided into the exchange interaction and the dipolar interaction, or zero-field splitting, which are discussed below.

Exchange Interaction

As a result of the exchange interaction, spin states associated with different multiplicities will have different energies. Multiplicity refers to the number of possible

[†] $|\uparrow\rangle$ $|\downarrow\rangle$ are written in some references, such as reference⁵⁰, as $|\alpha\rangle$ and $|\beta\rangle$, respectively.

spin states associated with a given total spin quantum number, S . It can be expressed as: $Multiplicity = 2S + 1$,⁶⁷ where $S = 0$ for a singlet and 1 for a triplet. For a system of two electrons, the total wavefunction should be antisymmetric with respect to particle exchange, due to the Pauli exclusion principle. As previously indicated, the antisymmetric spin wavefunction in a singlet results in a symmetric spatial wavefunction. As illustrated in Figure 2.6, the lowest energy symmetric spatial wavefunction contains no nodes, whereas the lowest anti-symmetric spatial wavefunction has one node. The node in the antisymmetric spatial wavefunction increases the spatial separation of the two electrons, thereby reducing the Coulombic repulsion between them. As a result, the symmetry of the spin wavefunction of the triplet and the antisymmetry of the spatial wavefunction result in an overall triplet wavefunction having a lower energy than the singlet state.

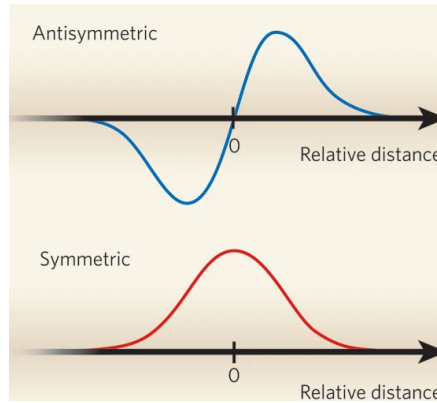


Figure 2.6 – Symmetric and antisymmetric wavefunction. The existence of a node in the lowest anti-symmetric spatial wavefunction increases electron spatial separation and therefore reduces Coulombic repulsion of the two negatively charged particles. This figure is obtained from Ref.⁶⁸

The exchange interaction is described as⁶⁹

$$\hat{H}_{ex} = J \hat{S}_1 \cdot \hat{S}_2, \quad (2.21)$$

where J is the exchange constant, defined as $J = 2J_{ex}$, where J_{ex} represents the exchange integral derived from Coulombic interactions in electronic wavefunctions

(Equation 2.14).^{53,70}

Zero-Field Splitting

In the zero-field condition, the energies of the three triplet states are non-degenerate. This mostly results from the dipole-dipole interactions of the two unpaired electrons and their magnetic moments.^{50,71} The energy splitting of the three triplets is referred to as ‘zero-field splitting’, which is typically represented via an additional Hamiltonian term

$$\hat{H}_{zfs} = S \cdot DS, \quad (2.22)$$

where D denotes the zero-field splitting tensor (matrix), and S represents the spin vector operator. D is diagonalisable, indicating the presence of a particular coordinate system in which only three components (D_x , D_y , D_z) characterise the interaction. It is also traceless, meaning that its eigenvalues sum to zero in the context of dipolar interactions ($Tr(D) = D_x + D_y + D_z = 0$).⁷¹

$$D = \begin{pmatrix} D_x & 0 & 0 \\ 0 & D_y & 0 \\ 0 & 0 & D_z \end{pmatrix} \quad (2.23)$$

According to the standard definition,

$$|D_z| \geq |D_x| \geq |D_y|. \quad (2.24)$$

The z-axis thus relates to the maximum dipolar coupling.⁷¹ We can use two zero-field splitting factors, D and E , instead of three to define the interaction, as D is traceless. The D and E parameters are given by

$$D = \frac{3}{2}D_z, \quad E = \frac{1}{2}(D_x - D_y). \quad (2.25)$$

Corresponding with the previously stated definition of Equation 2.24,^{71,72}

$$-1 \leq \frac{3D}{E} \leq 0. \quad (2.26)$$

E always has the opposite sign to D . Because of this, we can write the equation 2.22 as

$$H_{zfs} = D \left(S_z^2 - \frac{1}{3} S^2 \right) + E (S_x^2 - S_y^2). \quad (2.27)$$

In this context, S_x , S_y , and S_z represent the x , y , and z components of the spin operator vector S . The D parameter is inversely proportional to the cube of the average interspin separation ($D \propto \frac{1}{r^3}$), reflecting the spatial extent of the triplet exciton. Therefore, a smaller D suggests a greater exciton size (due to increased spin separation), whereas a larger D implies a more localised exciton. The E parameter correlates with the rhombicity of the D -matrix, indicating that larger E suggests greater asymmetry.⁷¹ Using electron paramagnetic resonance (EPR) measurements, the D and E parameters are calculated by fitting the EPR spectrum to a spin Hamiltonian model that includes zero-field splitting and Zeeman interactions.⁷³ However, to determine the signs, complex magnetic resonance measurements are required. The measured D value varies between 4 to 10 μeV for the majority of π -conjugated molecules.⁵⁰

2.4.4 Triplet Pair

When a singlet exciton undergoes spin-correlated separation into two triplet excitons in the singlet fission, there is an intermediate state of two correlated triplet excitons. This state consists of four electrons. From the one-electron basis, we can identify 16 potential states for the four-electron system: $|\uparrow\uparrow\uparrow\uparrow\rangle, |\uparrow\uparrow\uparrow\downarrow\rangle, \dots, |\downarrow\downarrow\downarrow\downarrow\rangle$.⁵² We obtain 16 pure spin states from linear combinations of these states, which are 2 singlet states ($S = 0$), 9 triplet states ($S = 1$), and 5 quintet states ($S = 2$).

Many theoretical studies have been conducted on the triplet pair state.^{44,52,74} This system can be simplified by considering two pairs of interacting electrons, or two $S = 1$ triplets, limiting our consideration to the nine lowest-lying states, as described by Merrifield.⁴⁰ These states are one singlet, three triplets, and five quintets. The singlet state is represented as

$$|S\rangle = \sqrt{\frac{1}{3}}(|xx\rangle + |yy\rangle + |zz\rangle), \quad (2.28)$$

where $|xx\rangle$ represents $|T_x, T_x\rangle$, in the low-field basis for each triplet in the pair. The correlated triplet pair state, referred to as $^1(TT)$, is considered to be the singlet $S = 0$ state. The triplet and quintet states are represented in the low-field basis as follows:

$$\begin{aligned} |T_x\rangle &= \frac{1}{\sqrt{2}}(|yz\rangle - |zy\rangle) \\ |T_y\rangle &= \frac{1}{\sqrt{2}}(|zx\rangle - |xz\rangle) \\ |T_z\rangle &= \frac{1}{\sqrt{2}}(|xy\rangle - |yx\rangle) \\ |Q_a\rangle &= \frac{1}{\sqrt{2}}(|xx\rangle - |yy\rangle) \\ |Q_b\rangle &= \frac{1}{\sqrt{6}}(|xx\rangle + |yy\rangle - 2|zz\rangle) \\ |Q_x\rangle &= \frac{1}{\sqrt{2}}(|yz\rangle + |zy\rangle) \\ |Q_y\rangle &= \frac{1}{\sqrt{2}}(|zx\rangle + |xz\rangle) \\ |Q_z\rangle &= \frac{1}{\sqrt{2}}(|xy\rangle + |yx\rangle). \end{aligned} \quad (2.29)$$

This triplet pair, consisting of nine spin sublevels, serves as an intermediate state in the singlet fission process. Several investigations have demonstrated the existence of the triplet-pair state, including vibrational spectroscopy,^{75,76} electron spin resonance (ESR),^{69,77,78} and transient absorption spectroscopy.^{79–84} Multiple studies indicate that the triplet pair state can be emissive, hence confirming the existence of this state.^{80,84–86}

Figure 2.7 b presents an overview of the nine sublevels of the triplet pair state and the energy level splitting in the presence of an external magnetic field. As illustrated in the figure, the singlet is separated energetically from the triplet and quintet states by J and $3J$, respectively.^{69,87} Furthermore, the vector model

(Figure 2.7 a) displays an example of a $m_S = 2$ quintet state. In the presence of an external field, the states where $m_S = 0$ remain unchanged. Both the triplet and quintet sublevels exhibit zero-field splitting, each characterised by distinct ZFS parameters, where D_T and E_T for triplet states, and D_Q and E_Q for quintet states.⁷⁸

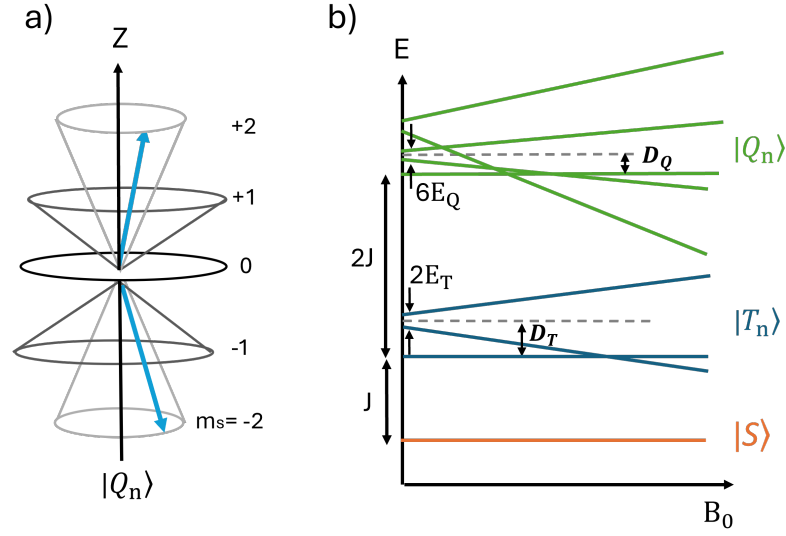


Figure 2.7 – The nine sublevels of the triplet pair state: one singlet, three triplets, and five quintets. The quintet is shown in the vector model in (a). The energy level splittings under the influence of an external magnetic field are demonstrated in (b). This figure is reproduced from Ref.⁸⁸

2.4.5 The Spin Hamiltonian

We can now formulate the spin Hamiltonian of the triplet pair state based on previous information. All interactions have been addressed except the intertriplet dipolar coupling. As mentioned before, the triplet pair state consists of two interacting triplets. There will be zero-field splitting, or intratriplet dipolar coupling, in each triplet. The two triplets will also exhibit a dipolar coupling that depends on the distance r separating them. While this is similar to the previously discussed ZFS, the tensor characterising this interaction will be referred to as X for clarity. Generally, $X \approx \frac{D}{100}$. This subsequently provides us with the Hamiltonian,^{89,90}

$$\begin{aligned}
\hat{H} = & \underbrace{J\hat{\mathbf{S}}_A \cdot \hat{\mathbf{S}}_B}_{\text{Exchange}} + \underbrace{X \left[\hat{S}_A \cdot \hat{S}_B - 3(\hat{S}_A \cdot \hat{r})(\hat{S}_B \cdot \hat{r}) \right]}_{\text{Intertriplet Dipolar}} \\
& + \sum_{i=A,B} \left[\underbrace{g_i \mu_B \mathbf{B} \cdot \hat{\mathbf{S}}_i}_{\text{Zeeman}} + \underbrace{D \left(\hat{S}_{i,z}^2 - \frac{1}{3} \hat{S}_i^2 \right) + E \left(\hat{S}_{i,x}^2 - \hat{S}_{i,y}^2 \right)}_{\text{ZFS}} \right], \quad (2.30)
\end{aligned}$$

where, J represents the intertriplet exchange energy, X denotes the magnitude of intertriplet dipole coupling, \hat{r} is the unit vector between the two molecules, B indicates the external magnetic field, and D and E ($\gg X$) are the intratriplet zero-field splitting parameters.

Without an external field, the nine spin states are eigenstates of this Hamiltonian. The triplet pair state exhibits two regimes, strongly coupled and weakly coupled. The exchange interaction, or the interactions between the two triplets, is high ($J \gg D$) in the strongly coupled pair. This type of spin states are represented as $^1(\text{TT})$, $^3(\text{TT})$, and $^5(\text{TT})$. However, the spins change over time, resulting in weak interactions between the two triplets, leading to $J \ll D$. This produces a weakly coupled triplet pair state, $^1(\text{T..T})$. This state is no longer an eigenstate, and the spin is not a good quantum number. This weakly coupled triplet pair state often exhibits a mixed spin nature.

2.4.6 Spin Evolution

Several dynamic processes may cause spins to evolve, especially in spin ensembles. Some chemical reactions can lead to spin quenching, which is a loss of a particular spin state due to interactions. For example, a triplet spin state may interact with molecular oxygen,⁹¹ or triplet energy may transfer to other molecules during sensitisation measurements. Furthermore, spins evolve with time via mechanisms such as relaxation and spin mixing.

Spin Mixing

As previously stated, transitions between spin states are possible. This is presented in the vector-model illustration of singlet and triplet states in Figure 2.4 a. Spin mixing occurs in the weakly coupled triplet pair state $^1(T..T)$, where the exchange interaction J is small. For instance, $^1(T..T)$ can be mixed with $^5(T...T)$.⁹² Thus, the weakly coupled pair is considered to consist of triplets, $|T\rangle$, quintets, $|Q\rangle$, and singlet-quintet mixtures, $|SQ\rangle$. Zeeman interaction is responsible for the spin mixing efficiency. Therefore, spin mixing becomes inefficient when the spin states are energetically separated. This phenomenon results in the detection of magnetic field effects, as illustrated in Chapter 4.

Spin mixing is primarily caused by spin-orbit coupling (section 2.5.2).^{93,94} Additionally, hyperfine interactions between electron and nuclear spins can contribute to spin mixing.⁹⁴ Other factors can influence spin mixing, such as the presence of magnetic fields, the interaction between electrons, and the material electronic structure.^{93,95–97}

Quantum Beating

As indicated previously, the strongly coupled triplet-pair state $^1(TT)$ is mostly a singlet state. However, the spin wavefunction $|S\rangle$ of this state is a linear combination of the $|xx\rangle$, $|yy\rangle$, and $|zz\rangle$ triplet pairs, as seen in Equation 2.28. Therefore, under the condition of weak exchange coupling, $|S\rangle$ is not an eigenstate of the Hamiltonian; rather, it is a superposition of eigenstates. Over time, each eigenstate evolves with a phase that is proportional to its energy. Consequently, the singlet state will exhibit time dependence:

$$|S(t)\rangle = \frac{1}{\sqrt{3}} \left(e^{-iE_{xx}t/\hbar} |xx\rangle + e^{-iE_{yy}t/\hbar} |yy\rangle + e^{-iE_{zz}t/\hbar} |zz\rangle \right). \quad (2.31)$$

Equation 2.31 is valid if the spin wavefunction $|S(t)\rangle$ represents a weakly exchange-coupled $S = 0$ triplet pair, denoted as $^1(T...T)$.⁹⁸ Due to the differences in E_{xx} , E_{yy} , and E_{zz} , the coupling $|\langle S_1 | ^1(T...T) \rangle|^2$ will therefore change in time,

leading to oscillations in the delayed fluorescence. At zero applied magnetic field, we anticipate three oscillation frequencies governed by the ZFS parameters, D and E .⁴⁹ Such oscillations are known as quantum beats, and they have been observed in the delayed fluorescence of tetracene crystals on a nanosecond timescale at room temperature.^{49,99} The observations of the quantum beating provide evidence for the weakly coupled triplet pair state existence.

Following our discussion of some of the basic spin physics necessary for the investigation of singlet fission, we will now investigate some concepts of photophysical processes.

2.5 Photophysical Processes

In Figure 2.8, a Jablonski diagram presents the main photophysical processes. A ground state (S_0) absorbs a photon during the absorption process, which results in transitions to a higher energy singlet state (purple arrows). A rapid internal conversion (indicated by grey dotted arrows) may subsequently return the molecule to the S_1 state. It is possible for S_1 to decay back to the S_0 state either radiatively, as illustrated by the orange arrows for fluorescence, or non-radiatively via internal conversion. Spin-orbit coupling can also promote a transition to vibrational levels in a triplet manifold through the intersystem crossing process (red arrow). Radiative decay from T_1 states to the ground state can occur through phosphorescence (green arrows); however, non-radiative decay often overcomes this weakly permitted transition. Upon the population of S_1 and T_1 states, additional absorption can occur, leading to transitions to higher-energy states within the same spin manifold (blue arrows), which is commonly known as photo-induced absorption (PIA) or excited-state absorption (ESA). These transitions are probed in the transient absorption spectroscopy. In the following sections, we explore each process in detail.

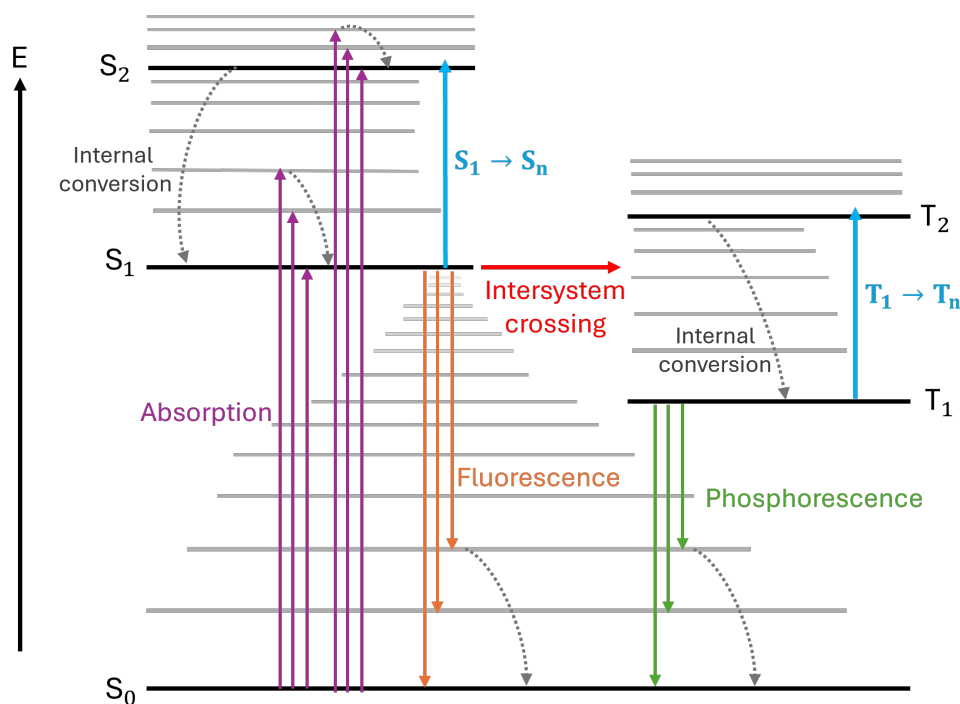


Figure 2.8 – Jablonski diagram, summarising key photophysical processes:

(1) Absorption (purple arrows) is the transition from the ground state S_0 to any higher-lying singlet states. (2) Fluorescence (orange arrows): S_1 decays back to its ground state. (3) Intersystem crossing (red arrow): the transition from singlet to vibrational states of the triplet manifold. (4) Phosphorescence (green arrows): occurs as T_1 states decay radiatively to the ground state. (5) Internal conversion decays (grey dotted arrows): is the rapid decay from the excited singlet/triplet states to lower-lying states, or to the ground state. (6) Excited state absorption transitions (blue arrows) from S_1 and T_1 to higher-lying states S_n and T_n , respectively, which are probed in transient absorption spectroscopy.

2.5.1 Absorption and Emission

Photon absorption or emission causes the transitions between the electronic states of a molecule. The vibrational sublevels associated with each electronic state give rise to fine structure in the observed transitions. Upon photon absorption, an electron can be excited from HOMO (the highest occupied molecular orbital) to LUMO (the lowest unoccupied molecular orbital), producing a radiative trans-

ition. Fermi's Golden Rule defines the rate of the transition between the initial and final states (k_{if}) for the radiative transitions, using the wavefunctions Ψ_i and Ψ_f :

$$k_{if} = \frac{2\pi}{\hbar} \left| \langle \Psi_f | \hat{H}' | \Psi_i \rangle \right|^2 \rho(E_f), \quad (2.32)$$

where, \hat{H}' represents the Hamiltonian that describes the perturbation of the transition, whereas $\rho(E_f)$ is the density of the final state. According to the Born-Oppenheimer approximation, the wavefunctions can be divided into their electronic, vibrational, and spin components. The transition from the electronic component is the only part that depends on the position of the electron, r . Therefore, the transition rate is now described as

$$k_{if} = \frac{2\pi}{\hbar} \underbrace{|\langle \Psi_{el,f} | \hat{\mu}(\mathbf{r}) | \Psi_{el,i} \rangle|^2}_{\text{TDM}} \underbrace{|\langle \Psi_{spin,f} | \Psi_{spin,i} \rangle|^2}_{\text{SSR}} \underbrace{|\langle \Psi_{vib,f} | \Psi_{vib,i} \rangle|^2}_{\text{FCO}} \rho(E_f). \quad (2.33)$$

This equation consists of three components: the transition dipole moment (TDM), or orbital selection rule, the spin selection rule (SSR), and the Franck Condon Overlap (FCO). Each of them has significant impacts on the radiative transitions. In addition, the density of the final states will affect the transition rate.

Transition Dipole Moment (TDM)

Transition dipole moment term ($|\langle \Psi_{el,f} | \hat{\mu}(\mathbf{r}) | \Psi_{el,i} \rangle|$) is the first component that affects the radiative transition rate. Under spatial inversion, the sign of the dipole operator $\hat{\mu}$ reverses because it has odd parity.^{50,53} Therefore, if the parity is identical for the initial and final state wavefunctions, then the integrand has an odd parity, resulting in the integral over all space being equal to zero. Consequently, the rate of its transition is equal to zero. This type of transition, which occurs between parity-matched states, is known as 'Symmetry forbidden'. The majority of molecules have an even parity ground-state wavefunction, which means that the absorption of a photon is allowed only for transitions to odd-parity excited states. Excited states that cannot undergo transitions with the

ground state owing to symmetry-forbidden transitions are generally known as ‘dark states’. Regardless of the wavefunctions symmetry, the transition strength rises with the overlap of the initial and final wavefunctions as well as the wavefunctions’ spatial extent. Stronger photon interactions are observed in conjugated systems where the wavefunctions exhibit greater delocalisation. In some cases, symmetry can cause parts of the wavefunction to interfere destructively, cancelling out the transition dipole moment and making an otherwise allowed transition forbidden.⁵³

Spin-Selection Rule (SSR)

The second factor affecting the radiative transition rate in Equation 2.33 is $|\langle \Psi_{\text{spin},f} | \Psi_{\text{spin},i} \rangle|$. The spin factor is equal to one when the spin quantum number (S) of the initial and final electronic states is identical. This case is known as ‘spin-allowed’. If the spins of the initial and final electronic states differ, the spin factor becomes zero, calling the case ‘spin-forbidden’.⁵⁰ Transitions between states with different spins that are considered to be spin-forbidden are known to occur weakly. For instance, while it is spin-forbidden, emission of photons from a triplet state to the ground singlet state is possible; this phenomenon is known as phosphorescence. This differs from ‘fluorescence’, which is the spin-allowed mechanism. Another spin-forbidden transition that takes place, but occurs weakly, is intersystem crossing (ISC). These spin-forbidden transitions can occur due to spin-orbit coupling, a physical mechanism that will be discussed in section 2.5.2. Compared to forbidden transitions, spin-allowed transitions happen on a considerably rapid timescale. Fluorescence occurs over a timescale of nanoseconds to microseconds in π -conjugated molecules, whereas phosphorescence occurs over the timescale of milliseconds to seconds.⁵⁰

Frank-Condon Overlap (FCO)

In organic molecules, the FCO is the origin of the majority of the observed spectroscopic line shapes. It is responsible for capturing the vibrational contribution to

radiative transitions. There are multiple vibrational sublevels for each electronic level. These vibrational sublevels are reached via photon absorption or emission. In the nuclear coordinate system, a radiative transition is classified as ‘vertical’, as presented in Figure 2.9. This figure shows the electronic energy potentials for two states along the nuclear coordinate axis (Q). Each state has multiple vibrational energy sublevels. Photon absorption does not usually occur simultaneously with nuclear motion, since electronic transitions occur more rapidly than nuclear movement. The transition occurs vertically with respect to the nuclear coordinate. The maximum intensity for this transition occurs when the overlap between the initial and final states is at its maximum.

As shown in Figure 2.9, the intensity of the 0-0 transition, which is the lowest vibrational state in both excited and ground states, is less than that of the 0-1 transition. This is due to a slight shift between the ground and excited states in nuclear coordinates. Generally, the fluorescence from the excited state, or radiative emission transitions, follows the same vibrational progression as absorption transitions.

Kasha’s Law states that fluorescence emission originates from the lowest energy excited state, regardless of which higher energy excited state was initially populated.¹⁰⁰ Rapid vibrational relaxation occurs to the lower vibrational level in the excited state before returning to the ground state by fluorescence emission.

In most organic molecules, the emission spectra exhibit a red shift in comparison to the absorption spectra. This energy difference is known as the ‘Stokes shift’.¹⁰¹ This happens because the 0-0 vibronic transition in absorption occurs at a higher energy than the 0-0 vibronic transition in emission. Stokes shifts may result from the coupling of low-energy vibrational modes to the electronic transition. In addition, solvation dynamics, involving interactions with the solvent, can cause a Stokes shift in organic molecules in solution. This is similar to how low-energy vibrations affect absorption and emission by redistributing energy.⁵⁰

If the ground state and excited state vibrational levels are separated identically, the emission spectrum will appear as a mirrored counterpart of the absorp-

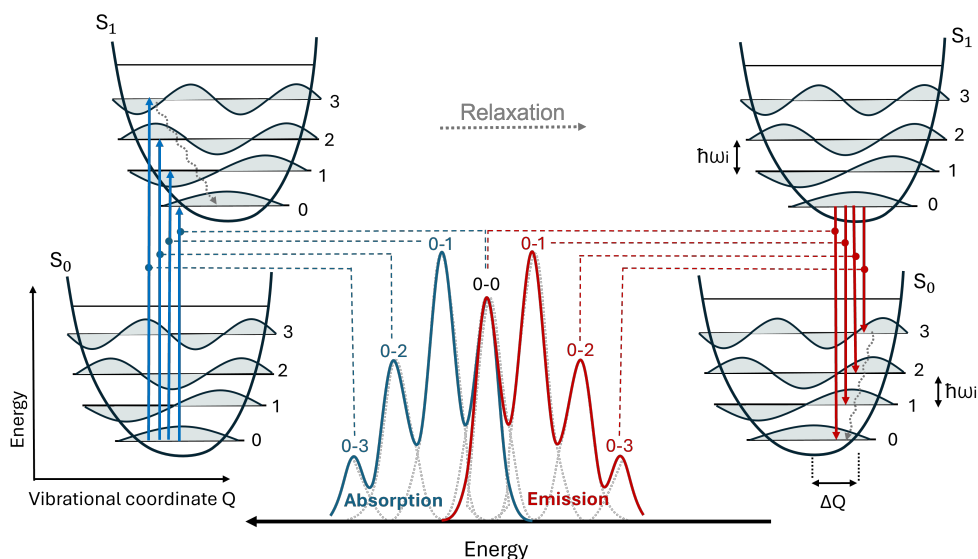


Figure 2.9 – Franck-Condon principle. A vibronic transition from the ground state to the electronic excited state (blue up-arrows) occurs when a photon is absorbed. Rapid vibrational relaxation (gray dotted arrows) occurs to the lower vibrational level prior to the molecule reverting to the ground state via fluorescence emission (red down-arrows). This vibrational fine structure in the absorption and emission spectra is termed the vibrational progression. No Stokes shift is seen since both absorption and emission occur across the 0–0 vibronic transition. The Stokes shift often results from coupling to low-energy vibrational modes. See text for details.

tion spectrum (Figure 2.9). The shape of the spectra is called vibrational progression, since it arises from the vibrational transitions. However, the mirror-image relationship between absorption and emission spectra does not always occur. This is because the potential energy surfaces of the ground and excited states are not always the same shape, and the vibrational mode energies change between the two states.¹⁰¹ Moreover, the emission often originates from the lowest excited state, which is distinct from the ground state where the absorption occurs. As a result, changing the emission spectrum shape¹⁰². Phenomena like molecular aggregation additionally impact the shape of the spectra.

The Effects of Molecular Aggregation

Molecular aggregation refers to the process where multiple molecules stick together to form larger assemblies, held together by intermolecular forces like Van der Waals interactions[†], π -stacking, or hydrogen bonds. In aggregation, there are two limiting types: H-aggregation (face-to-face stacking) and J-aggregation (head-to-tail stacking). Several studies have been conducted to investigate the effect that such aggregation has on absorption and emission.^{104,105}

In H-aggregation, the lowest-lying excited state arises when the dipole moments of the monomers are oriented antiparallel. For this state, the net dipole moment is zero, which means that the radiative transitions to it are forbidden because it is a dark state. In contrast, in the higher-lying excited state, the dipoles are parallel, leading to a radiative state, as presented in Figure 2.10. Because of this, the emission and absorption spectra change. In H-aggregates with strong vibronic coupling, the 0-0 transition becomes less intense, while transitions to higher energy levels become more intense. Moreover, H-aggregates usually display weak fluorescence as fast internal conversion to the dark lower-lying state outcompetes radiative decay from the higher-lying state.

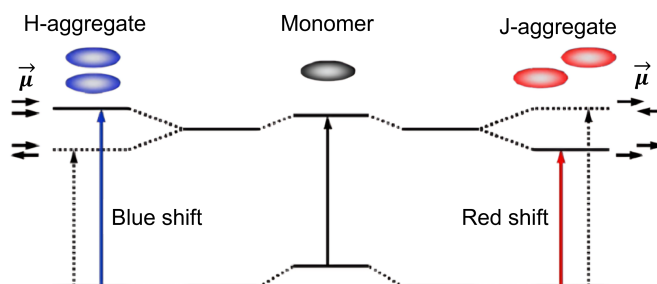


Figure 2.10 – Molecular Aggregation. The H- and J-aggregates energy diagram. H-aggregation is characterised by a weak 0-0 emission, while J-aggregation is characterised by a strong 0-0 emission. This Figure is obtained from Ref.¹⁰⁶

[†]Van der Waals interaction is a weak intermolecular interactions dependent on the spatial separation between molecules. It occurs when nearby atoms get close enough to allow their outer electron clouds to slightly contact.¹⁰³

In contrast, J-aggregates show an opposite situation. The lower energy state is now radiative, exhibiting parallel dipole moments, whereas the higher energy state is dark. This results in enhanced intensity for the lowest energy transitions (0-0 peak) and decreased intensity for the higher energy peaks.

2.5.2 Non-Radiative Transitions

As shown in the Jablonskii diagram (Figure 2.8), non-radiative transitions occur between states without photon mediation. These non-radiative transitions include mechanisms like vibrational relaxation, internal conversion, and intersystem crossing. Vibrational relaxation is defined as the transition from higher energy vibrational states to lower energy vibrational levels. The difference in energy is exported to the environment as thermal energy. It is also possible for electronic states to undergo transitions between vibrational levels. Internal conversion occurs when the spin states of the two levels are identical, while intersystem crossing occurs when there is a change in the spin state. The non-radiative transition rate is often approximated as^{50,51}

$$k_{nr} \propto \exp\left(-\gamma \frac{\Delta E}{\hbar\omega_0}\right), \quad (2.34)$$

where γ is a constant that depends on molecular parameters, ω_0 is the angular frequency of the highest energy vibration of the final electronic state, and ΔE is the energy gap between the electronic states.⁵⁰

It is generally believed that phonons, which are quasi-particles of vibrational energy, facilitate non-radiative transitions.¹⁰⁷ Spin-orbit coupling, which is the interaction between an electron's spin and its orbital motion around the nucleus, may lead to a relaxation of spin selection rules, hence enhancing the rate and yield of intersystem crossing. Non-radiative transitions may also be promoted by conical intersections, which are the points where two electronic potential energy surfaces intersect.^{108,109} At the conical intersection point, no nuclear motion or vibration is necessary to alter the electronic state. As a result, transition through this intersection is quick and effective.

Spin-orbit coupling (SOC)

As discussed previously, it is forbidden for the transition to occur between singlet and triplet states based on the spin selection rules. This is because spin is a type of angular momentum; thus, as a consequence of the conservation of angular momentum, this transition is forbidden. However, a perturbation called spin-orbit coupling (SOC) can facilitate the transition from excited singlet states to triplet manifolds (ISC). It also enables the first excited triplet state radiative decay (phosphorescence). Spin-orbit coupling can be expressed as the coupling between the total orbital angular momentum (L) and the total spin angular momentum (S) of the electrons, where the sum (L+S) must be conserved. Therefore, the typical spins conservation is slightly relaxed, which makes it possible for phosphorescence and ISC to weakly occur. It is described by the spin-orbit coupling term in the Hamiltonian^{51,110}

$$H_{\text{SO}} = \alpha_{\text{fs}}^2 \sum_{\alpha, i} \frac{Z_{\alpha}}{|\mathbf{r}_{\alpha} - \mathbf{r}_i|^3} \mathbf{L}_i \cdot \mathbf{S}_i \propto \frac{Z^4}{n^3(l+1)(l+\frac{1}{2})l}. \quad (2.35)$$

Here α_{fs} is the fine-structure constant, Z_{α} represents the effective charge of the α^{th} nucleus, L_i and S_i are the orbital and spin angular momentum operators of the i^{th} electron, respectively. Additionally, $|\mathbf{r}_{\alpha} - \mathbf{r}_i|$ indicates the distance between the α^{th} nucleus and i^{th} electron. On the right hand side, n and l are quantum numbers. Equation 2.35 illustrates that the spin-orbit coupling increases significantly in the presence of heavy atoms, and when electrons and the nucleus are close to each other (small n and l).

Furthermore, the orbital character of the initial state (Ψ_i) and final state (Ψ_f) may also enhance spin-orbit coupling, which can be expressed as

$$\langle H_{\text{SO}} \rangle = \langle \Psi_f | H_{\text{SO}} | \Psi_i \rangle. \quad (2.36)$$

Considering that (L + S) may generally be conserved, if the orbital character of the initial (Ψ_i) and final (Ψ_f) states are different, $\langle H_{\text{SO}} \rangle$ is enhanced. This phenomenon is described by El-Sayed's rule,^{111,112} which states that the rate of

intersystem crossing from $^1(n, \pi^*)$ to $^3(\pi, \pi^*)$ is more rapid than that from $^1(\pi, \pi^*)$ to $^3(\pi, \pi^*)$.^{113,114} This notation includes the spin multiplicity (1 and 3) and the (HOMO, LUMO) characteristics, whereas 'n' indicates a non-bonding orbital.

Additionally, 'vibronic spin-orbit coupling' can also enhance $\langle H_{SO} \rangle$, when vibrational modes modify the spin-orbit Hamiltonian.^{113–115} Simply put, a vibration may be suppressed or enhanced to conserve the total angular momentum (L+S).

Intersystem crossing (ISC)

Intersystem crossing is a non-radiative process in which a molecule transitions between electronic states of different spin multiplicity, most commonly from a singlet state to triplet manifolds. The ISC rate is provided by Fermi's Golden Rule:⁵¹

$$k_{ISC} = \frac{2\pi}{\hbar} \left| \langle T_f | \hat{H}_{SO} | S_i \rangle \right|^2 [FCWD]. \quad (2.37)$$

Here $|S_i\rangle$ and $|T_f\rangle$ are the initial singlet and final triplet states spatial wave-functions. [FCWD] represents the 'Franck-Condon-weighted density of states', which is the density of vibrational triplet states multiplied by the Franck-Condon overlap factor. Therefore, the triplet formation rate is determined by spin-orbit coupling strength in addition to the vibrational overlap between the singlet and triplet states.⁵¹

Comparable to the energy gap rule for internal conversion (Equation 2.34), the Franck-Condon factor depends on the vibrationally-relaxed energy gap ΔE between the states. Therefore, in most organic molecules, ISC between the singlet state and triplet manifolds is typically slow due to the high exchange energy. If two states (with differing multiplicity) have a small energy difference, the intersystem crossing rate (k_{ISC}) between them will be high, even with a small spin-orbit coupling, \hat{H}_{SO} . This will be a significant factor when we discuss our findings in chapters 4-6. Anthracene in solution exhibits rapid intersystem crossing from S_1 to T_2 due to the high Franck-Condon factor and small energy gap.^{116–118} Additionally, intersystem crossing can occur on a rapid timescale (\sim ps) in molecular

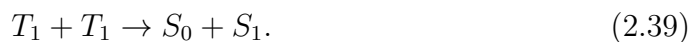
systems with heavy atoms, for example, transition metal complexes.⁵¹

2.5.3 Exciton-Exciton Annihilation

With the diffusion of excitons within a material, they may encounter and interact with each other. This interaction may lead to a phenomenon known as exciton-exciton annihilation. Both singlet and triplet states can annihilate via singlet-singlet annihilation (SSA) or triplet-triplet annihilation (TTA). At high excitation densities, singlet-singlet annihilation occurs when two molecules in the excited singlet state S_1 interact. During this interaction, one molecule is promoted to a higher excited state (e.g. S_n , $n > 1$), while the other returns to the ground state S_0 . The promoted state often relaxes rapidly back to S_1 ,^{119,120}



Similarly, two triplet excitons (T_1) can undergo triplet-triplet annihilation (TTA), where their interaction leads to the formation of one singlet exciton (S_1) and one molecule returning to the ground state (S_0),



TTA functions as the opposite mechanism of singlet fission (SF), as detailed in Section 2.6. Because both SSA and TTA are bimolecular processes, they rely on the excitation density, or the effective concentration of the excitons.

There are two additional mechanisms for exciton diffusion to consider: triplet sensitisation and excimer generation. These processes may occur in solid and solution states.

Triplet Sensitisation

Triplet sensitisation is a process in which a molecule in the excited triplet state (sensitizer) transfers its energy to a nearby molecule, promoting it from its ground

state to its triplet excited state. Using this process, a triplet excited state can be generated for a material apart from direct photoexcitation.¹²¹

To ensure efficiency and high yield in the sensitisation process, the triplet ‘donor’ should create triplet excitons via mechanisms such as intersystem crossing in a very short time scale. Moreover, the triplet energy of the donor must be close to or greater than the acceptor triplet energy.¹²²

Excimer Formation

An excimer, also known as ‘excited dimer’, is a loosely coupled ‘dimer’ that is formed when a molecule in an excited electronic state (M^*) interacts with an identical molecule in its ground state (M). The excimer state is not chemically bound, but it is associated by either a Coulombic or Van der Waals interaction.⁵⁰ Singlet-state excimers can emit, producing a broad and featureless emission spectrum, followed by dissociation, as their ground state is not bound. It is believed that device performance decreases due to the creation of excimers, which also compete with singlet fission.^{50,123} Nevertheless, their function in the singlet fission mechanism remains unclear. In singlet fission systems, the broad and red-shifted emissions are sometimes assigned to either excimer states or the triplet pair (TT) state emission.^{80,123,124}

2.6 Singlet Fission and triplet-triplet annihilation

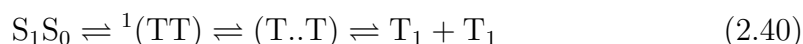
2.6.1 The Mechanism

Based on earlier explanations of spin chemistry and photophysics, we can now describe the process of singlet fission and triplet-triplet annihilation. Singlet fission refers to a carrier-generating mechanism observed in organic semiconductors, as one spin-0 singlet exciton splits into double spin-1 triplet excitons. Triplet-triplet annihilation (TTA) is the photophysical opposite mechanism, where two spin-1

low-energy triplet excitons merge to form a single spin-0 high-energy singlet exciton. The singlet excited state energy should be higher than double the energy of the lowest-lying triplet state ($2T_1$). Therefore, in terms of energy, singlet fission is a downconversion process, while triplet-triplet annihilation is an upconversion mechanism.

The process of singlet fission starts when the ground singlet state S_0 absorbs a photon, leading to the generation of the singlet excited state S_1 . Interaction with a nearby ground-state molecule results in a strongly coupled triplet-pair state, $^1(TT)$, with overall singlet spin character. Both the S_1 and $^1(TT)$ are considered to be emissive states. $^1(TT)$ emission results from Herzberg-Teller intensity borrowing from the S_1 state.^{84†}

The intermediate strongly coupled triplet pair separates to form a weakly coupled triplet-pair state, $^1(T..T)$, which consists of a superposition of spin states. This state undergoes spin mixing, which could be adjusted through the application of a magnetic field.^{40–43} The weakly coupled triplet pair eventually dissociates into two uncoupled triplet excitons, T_1 , each possessing approximately half the energy of the S_1 state. There are two components associated with this separation: the exciton physical separation via hopping or diffusion, and the spin decoherence of the two triplets. A typical representation of singlet fission process is:^{31,44,84,125,126}



The inverse process allows triplet pairs to electronically couple to become singlets, and this is known as ‘triplet-triplet annihilation’. Each stage of the singlet fission mechanism described in Equation 2.40 is considered to have a reverse process. The correlated triplet pair can regenerate the S_1 state, whereas the weakly bound triplet pair state $^1(T..T)$ can regenerate the correlated $^1(TT)$ (or $^3(TT)$ and $^5(TT)$). Eventually, the free triplet excitons can recouple via annihilation to

[†]Herzberg-Teller intensity refers to a phenomenon where vibrational modes ‘borrow’ intensity from allowed electronic transitions, allowing forbidden transitions to become observable in spectra.

regenerate the triplet pair again. Consequently, a ‘prompt’ fluorescence can be detected from the S_1 state, as well as a ‘delayed’ fluorescence arising from the following singlet state re-population. Early investigations into singlet fission were motivated by the discovery of delayed fluorescence.^{127,128} An external magnetic field can influence both the prompt and delayed fluorescence, as explained in Section 2.6.2.^{31,40,128,129}

The free triplet state can be created straight from the S_1 state through an alternative process, which is intersystem crossing. ISC is significantly slower than singlet fission except in molecules containing heavy atoms. Using electron spin resonance (ESR), we can verify the origin of the triplet states.^{130,131}

Charge Transfer States

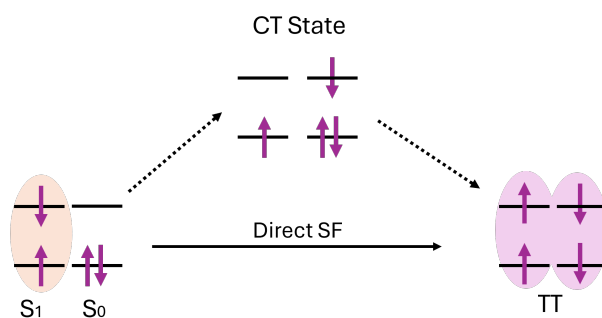


Figure 2.11 – Singlet fission pathways. $^1(TT)$ state can be generated from S_1 state by either the direct SF process (two-electron transfer) or an indirect method using charge transfer mediated.⁴

It is widely believed that charge transfer states mediate the generation of the triplet pair state from the S_1 state, as illustrated in Figure 2.11.^{4,36,132} This state could be either actual or virtual, and some states might display charge transfer characteristics. While it is uncommon to detect the charge-transfer state involved in singlet fission, it has been recorded in some investigations.¹³³

2.6.2 Magnetic Field Effects MFE in Singlet Fission

At this point, we have discussed how magnetic fields impact the spin Hamiltonian that describes the triplet pair states. Understanding the nature of the intermediate triplet-pair states and their fate is key to fully exploiting singlet fission or triplet-triplet annihilation.^{85,89,134–136} As shown in Eq.(2.30), the triplet-pair spin Hamiltonian that governs the nature of the triplet-pair intermediates can be expressed in terms of the spin operators $\hat{\mathbf{S}}_i$ on sites A and B

$$\begin{aligned} \hat{H} = & J\hat{\mathbf{S}}_A \cdot \hat{\mathbf{S}}_B + \hat{\mathbf{S}}_A D_{AB} \hat{\mathbf{S}}_B \\ & + \sum_{i=A,B} \left[g_i \mu_B \mathbf{B} \cdot \hat{\mathbf{S}}_i + D_i \left(\hat{S}_{i,z}^2 - \frac{1}{3} \hat{S}_i^2 \right) + E_i \left(\hat{S}_{i,x}^2 - \hat{S}_{i,y}^2 \right) \right], \end{aligned} \quad (2.41)$$

where J is the inter-triplet exchange coupling ($J \gg D$ for $^1(\text{TT})$ or $^5(\text{TT})$ states and $J \ll D$ for $(\text{T}..\text{T})$ states), D_{AB} indicates the inter-triplet dipole coupling, \mathbf{B} is the applied magnetic field strength and D and E ($\gg D_{AB}$) are the intra-triplet zero-field splitting parameters. It is worth noting that the inter-triplet dipolar term acts only as a weak perturbation. Other terms, such as the interactions between unpaired electrons and nuclei, are not included for simplicity.

The strongly exchange-coupled triplet pairs are eigenstates of the triplet-pair spin Hamiltonian in Eq. 2.41 when $J \gg D$. These states can in principle exist as pure spin singlet, triplet or quintet states: $^1(\text{TT})$, $^3(\text{TT})$, $^5(\text{TT})$ with total spin quantum number $S = 0, 1, 2$, respectively. Recent work shows that the singlet $^1(\text{TT})$ state, the primary product of singlet fission, can relax radiatively or non-radiatively to the singlet ground state.⁵² Alternatively, it can separate to form $(\text{T}..\text{T})$ or free triplet states, or it can interconvert to $^5(\text{TT})$ via singlet-quintet spin mixing mediated by the zero-field splitting interaction and affected by the strength and potential fluctuations in the exchange interaction.^{130,131}

The weakly coupled triplet-pair states $(\text{T}..\text{T})^l$ are formed in crystalline (hetero)acene materials by triplet hopping from $^1(\text{TT})$. They make up the nine ($l = 1, 2, \dots, 9$) eigenstates of the spin Hamiltonian, Eq. 2.41, in the limit of weak exchange coupling, when $J \ll D$. $(\text{T}..\text{T})^l$ are not spin eigenstates: spin is no longer a good quantum number and so the $(\text{T}..\text{T})^l$ states have mixed-

spin character. This means that the rate of transition from $^1(\text{TT})$ to $(\text{T}..\text{T})^l$ is modulated by the number of $(\text{T}..\text{T})^l$ states with singlet character $|C_S^l|^2$, where $C_S^l = \langle ^1(\text{TT}) | (\text{T}..\text{T})^l \rangle$. The more $(\text{T}..\text{T})^l$ states have singlet character, the higher the rate of singlet fission. $|C_S^l|^2$ depends on molecular orientation and applied magnetic field (through the Zeeman interaction, Eq. 2.41).^{42,89,137–139}

Fluorescence-detected magnetic field effects are dominated by the formation or recombination of $(\text{T}..\text{T})^l$ through the $|C_S^l|^2$ factors which represent the number of $(\text{T}..\text{T})^l$ states with singlet character and are governed by the spin Hamiltonian in Eq. 2.41.^{30,69,98} The dependence of the competition between singlet fission and ‘prompt’ fluorescence on the parameters of the spin system can provide further insight into the singlet fission process. For identically oriented molecules, with parallel long axes (the typical case for (hetero)acene crystals), at zero-field the number of $(\text{T}..\text{T})^l$ states possessing singlet character is three, as shown in Figure 2.12 a. At intermediate fields where $g\mu_B B \sim D$ this increases to five before dropping to two at higher fields.⁴² This leads to the characteristic ‘singlet fission’ magnetic field dependence observed originally in tetracene crystals¹²⁹: a drop in fluorescence as the field increases and spin mixing is favored, followed by an increase in fluorescence at higher fields, where fewer $(\text{T}..\text{T})^l$ states are able to mix with the singlet state (Figure 2.12 b). On the other hand, where triplet-triplet annihilation causes delayed fluorescence, for example when measuring at later times after excitation or in anthracene crystals where singlet fission is not energetically feasible, increased coupling of the $(\text{T}..\text{T})^l$ states to singlet states will give increased delayed fluorescence, hence the magnetic field dependence of the delayed fluorescence has the same shape as that of singlet fission, but with opposite sign.³⁰

As indicated above, the low-field MFEs are attributed to the influence of spin mixing in the weakly coupled triplet pair. At higher fields (more than 1 T), reductions in fluorescence intensity are observed, due to level crossings within the TT manifold, which involves the $^1(\text{TT})$ state. Figure 2.12 c,d shows level-crossings in the highly coupled TT pair at a high-field MFE. MFEs will be discussed in greater detail in Chapter 4.

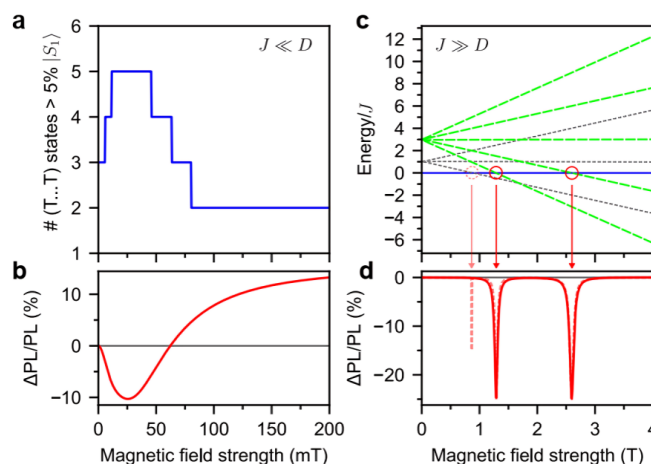


Figure 2.12 – Magnetic field effects in singlet fission: The fluorescence intensity from the S_1 state changes at low fields due to spin mixing in the weakly coupled (T...T) pair. First, as seen in (a), more states with notable singlet character are available, which results in a drop in fluorescence, as indicated in (b). The fluorescence rises as the field intensity increases because the spin levels become energetically separated and spin mixing becomes less efficient. Level crossings in the highly coupled TT pair energies, illustrated in (c), result in fluorescence dips at extremely high fields, as seen in (d). This figure reproduced from Bossanyi *et al.*^{89,90}

2.6.3 Singlet Fission in Acenes

For decades, singlet fission characteristics of acenes such as anthracene, tetracene, pentacene, and hetero-acenes such as diF-TES-ADT have been extensively investigated. In 1965, the first evidence of singlet fission was found in anthracene crystals.¹²⁷ Shortly thereafter, SF was also detected in tetracene crystals.^{32,129} As molecular length rises, the acenes exhibit a sequence of molecules with decreasing triplet energy, starting with anthracene at 1.83 eV, tetracene at 1.25 eV, and pentacene at 0.81 eV.^{9,140} It has been reported that anthracene exhibits a poor triplet yield, about 6% resulting from singlet fission.⁹, while the yields of pentacene and tetracene are almost 200%.^{141,142} However, the low stability of acenes is a major disadvantage of their viability for device applications. In the presence of oxygen, tetracene and pentacene may easily undergo photooxidation and

photodimerization.^{143,144}

According to singlet and triplet relative energy levels, the properties of SF and TTA in acenes may be broadly classified into three types. The first category consists of endothermic molecules, such as anthracene, which cannot undergo singlet fission. In anthracene, which is a short acene, the energy of two triplet states is significantly greater than that of the singlet state. This makes SF energetically unfavorable, leading to a high photoluminescence quantum yield.^{32,145} However, TTA can occur, resulting in the creation of singlet states.³⁰

The second type includes exothermic molecules, such as pentacene, which undergo fast singlet fission. In the long acene like pentacene, the twice triplet energy is significantly lower than the singlet energy.^{142,146} Thus, singlet fission proceeds extremely fast (~ 100 fs), generating triplets with a yield of around 200%.¹⁴² This results in a very small photoluminescence quantum yield, especially because triplet-triplet annihilation cannot create the bright singlet state. In Chapter 7, we examine this type of molecule, revealing that the pentacene dimer exhibits a rapid singlet fission mechanism.

The last type is isoenergetic materials, such as diF-TES-ADT, tetracene, and rubrene, where singlets and twice triplets have about the same energy. Singlet fission occurs at a slower rate than in pentacene, often within the range of picoseconds,¹⁴⁷ however it happens together with triplet-triplet annihilation, resulting in interesting photophysical phenomena. This type of material was investigated in Chapters 4-6.

Chapter 3

Materials and Methods

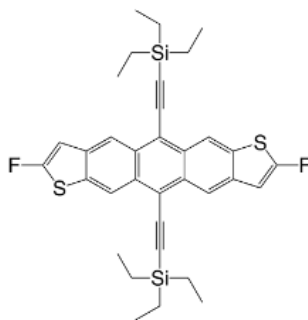
This chapter presents the molecules and materials utilised to fabricate the samples for the studies detailed in the following chapters. We explain the methodologies used for the preparation and characterization of these samples. In conclusion, we present the experimental methods used to obtain most of the data provided in this thesis.

3.1 Materials

All materials included in this thesis were synthesised and provided by collaborators, as indicated below, except for rubrene, which was bought from commercial providers and used in its delivered form. The materials in their solid form were maintained in an inert nitrogen atmosphere inside the glovebox, limiting their exposure to oxygen and light. Solvents used for the preparation of samples that are sensitive to O₂ and moisture were also stored in the nitrogen-filled glovebox.

3.1.1 diF-TES-ADT

2,8-difluoro-5,11 bis(triethylsilylethynyl) anthradithiophene or **diF- TES-ADT**, is an organic semiconductor that contains both benzene rings and thiophene. Thus, it is considered as an example of a heteroacene.¹⁴⁸ DiF-TES-ADT is a suitable candidate for the study conducted in Chapter 4 due to several characterist-



ics: It exhibits a basic brickwork crystalline structure in comparison to tetracene. No observable phase transition was recorded between 100 K and room temperature^{149,150}. In addition, this material exhibits notable air and photo-stability, enabling the generation of reproducible samples with similar properties. Finally, the ¹(TT) state in this material has been associated with distinctive emission signatures.^{84,150} This material was synthesized by John E. Anthony at the University of Kentucky.

3.1.2 Tetracene dimers and TDA monomer

DPT-dimers were synthesized using the monomeric tetracene dialdehyde (Tetracene-2,6-dicarboxaldehyde)(**TDA**) combined with m-xylylenediamine for **DPT-dimer 1**, 1,3-Cyclohexanebis(methylamine) for **DPT-dimer 2**, and 1,3-Bis[2-(4-aminophenyl)-2-propyl]benzene for **DPT-dimer 3**, as illustrated in Figure 3.1. The chemistry of dynamic covalent bonds, such as Schiff-base formation, can selectively yield the thermodynamically most stable molecules.^{151,152} The carbon-carbon distance between the two tetracene units ranges from 3.79 Å in DPT-dimer 1-2 and 3.89 Å in DPT-dimer 3, showing the existence of π - π interactions. TDA monomer and DPT-dimers were synthesized by Wataru Ishii at Kyushu University in Japan.

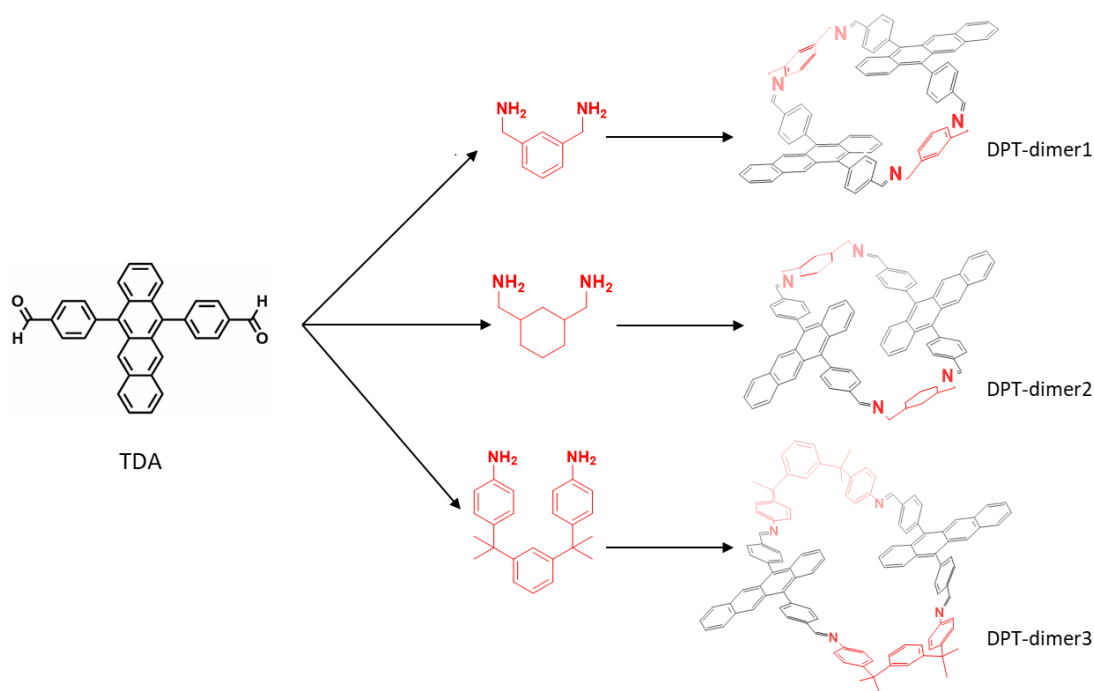
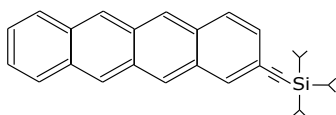


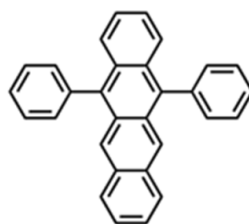
Figure 3.1 – Synthetic scheme of tetracene dimers. Monomeric tetracene dialdehyde (TDA) was used to synthesize DPT-dimer1 (top), DPT-dimer2 (middle), and DPT-dimer3 (bottom).

3.1.3 Mono-TIPS tetracene



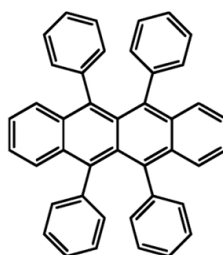
Mono-TIPS Tc, a functionalized tetracene derivative, contains a tetracene core with a TIPS group (TIPS= triisopropylsilyl) at one terminal position. mono-TIPS Tc is synthesized by John Anthony at the University of Kentucky.

3.1.4 5,12-diphenyltetracene (DPT)



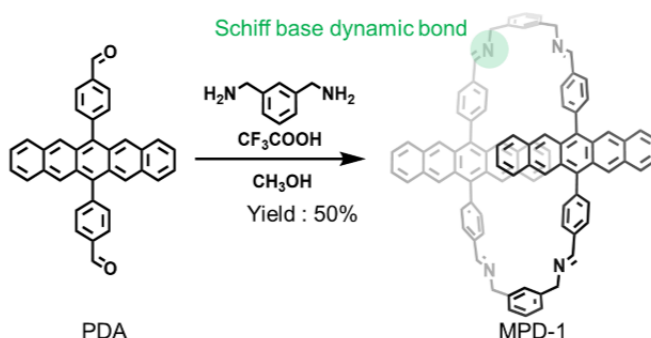
Diphenyltetracene **DPT**, a derivative of tetracene, consists of a tetracene backbone functionalized with phenyl groups. Due to its efficient fluorescence and potential for singlet fission, DPT is frequently employed in studies related to organic semiconductors and energy transfer mechanisms.^{153,154} It has an excellent solubility in toluene.¹⁵³ DPT monomer was synthesized by Wataru Ishii at Kyushu University in Japan.

3.1.5 5,6,11,12-tetraphenyltetracene (rubrene)



5,6,11,12-tetraphenyltetracene or **Rubrene** is a tetracene molecule with four phenyl (benzene) rings attached. In its single crystal form, rubrene exhibits the highest recorded charge carrier mobility.¹⁵⁵ It is particularly known for its high photoluminescence quantum yield and efficient singlet fission properties.¹⁵⁶ The energy of the triplet state in rubrene is about half the energy of the singlet state, which facilitates efficient triplet–triplet annihilation.¹⁵⁷ Rubrene was purchased from Sigma-Aldrich (Cat. No. 551112), and used in its delivered form.

3.1.6 Pentacene MPD-1 dimer and PDA monomer



MPD-1 was synthesized using the monomeric pentacene dialdehyde, 4,4'-(pentacene 6,13-diyl)dibenzaldehyde **PDA** and m-xylylenediamine. The dynamic covalent bond chemistry, such as Schiff-base formation, can selectively produce the thermodynamically most stable compounds.^{151,152} The proximate carbon-carbon distance between the two pentacene units ranges from 3.3 to 3.7 Å, indicating the presence of π - π interactions. PDA and MPD-1 were synthesized by Wataru Ishii at Kyushu University in Japan.

3.2 Sample Preparation

3.2.1 diF-TES-ADT Films

For steady-state absorption and photoluminescence, we prepared spin-coated thin films by dissolving the material in anhydrous toluene at a concentration of 15 mg ml⁻¹ to make the solution. On a pre-cleaned quartz-coated glass substrate, 20 μ L of the prepared solution was spin-coated at 1200 rpm for 50 seconds. The samples were encapsulated inside nitrogen-filled gloveboxes to reduce photo-degradation. The films were then stored in a nitrogen-filled glove box to reduce any risk of exposure to oxygen and light.

For magnetic field effect and time-resolved photoluminescence measurements, a drop-cast film was prepared by dissolving the material in toluene at a concentration of 15 mg ml⁻¹ to make the solution. A pre-cleaned quartz-coated glass

substrate was briefly preheated on a hot plate at 50 °C before drop-casting the solution. Then, 100 μL of the solution was drop-cast onto the warm substrate and allowed to evaporate on the hot plate for approximately 15 minutes to enhance the crystallinity of the film. The sample was prepared inside a nitrogen-filled glovebox, where all films and solutions preparations took place.

Thin film samples for transient electron spin resonance trESR experiments were prepared by distributing 5 μL of a 15 mg ml^{-1} solution of diF-TES-ADT in anhydrous toluene onto 2.1 mm x 17 mm pre-cleaned quartz substrates. At ambient pressure and temperature, the solvent was left to evaporate within a nitrogen-filled glovebox. Two quartz substrates with drop-cast film were then placed back-to-back within a 2.9 mm OD, 2.5 mm ID quartz EPR tube, back-filled with He to 500 mbar and flame-sealed. Reference transient ESR measurements were also performed on frozen solution samples. A 250 μM solution of diF-TES-ADT was prepared in anhydrous toluene, and 70 μL were transferred to a 3.8 mm OD, 3.0 mm ID quartz EPR tube, and the sample was flame-sealed after several freeze-pump-thaw cycles. The samples used in ESR measurements were prepared by Arnau Bertran at the University of Oxford.

3.2.2 Tetracene dimers and monomers

The solutions used for steady-state absorption, photoluminescence, and transient absorption TA spectroscopy of DPT dimers, as well as TDA, DPT, and rubrene monomers, were prepared in amber glass vials by dissolving a minimal quantity of solid material in 2 ml of toluene, stored inside the glovebox. The solution was thoroughly shaken until all solids were dissolved. Subsequently, a 1 mm path-length quartz cuvette was filled with a suitable volume of solution and sealed inside the glovebox under an inert environment to prevent exposure to molecular oxygen. Using calibration curves and molar absorption coefficients, the concentration of the solution is determined.

3.2.3 Pentacene MPD-1 dimer and PDA-monomer

Picosecond/nanosecond transient electronic absorption spectra of PDA monomer and MPD-1 dimer were recorded in fresh degassed toluene at ca. 2×10^{-4} M and 1×10^{-4} M, respectively, as well as in polystyrene film at 0.05 mol% (and 0.005 mol% for MPD-1 dimer).

For MPD-1 dimer thin films, we prepared the stock solution by dissolving 1 mg of MPD-1 dimer in 8.5 ml of dichloromethane. An additional 3 ml of dichloromethane was used to dissolve 100 mg of polystyrene before being mixed with 480 ml of the stock solution. 140 μ l of the solution was spin-coated onto a pre-cleaned quartz-coated glass inside a nitrogen-filled glovebox, where all thin films and solutions preparations were carried out. Finally, we encapsulated the sample using a thin glass coverslip. These procedures were also used to prepare the samples for time-resolved photoluminescence spectroscopy, steady-state absorption and photoluminescence, and magnetic field effects.

PDA monomer and MPD-1 dimer used in trEPR, ^1H -NMR, MALDI-TOF-MS, high-resolution MS, echo detected, and concentration-dependent absorption spectra were prepared by Wataru Ishii at Kyushu University in Japan.

3.3 Sample Characterisation Techniques

For the optical and morphological characterisation of samples, we employed different techniques as detailed below.

3.3.1 Grazing Incidence Wide-Angle X-ray Scattering GI-WAX

X-ray scattering provides valuable information about the structural properties of a sample. Constructive interference of scattered X-rays, as described by Bragg's law, is defined by the following equation:

$$n\lambda = 2d \sin \theta, \quad (3.1)$$

where λ is the incident X-ray wavelength, n represents the order of diffraction ($n = 1$), θ is the angle of incidence (Bragg angle), and d is the spacing between crystal planes. Analyzing how scattered X-ray intensity varies with angle reveals structural information about the sample through diffraction peaks associated with specific spacings (d -values).

The incident X-ray beam in GIWAXS measurements is oriented at a very small angle to the sample surface ($\theta=0.2^\circ$), enabling it to nearly align parallel to the plane of the sample. Adjusting the angle allows selective investigation of either the surface properties or the internal structure of the sample. A two-dimensional detector is used to detect scattered X-rays. Thus, GIWAXS not only provides crystallographic data but also reveals the orientation of crystallites relative to the substrate surface.

The grazing incidence wide-angle x-ray scattering images, presented in Chapter 4, for diF-TES-ADT samples were performed by Rachel Kilbride at the University of Sheffield. The measurements were conducted using a Xeuss 2.0 laboratory beamline (Xenocs) equipped with a liquid gallium MetalJet source (Excillum), producing X-rays with an energy of 9.243 keV ($\lambda = 1.34 \text{ \AA}$). A collimated X-ray beam was directed at sample surfaces inclined at a grazing angle of 0.15° , and scattered X-rays were detected by a Pilatus 3R 1M 2D X-ray detector (Dectris) positioned $\sim 307 \text{ mm}$ from the sample center. The sample-to-detector distance was calibrated using a silver behenate standard in transmission geometry. During measurement, the entire flight path, including collimation tubes and sample chamber, was held under vacuum to minimize background air scatter. GIWAXS data were corrected, reshaped, and reduced using code based on pyFAI and pygix Python libraries.¹⁵⁸

3.3.2 Atomic Force Microscopy AFM

AFM, or atomic force microscopy, is a type of scanning probe method that enables high-resolution imaging of surface topography. The technique involves scanning the sample surface with a sharp tip mounted on a cantilever, as shown in Figure 3.2. As the tip moves over the surface, the cantilever deflects. These deflections can be measured by reflecting a laser beam off the cantilever's upper surface. A photodiode detects the reflected laser beam, allowing precise monitoring of the tip deflection relative to its position on the surface. To keep the tip at a consistent height above the sample, a feedback control system is used.

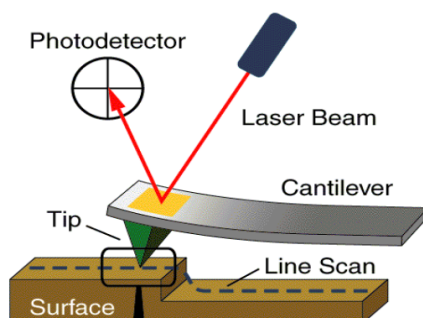


Figure 3.2 – Principle of atomic force microscope. See text for details. This Figure is obtained from Ref.¹⁵⁹

Atomic force microscopy images, presented in Chapter 4, were measured by Rachel Kilbride at the University of Sheffield. The measurements were conducted using a Dimension 3100 (Veeco) microscope, equipped with a Nanoscope 3 A feedback controller. Scout 350 RAl (NuNano) cantilevers were used with a resonant frequency of 350 kHz and spring constant of 42 N/m. The data was analyzed using Gwyddion software (Version 2.60)¹⁶⁰.

3.3.3 Ground-State Absorption

Steady-state absorption spectroscopy, or UV-vis absorption spectroscopy, is a fundamental method for the optical characterisation of materials. The lineshape of the absorption spectra provides valuable information on the energy levels associated with the bright states. Additionally, an interpretation of intermolecular

interactions and the transition between vibronic levels can be obtained, as discussed in section 2.5.1.

Ground-state absorption measurement involves recording the transmitted light intensity across a range of wavelengths (λ) as it passes through the material. A commercial Cary double-beam spectrometer (Cary 60 UV-Vis Spectrophotometer, Agilent Technologies) is used to measure the steady-state absorption spectra reported in this thesis. The spectrophotometer works by sending light to the sample from a broadband Xenon lamp via a scanning monochromator. Using a photomultiplier tube, the intensity of the transmitted light $I(\lambda)$ is measured. According to the Beer-Lambert law, the transmission $T(\lambda)$ is given by

$$T(\lambda) = \frac{I(\lambda)}{I_0(\lambda)} = e^{-\alpha(\lambda)d}, \quad (3.2)$$

where $\alpha(\lambda)$ denotes the wavelength-dependent absorption coefficient, d represents the thickness of the sample, and $I_0(\lambda)$ is the intensity of the incident light beam, which is recorded internally by a secondary detector in the Cary 60. Absorption spectra are presented in terms of absorbance A (also known as optical density, OD), which is a dimensionless quantity, where

$$A(\lambda) = -\log_{10} T(\lambda) = \alpha(\lambda)d \log_{10} e. \quad (3.3)$$

Depending on different electronic transitions, the absorption spectra include a series of vibronic peaks in the conjugated organic molecules.

3.3.4 Steady-State Photoluminescence PL Measurements

Photoluminescence spectroscopy involves the excitation of a material with a laser source, which promotes electrons to higher energy states. The photo-excited sample emits light (photoluminescence) when the electrons return to their ground state. The intensity of the light is collected as a function of wavelength. By analyzing the light intensity, PL spectroscopy provides insights into the properties of materials.

In its simplest form, photoluminescence arises from the lowest excited singlet state (S_1), producing an emission spectrum that closely mirrors the corresponding absorption spectrum. Similar to the absorption, photoluminescence lineshape can change due to intermolecular interactions, as discussed in Section 2.5.1. Besides the S_1 emission, photoluminescence spectroscopy may potentially reveal other excited-state emissions. For example, excimer production may result in the appearance of extra broad features in photoluminescence spectra, as discussed in Section 2.5.3. In addition, it is reported that photoluminescence spectroscopy can be used to observe the strongly bound triplet-pair state $^1(TT)$.⁸⁴

The majority of the PL spectra shown in the findings chapters were measured using a home-built setup. A 405 nm diode laser, with a maximum power of 1 mW, is emitted into free space and directed towards the sample, where it is focused. The light is collected and collimated using the same lens. The collimated beam is sent into a long-pass filter and then to a fiber linked to the spectrometer. The detection range in the visible and near-infrared spectrum spans around 400 to 2200 nm. Spectra were recorded using OceanView software.

In addition, an alternative home-built optical setup was also used to measure steady-state photoluminescence spectra, which is described in Section 3.5.1.

3.4 Transient Absorption Spectroscopy

Transient absorption (TA) spectroscopy is a pump-probe spectroscopy technique. The most fundamental elements of TA spectroscopy are displayed in Figure 3.3. A pump pulse is used to photo-excite the sample. After an adjustable time delay Δt , a broadband probe pulse is focused onto the sample at the same position as the pump, ensuring spatial overlap of the two pulses. A detector continuously records the spectra of the probe pulses after they pass through the sample. The pump frequency is half that of the probe, allowing for the measurement of the probe's spectrally resolved absorbance under both photoexcited and unexcited conditions. The recorded TA signal, ΔA , is the subtraction of the absorption

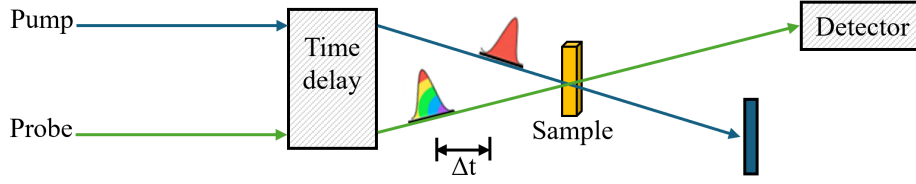


Figure 3.3 – Transient absorption spectroscopy (pump-probe technique).

The fundamental principle of the TA spectroscopy technique is clarified by the probe pulse reaching the sample after a controlled delay time Δt following the pump pulse. At the sample, the pump and probe beams are focused and spatially overlapped. An adjustable delay stage is positioned between the beams to control the delay time. A detector continuously records the spectrum of the probe pulses after they pass through the sample.

spectra measured with and without pump excitation:

$$\Delta A = A_{on} - A_{off}. \quad (3.4)$$

After a large number of laser shots, the average of ΔA is automatically calculated for each time delay. In some TA setups, the data is displayed as ΔT rather than ΔA , which can be simply converted to ΔA via the equation

$$\frac{\Delta T}{T} = \frac{T_{on} - T_{off}}{T_{off}} = 10^{-\Delta A} - 1 \quad (3.5)$$

The overall transient absorption signal is obtained through multiple processes. The process begins by exciting the sample to S_1 (the first excited state) using the probe beam, while the pump pulse is deactivated (A_{off}). This process generates a simple UV-vis absorption spectrum. When the pump is on (A_{on}) and followed by the probe, some molecules are promoted by the pump to the excited states, such as S_1 , or to triplet states via the following photophysical processes, like intersystem crossing or singlet fission. When the probe pulse arrives, the molecules absorb some of the light, allowing new optical transitions to occur, including $S_1 \rightarrow S_N$ or $T_1 \rightarrow T_N$. This produces the positive features, or photo-induced absorption (PIA), in the transient absorption spectra.

With the arrival of the probe beam, a portion of the ground-state molecules has already transitioned to the excited state due to absorption of the pump photons. This reduces the number of ground-state molecules available to absorb the probe photons, resulting in a notable drop in absorbance. This is shown as a negative transient absorption (TA) feature, known as the ground-state bleach (GSB). The approximate percentage of molecules excited during the transient absorption experiment can be estimated by comparing the steady-state absorbance at the pump wavelength with the maximum amplitude of the GSB. The GSB arises because excited molecules are no longer in the ground state and thus no longer absorb light at the original wavelength, leading to a negative ΔA .¹⁶¹ If the pump pulse is sufficiently intense to excite nearly all molecules within the pump-probe overlap region, there will be no remaining ground-state molecules to absorb at that wavelength. This would result in a complete bleach, corresponding to the maximum negative ΔA .

However, in real experiments, only a small fraction of the molecules is typically excited to ensure measurements remain within the linear regime and avoid nonlinear effects. Over-excitation in transient absorption experiments can lead to nonlinear effects that distort the true photophysics of the system. These include bimolecular triplet-triplet annihilation, state saturation, and photodegradation. Therefore, excitation levels are generally kept low to avoid such artifacts and maintain accurate interpretation.¹⁶²

In addition to ground-state bleach, other spectral features also contribute to the transient absorption signal. For instance, some molecules may return to the ground state via radiative decay, resulting in a negative absorption feature known as stimulated emission (SE). These negative features (GSB and SE), along with positive photoinduced absorption (PIA) signals, together define the overall shape of the transient absorption spectrum.

3.4.1 Picosecond Transient Absorption Spectroscopy

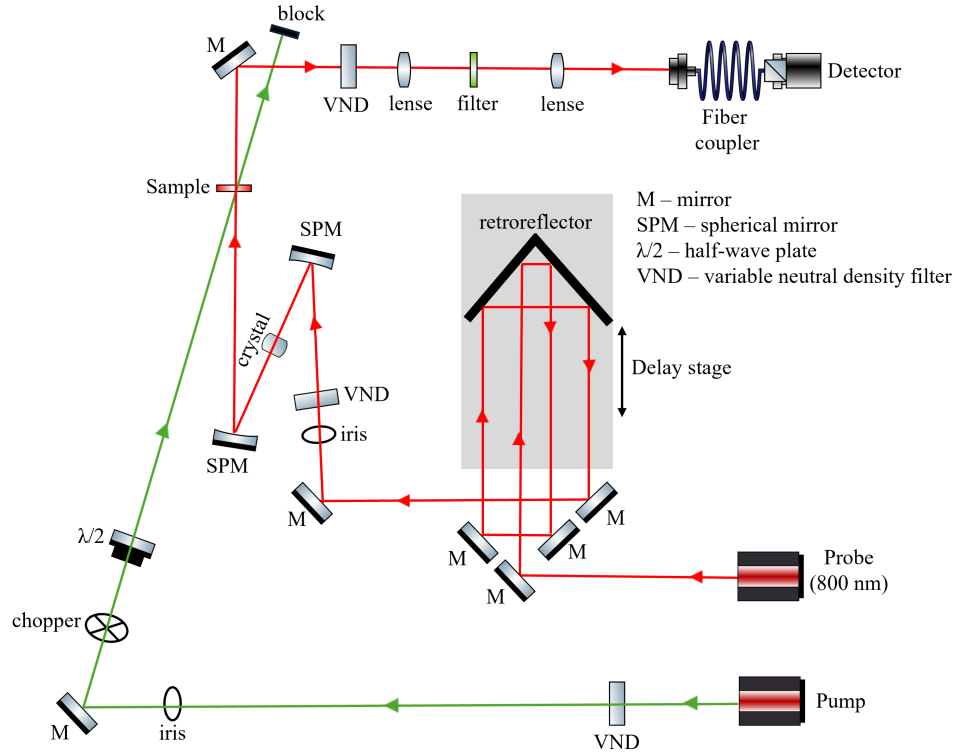


Figure 3.4 – Picosecond transient absorption setup. Using a non-linear crystal, the 800 nm beam is focused to produce the probe pulses. The probe beam is focused and aligned to spatially overlap with the pump beam at the sample position. The pump beam is modulated at a frequency equal to half that of the probe beam using a chopper. A delay stage is used to control the pump-probe delay time. Using a half-wave plate in the pump line, the pump and probe polarizations are set to the magic angle.

A customised version of a commercial instrument (Helios Fire, Ultrafast Systems) is used for our picosecond transient absorption setup. TA data are obtained with a time resolution of approximately 100 fs, covering a time range from less than 1 ps to ~ 7 ns. The pump and probe pulses are produced using a Ti:sapphire regenerative amplifier (Spitfire ACE PA-40, Spectra-Physics) that produces 800 nm pulses (40 fs FWHM, 10 kHz, 1:2 mJ). To create adjustable narrowband pump pulses, a part of the amplifier output is sent to an optical parametric amplifier (TOPAS Prime, Light Conversion). Another part of the 800 nm beam focused

on a continuously moving CaF_2 crystal for a UV-vis probe (350–750 nm), a sapphire crystal for visible probes (450–800 nm), or a YAG crystal for NIR probes (800–1600 nm). To control the pump-probe delay time, a motorised delay stage is used. The probe is detected using (Helios, Ultrafast Systems) besides CMOS and InGaAs detectors in order to detect the UV-visible and NIR spectral bands, respectively. The polarisations of the pump and probe were adjusted to the magic angle ($\theta = 54.7^\circ$).

It is important to note that for the transient absorption measurements, solutions were prepared under an inert atmosphere inside a glovebox to prevent oxygen exposure. All measurements were conducted within an hour of sample preparation. In addition, a small piece of staple wire is inserted into a pre-cleaned cuvette purged with nitrogen before being closed with a septum-equipped cover. To prevent oxygen exposure and provide precise results, the solution is replaced with a fresh one using a syringe after each TA measurement. The staple wire is used to stir the solution using a magnetic stirrer to avoid thermal and photo-degradation. This approach prevents repeated exposure of the same molecules to the laser during transient absorption measurements.

Each set of transient absorption data in solution presented in this thesis was obtained from two repeated measurements, with a fresh solution used for each. The final result was obtained by averaging these two measurements using Surface Explorer 4.3.0 (Ultrafast Systems). Additionally, to confirm the stability of the solution and to verify that it has not degraded, steady-state absorption is measured before and after each TA measurement. This allows for the adjustment of laser power before the following TA measurement if the absorption demonstrates a significant degradation.

3.4.2 Nanosecond Transient Absorption Spectroscopy

Acknowledgements: The initial planning and alignment techniques were supported by Shuangqing Wang and Ravi Kumar. James P. Pidgeon contributed to finalizing and operating the setup. Eman Bu Ali was otherwise primarily respons-

ible for constructing the nanosecond TA setup. We also express our appreciation to Sayantan Bhattacharya and Rahul Jayaprakash for their valuable discussions.

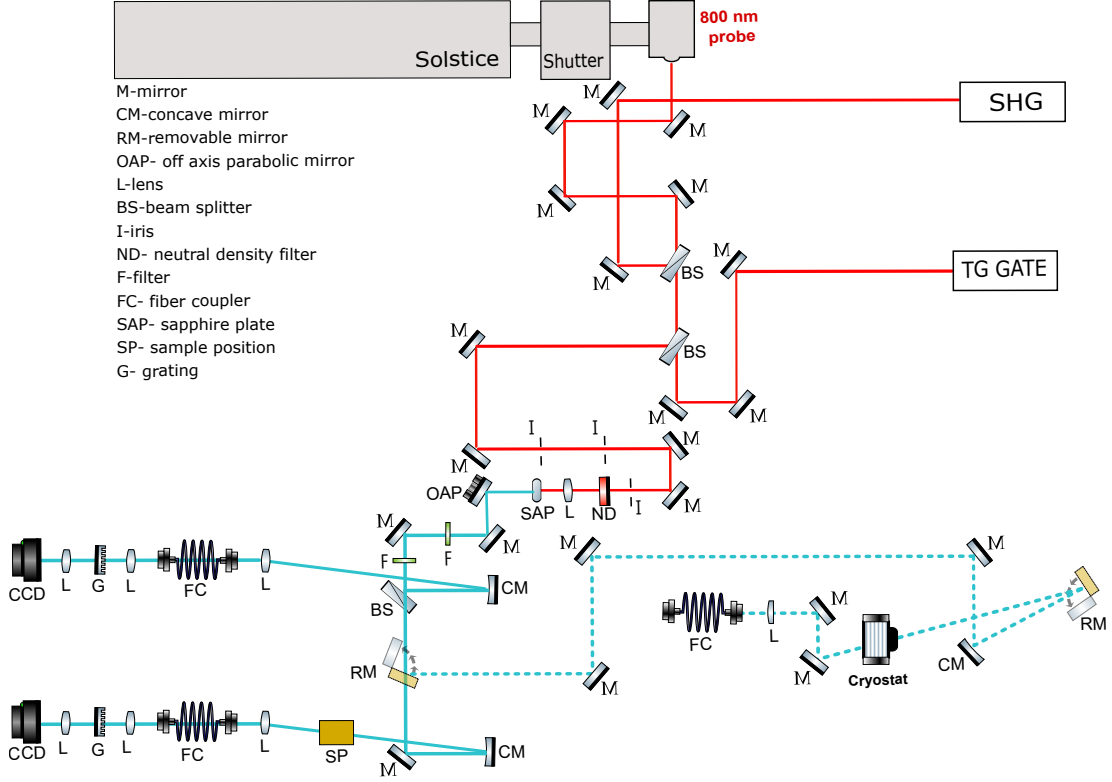


Figure 3.5 – Nanosecond transient absorption setup (probe path). Details are provided in the text. Elements in the schematic are not to scale. The solid light blue line presents the room temperature TA path, whereas the dotted light blue line shows the low-temperature path. Montana Instruments-Cryostation is used to control the temperature applied to the sample.

Our nanosecond to millisecond transient absorption setup enables the collection of TA data from approximately 1 ns to 1 ms, giving about 1 ns time resolution. The probe and pump beam paths are presented in Figure 3.5 and 3.6, respectively, allowing a clearer presentation of each path. Figure 3.5 represents a home-built TA probe/reference setup in which a probe beam is generated using 800 nm pulses (1 kHz repetition rate, 90 fs pulse width), provided by a Ti:sapphire ultrafast amplifier (Solstice, Spectra-Physics). The white light probe ($\lambda=450\text{--}750\text{ nm}$) is produced by focusing a portion of the 800 nm pulse onto a sapphire crystal,

subsequently divided into a probe and reference beams using a 50:50 beamsplitter. Using a reference helps in correcting for the probe pulses shot-to-shot fluctuations, thereby improving the signal-to-noise ratio compared to measurements taken without a reference. A removable mirror is used to direct the probe beam along two possible paths: room-temperature path (solid light blue line) and low-temperature path (dotted light blue line). Montana Instruments Cryostation (Magneto-optic module) is employed to control the applied temperature, where the sample is mounted in a closed-cycle chiller to produce a temperature range of 3.4 to 350 K.

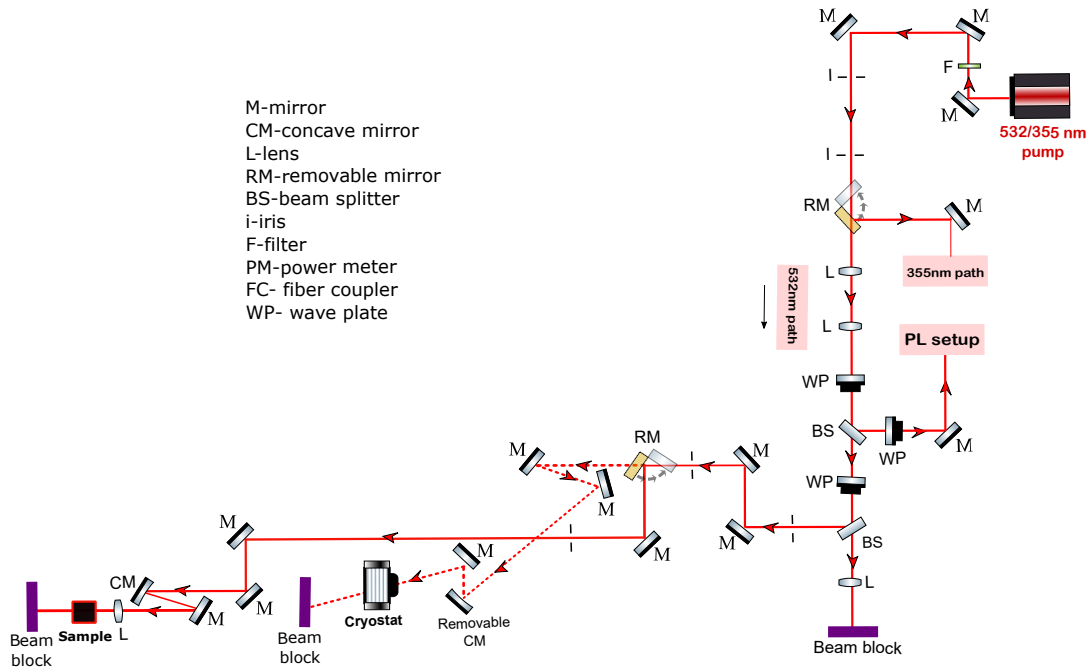


Figure 3.6 – Nanosecond transient absorption setup (pump path). Details are provided in the text. Elements in the schematic are not to scale. The solid line presents the room temperature TA path, whereas the dotted line shows the low-temperature path. Montana Instruments-Cryostation is used to control the temperature applied to the sample.

The pump beam path, on the other hand, is shown in Figure 3.6. In this configuration, a frequency-doubled output of a Q-switched Nd:YVO₄ laser (Picolo-AOT, Innolas) is used to provide the pump laser beam, which generates 5 kHz

pulses with a wavelength of 355/532 nm and a temporal width of 500 ps. Similar to the probe, a removable mirror directs the pump laser beam along two different paths: room-temperature path (solid line) and low-temperature path (dotted line). The pump and probe are focused and spatially overlapped on the sample position. A digital delay generator (DG645, Stanford) is used to effectively control the pump-probe delay time. For the 532 nm laser pump, a notch filter (NF533-17, Thorlabs) is positioned after the sample to minimize the pump scatter, while a 395 nm long-pass filter (GG395) is employed for 355 nm scatter. A volume phase holographic grating is used to disperse both the probe and reference beams, which are then guided onto two linear image sensors (S7030, Hamamatsu). A custom-made acquisition board (Entwicklungsbuero Stresing) controls and reads out the signals from these sensors. Transient absorption data is collected using home-built software and subsequently analysed with Surface Explorer 4.3.0 (Ultrafast Systems).

3.5 Magnetic Field Effect

The impact of the magnetic field, as discussed in Chapter 4, was evaluated by recording PL spectra at various magnetic field strengths ranging from 0 mT to 280 mT. These measurements were also performed at different delay times, ranging from 5 ns to 1 μ s. The PL spectra were recorded while repeatedly changing the magnetic field strength in both upward and downward directions to ensure that the PL spectra obtained in both cases have the exact shape and magnitude. This was done to exclude any potential impacts of sample photo-degradation or laser power fluctuations and to reinforce our confidence in the reliability of the noted effects of the magnetic field (See Appendix A.4 for further details). The laser power level was monitored using a power meter to evaluate laser stability and record any power fluctuations. The magnetic field effect can be calculated by integrating photoluminescence spectra over the entire wavelength range, and the resulting values are subsequently used in the equation:

$$\frac{\Delta PL}{PL}(B) = \frac{PL(B) - PL(0)}{PL(0)}$$

3.5.1 Temperature-Dependent MFE measurements

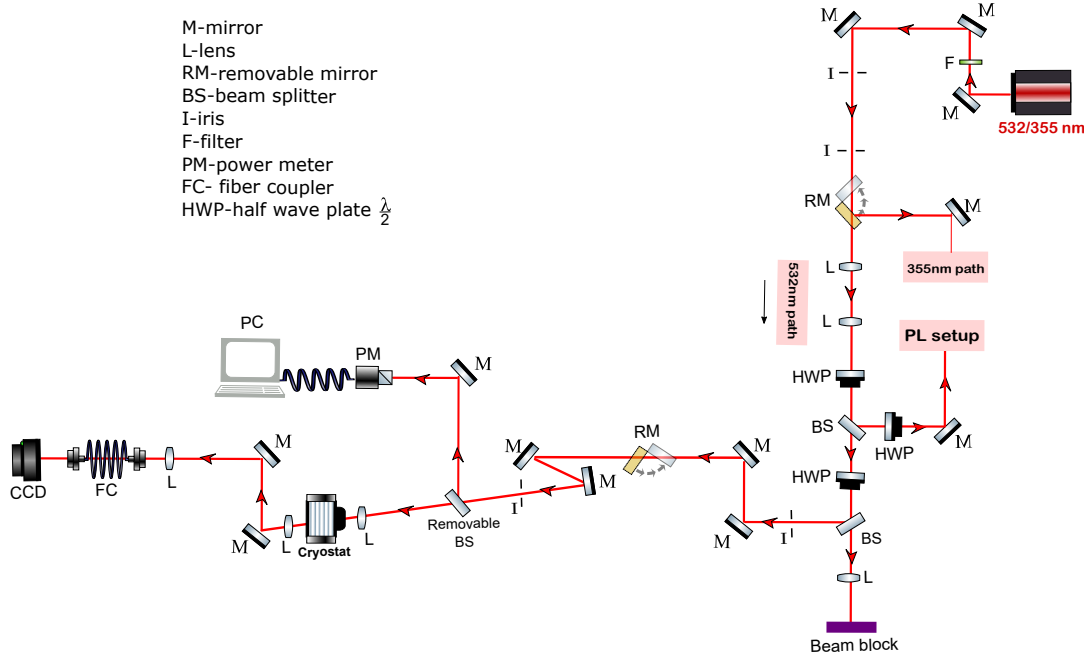


Figure 3.7 – Schematic of magnetic field effects on photoluminescence setup.

Details are provided in the text. Elements in the schematic are not to scale. Montana Instruments-Cryostation is used to control the temperature and magnetic field strength applied to the sample.

Acknowledgements: The initial planning and alignment techniques were supported by Shuangqing Wang, while Eman Bu Ali was primarily responsible for constructing the magnetic field effects setup.

A home-built setup is used for our magnetic field effects on photoluminescence measurements, as illustrated in Figure 3.7. A frequency-doubled output of a Q-switched Nd:YVO₄ laser (Picolo-AOT, Innolas) generates 5 kHz laser pulses with a temporal width of 500 ps and wavelengths of 355 and 532 nm. A removable beam splitter is employed to divide the laser beam into two optical paths:

the first path directs the beam into the Montana cryostat for magnetic field effect measurements, while the second path guides the beam onto a power meter sensor, to continuously monitor laser intensity fluctuations and stability. The laser power profile is recorded using Optical Power Monitor software, which generates diagrams that can be saved for documentation and future reference.

The sample is fixed in a closed-cycle He cryostat (Magneto-optic module, Montana Instruments), which controls both magnetic field intensity and temperature applied to the sample. This cryostat offers access to a 0.7 T bi-polar magnetic field. The sample is thus placed on a cold flange between the poles using double-sided tape, with a radiation shield, a vacuum housing with integrated poles, and an electromagnet installed to initiate cooling. Once cooled, bipolar field strength can be controlled. It is worth mentioning that the temperature shown on the cryostat reflects the temperature at the cold flange, where cooling is directly applied. The sample itself might not be exactly at this temperature, particularly at very low temperatures. The difference results from imperfect thermal contact between the sample and the cold flange. Photoluminescence Spectra are recorded using a time-gated intensified charge-coupled device (ICCD; iStar DH334T-18U-73, Andor). A 532 nm notch filter and two 550-colored glass long-pass filters (OG550, Schott) were placed in front of the ICCD detector for the PL measurements.

To achieve accurate and stable magnetic field effect measurements, a few critical steps should be followed. First, the laser power should be sufficiently stable before initiating the experiment by allowing Picolo-AOT laser source to remain in the warmed-up mode for at least one day prior to the experiment, and in the emission mode for a few hours before initiating data collection. This reduces laser power fluctuations and maintains measurement stability. Second, the photoluminescence intensity of the sample must be sufficiently intense to provide a high signal-to-noise ratio and a well-defined PL spectrum. Third, within the ICCD software (Andor Solis for Spectroscopy: ICCD-05789), it is advisable to increase the PL accumulation number (e.g. 50 - 70) to reduce background noise

and enhance spectral intensity. Simultaneously, the exposure time should be kept short (e.g. 0.2 seconds) to speed up data collection. For measurements taken at later time points, increasing the gain is recommended to improve signal strength. Additionally, prior to data collection, it is important to minimize the beam spot size (with an ICCD slit width of roughly 150-200 μm) and center the beam precisely on the slit. This alignment can be adjusted using the optics in front of the ICCD detector and verified using the ‘Image’ mode in the ICCD software. Following these guidelines will help achieve high-quality MFE curves with minimal fluctuation.

In addition to the magnetic field effect measurements, the time-resolved photoluminescence and temperature-dependent steady-state PL measurements reported in this thesis were also performed using this setup.

3.6 Transient Electron Spin Resonance (trESR)

Transient Electron Spin Resonance (trESR) is a spectroscopic technique that probes the behavior of paramagnetic species, like radical pairs or triplet states, on a timescale of nanoseconds or longer, after a pulsed laser excitation.¹⁶³ It uses the Zeeman interaction, in which an external magnetic field is swept while a continuous microwave field is applied. Transitions between spin sublevels are observed when the Zeeman splitting matches the microwave frequency. trESR is particularly suited for detecting long-lived spin states (lifetimes $>1 \mu\text{s}$) that have non-zero spin. Their mechanism of formation is encoded in the spin polarization pattern of the trESR spectra, arising from non-equilibrium populations of the spin sub-levels.¹⁶⁴ This makes it a powerful technique for identifying triplet states that originate from singlet fission, intersystem crossing, or even for directly observing quintet states within the triplet pair (TT) manifold. The ability to detect $^5(\text{TT})$ states directly using trESR was a major step forward in confirming the role of correlated triplet pair state in singlet fission.⁹²

Spectral signatures expected for triplet and quintet states resulting from dif-

ferent mechanisms are shown in Figure 3.8. This figure presents the spin-selective population of zero-field populations by intersystem crossing (ISC) and selective population of the $m_S = 0$ sublevel by singlet fission. The contributions of the different transitions are shown as dashed lines and the overall spectrum resulting from their sum is shown as a solid line. The energy level diagrams with line thickness representing relative sublevel populations are shown for a magnetic field aligned with the Y -axis of the zero-field interaction.

TrESR can also be used to extract zero-field splitting (ZFS) parameters D and E by fitting the experimental spectra using software such as EasySpin. The trESR measurements presented in Chapter 4 and Chapter 7 were carried out by Dr. Arnau Bertran at the University of Oxford and Wataru Ishii at Kyushu University, respectively (see Appendices A.6.6 and C.6 for details).

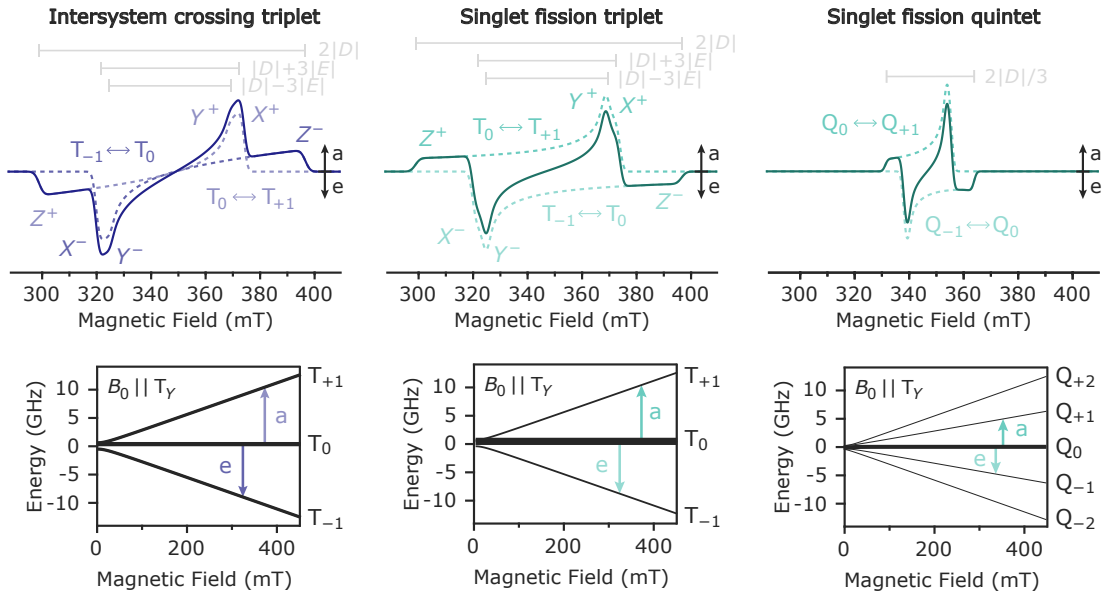


Figure 3.8 – Calculated spectral signatures expected for triplet and quintet states resulting from different mechanisms: spin-selective population of zero-field populations by intersystem crossing (ISC) and selective population of the $m_S = 0$ sublevel by singlet fission. The contributions of the different transitions are shown as dashed lines and the overall spectrum resulting from their sum is shown as a solid line. The energy level diagrams with line thickness representing relative sublevel populations are shown for a magnetic field aligned with the Y -axis of the zero-field interaction.

3.7 Nutation measurement

In EPR, nutation refers to the oscillatory motion of the electron spin vector around the effective magnetic field, which is induced by a resonant microwave pulse. The nutation experiment is used to assign the spin multiplicity of the observed EPR signals by applying microwave pulses of varying duration while the resulting spin echo intensity is recorded. When a spin system is exposed to a resonant microwave field, it undergoes coherent oscillations (nutations) between spin states. The frequency of these nutations depends on the spin quantum number, allowing distinction between spin states such as doublet ($S = \frac{1}{2}$) and triplet ($S = 1$). By monitoring the echo signal as a function of pulse length, the spin character of the excited state can be determined.^{165,166}

Chapter 4

Intersystem crossing out-competes triplet-pair separation from $^1(\text{TT})$ below 270 K in anthradithiophene films

Singlet fission (SF) and triplet-triplet annihilation (TTA) are processes which may be exploited to boost the efficiency of solar energy technology. Despite being studied since the late 1960s, the mechanism of singlet fission is still not fully understood. This is partly because the main technique used to study singlet fission, optical or visible/near-IR transient absorption spectroscopy, cannot distinguish between the strongly coupled triplet-pair state $^1(\text{TT})$, weakly interacting triplet pairs ($\text{T}.. \text{T}$), and independent triplet states $\text{T}_1 + \text{T}_1$. To solve this problem, we combine transient optical spectroscopy performed as a function of magnetic field and transient electron spin resonance (ESR) spectroscopy to probe the different steps involved in the singlet fission mechanism. By using transient photoluminescence spectroscopy performed as a function of magnetic field to se-

[†]This chapter has been adapted from the following publication¹⁶⁷: Bu Ali *et al.*, *Journal of the American Chemical Society*, 147, 28638–28650 (2025). The majority of the work presented here is my own; contributions from collaborators are explicitly noted.

lectively probe the second step of singlet fission: $^1(TT) \rightleftharpoons (T..T)$, we show that in a well-studied model system, anthradithiophene (diF-TES-ADT), this step is highly temperature-dependent, even though the first step, $^1S \rightarrow ^1(TT)$, is not. Transient ESR measurements confirm the absence of singlet fission at temperatures between 40 and 250 K for this system, with clear signatures of triplets generated by intersystem crossing and evidence for decay by triplet-triplet annihilation, further supported by magnetic field effect measurements. We conclude that in polycrystalline diF-TES-ADT, intersystem crossing out-competes triplet hopping at temperatures below 270 K, enabling direct intersystem crossing from the bound triplet pair $^1(TT)$ to an independent triplet state T_1 localized on a single chromophore. The generated triplets can re-encounter and decay through triplet-triplet annihilation.

4.1 Introduction

Singlet fission (SF) involves conversion of a high-energy photoexcited singlet exciton into a pair of lower energy triplet excitons.^{4,168} This multiexciton generation process has been studied over the past decade primarily because of its promise to improve solar cell efficiency through carrier multiplication^{4,136,169–171}, as a high-energy photon can generate two electron–hole pairs, reducing losses due to thermalization^{172,173}. Triplet-triplet annihilation (TTA) is the inverse process, in which a pair of low-energy triplet excitons are converted to a single high-energy singlet exciton.¹⁷⁴ This process has been implicated in improving the performance of organic light emitting diodes (OLEDs)^{22,23}, solar photovoltaics^{24,25}, biomedical applications²⁶ including targeted drug delivery and optogenetics^{27,28} and 3D printing.¹⁷⁵

As shown schematically in Fig. 4.1, the commonly accepted scheme of singlet fission is that a photo-excited singlet state S_1 and a ground state singlet state S_0 form a triplet-pair state, initially in an overall singlet configuration, known as $^1(TT)$.^{9,36–39} Subsequently, this intermediate triplet pair separates to form a

weakly bound triplet-pair state (T..T), and eventually two uncoupled triplet excitons. This is represented as $S_1 S_0 \rightleftharpoons {}^1(TT) \rightleftharpoons (T..T) \rightleftharpoons T_1 + T_1$ ^{37,126}. Triplet-triplet annihilation is the inverse process, starting with independent triplets and resulting in an emissive singlet state.

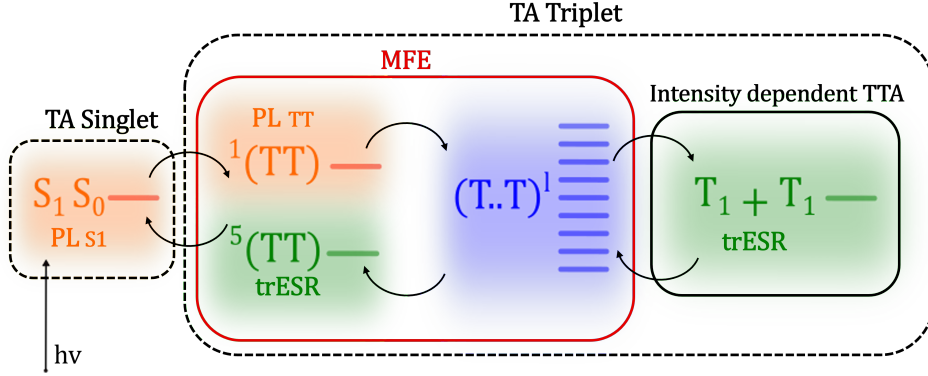


Figure 4.1 – A schematic illustration of the different steps involved in the singlet fission process. The diagram illustrates the processes leading from the excited singlet state S_1 to two triplet states $T_1 + T_1$ and the techniques used to probe them: the presence of S_1 and triplet states after photoexcitation is detectable by transient absorption spectroscopy (dashed black lines); the presence and dynamics of S_1 and ${}^1(TT)$ can be detected by fluorescence spectroscopy (orange shades); ${}^5(TT)$ and $T_1 + T_1$ are observable via trESR (green shades); the formation or recombination of (T..T) can be monitored through magnetic field effects (MFE) on photoluminescence (red line); processes that depend on exciton density, such as TTA, can be probed through intensity-dependent optical and ESR measurements (solid black line).

Understanding the nature of the intermediate triplet-pair states, and their fate, is key to fully exploiting singlet fission or triplet-triplet annihilation^{85,89,134–136}. The triplet-pair spin Hamiltonian that governs the nature of the triplet-pair intermediates ${}^1(TT)$, ${}^5(TT)$ and (T..T) in Fig. 4.1 can be expressed in terms of the spin operators $\hat{\mathbf{S}}_i$ on sites A and B

$$\begin{aligned} \hat{H} = & J\hat{\mathbf{S}}_A \cdot \hat{\mathbf{S}}_B + \hat{\mathbf{S}}_A D_{AB} \hat{\mathbf{S}}_B \\ & + \sum_{i=A,B} \left[g_i \mu_B \mathbf{B} \cdot \hat{\mathbf{S}}_i + D_i \left(\hat{S}_{i,z}^2 - \frac{1}{3} \hat{S}_i^2 \right) + E_i \left(\hat{S}_{i,x}^2 - \hat{S}_{i,y}^2 \right) \right], \end{aligned} \quad (4.1)$$

where J is the inter-triplet exchange coupling ($J \gg D$ for $^1(TT)$ or $^5(TT)$ states and $J \ll D$ for $(T..T)$ states, see below), D_{AB} indicates the inter-triplet dipole coupling, \mathbf{B} is the applied magnetic field strength and D and E ($\gg D_{AB}$) are the intra-triplet zero-field splitting parameters. We note that the inter-triplet dipolar term acts only as a weak perturbation. Other terms, such as the interactions between unpaired electrons and nuclei, are not included for simplicity.

Recent work^{69,89,92,176–178} has highlighted the importance of inter-triplet exchange interactions J and their time dependence. Our scheme in Fig. 4.1 reflects this by including both strongly exchange-coupled ($^1(TT)/^5(TT)$) and weakly exchange-coupled $(T..T)$ triplet-pairs as separate states with interconversion between them. In many archetypal (hetero)acene systems, such as diF-TES-ADT, pentacene and tetracene, the primary step of singlet fission is the formation of a strongly exchange-coupled triplet-pair state, $^1(TT)$, where triplets within the pair reside on neighboring sites with orbital overlap.^{37,44,45,172,179}

The strongly exchange-coupled triplet pairs are eigenstates of the triplet-pair spin Hamiltonian in Eq. 4.1 when $J \gg D$. These states can in principle exist as pure spin singlet, triplet or quintet states: $^1(TT)$, $^3(TT)$, $^5(TT)$ with total spin quantum number $S = 0, 1, 2$, respectively. Recent work shows that the singlet $^1(TT)$ state, the primary product of singlet fission, can relax radiatively or non-radiatively to the singlet ground state⁵². Alternatively, it can separate to form $(T..T)$ or free triplet states, or it can interconvert to $^5(TT)$ via singlet-quintet spin mixing mediated by the zero-field splitting interaction and affected by the strength and potential fluctuations in the exchange interaction^{130,131}. Evidence of quintet states is now well-established in exothermic singlet fission systems based on pentacene^{34,176,180–185}, and has been observed in TIPS-tetracene^{92,186} and a small number of other systems.^{187–190} However, quintets have not yet been observed in other archetypal endothermic singlet fission systems such as crystalline tetracene or diF-TES-ADT, despite the presence of strongly exchange-coupled $^1(TT)$ states^{37,45}.

We note that an equivalent description of ‘strongly exchange-coupled’ triplet-

pair states is of mixed triplet-pair/charge-transfer (CT) states, where the degree of CT character is directly related to the exchange interaction⁷⁴. The CT character of the $^1(\text{TT})$ state has recently been probed directly using time- and angle-resolved photoemission spectroscopy¹⁷⁷. This measurement shows that over time the CT character of the initially created $^1(\text{TT})$ state reduces as the triplets hop away from each other to form $(\text{T}..\text{T})$ ¹⁷⁷, as expected according to Wakasa *et al.*'s model of dynamic exchange¹⁷⁸ and comparison between transient absorption and emission spectroscopy measurements⁴⁵.

The $(\text{T}..\text{T})^l$ states formed in crystalline (hetero)acene materials by triplet hopping from $^1(\text{TT})$ are the so-called 'weakly coupled' triplet-pair states. They make up the nine ($l = 1, 2, \dots, 9$) eigenstates of the spin Hamiltonian, Eq. 4.1, in the limit of weak exchange coupling, when $J \ll D$. $(\text{T}..\text{T})^l$ are not spin eigenstates: spin is no longer a good quantum number and so the $(\text{T}..\text{T})^l$ states have mixed-spin character. This means that the rate of transition from $^1(\text{TT})$ to $(\text{T}..\text{T})^l$ is modulated by the number of $(\text{T}..\text{T})^l$ states with singlet character $|C_S^l|^2$, where $C_S^l = \langle ^1(\text{TT}) | (\text{T}..\text{T})^l \rangle$. The more $(\text{T}..\text{T})^l$ states have singlet character, the higher the rate of singlet fission. $|C_S^l|^2$ depends on molecular orientation and applied magnetic field (through the Zeeman interaction, Eq. 4.1)^{42,89,137–139}.

Despite the depth of understanding of singlet fission in crystalline systems, and the consensus on the mechanism shown in Fig. 4.1, several key questions remain to be resolved. A complete understanding of the singlet fission mechanism across different types of materials is complicated by the fact that different spectroscopic techniques selectively probe different parts of the process, see Figure 4.1 - no single technique can be relied on to understand the entire photocycle. Transient absorption spectroscopy, for example (dashed black lines in Fig. 4.1) probes excited state population. It can differentiate between S_1 and triplets, but is unable to distinguish $^1(\text{TT})$, $^5(\text{TT})$, $(\text{T}..\text{T})$, and T_1+T_1 since they usually exhibit comparable signatures¹⁹¹. Photoluminescence (PL) spectroscopy (orange shading in Fig. 4.1) offers information on S_1 and $^1(\text{TT})$ populations^{37,139}, but can only indirectly monitor $(\text{T}..\text{T})$ or T_1+T_1 populations.

Transient electron spin resonance (trESR) spectroscopy allows the measurement of states with non-zero overall electron spin, such as triplet and quintet states (green shading in Fig. 4.1). The spin polarization pattern of the trESR spectra reveals the mechanism of formation of the detected photo-induced states and their role in decay processes.¹⁶⁴

Light intensity-dependent optical and trESR measurements (solid black line in Fig. 4.1) can provide additional information on processes that depend on exciton density, such as triplet-triplet annihilation^{37,138}.

Finally, fluorescence-detected magnetic field effects (red line in Fig. 4.1) are dominated by the formation or recombination of $(T..T)^l$ through the $|C_S^l|^2$ factors which represent the number of $(T..T)^l$ states with singlet character (see above) and are governed by the spin Hamiltonian in Eq. 4.1^{30,69,98}. The dependence of the competition between singlet fission and 'prompt' fluorescence on the parameters of the spin system can provide further insight into the singlet fission process. For identically oriented molecules, with parallel long axes (the typical case for (hetero)acene crystals), at zero-field the number of $(T..T)^l$ states possessing singlet character is three. At intermediate fields where $g\mu_B B \sim D$ this increases to five before dropping to two at higher fields⁴². This leads to the characteristic 'singlet fission' magnetic field dependence observed originally in tetracene crystals¹²⁹: a drop in fluorescence as the field increases and spin mixing is favored, followed by an increase in fluorescence at higher fields, where fewer $(T..T)^l$ states are able to mix with the singlet state. On the other hand, where triplet-triplet annihilation causes delayed fluorescence, for example when measuring at later times after excitation or in anthracene crystals where singlet fission is not energetically feasible, increased coupling of the $(T..T)^l$ states to singlet states will give increased delayed fluorescence, hence the magnetic field dependence of the delayed fluorescence has the same shape as that of singlet fission, but with opposite sign³⁰.

In this work, we study the temperature-, fluence-, and magnetic field-dependence of photoluminescence of a well-characterized anthradithiophene (diF-TES-ADT) singlet fission system^{37,45}. Previous studies based on transi-

ent absorption and photoluminescence spectroscopy have suggested that the first step of singlet fission, the generation of $^1(\text{TT})$, is temperature-independent in polycrystalline films of this material.^{37,45} However, as we show here, magnetic field-dependent photoluminescence spectroscopy reveals that the separation to form $(\text{T}..\text{T})$ is highly temperature-dependent in this material. TrESR measurements demonstrate the absence of singlet fission at temperatures below 250 K and no indication of quintet states, indicating population of triplet states by an intersystem crossing (ISC) process instead.

We explain these apparently contradictory observations by proposing that the biexcitonic $^1(\text{TT})$ state, formed at all temperatures and delocalized over two molecules, can itself undergo intersystem crossing to form a T_1S_0 state, with a triplet localized on only one molecule. While full singlet fission to produce $(\text{T}..\text{T})$ does not occur at low temperatures (below 270 K), the intersystem-crossing-generated triplets can nevertheless undergo thermally-activated triplet-triplet annihilation over a wide range of temperatures.

4.2 Results and discussion

4.2.1 Model system

We selected 2,8-difluoro-5,11-bis(triethylsilylethynyl) anthradithiophene (diF-TES-ADT, see molecular structure in Fig. 4.2) as a model system to investigate the mechanism of singlet fission and triplet-triplet annihilation by measuring magnetic field effects (MFE) on photoluminescence.⁴³ diF-TES-ADT is a well-characterized system^{37,45,192,193} with a simple brickwork crystalline structure and no apparent phase transition between 100 K and room temperature (RT).¹⁹⁴ This material, furthermore, is air- and photo-stable, allowing for reproducible preparation of samples with the same properties.¹⁹⁵

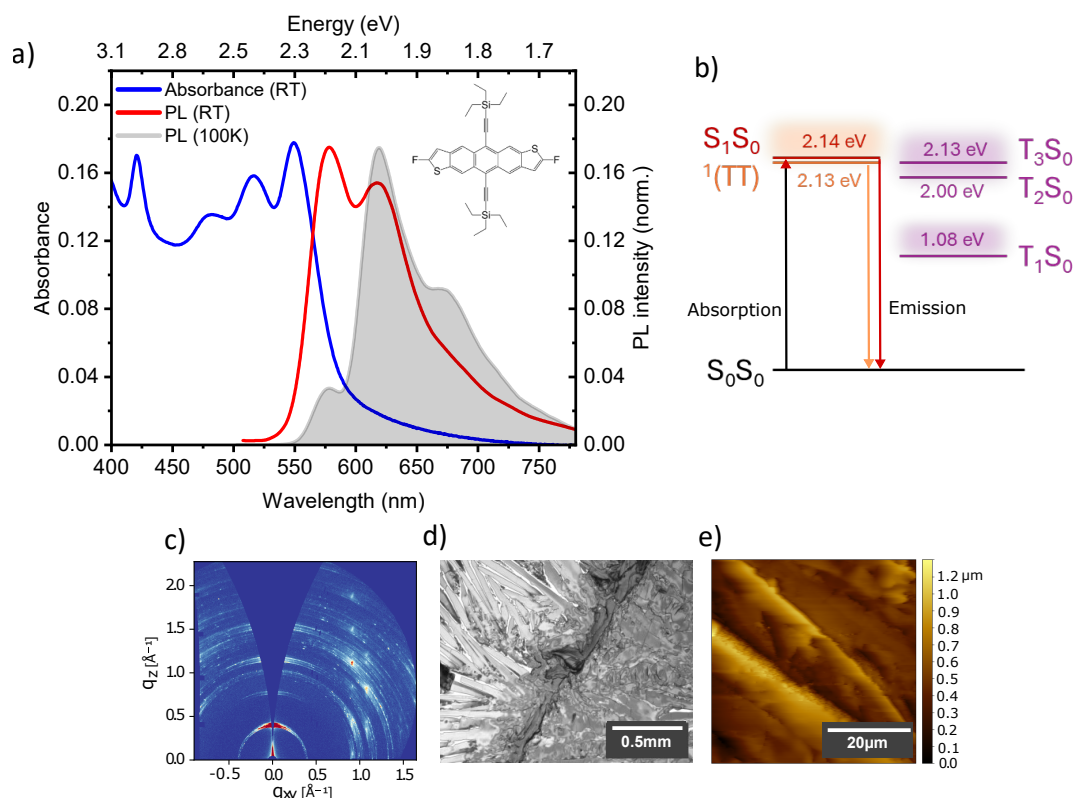


Figure 4.2 – Optical and morphological characterization of diF-TES-ADT films. (a) diF-TES-ADT thin film steady-state room temperature absorption spectrum (blue) and photoluminescence (PL) spectra at room temperature (red) and 100 K (gray shaded). The chemical structure of diF-TES-ADT is shown in the inset. (b) Energy level diagram for diF-TES-ADT based on phosphorescence and transient absorption experiments in Ref.^{45,196}. (c) GIWAXS pattern, (d) polarized microscope image, and (e) AFM scan of a diF-TES-ADT drop-cast film indicating highly crystalline domains. Scale bars are shown in the figure. Morphological characterization of the spin-coated films are presented in the Appendix, Fig. A.1a.[†]

Absorption and photoluminescence spectra of diF-TES-ADT in thin films measured at room temperature (Fig. 4.2a) display the vibronic progression associated with the transition between the electronic ground state S_0 and the first excited state S_1 .^{194,197} However, when the temperature is reduced to 100 K, the emission spectrum exhibits a distinct peak that is displaced towards longer wavelengths compared to the RT spectrum. Over the same temperature range,

[†]GIWAXS and AFM data were measured by Rachel Kilbride.

the absorption spectrum narrows and redshifts slightly, but otherwise remains largely unchanged.^{37,45} The emission at 100 K has been assigned to a strongly coupled triplet pair state $^1(\text{TT})$.^{37,45} Further temperature-dependent steady-state PL measurements demonstrate an increase of a strongly coupled triplet pair state $^1(\text{TT})$ emission down to 100 K,^{37,45} as illustrated in Figure 4.3.

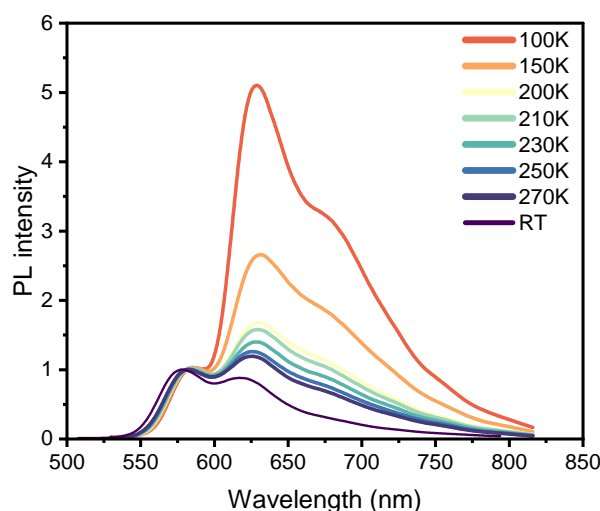


Figure 4.3 – Temperature-dependent steady-state PL of a diF-TES-ADT, excited at 532 nm. It exhibits an increase of the $^1(\text{TT})$ emission at low temperatures along with a decrease in the contribution from singlet states.

To characterize the morphology and microstructure of the diF-TES-ADT films used in this work, we used grazing incidence wide angle X-ray scattering (GIWAXS), atomic force microscopy (AFM) and polarized microscopy (Fig. 4.2). AFM and polarized microscopy measurements show that the drop-cast diF-TES-ADT film is composed of a micron-scale crystalline texture (Fig. 4.2c,d). This is confirmed using GIWAXS measurements with the 2D GIWAXS pattern consisting of several distinct scattering features indicating a highly crystalline film (Fig. 4.2b). Further inspection of corresponding 1D GIWAXS intensity profiles shows that the crystal structure is consistent with the previously reported brick-work packing with a predominantly edge-on lamellar motif (see Appendix Fig. A.2 for further details).

4.2.2 Temperature-dependent magnetic field effect reveals the absence of SF below 270 K

For a more detailed investigation of the steps of the singlet fission mechanism following $^1(TT)$ formation, the impact of a magnetic field on the photoluminescence was evaluated by measuring PL spectra at magnetic field intensities ranging from 0 mT to 300 mT, and at delay times from 5 ns to 1 μ s. The PL spectra were recorded while repeatedly changing the magnetic field strength in both upward and downward directions to ensure that the PL spectra obtained in both cases have the same shape and magnitude. The full measurement procedure is described in Appendix A.4.

Figure 4.4 displays the MFE data of a diF-TES-ADT drop-cast film at room temperature and 100 K. In Fig. 4.4(a,c), the data is plotted as a function of magnetic field strength for a range of gate delay times. Our data at room temperature (Fig. 4.4a) reproduces the results of earlier work by Bossanyi *et al.*:³⁷ the prompt fluorescence intensity, from 5 ns to 20 ns, reflects singlet fission behavior, characterized by a decrease in $\Delta PL/PL(\%)$ at lower magnetic fields and an increase at higher fields¹²⁹ and the delayed fluorescence from 30 ns to 1 μ s displays the inverted behavior characteristic of triplet-triplet annihilation³⁰. To more clearly visualize the temporal evolution, the same data is depicted in Fig. 4.4b as a function of delay time for various magnetic field strengths, ranging from 0 mT to 300 mT. This graph shows that singlet fission is active over a time scale of 5 ns to 30 ns, whereas triplet-triplet annihilation dominates at long times and starts to outweigh the singlet-fission contribution beyond about 30 ns.

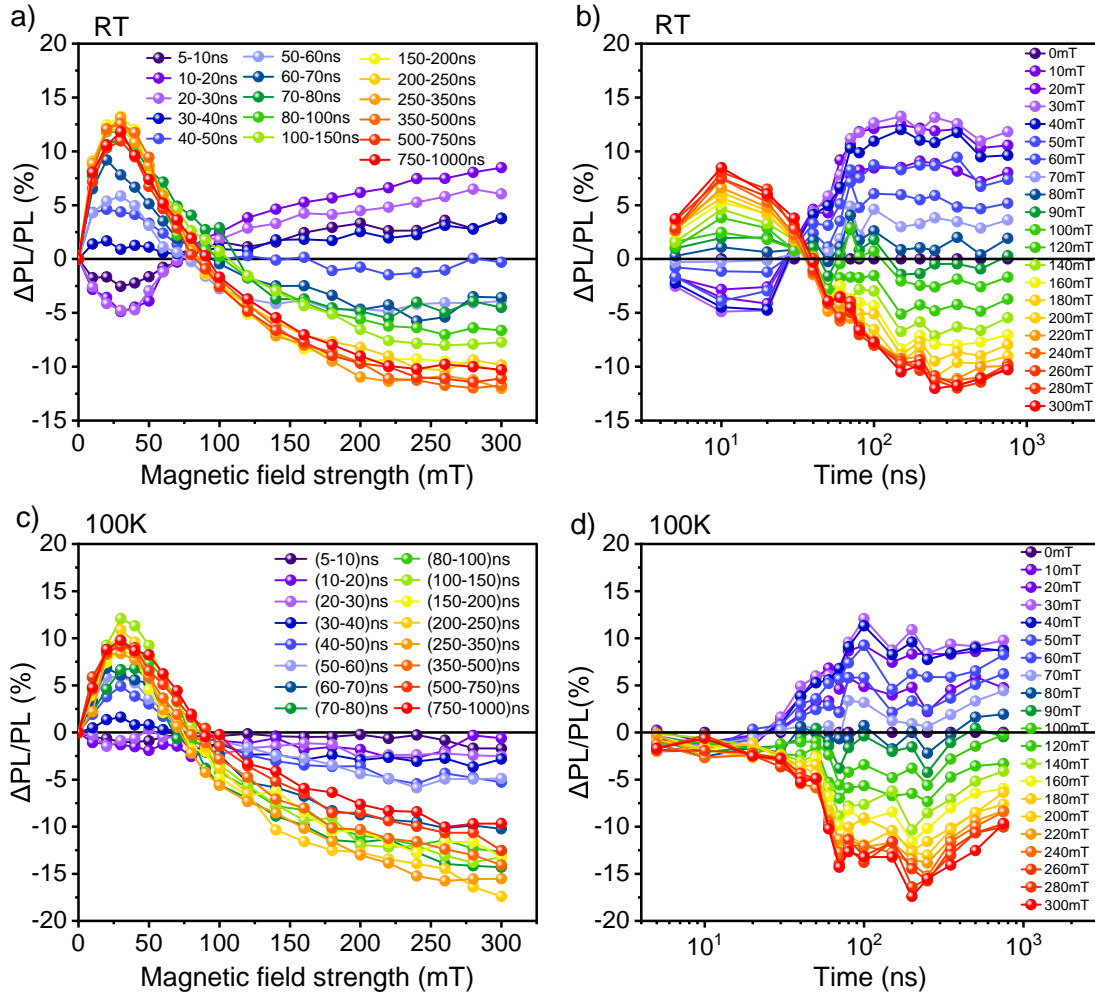


Figure 4.4 – Magnetic field effects on photoluminescence. MFE for diF-TES-ADT drop-cast film, measured using 532 nm excitation across different delay times at room temperature and 100 K. $\Delta\text{PL}/\text{PL}(\%)$ is reported as a function of (a,c) magnetic field strength (from 0 to 300 mT) and (b,d) delay time (from 5 ns to 1 μs).

We next investigated the temperature-dependence of the MFE. Figure 4.4b shows the change in $\Delta\text{PL}/\text{PL}(\%)$ as a function of magnetic field strength at 100 K, employing identical time intervals and magnetic field strengths as for the room temperature data discussed above. Surprisingly, upon reducing the temperature to 100 K, no MFE was observed between 5-20 ns suggesting that singlet fission does not occur at 100 K. However, the signature from triplet-triplet annihilation persisted with a similar magnitude and duration, from 30 ns to 1 μs , as observed at room temperature. This change in behavior is highlighted in Fig. 4.4c, where the

time-dependence of the magnetic field effect on the photoluminescence emphasizes the absence of singlet fission but, surprisingly, persistence of triplet-triplet annihilation.

In order to identify the temperature at which the singlet fission signature is no longer observable, we performed MFE measurements on a drop-cast diF-TES-ADT sample at a series of temperatures between 100 K and room temperature and the results are shown in Fig. 4.5. At early delay times, 5-10 ns, the signature from singlet fission is only apparent at 270 K and room temperature (Fig. 4.5a), suggesting an onset of singlet fission between 250 K and 270 K (Fig. 4.5b). On the other hand, the signature from triplet-triplet annihilation, shown for a delay time of 100-200 ns, is observed across the whole temperature range (Fig. 4.5c). These results suggest that triplet-triplet annihilation is present independently from singlet fission.

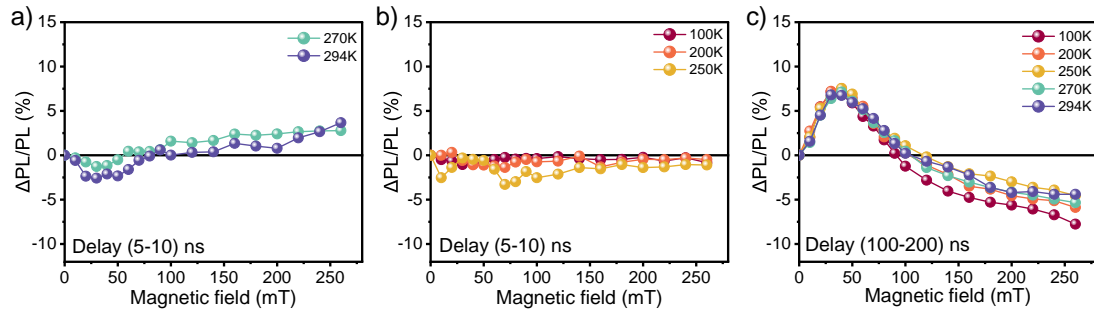


Figure 4.5 – Temperature-dependent magnetic field effect. MFE of diF-TES-ADT drop-cast film at different delay times; (a,b) 5-10 ns at temperatures ranging from 270 K to RT, and from 100 K to 250 K, respectively. (c) 100-200 ns across the temperature range from 100 K to RT.

The triplet-triplet annihilation process was probed further through fluence-dependent MFE measurements shown in Fig. 4.6. Using a drop-cast diF-TES-ADT film at 100 K and a delay time of 100-250 ns, the magnetic field effect on photoluminescence was recorded while increasing the laser power from 11 μ W to 2.3 mW. A noticeable decrease in the MFE is observed as the laser power increases. Similar behavior in a perylene/PtOEP system has been recently attrib-

uted to bimolecular triplet-triplet annihilation¹³⁸. At low excitation power, the probability that two triplets encounter and annihilate within their lifetime is low and at first increases quadratically with excitation intensity. At high excitation intensities, the triplet density becomes so high that most triplets annihilate within their excited state lifetime, giving a probability of triplet decay by triplet-triplet annihilation tending towards unity. In this regime, the delayed fluorescence intensity starts to depend linearly on excitation intensity. The strength of the magnetic field effect on the delayed fluorescence is determined by the relative magnitude of the first-order rate constant describing spin-independent triplet decay compared to the second-order rate constant of the spin-dependent triplet-triplet annihilation process and the triplet density.¹³⁸ The delayed fluorescence is influenced most by an applied magnetic field at low excitation intensities and therefore low triplet densities. At high excitation intensities, the impact of the magnetic field on singlet formation is reduced as a larger proportion of triplet pairs undergoes fusion before experiencing significant spin evolution under the applied magnetic field. The fluence-dependent MFE experiments therefore confirm that our data at 100 K can be explained by a bimolecular triplet-triplet annihilation process.

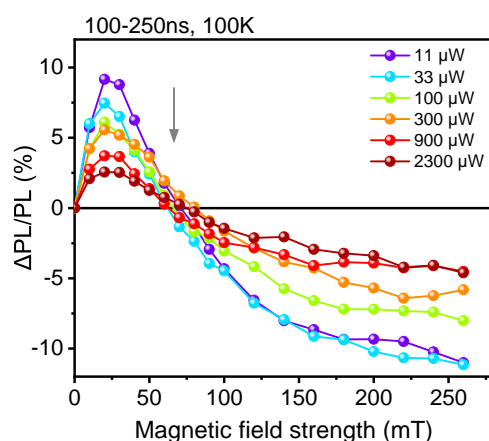


Figure 4.6 – Fluence-dependent magnetic field effect data of diF-TES-ADT drop-cast film. The data is measured using 532 nm excitation at 100 K and a delay time of 100-250 ns. The magnetic field effect on photoluminescence was recorded while increasing the laser power from 11 μ W to 2.3 mW

4.2.3 Transient electron spin resonance (trESR) demonstrates the production of triplet states by ISC at low temperatures

To provide further insights into the apparent absence of singlet fission at low temperatures and into the origin of the triplet states that are observed to be involved in TTA, the magnetic field effect measurements were complemented by transient electron spin resonance (trESR)[†]. trESR spectroscopy directly probes the nature and dynamics of photoinduced spin states with $S > 0$. Their mechanism of formation is encoded in the spin polarization pattern of the trESR spectra, arising from non-equilibrium populations of the spin sub-levels.¹⁶⁴ Triplet and quintet states formed by singlet fission are usually characterized by an initial spin polarization pattern resulting from selective population of the $m_S = 0$ sub-level due to spin conservation during the singlet fission process. The initial, ESR-silent, strongly coupled triplet pair $^1(TT)$ is generated in a spin-zero state from the excited singlet state precursor and results in population of the eigenstates of the coupled pair of triplets, and the resulting separated triplet states, with probabilities determined by their singlet content.^{92,176} The spectral signatures of triplets populated by intersystem crossing (ISC), on the other hand, are determined by spin-selective population of the zero-field spin sub-levels driven by spin-orbit coupling, resulting in clearly distinct spin polarization patterns.¹⁶⁴

Fig. 4.7 shows the results of transient ESR measurements performed on drop-cast diF-TES-ADT films at temperatures between 40 K and 250 K. The full evolution of the ESR spectrum as a function of time after photoexcitation for each temperature is shown on the left (red = emissive, blue = absorptive transition), and transients extracted at selected field positions as well as spectra extracted at early times after photoexcitation are shown in the middle and on the right.

[†]Arnau Bertran, Gabriel Moise, and Claudia Tait performed trESR measurements and simulation.

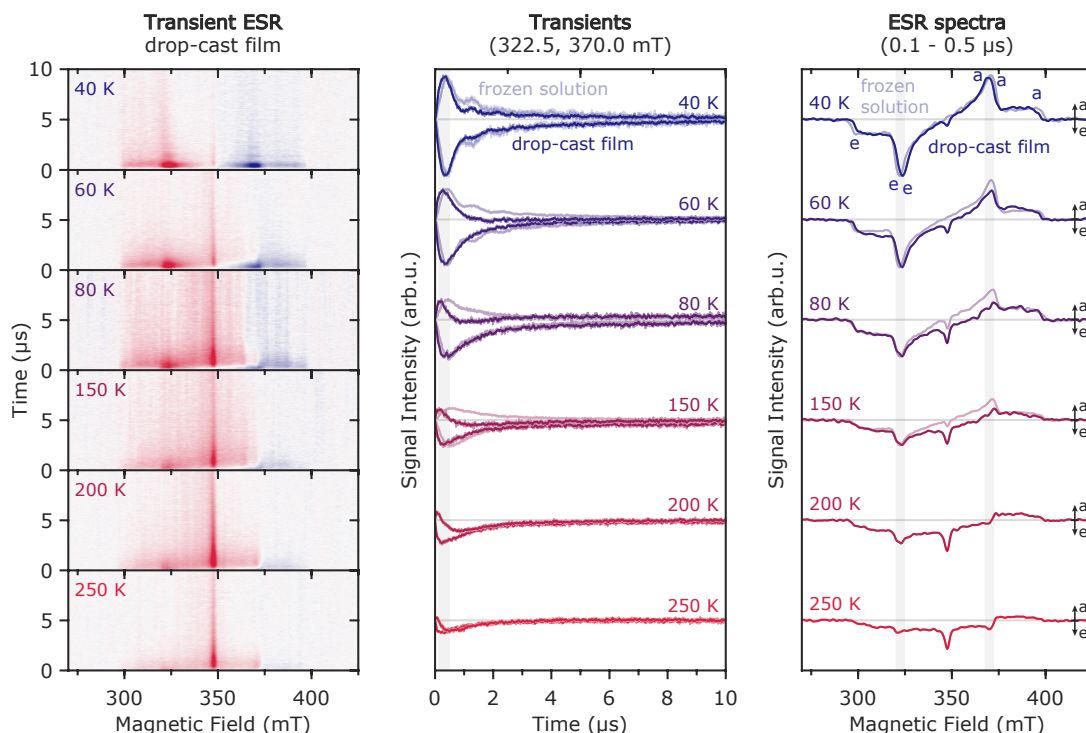


Figure 4.7 – Transient ESR measurements on diF-TES-ADT drop-cast films at a series of temperatures. Time-dependent evolution of the ESR spectra as a function of time after laser excitation (*left*, red = emissive, blue = absorptive), transients extracted at the field positions corresponding to the X canonical field positions (322.5 mT and 370.0 mT, *center*) and spectra extracted at early times after laser excitation (0.1 - 0.5 μ s, *right*). For temperatures up to 150 K, the scaled transients and ESR spectra recorded on frozen solutions are displayed in the background. See Appendix A.6 for experimental details.

At 40 K, the ESR spectrum recorded for diF-TES-ADT in drop-cast films exhibits a triplet state ESR spectrum with an eeeaaa (e = emissive, a = absorptive) spin polarization pattern. The spectrum is characterized by zero-field splitting parameters $|D| = 1370 \pm 5$ MHz and $|E| = 50 \pm 5$ MHz, in good agreement with previously reported values from optically detected magnetic resonance (ODMR).⁴⁵ The spin polarization pattern corresponds to relative populations of $p_X : p_Y : p_Z = 0.45 : 0.36 : 0.19$ across the zero-field spin sub-levels of the triplet state (for $D > 0, E < 0$ in analogy to triplet states on other polyacenes, and

supported by DFT calculations, see Fig. A.18 in the Appendix for details). This is characteristic of triplet states on polyacenes generated by intersystem crossing (ISC), with selective population of the T_X and T_Y sub-levels, associated with the two in-plane symmetry axes, by vibrational spin-orbit coupling.^{198,199} This spin polarization pattern is clearly distinct from the *aeaae* pattern expected for triplet states generated through singlet fission with selective population of the high-field T_0 sub-level independent of orientation (see Fig. A.17 in the Appendix). Therefore, we conclude that the triplet state observed for diF-TES-ADT at low temperatures is generated by ISC, as further confirmed by the excellent agreement between the spin polarization pattern of the ESR spectra recorded for the drop-cast film and for diF-TES-ADT in dilute frozen solution ($|D| = 1420 \pm 5$ MHz, $|E| = 32 \pm 5$ MHz, $p_X : p_Y : p_Z = 0.45 : 0.36 : 0.19^\dagger$).

As the temperature is increased from 40 K to 250 K, the transient ESR spectra recorded for the drop-cast films at 0.1-0.5 μ s after photoexcitation change from a symmetric *eeaaaa* spin polarization pattern to a mostly emissive spin polarization. At each temperature, the spin polarization evolves from a symmetric *eeaaaa* pattern at very short times after laser excitation to a mostly emissive spin polarization at longer times. The net emissive contribution becomes more evident and starts contributing at earlier times as the temperature increases. Overall, the signal intensity of the observed triplet states decreases for increasing temperatures. The observation of a net emissive polarization building up over time is unique to the drop-cast films, while a symmetric polarization pattern still persists for the frozen solution spectra in the probed temperature range (40 K to 150 K, below the freezing point of toluene at 178 K), as evident from the comparison of transients and ESR spectra in Fig. 4.7 (see also Fig. A.16 in the Appendix for the full dataset recorded in frozen solution).

A narrow emissive feature at 348 mT ($g \approx 2.004$) also becomes more prominent for increasing temperatures. Similar features have been observed in other

[†]The slight change in ZFS parameters for diF-TES-ADT in drop-cast films and in solution is likely due to effects of the different molecular environment on the spin density distribution.

singlet fission materials^{182,200} and can originate either from motionally averaged highly mobile triplet states or from radical pairs formed by photoinduced charge transfer. In diF-TES-ADT, the delayed rise of this contribution compared to that of the triplet state signal (see Fig. A.19 in the Appendix for details), the narrow spectral width and the emissive polarization, lead us to speculate that this contribution is due to a spin-correlated radical pair formed by charge separation after formation of the triplet state by ISC, and probably in conjunction with the triplet-triplet annihilation process, given that the relative weight of this contribution increases with the increased emissive triplet state polarization resulting from spin-selective annihilation. The emissive polarization is inherited from the spin-polarized triplet mentioned.²⁰¹ A detailed explanation of motional narrowing and spectral broadening is provided in Appendix A.6.4.

We did not observe any contribution from strongly coupled triplet pairs forming a quintet state for diF-TES-ADT at any of the investigated temperatures (see Fig. A.17 in the Appendix for a simulation of the expected spectrum), in contrast to what has been previously observed for exothermic singlet-fission materials.^{92,176,180}

A delayed net emissive triplet state spin polarization has been previously proposed to result from triplet-triplet annihilation in antiferromagnetically coupled triplet pairs²⁰² and first observed experimentally in anthracene-tetracyanobenzene and phenazine-tetracyano-quinodimethane molecular crystals.²⁰³ The origin of the delayed net emissive spin polarization can be traced back to the spin selectivity of triplet-triplet annihilation. The encountering triplets can form pairs with total spin 0, 1 or 2, but annihilation is selective for encounter pairs with overall spin 0 due to spin conservation. The remaining coupled triplet pairs with overall spin 1 or 2 undergo spin mixing driven by spin-spin interactions and, combined with the selective annihilation of any pairs with overall spin 0, this leads to the build-up of a spin polarization that is inherited by the individual triplet states after separation.²⁰² Generation of this spin polarization requires mobile triplet states, which can encounter within the material and separate again, and

the presence of spin-spin interactions in the coupled triplet pairs surviving the encounter. The absence of a net emissive spin polarization at low temperatures (\leq ca. 40 K), where triplet exciton diffusion is frozen out, and the increase of this contribution for increasing temperatures, and therefore increasing triplet exciton mobility, supports interpretation of the evolution of spin polarization observed for diF-TES-ADT films in terms of triplet-triplet annihilation.

The presence of triplet-triplet annihilation is further confirmed by fluence-dependent trESR measurements performed at 100 K and shown in Fig. 4.8. An increasing contribution of the delayed net emissive polarization, relative to the initial eeeaaa polarization pattern, is observed for higher laser fluences, indicating dependence of this polarization on the number of triplet excitons, as expected for polarization originating from a bimolecular triplet-triplet annihilation process.²⁰³

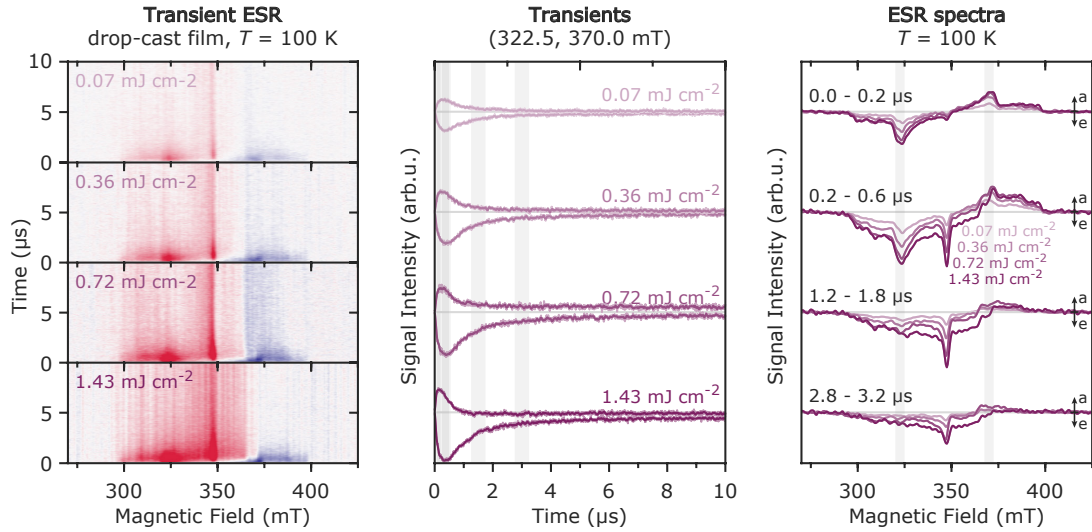


Figure 4.8 – Transient ESR measurements on diF-TES-ADT drop-cast films at 100 K for different laser fluences. Time-dependent evolution of the ESR spectra as a function of time after laser excitation (*left*, red = emissive, blue = absorptive), transients extracted at the field positions corresponding to the X canonical field positions (322.5 mT and 370.0 mT, *center*) and comparison of spectra extracted at different times after laser excitation (*right*). See the methods section for experimental details.

The evolution of spin polarization of the triplet state spectra observed for the diF-TES-ADT films at different temperatures and laser fluences can be modeled

using a kinetic scheme originally proposed by Corvaja *et al.*²⁰³ and including the spin-selective unimolecular decay of the triplet sub-level populations, spin relaxation, and importantly, the bimolecular decay by triplet-triplet annihilation (see Section A.6.5 in the Appendix). The resulting simulations of spectra extracted at short times after photoexcitation are compared to the experimental results in Fig. 4.9. To minimize the number of fitting parameters, the rate constants for spin-selective triplet decay and relaxation were first extracted from simulations of the frozen solution trESR spectra. Simulations for the drop-cast films were then performed by only varying the rate constants for triplet-triplet annihilation. As can be seen from the comparison of the experimental results with simulations in Fig. 4.9, the kinetic scheme of Corvaja *et al.* captures all the important features of the trESR spectra for the different experimental conditions. The simulations confirm that triplet-triplet annihilation plays an increasing role at higher temperatures and higher excitation intensities.

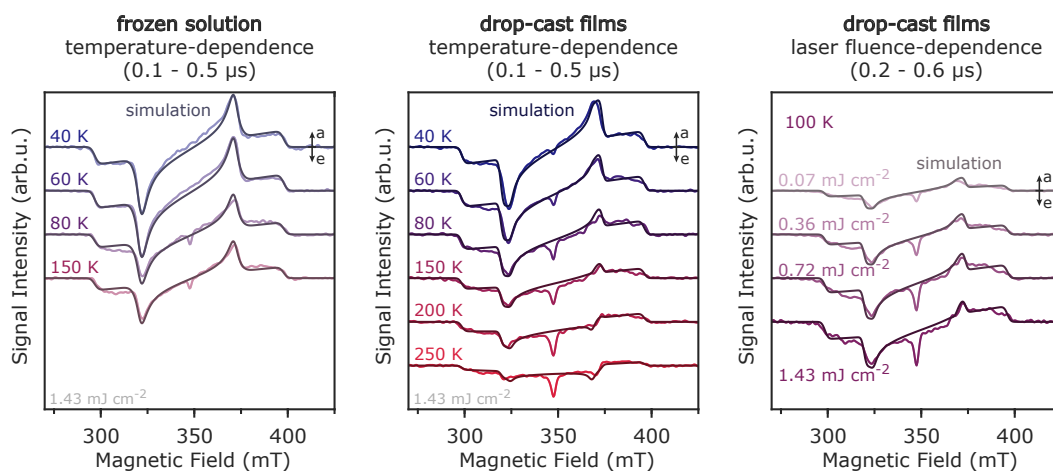


Figure 4.9 – Comparison of experimental transient ESR spectra with simulations: results of measurements on diF-TES-ADT frozen solutions and drop-cast films at a series of temperatures and at different laser fluences are modeled considering spin-selective decay kinetics, relaxation processes and the effect of triplet-triplet annihilation. See Appendix A.6.5 for simulation parameters and details of the simulation procedure.

The absence of singlet fission-generated triplet states in trESR measurements

and no evidence for the occurrence of singlet fission in the MFE data recorded below 270 K (Fig. 4.5) in combination with the observation of features originating from triplet-triplet annihilation in both MFE and trESR measurements, indicate that bimolecular triplet-triplet annihilation dominates at low temperatures. TrESR further demonstrates that the triplets which undergo bimolecular triplet-triplet annihilation are initially generated by intersystem crossing. However, transient absorption and emission spectroscopy^{37,45} show that $^1(TT)$ is formed with a ≈ 200 ps time-constant, independent of temperature.^{37,45} Therefore, spin-forbidden intersystem crossing from S_1 is unlikely to compete with the initial $^1(TT)$ formation, and this is supported by the lack of long-lived triplets in transient absorption spectroscopy at room temperature.⁴⁵ We therefore conclude that the ISC-generated triplets observed in trESR originate from $^1(TT)$ *via* intersystem crossing. At room temperature, we hypothesize that $^1(TT)$ separation to form (T..T) is competitive with intersystem crossing and full singlet fission occurs according to $S_1S_0 \rightarrow ^1(TT) \rightarrow (T..T)$, as observed in the MFE measurements. At temperatures below 270 K, however, intersystem crossing out-competes triplet-pair separation and free triplets are mainly generated by intersystem crossing. $^1(TT) \rightarrow T_1$ is not unprecedented, as intersystem crossing is known to occur in carotenoids from the lowest-lying S_1 state²⁰⁴ and, in these molecules, S_1 can be described as an intramolecular $^1(TT)$ state.⁵²

In addition, the near-degeneracy between $^1(TT)$ and high-lying triplet states T_2 and T_3 in diF-TES-ADT should favor intersystem crossing. We can estimate these triplet state energies from previous studies: from phosphorescence spectra⁴⁵ $E_{T_1} = 1.08$ eV, and from transient absorption spectra¹⁹⁶, the vertical triplet energies (at the T_1 geometry) are $E_{T_2} = 2.20$ eV and $E_{T_3} = 2.33$ eV. Assuming relaxation along the triplet potential energy surface to be on the order of 200 meV^{205,206}, we put the relaxed triplet energies at $E_{T_2} = 2.00$ eV, $E_{T_3} = 2.13$ eV. These triplets are almost degenerate with $^1(TT) - E_{(TT)} = 2.13$ eV⁴⁵. It is therefore reasonable that intersystem crossing can occur from $^1(TT)$ to T_2S_0 and/or T_3S_0 followed by rapid internal conversion to T_1S_0 , as shown in the energy level diagram in

Figure 4.2 b.

We note that it is possible that T_1 is generated from $^1(\text{TT})$ via a different mechanism, where $^1(\text{TT})$ converts first to $^3(\text{TT})$ before internally converting to T_1 . However, since the $^3(\text{TT})$ states are antisymmetric relative to interchange of the two partners and the $^1(\text{TT})$ and $^5(\text{TT})$ are symmetric, the $^1(\text{TT}) \rightarrow ^3(\text{TT})$ conversion is less efficient than $^1(\text{TT}) \rightarrow ^5(\text{TT})$. Therefore, we would expect that if $^3(\text{TT})$ were generated, $^5(\text{TT})$ should also be generated, and we see no evidence of quintets in the trESR data.

4.2.4 MFE simulation and kinetic modelling

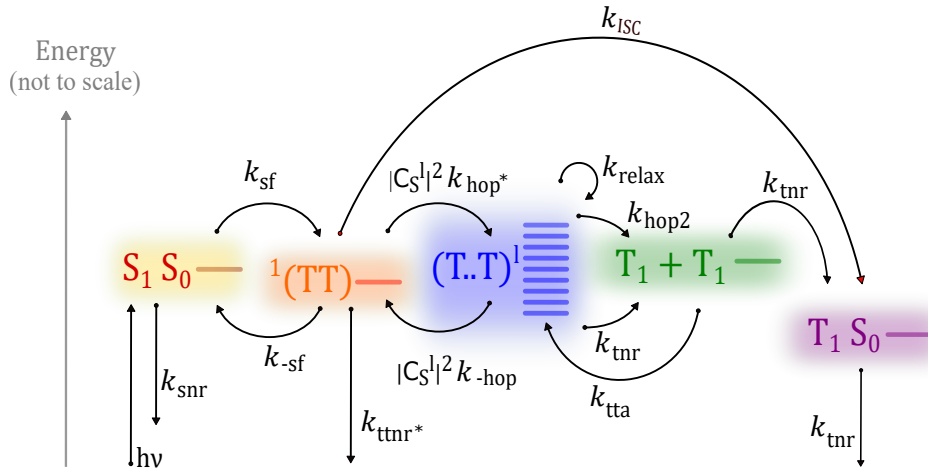


Figure 4.10 – The updated kinetic scheme involving singlet fission at temperatures ranging from 270 K to RT and intersystem crossing at temperatures below 270 K. The rates used in our model are marked in the figure. Here k_{snr} , k_{ttnr*} and k_{tnr} include both radiative and non-radiative decay to the ground-state. The relative energies are NOT to scale (separation between T..T levels is on the order of 1-10 μeV , and exchange energy $2J$ between S_0S_1/S_0T_1 is on the order of 1 eV, while the difference between $^1(\text{TT})$ and T_1+T_1 is $\sim 30 \text{ meV}$).

To test our hypothesis, we simulated the MFE data at both RT and 100 K using a model based on the modified Merrifield kinetic model described in Ref.³⁷ This modified Merrifield model has been shown to correctly simulate the pre-

dicted room temperature MFE data at both early and late delay times for diF-TES-ADT films.³⁷ Here, we further modified the model to include temperature-dependent triplet hopping and intersystem crossing from $^1(TT)$.

Figure 4.10 presents the scheme of our kinetic model. The associated rate equations are:

$$\begin{aligned}
 \frac{d[S_1]}{dt} &= -(k_{sf} + k_{snr}) [S_1] + k_{-sf} [^1(TT)] \\
 \frac{d[^1(TT)]}{dt} &= k_{sf} [S_1] - \left(k_{-sf} + k_{ISC} + k_{hop}^* \sum_{l=1}^9 |C_S^l|^2 + k_{ttnr}^* \right) [^1(TT)] \\
 &\quad + k_{-hop} \sum_{l=1}^9 |C_S^l|^2 [(T..T)^l] \\
 \frac{d[(T..T)^l]}{dt} &= k_{hop}^* |C_S^l|^2 [^1(TT)] - (k_{-hop} |C_S^l|^2 + k_{hop2} + k_{tnr} + k_{relax}) [(T..T)^l] \\
 &\quad + \frac{1}{9} k_{tta} [T_1]^2 + \frac{1}{8} k_{relax} \sum_{j \neq l} [(T..T)^j] \\
 \frac{d[T_1]}{dt} &= (k_{tnr} + 2k_{hop2}) \sum_{l=1}^9 [(T..T)^l] + k_{ISC} [^1(TT)] - 2k_{tta} [T_1]^2 - k_{tnr} [T_1]
 \end{aligned}$$

The rate constants used to model the magnetic field effects were obtained by fitting time-resolved photoluminescence measurements on a diF-TES-ADT film as a function of temperature and laser fluence, as described in Ref.³⁷ In that work, we also simulated the magnetic field effects using only rates obtained from time-resolved spectroscopy. Here, having modified the rate model from our previous work to include temperature-dependent triplet hopping and intersystem crossing terms, we modified the original rates only slightly to reduce the number of fitting parameters to a minimum (see Appendix A.5 for more details). For example, while in Ref.³⁷, k_{ttnr} was used to describe both ISC and the non-radiative decay of $^1(TT)$, here we explicitly include k_{ISC} and denote the rate constant of non-radiative processes as k_{ttnr}^* , to distinguish it from the overall rate used previously. In addition, we modified k_{hop} to include a temperature dependence: $k_{hop}^* = k_{hop}^\circ e^{(\frac{-\Delta E}{k_B T})}$, where k_{hop}° is calculated based on k_{hop} at RT from Ref.³⁷, k_B is the Boltzmann constant, and ΔE is the activation energy for triplet-pair separation ($\Delta E=20$ meV according to Ref.⁴⁵).

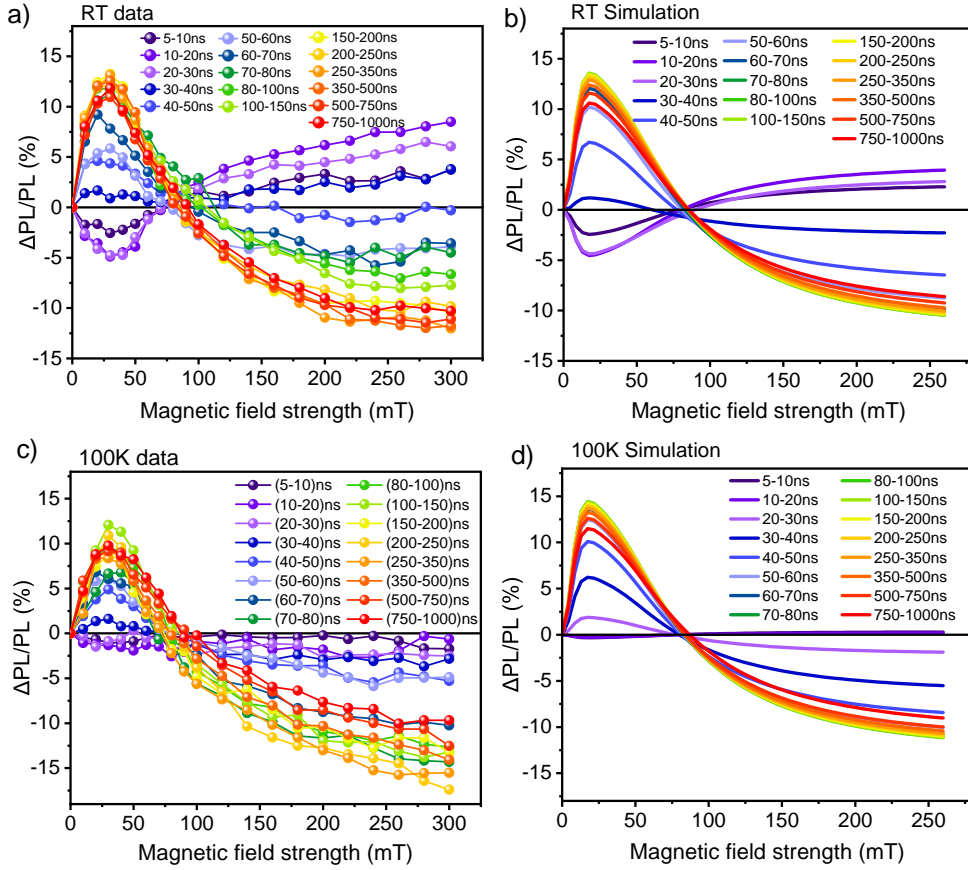


Figure 4.11 – Comparison of experimental results and simulations of MFEs on the photoluminescence. The diF-TES-ADT drop-cast film is measured at 532 nm across different delay times, from 5 ns to 1 μ s, at (a,b) room temperature and (c,d) 100 K, respectively. The simulation and the data of the MFE at RT and 100 K are in reasonably good agreement in terms of the shape, intensity, and zero-crossing over the entire time range.

As presented in Figure 4.11, we find that the simulation and the data of the MFE at RT (Fig. 4.11a,b) and 100 K (Fig. 4.11c,d) are in reasonably good agreement in terms of the shape, intensity, and zero-crossing over the entire time range. There are some discrepancies in the dynamics, which are due to the simplicity of the model, but overall the physics of the system is well represented by the model.

In addition, Figure 4.12 shows simulations of the power-dependent MFE data reported in Fig. 4.6. For this simulation, the reported laser power, measured in μ W, had to be converted to the exciton density, measured in cm^{-3} . However, the

potential excitation densities vary by approximately three orders of magnitude due to the non-uniform thickness of the drop-cast film. Accurately determining the excitation densities for this specific sample is somewhat challenging. Consequently, we use the thin film's excitation densities in our simulation since we possess precise measurements of the film's thickness. Details of the fluence dependence simulation and exciton density calculation are included in Section A.5.3.

The simulation in Fig. 4.12b reproduces the drop in the TTA-MFE as the exciton density rises and broadly shows good agreement with the experimental MFE behavior of Fig. 4.12a.

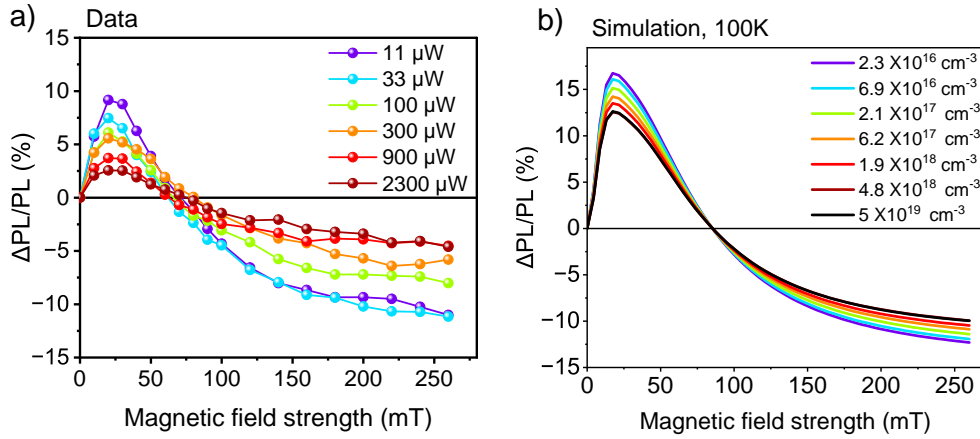


Figure 4.12 – Fluence-dependent MFE simulation. Comparison of (a) experimental results and (b) simulation of the fluence-dependent magnetic field effect of diF-TES-ADT drop-cast film measured at 523 nm at 100 K. The simulation shows the drop in the TTA-MFE as the exciton density rises and broadly shows good agreement with the experimental MFE behavior.

4.3 Conclusion

In conclusion, in this study we showed that, despite a temperature-independent formation of strongly exchange-coupled $^1(TT)$ in crystalline diF-TES-ADT films, demonstrated in earlier work^{37,45}, the formation of weakly coupled (T..T) is highly temperature-dependent. Fluorescence-detected magnetic field effects, for

example, showed no signature of singlet fission below 270 K and transient ESR showed no signatures of quintet states or singlet fission-generated triplets at any temperature between 40 and 250 K. Instead, our results suggest direct intersystem crossing (ISC) from bound triplet pairs to individual triplet states, $^1(\text{TT}) \rightarrow \text{T}_1\text{S}_0$, takes place at low temperatures, whereas singlet fission only becomes dominant at higher temperatures. These findings, supported by magnetic field effect and trESR experiments, reveal an additional decay pathway of the biexcitonic $^1(\text{TT})$ state through ISC and therefore an additional variable to consider when designing singlet fission materials for quantum or solar applications.

In organic systems without heavy atoms, ISC is mostly driven by vibronic spin-orbit coupling.¹¹³ A competition between ISC from S_1 and singlet fission has previously been observed in crystalline tetracene²⁰⁷ and other systems,^{190,208–210} where ISC was enhanced by small energy gaps or near degeneracy of S_1 and high energy triplet states or spin-orbit charge-transfer ISC.²¹⁰ This work thus adds to an increasing amount of evidence that ISC can out-compete singlet fission, in the case of diF-TES-ADT, even following the initial step of singlet fission forming the $^1(\text{TT})$ state, through a potentially important additional loss pathway.

Even though singlet fission is suppressed at low temperatures in diF-TES-ADT, triplet-triplet annihilation of the ISC-born triplet states remains allowed down to cryogenic temperatures, where decreased triplet state mobility starts to prevent encounters. Generation of the $^1(\text{TT})$ state not only by singlet fission but also by bimolecular triplet-triplet annihilation, as observed in previous optical studies,³⁷ allows comparison of the role and dynamics of this state in the two multiexciton processes. We find that, in diF-TES-ADT films, bimolecular triplet-triplet annihilation does not populate quintet states efficiently enough, or the formed states are not long-lived enough to be observed with trESR, as opposed to significant evidence for contribution of these states to the singlet fission mechanism in several other materials.^{34,92,176,180–190} This finding could indicate stabilization of $^1(\text{TT})$ with respect to $^5(\text{TT})$, as expected from configuration interaction arguments⁷⁴ and may have implications for triplet-triplet annihilation

up-conversion.

Finally, our study further highlights the importance of combining a range of different optical and magnetic resonance spectroscopic techniques to obtain a full picture of the photophysical processes in materials for singlet fission and triplet-triplet annihilation. Only by combining the ability to identify formation of the $^1(TT)$ state by photoluminescence spectroscopy, the unequivocal assignment of the formation mechanism of the observed independent triplet states to ISC based on the spin polarization pattern in trESR spectra and the evidence from both temperature- and fluence-dependent magnetic-field-dependent photoluminescence and trESR experiments for bimolecular triplet-triplet annihilation, we were able to fully unravel the photophysics of the diF-TES-ADTsystem.

Chapter 5

The investigation of excitation dependence reveals ultrafast intersystem crossing in tetracene dimers

Intersystem crossing (ISC), facilitated by spin–orbit coupling between singlet and triplet states, leads to population of the triplet manifold, which is fundamentally responsible for phosphorescence.^{211,212} The timescales for ISC are often much slower than those of the corresponding singlet transitions. Nevertheless, examples of ultrafast intersystem crossing are present, although mostly in molecular systems including heavy atoms.⁴⁷ In this chapter, we investigate the ultrafast intersystem crossing and triplet generation in tetracene derivatives using picosecond transient absorption spectroscopy as a function of excitation wavelength. We find that triplets are generated by ultrafast intersystem crossing in some tetracene dimers and monomers. The results suggest that intersystem crossing is influenced by the excitation wavelength, and the triplet yield increases at higher excitation energy.

[†]The majority of the work presented in this chapter is my own; contributions from collaborators are explicitly noted.

5.1 Introduction

For over fifty years, researchers have used polyacene crystals, such as pentacene, tetracene, anthracene, and naphthalene, as models to study the fundamental electrical and optical characteristics and reactions of various organic semiconductors.^{213,214} Researchers have also demonstrated the effectiveness of polyacenes as materials for singlet fission. In singlet fission, the photoexcited singlet excited state S_1 rapidly converts into the singlet-triplet pair state $^1(TT)$, which, by spin evolution, produces the quintet triplet pair state $^5(TT)$. New theoretical investigations have demonstrated that specific sub-levels of the quintet can be selectively populated when the chromophores' orientations are parallel.^{20,215} In Chapter 7,³⁴ we demonstrate that a long quantum coherence time of the quintet state can be achieved by arranging two pentacene chromophores in parallel orientation; however, this state can not be optically read out. In this chapter, we investigate tetracene derivatives, which are energetically more comparable to diF-TES-ADT. Our objective is to identify a system that not only forms a quintet state but also allows for optical readout. To achieve this, we first examine whether these tetracene-based systems undergo efficient singlet fission.

The $^5(TT)$ manifold, which is born in SF, is seen as a new platform for the production of a quantum bit (qubit) because of its optically excited strong spin polarization and its capacity to perform fast quantum gate operations using microwave pulses.^{20,166} One of the primary advantages of molecular-based quantum bits is that their structure is atomically uniform and may be chemically modified to precisely regulate their properties and structure.^{216,217} Preparing the initial pure quantum state in the qubit and having a suitably long quantum coherence time are needed for any quantum applications.

Among the various materials investigated for their potential in such applications, tetracenes and pentacenes stand out as the most extensively studied molecules.^{41,48,49} Crystalline tetracene has dominated most of the singlet fission research.^{218,219} In tetracene crystals, the triplet state's yield is far over 100%, and

even somewhat near to 200%.²¹⁹ However, the investigation of singlet fission mechanisms in crystalline tetracene is complicated due to the complexity of this material, arising from the presence of multiple defect states and the singlet exciton delocalization.²²⁰ As the smallest feasible systems capable of undergoing singlet fission, covalently bonded tetracene dimers are therefore suggested.^{34,48}

Bardeen introduced a set of linear tetracene dimers that were covalently bonded.^{221,222} Nevertheless, despite the significantly high singlet fission yields observed in crystalline tetracene, these linear molecules exhibit singlet fission yields of 2–3%. The low yield in these molecules is attributed to the weak interaction between the two tetracene subunits. Furthermore, another study has reported comparable low triplet quantum yields ($\sim 9\%$) in a set of synthesized covalently bonded linear dimers.²²³ The findings indicate that the weak interactions among the dimers subunits account for reducing singlet fission yields, which was additionally confirmed by theoretical calculations.²²⁴ To enhance the singlet fission yield, it is essential to modify the two tetracene subunits' interaction by altering their relative orientations.³⁴

In the present work, new macrocyclic parallel tetracene dimers were synthesized by Wataru Ishii at Kyushu University in Japan to examine their photo-physics and determine the ideal conditions for singlet fission. These dimers are connected by Schiff-base chemistry (Fig 5.1), which is used for the production of dynamic covalent bonds.^{151,225,226} The benzene ring and the π - π interactions between tetracene units form a rather rigid bridge structure. This stops the tetracene moieties from rotating freely and lines up the tetracene units in parallel. The close parallel arrangement of neighbouring tetracene was expected to facilitate rapid intramolecular singlet fission and the selective formation of quintet states. However, we do observe a low yield of triplets. These form even in the monomer with an excitation-wavelength dependence. We explore the mechanism of triplet formation in these molecules using excitation wavelength-dependent transient absorption spectroscopy and conclude ultrafast intersystem crossing (ISC) in DPT-dimer 1 and its monomer. These results are consistent with other

studies indicating that, under specific conditions, an ultrafast intersystem crossing process occurs in some tetracene dimers, monomers,^{227,228} and other organic molecules.^{229,230} We demonstrate, in this work, that intersystem crossing is sensitive to the excitation wavelength and the triplet yield increases at higher excitation energy. This finding lays the groundwork for future research into triplet state-involved photophysics and photochemistry in tetracene derivatives.

5.2 Results and discussion

5.2.1 Model systems

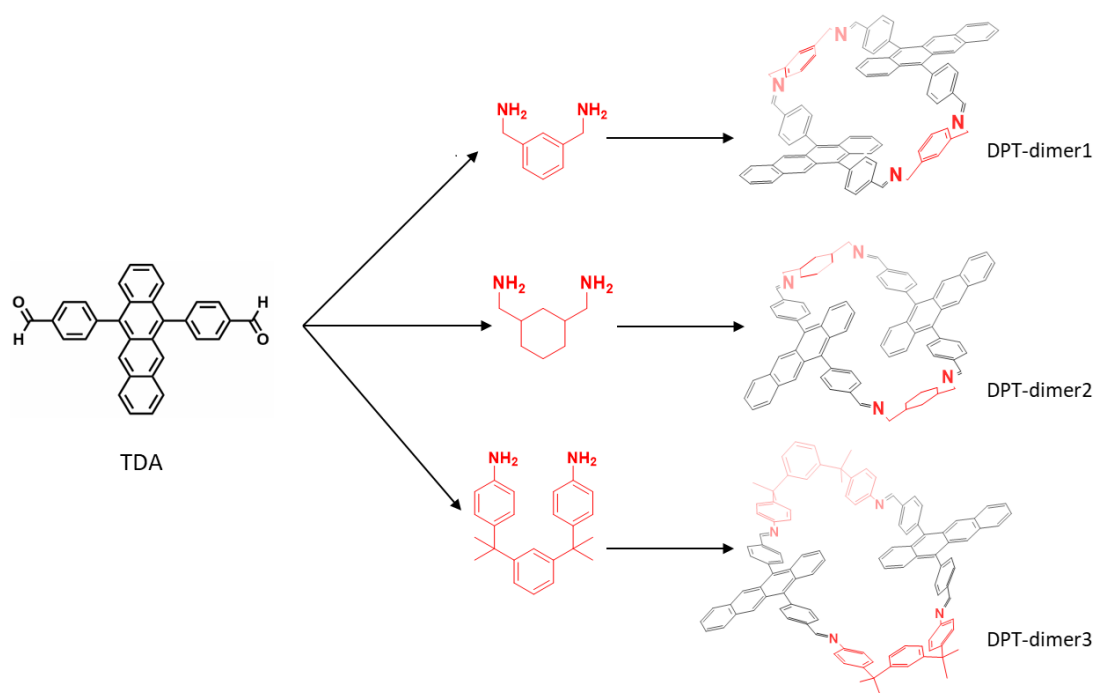


Figure 5.1 – Synthetic scheme. Monomeric tetracene dialdehyde (TDA) was used to synthesize DPT-dimer1 (top), DPT-dimer2 (middle), and DPT-dimer3 (bottom).[†]

DPT-dimers were synthesized using the monomeric tetracene dialdehyde (Tetracene-2,6-dicarboxaldehyde)(**TDA**) combined with m-xylylenediamine for **DPT-**

[†]TDA monomer and DPT-dimers were synthesized by Wataru Ishii at Kyushu University in Japan

dimer 1, 1,3-Cyclohexanebis(methylamine) for **DPT-dimer 2**, and 1,3-Bis[2-(4-aminophenyl)-2-propyl]benzene for **DPT-dimer 3**, as illustrated in Figure 5.1. The chemistry of dynamic covalent bonds, such as Schiff-base formation, can selectively yield the thermodynamically most stable molecules.^{151,152} The carbon-carbon distance between the two tetracene units ranges from 3.79 Å in DPT-dimer 1-2 and 3.89 Å in DPT-dimer 3, showing the existence of π - π interactions, as presented in Figure 5.2.

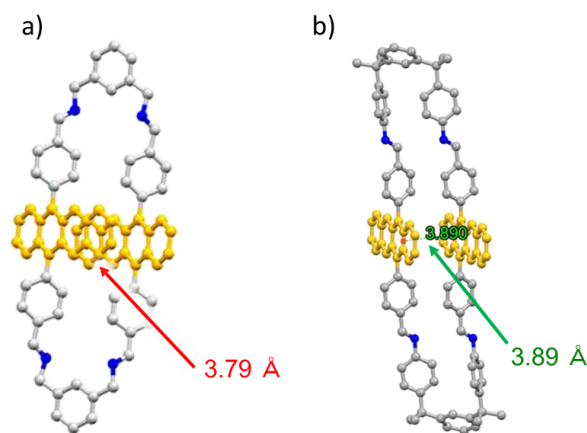


Figure 5.2 – Single crystal structure. The distance between the two tetracene units are (a) 3.79 in DPT-dimer 1-2 and (b) 3.89 in DPT-dimer 3 (Solvent molecules and hydrogen atoms are deleted for clarity).

Steady-state absorption spectra of TDA monomer (black solid line) and DPT-dimer 1 (blue solid line) in toluene at room temperature are presented in Figure 5.3. It is noticeable that the absorption spectrum of TDA monomer is slightly different from that of DPT-dimer 1. The absorption spectrum of TDA monomer shows three separate bands, where the most intense is located at 495 nm, followed by 463 and 435 nm. The vibronic progression 0-0, 0-1, and 0-2 causes the individual peaks to appear. Similarly, the DPT-dimer 1 spectrum shows three absorption peaks, observed at 498, 466, and 439 nm; however, the 466 nm band is now the most intense. The reduction of the 0-0 peak of the dimer is associated with H-aggregate formation (weak electronic coupling), as illustrated in the

right inset in Figure 5.3.¹⁰⁴ Note that DPT-dimer 1 absorption spectrum bands are broader than that of the monomer with a slight redshift of ~ 3 nm. This is due to the π - π interaction between the tetracenes.¹⁵ The excitonic interactions between tetracene chromophores in the dimer structure were investigated from the absorption spectra of DPT-dimer 1 at room temperature. Beer-Lambert plots of toluene solutions of DPT-dimer 1 showed that it is in the molecularly dispersed state up to 100 μ M (Figure 5.4).

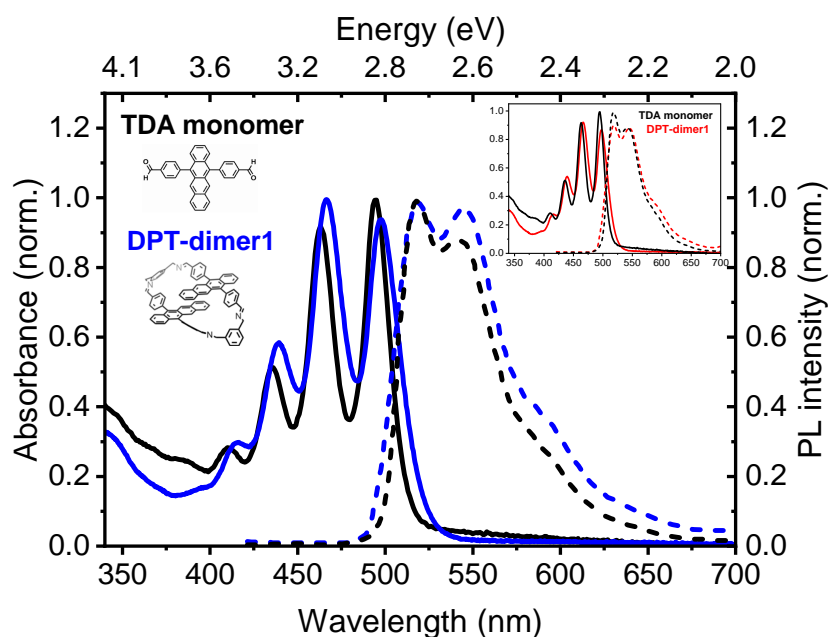


Figure 5.3 – Steady-state absorption and fluorescence. Normalized absorption (solid line) and fluorescence (dotted line) spectra of TDA monomer (black) and DPT-dimer1 (blue) in toluene solutions at room temperature. The left inset presents the chemical structure of TDA monomer and DPT-dimer 1, whereas the right inset depicts the absorption and fluorescence spectra, which were normalized to the 0-1 peak to emphasize H-aggregate formation, characterized by a suppression of the 0-0 peak.

The fluorescence spectrum of DPT-dimer 1 (blue dotted line) presents broad emission bands at around 517 and 544 nm, but the band at 544 nm has been enhanced due to the interactions between the two tetracene subunits. A noticeable red-shift of about 3 nm in DPT-dimer 1 compared to that of the TDA monomer (black dotted line) is shown in Fig.5.3. The concentrations of the monomer and

dimer solutions for this experiment were very low, around 100 μM , therefore minimizing any reabsorption effects. Thus, we don't believe that the observed decrease in the dimer peak at 517 nm is because of the self-absorption. Rather, the suppression of the 0-0 peak in the dimer, particularly when normalized to the 0-1 peak as shown in the right inset in Figure 5.3, suggests the presence of H-aggregate formation. Comparable spectroscopic features were also observed for a covalently bonded tetracene dimer and its monomer in Ref.¹⁵ Absorbance and photoluminescence spectra of the dimers 2 and 3 are similar to those of dimer 1. Consequently, we have concentrated on dimer 1 and its comparison to the monomer to streamline our discussion and provide a more focused analysis.

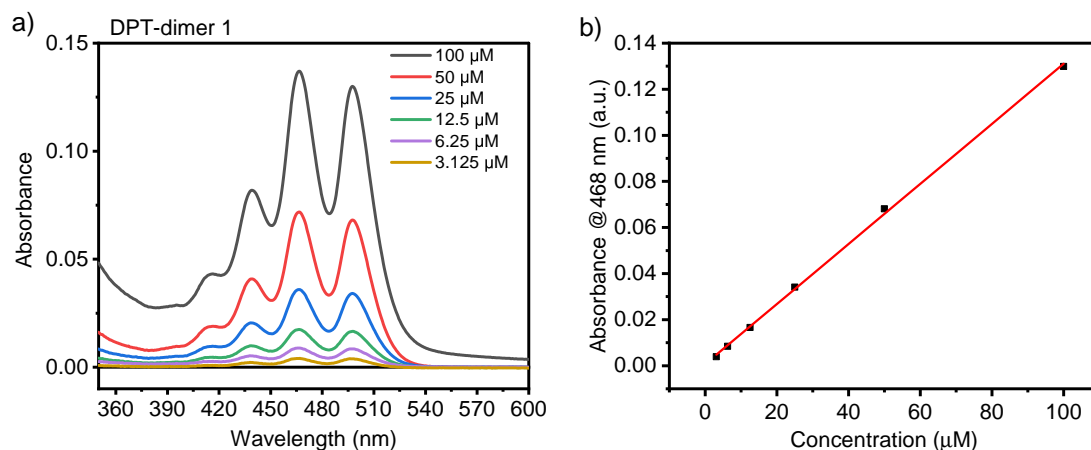


Figure 5.4 – Concentration-dependent absorption spectra of DPT-dimer 1.[†]

(a) Absorption spectra of DPT-dimer 1 in toluene solution at different concentrations ranging from 100 μM to 3.125 μM . (b) Beer-Lambert plot of DPT-dimer 1 in toluene at 468 nm. The fitted linear line (red) indicates DPT-dimer 1 is molecularly dispersed in toluene up to 100 μM at room temperature.

A normalized time-resolved fluorescence decay excited at 470 nm and detected at 630 nm of TDA monomer (black line) and DPT-dimer 1 (red line) is shown in Figure 5.5. The decays at 0.05 mol% in a polystyrene film at room temperature are shown in Figure (5.5 a), whereas Figure (5.5 b) displays the fluorescence decays at 100 μM in toluene solution at 77 K. In both polystyrene film and solution, DPT-

[†]This measurement has been conducted by Wataru Ishii at Kyushu University in Japan

dimer 1 exhibits longer-lived delayed fluorescence compared to the monomer's emission. In polystyrene film, the monomer's decay exhibits single-exponential behaviour with a short lifetime of $\tau=13$ ns. In contrast, DPT-dimer 1 exhibits a biexponential decay with two unique time constants; a rapid decay component of $\tau=13$ ns and a delayed component of $\tau=46$ ns. A similar trend was noted in the dimer solution at 77 K, characterized by a rapid decay time of $\tau=15$ ns and long-delayed fluorescence with $\tau=123$ ns. This long-lived component indicates that the covalent linking in the dimer introduces new activation pathways that are absent in the monomer. It may indicate delayed fluorescence arising from the intramolecular recombination of two triplets generated within the same dimer. Intermolecular triplet-triplet annihilation resulting from diffusive interactions between distinct molecules can be excluded, as the extended decay is observed for dimer 1 in both solution and film, but never for the monomer.^{219,221}

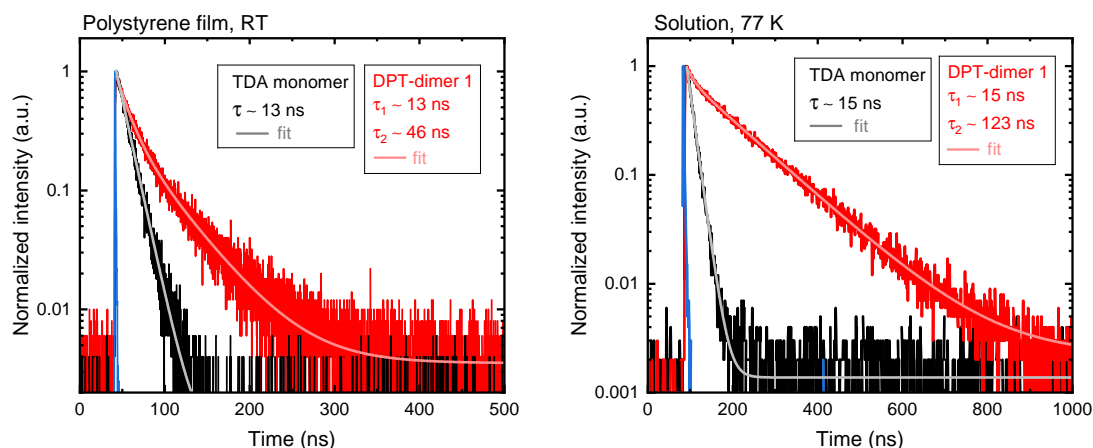


Figure 5.5 – Photoluminescence Lifetime.[†] Time-resolved fluorescence decays of TDA monomer (black line) and DPT-dimer 1 (red line) at (a) 0.05 mol% in polystyrene film at room temperature, and (b) 100 μ M in toluene solution at 77 K.

[†]This measurement has been conducted by Wataru Ishii at Kyushu University in Japan

5.2.2 Investigation of singlet fission and triplet formation in tetracene dimers

Femtosecond transient absorption (TA) was subsequently measured to investigate the dynamics of photogenerated states in TDA monomer and DPT-dimers in solution. Figure 5.6 displays the transient absorption's false-colour map (left), spectra (middle), and normalized dynamics of the main species (right) for the TDA monomer (Fig 5.6 a), DPT-Dimer 1 (Fig 5.6 b), DPT-Dimer 2 (Fig 5.6 c), and DPT-Dimer 3 (Fig 5.6 d) in toluene at room temperature. The data obtained following on-resonance 500 nm excitation wavelength with an average pump power of 1 mW. For reference, the absorption and emission spectra of the ground electronic state are presented in solid and dashed grey lines, respectively.

The positive transient absorption features over the spectral range indicate a photo-induced absorption (PIA). Compared to the steady-state absorption, ground-state bleach (GSB) depopulation accounts for the negative features at ~ 467 nm and 495 nm. TDA monomer after 500 nm excitation shows excited state absorption characteristics at 415, 476, and 630 nm. These features are identified in the TA plot as PIA1, PIA2, and PIA3, respectively. On the other hand, similar excited state absorption features are seen at ~ 415 , 483, and 636 nm in the dimers. Random change in intensity in the 500 nm region originates from the excitation pulse, which is scattered into the detector and cannot be fully removed by data processing.

In the TDA monomer (Fig 5.6 a), the pronounced excited state absorption (PIA1) at 415 nm has decayed on the nanosecond timescale ($\tau \sim 12$ ns), indicating a transfer of excitation energy to lower energy states. This species was attributed to singlet excitons based on a comparable study on tetracene in solution.²²⁸ A notable small feature (PIA2) at 476 nm appears on a 20 ps timescale and increases after the decay of S_1 state, signifying its long-living character. Several studies have shown that the lowest-lying triplet excited state of tetracene and its derivatives exhibits high absorption in the region between 400 and 500 nm.^{219,231–233}

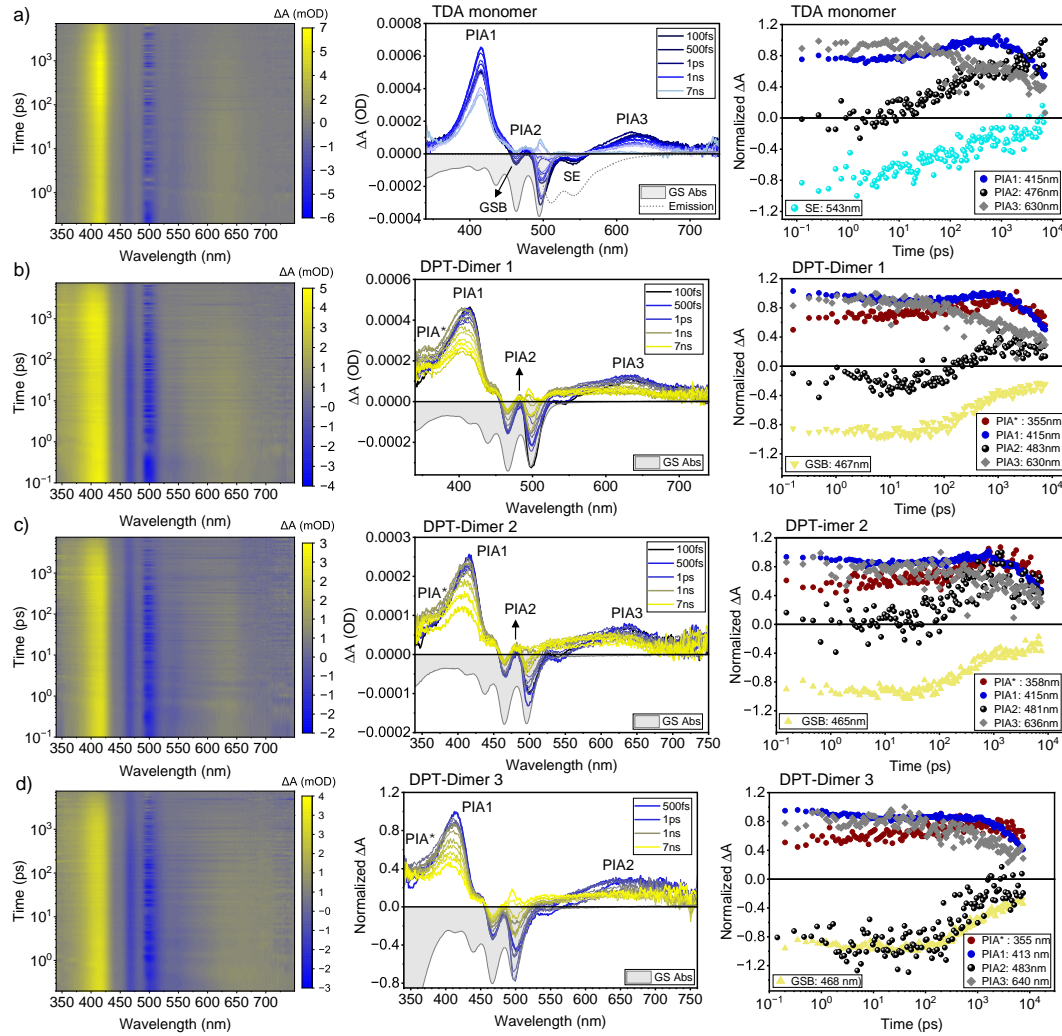


Figure 5.6 – Transient absorption spectroscopy of TDA monomer and DPT-dimers. Transient absorption false-colour map (left), spectra (middle), and normalized dynamics of the main species (right) for (a) TDA monomer, (b) DPT-Dimer 1, (c) DPT-Dimer 2 and (d) DPT-Dimer 3 in toluene at room temperature obtained at 500 nm excitation wavelength with an average pump power of 1 mW. Ground electronic state absorption and emission spectra are shown in solid and dashed grey lines, respectively, for reference.

As this peak is rising slower than the others, this strongly suggests the formation of triplet excitons through a slower process such as intersystem crossing. An additional photo-induced absorption peak (PIA3) is seen at 630 nm presenting a shorter lifetime, which can be attributed to singlet absorption, as reported in

Burdett’s study.²¹⁹ A negative feature appears at 543 nm matches well with the steady-state PL spectrum, caused by stimulated emission (SE) from TDA’s S_1 state.

In summary, the excitation of TDA monomer generates S_1 (SE, PIA1, PIA3) which decays radiatively and non-radiatively, including forming triplets (PIA2) on 10-100s of picosecond timescales.

Transient absorption spectra of tetracene dimers display similar species as the monomer. DPT-dimer 1 and 2 presented in Figure 5.6 (b,c) show comparable singlet state absorption at ~ 415 nm (PIA1) and 636 nm (PIA3). The singlet state lifetime is about 10 ns, which aligns with the photoluminescence lifetime measured in the time-resolved fluorescence decays in Figure 5.5. A few nanometer blue shifts over time are seen in the singlet feature at 415 nm (PIA1), which may be caused by dimer exciton delocalization.²³⁴ A small feature at 483 nm (PIA2) could be associated with triplets,²³⁵ but as it forms more slowly than the PIA2 feature in the TDA monomer at 476 nm (PIA2) (on a 500 ps timescale in dimer 1 and on 50 ps timescale in dimer 2), we conclude that singlet fission is not present - or is at least very inefficient - in these dimers. In the dimers, we do however observe a new PIA feature, PIA*, at 355 nm.

This feature aligns well with a strong steady-state absorption feature for tetracene radical cation near 355 nm, as reported in previous studies (Fig 5.7).^{236,237} This suggests that the feature at 355 nm in the dimers is indicative of a charge transfer (CT) state. A strong absorption feature is also observed around 400 nm in the steady-state spectrum of the tetracene radical cation (Fig 5.7). Based on this, we would expect a second CT-state-related band to appear near this wavelength in the transient absorption spectrum of the dimers. While the presence of a transient feature at 400 nm is consistent with this expectation, its assignment remains uncertain without further evidence. To confirm whether either or both of the 355 nm and 400 nm features correspond to CT states, additional experiments are required, particularly TA measurements in solvents with different polarity. Changing the solvent polarity is expected to cause a significant shift in the energy

of the CT band. Observing such solvent-dependent changes would support the CT-state assignment and help distinguish these features from other excited-state species.²³⁸

At 630 nm, the transient absorption spectra of the dimers exhibit a singlet characteristic that decays differently compared to the monomer. It has a reduced curvature and demonstrates a longer lifetime compared to the monomer. At this wavelength, another reported tetracene radical cation absorption peak is shown in the same references.^{236,237} The variation in the dynamics, together with the observed feature at 355 nm, may indicate a mixed singlet-CT state in DPT-dimers. Such state mixing in our dimer system aligns with the findings of Young *et al.*,²³⁹ who experimentally discovered the coherent mixed state in covalent dimers. This mixed charge transfer/Frenkel exciton (CT/FE) state can also explain the delayed fluorescence signal in the time-resolved fluorescence (Figure 5.5) despite the absence of singlet fission.^{239,240}

Alternatively, it could be a relaxation pathway in which the singlet evolves toward a charge-transfer character.²⁴¹

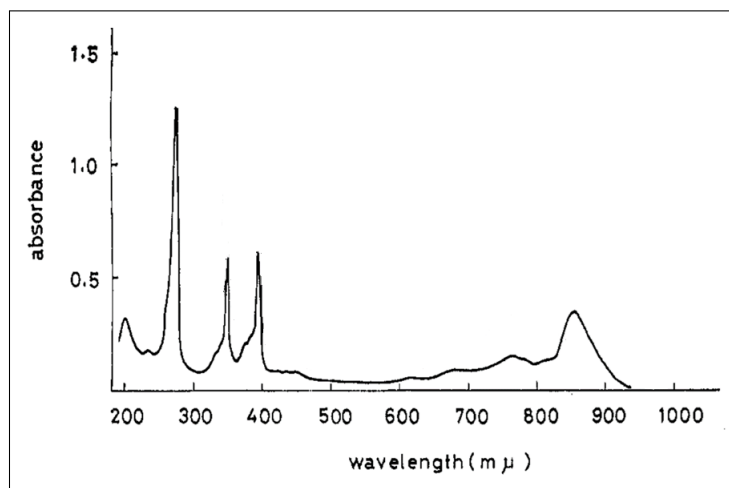


Figure 5.7 – Tetracene radical cation absorption spectrum. It exhibits a pronounced steady-state absorption feature at around 355 nm, in addition to a small absorption peak at 630 nm, which aligns well with PIA species in the TA data of the dimers. Reproduced from Ref.²³⁷

5.2.3 Excitation wavelength dependence shows high-level intersystem crossing

TDA monomer To characterize the tetracene behavior more comprehensively, excitation wavelength-dependent transient absorption studies were conducted focusing on DPT-dimer 1 and its monomer. Figure 5.8 presents transient absorption's false-colour map (left), spectra (middle), and normalized dynamics of the main species (right) of TDA monomer recorded at $\lambda_{\text{exc}} = 450$ nm (Figure 5.8 b) in addition to the previously recorded TA data at $\lambda_{\text{exc}} = 500$ nm (Fig 5.8 a), with an average pump power of 1 mW. Distinct variations are highlighted by the monomer's excitation-dependent TA measurements, which center on the generation of the triplet feature at 476 nm and the behaviour of singlet state absorption at 415 nm. It is noticeable that the singlet state decays faster at ($\lambda_{\text{exc}} = 450$ nm) compared to ($\lambda_{\text{exc}} = 500$ nm), indicating that the excitation wavelength affects the relaxation pathways and excited states lifetimes.²⁴²

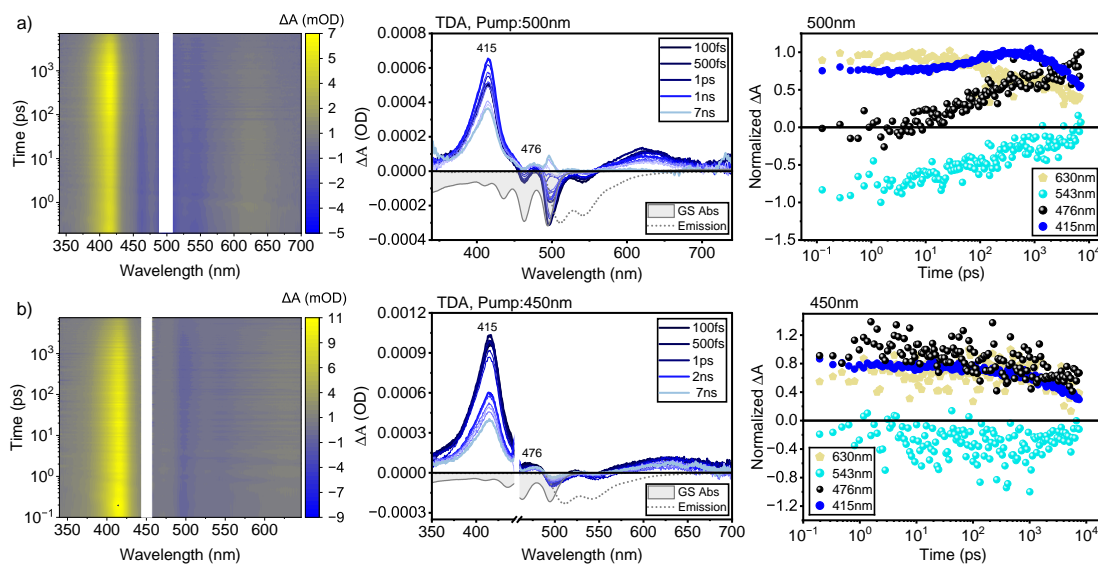


Figure 5.8 – Excitation wavelength dependence of transient absorption spectroscopy for TDA monomer. Transient absorption's false-colour map (left), spectra (middle), and normalized dynamics of the main species (right) of TDA monomer in toluene solution at the excitation wavelength (a) 500 nm and (b) 450 nm, with an average pump power of 1 mW.

At 476 nm, the dynamics in Figure 5.8 b demonstrate different behaviour compared to that given in Figure 5.8 a. While exciting TDA monomer with ($\lambda_{\text{exc}} = 500$ nm) resulted in a gradual triplet state generation by intersystem crossing, the excitation at ($\lambda_{\text{exc}} = 450$ nm) facilitated a more rapid generation of this state within the instrument response time of approximately 100 fs, and a longer decay time compared to the singlet states. This notable excitation-dependent behaviour is examined in greater detail in Figure 5.9, which highlights the distinctions in this species at different excitation wavelengths and compares it with a documented sensitised triplet absorption in tetracene solution.²³⁵ The triplet feature in our TA data exhibits a little blue-shift of about 5 nm and a broader shape compared to the sensitised triplet absorption feature (black dotted line).

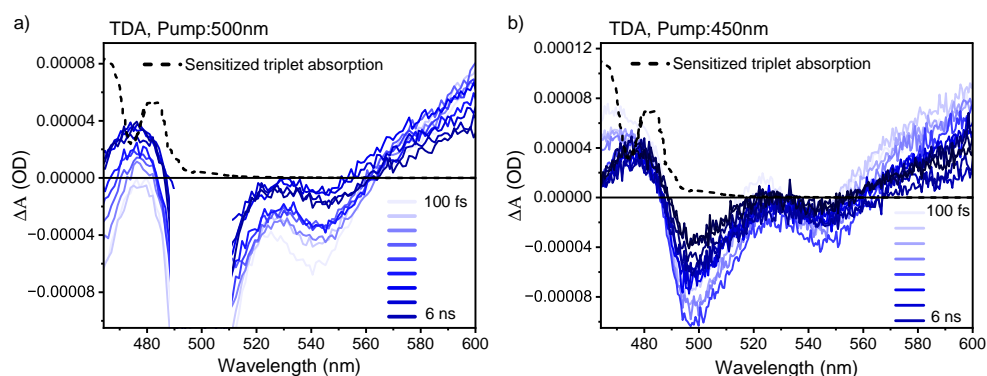


Figure 5.9 – Intersystem crossing triplet state formation presented in Fig 5.8 at 476nm. A zoomed-in feature associated with triplet state formation in TDA monomer at the excitation wavelength of (a) 500 nm and (b) 450 nm, highlighting a slow and fast intersystem crossing triplet formation, respectively. The dashed black lines present a sensitized triplet state absorption in tetracene solution reported in ref.²³⁵

A potential reason for this unexpectedly rapid triplet state population at 450 nm excitation is the dimerization or aggregation of TDA molecules, which subsequently promotes singlet exciton fission. To exclude this possibility, the data recorded at $\lambda_{\text{exc}} = 450$ nm was at the lowest achievable concentration ($\sim 3 \times 10^{-5}$ M), which is lower than the concentration used for the TA measurement at 500 nm pump ($\sim 4.5 \times 10^{-5}$ M). Hence, SF would most likely be seen in the higher con-

centration TA measurement, where molecular interactions are more pronounced, but this is not the case. Further detailed arguments are provided below for diphenyltetracene (DPT), section 6.2.4.

The most likely reason for the triplet state formation at 450 nm excitation is the occurrence of ultrafast intersystem crossing. Birech *et al.* (2014) reported a similar rapid intersystem crossing triplet state formation in tetracene monomer at 20 ps time scale after excitation.²²⁸ He proposed that the T_2 state is close to the S_1 state, hence promoting rapid intersystem crossing to the triplet manifold. He further developed a model to elucidate that, shown in Figure 5.10.

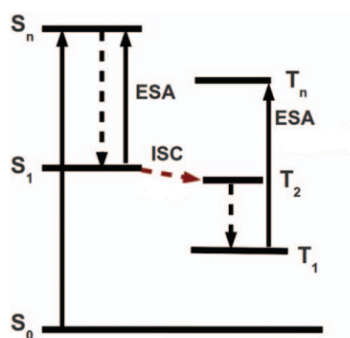


Figure 5.10 – Model proposed by Birech *et al.*²²⁸ to explain rapid intersystem crossing triplet exciton formation. The detected triplet signal arises from $T_1 \rightarrow T_n$ transitions within the monomer. With S_1 lying above T_2 in energy, the likelihood of rapid intersystem crossing increases, allowing it to compete effectively with internal conversion.

DPT-dimer 1 Similar to its monomer, excitation-dependent TA in DPT-dimer 1 reveals notable differences in the triplet formation at 483 nm, alongside the behaviour of the singlet state absorption at 415 nm. Figure 5.11 displays transient absorption spectra (left) and normalized dynamics of the main species (right) of DPT-dimer 1, obtained at 1 mW pump power. In addition to the previously recorded TA data at $\lambda_{\text{exc}} = 500$ nm (Fig 5.11 a), the TA at $\lambda_{\text{exc}} = 450$ nm in the visible region is presented in Figure 5.11 b. We conducted this measurement in the visible region to narrow down our observations on the behaviour of the triplet

species at 483 nm. A few months later, transient absorption at $\lambda_{\text{exc}}=450$ nm was remeasured using a UV-visible probe to get the data shown in (Fig 5.11 c). The concentrations of the dimer 1 solutions used in these measurements were 7.65×10^{-5} M, 7×10^{-5} M, and 3.8×10^{-5} M respectively.

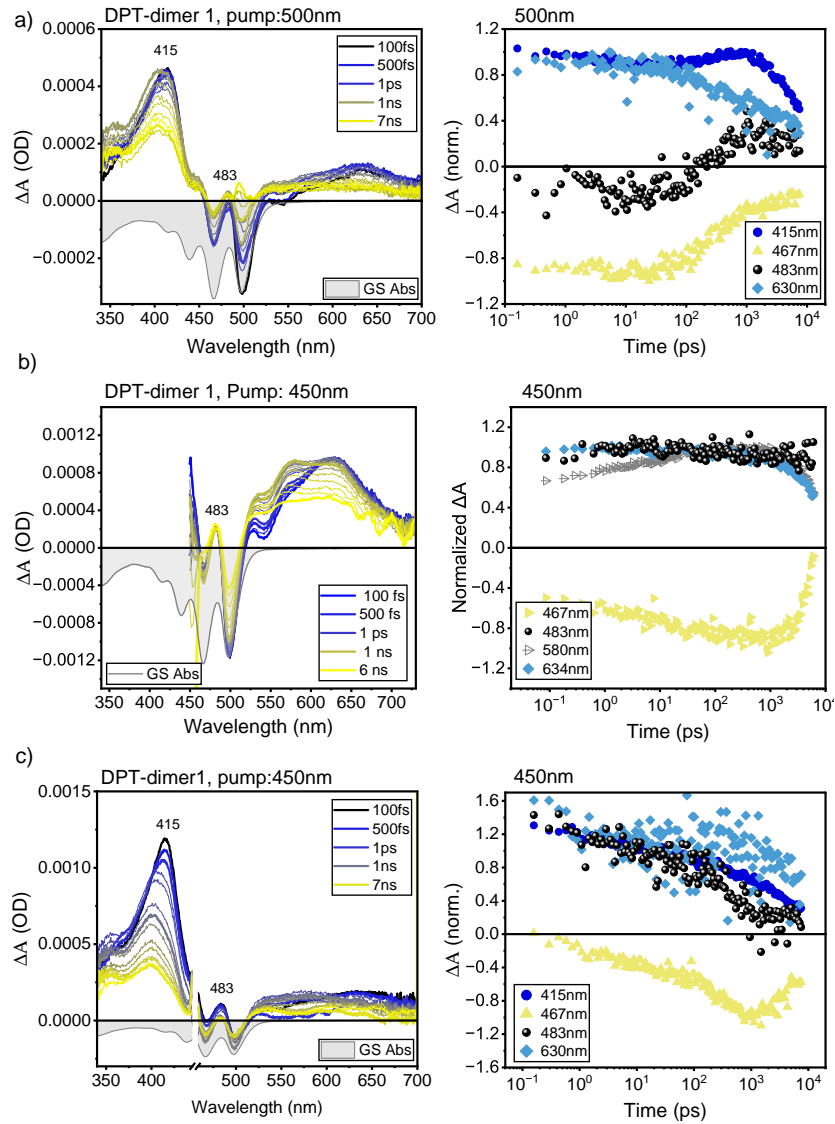


Figure 5.11 – Excitation wavelength dependence of transient absorption spectroscopy for DPT-dimer 1. Transient absorption spectra (left) and normalized dynamics of the main species (right) of DPT-dimer 1 at excitation wavelengths of (a) 500 nm, and 450 nm using (b) visible probe, and (c) UV-visible probe in toluene solution at concentrations of 7.65×10^{-5} M, 7×10^{-5} M, and 3.8×10^{-5} M, respectively. The average pump power is 1 mW.

As illustrated in the TDA monomer, the singlet state at 415 nm in the dimer decays more rapidly at ($\lambda_{\text{exc}} = 450$ nm) compared to ($\lambda_{\text{exc}} = 500$ nm), since the relaxation pathways and excited state lifetimes are affected by the excitation wavelength.²⁴² Triplet state absorption at 483 nm exhibits distinct behaviour depending on the excitation pump. The TA data demonstrated a gradual formation of the triplet state absorption at $\lambda_{\text{exc}} = 500$ nm (Fig 5.11 a), which might be attributed to the intersystem crossing. However, $\lambda_{\text{exc}} = 450$ nm forms a more rapid triplet species within the instrument response time (~ 100 fs) and possesses an extended lifetime, as illustrated in Figure 5.11 b. The data shown in Figure 5.11 c presents the TA measurement taken on the same sample at $\lambda_{\text{exc}} = 450$ nm after a few months. It reveals a similar fast triplet formation process but with a shorter triplet lifetime, indicating a faster decay of the triplet species. This change suggests possible sample degradation over time, likely occurring in the solid-state sample. Such degradation could affect molecular packing and influence the observed triplet-state kinetics.

A similarly reduced triplet lifetime was seen in the TDA monomer when excited at 450 nm (Fig. 5.8 b), attributed to a possible sample degradation over time. This measurement was also conducted a few months after the arrival of the sample. It is important to note that for all transient absorption measurements, all solutions were prepared inside a glovebox to prevent oxygen exposure, and the measurements were conducted within an hour of sample preparation. Further experimental details are provided in Section 3.4.1

At $\lambda_{\text{exc}} = 450$ nm, the potential for SF cannot be entirely dismissed given the existing information. Nonetheless, it is unlikely that SF occurs in the dimer since the triplet production demonstrates identical wavelength dependence in both the monomer and dimer. Therefore, rapid triplet generation is presumably a result of ultrafast intersystem crossing. A newly published study by Bogomolov *et al.*²²⁷ reported a rapid intersystem crossing triplet exciton formation in tetracene dimer. This work shows that, due to the presence of a low-lying charge transfer state and the small energy gap between the singlet S_1 and triplet T_2 , the intersystem

crossing process occurs significantly faster in the dimer compared to bare tetracene. This fast ISC process produces a dark state in tetracene, which is attributed to the temperature-independent process. Therefore, the tetracene dimer may be viewed as a shared structural unit capable of facilitating both singlet fission and rapid intersystem crossing.

Figure 5.12 presents a zoomed-in feature associated with triplet state formation in DPT-dimer 1, highlighting the significant difference in the intersystem crossing dynamics. It clearly shows the gradual and rapid triplet generation at 500 nm (Fig 5.12 a) and 450 nm (Fig 5.12 b), respectively. This triplet feature matches well with the sensitized triplet state absorption (black dotted line) reported in Ref.²³⁵

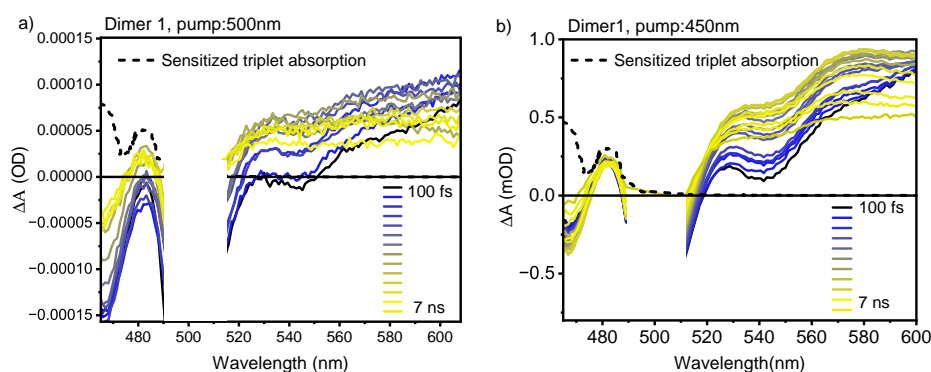


Figure 5.12 – Intersystem crossing triplet state formation presented in Fig 5.11 at 483nm. A zoomed-in feature associated with triplet state formation in DPT-dimer 1 at the excitation wavelength of (a) 500 nm and (b) 450 nm, highlighting a slow and fast intersystem crossing triplet formation, respectively. The dashed black lines present a sensitized triplet state absorption in tetracene solution reported in Ref.²³⁵

5.3 Conclusion

We investigated, in this chapter, the photophysical properties of new macrocyclic parallel tetracene dimers, and illustrated the mechanism of triplet formation using excitation wavelength-dependent transient absorption spectroscopy. Utilizing picosecond transient absorption spectroscopy in solution, DPT-Dimer 1 and its

monomer display ultrafast intersystem crossing triplet production at higher excitation energy (450 nm), whereas exciting the molecule with lower energy (500 nm) reveals a slow intersystem crossing process. These results suggest that intersystem crossing is influenced by the excitation wavelength in this system, and the triplet yield increases at higher excitation energy. Therefore, tetracene dimer may be viewed as a shared structural unit capable of facilitating both singlet fission and rapid ISC processes.

Moreover, transient absorption experiments in the dimers exhibited the generation of new excited-state species, aligning with the absorbance of the tetracene radical cation. This feature indicates the existence of a charge transfer state in tetracene dimers. Additionally, we observed possible mixing of electronic states in the dimers, where the excited singlet state absorption at 630 nm aligns with another radical cation absorbance feature, resulting in a dynamic change in the dimers relative to the monomer. In this species, the singlet and charge transfer states are coherently mixed, resulting in a hybridization of these states.

These findings demonstrate the complexity and variety of excited-state dynamics in tetracene derivatives. We showed how molecular structure and excitation conditions impact triplet-state formation, which provides useful information regarding how these variables affect intersystem crossing, singlet fission, and charge transfer processes. While our results provide new information on excitation-dependent ISC and the CT state in macrocyclic dimers, comparable behaviours have been seen in previous research on tetracene-based systems.^{227,243,244} Our results provide useful guidelines for developing tetracene-based systems for quantum technologies, solar energy conversion, and other photophysical applications. Furthermore, these results contribute to understanding unusual behaviours reported in photovoltaics, light-emitting devices, and transient absorption measurements, as well as guiding the optimization of experimental settings and the interpretation of spectroscopic data.

Chapter 6

Excitation wavelength dependence in tetracene monomers

In the previous chapter, newly synthesized tetracene dimers and their monomer demonstrated excitation wavelength dependence through picosecond transient absorption spectroscopy. The excitation energy affects these tetracene derivatives and has demonstrated a strong correlation between excitation energy and intersystem crossing dynamics. This finding indicates that higher energy in the excited state promotes effective spin conversion, perhaps via vibronic coupling or state mixing processes. In this chapter, we aim to explore if this behaviour is intermolecularly impacted or whether it is fundamental to tetracene-based systems. Therefore, we broaden our study to include more monomeric tetracene compounds. Through excitation wavelength-dependent picosecond transient absorption spectroscopy, we investigate the photophysical properties of different tetracene derivatives in solution. By providing a comprehensive analysis of the excited state dynamics, we showed excitation-dependent behaviour in some monomers, displaying unique characteristics, along with the detection of ultrafast intersystem

[†]The majority of the work presented in this chapter is my own; contributions from collaborators are explicitly noted.

crossing triplet formation. By comparing these monomers, this chapter provides deeper insight into the fundamental photophysical pathways governing ISC in tetracene-based systems.

6.1 Introduction

Over the past decade, considerable amounts of research have been done on crystalline tetracene, which is utilized as an active semiconductor in the development of new organic electronic devices, such as organic light-emitting transistors (OLETs),²⁴⁵ organic field-effect transistors (OFETs),^{246–248} and organic solar cells (OSCs).^{249,250} Heterojunction solar cells, where p–n junctions are formed by combining materials with different band gap values,²⁵¹ have shown a notable solar energy conversion efficiency using tetracene and pentacene.^{252–254} Furthermore, these molecules demonstrate singlet exciton fission, a process that can potentially enhance the overall efficiency of solar cells by up to 30%.^{12,255}

Several conjugated materials, including acenes,^{218,219,256,257} carotenoids,²⁵⁸ and other organic materials have been reported to undergo SF.⁴⁸ However, a limitation is that singlet fission efficiency might vary based on the morphology of the material. For instance, SF in the same material exhibits higher efficiency in single crystals compared to amorphous films.²¹⁸ Furthermore, owing to the proximity of the two triplet excitons generated by SF, the impact of annihilation on reducing the total triplet yield remains ambiguous.²²²

In some organic photovoltaic materials, triplet excitons are generated via direct intersystem crossing (ISC) but with variable yields. Some commonly used photovoltaic materials exhibit relatively high intersystem crossing yields. C₆₀, for example, efficiently generates triplet states due to its large size, which reduces electron–electron repulsion, combined with its high spherical symmetry that promotes electronic degeneracy.⁴⁶ In tetracene, S₁ and T₂ states are nearly isoenergetic, facilitating the intersystem crossing process.^{231,259} However, triplet production by intersystem crossing is usually slow in some hydrocarbon mater-

ials, around nanosecond to microseconds.²⁶⁰ This enables alternative relaxation processes to compete with intersystem crossing, which reduces triplet yields.

A previous study investigated the characteristics of the triplet state in tetracene and rubrene via laser flash photolysis.²³¹ It was reported that intersystem crossing in rubrene is a thermally activated phenomenon with a temperature dependency of the Arrhenius type. The energy of the second excited triplet state T_2 of rubrene was determined from the observed activation energy. S_1 is energetically too low in rubrene to efficiently populate T_2 , thus diminishing intersystem crossing.^{89,231} In tetracene, it is reported that T_2 is positioned below S_1 , and the intersystem crossing between (S_1 - T_2) is very efficient.^{231,259} These findings demonstrate the critical role of the T_2 state in molecular deactivation mechanisms. The energy difference between S_1 and T_2 states may now elucidate the distinctive behaviours of several molecules, including those studied in this chapter.

Here, we examine the photophysical properties and the excitation wavelength dependence, focusing specifically on triplet-related characteristics, of several tetracene derivatives. In the solution base, 5,12-diphenyltetracene (DPT) and mono-TIPS tetracene are studied with a contribution of tetracene-2,6-dicarboxaldehyde (TDA), presented in chapter 5, and 5,6,11,12-tetraphenyltetracene (rubrene), which have been employed for comparison. The main emphasis of our experimental work in this chapter is the investigation of the ultrafast dynamics of singlet and triplet excitons using excitation wavelength-dependent picosecond transient absorption spectroscopy.

We have shown in the previous chapter that TDA displays rapid intersystem crossing triplet formation at higher excitation energy, whereas exciting at lower energy results in a slower intersystem crossing process. In rubrene solution, it is reported that only excited singlet state absorption ($S_1 \rightarrow S_N$) is detected, as triplet state absorption ($T_1 \rightarrow T_N$) remains undetectable due to a low intersystem crossing quantum yield ($\sim 0.05\%$ ²⁶¹).^{156,262} This aligns with our observations that the rubrene solution exhibits no ISC triplet formation or dependence on excitation wavelength. Transient absorption spectra of mono-TIPS tetracene monomer,

excited at 500 nm and 400 nm, demonstrate excitation-dependent behaviour. A slow intersystem crossing is seen at 400 nm excitation, while no triplet features are generated at 500 nm, indicating a reliance on the excitation wavelength. Lastly, exciting DPT at various pump wavelengths consistently exhibited ultrafast ISC, suggesting a robust and intrinsic ISC mechanism independent of excitation energy.

6.2 Results and discussion

6.2.1 Model systems

We extended our excitation-dependent study to incorporate different monomeric tetracene molecules for additional investigation. The initial molecule is a newly synthesized tetracene monomer[†], functionalized at one end with a TIPS group; this configuration is known as **(mono-TIPS Tc)**. The second molecule is 5,12-diphenyltetracene (**DPT**)[‡]. Finally, we used 5,6,11,12-tetraphenyltetracene (**rubrene**) as the last molecule due to its comparable behaviour to the other tetracene monomers. Figure 6.1 displays the normalized absorption and photoluminescence spectra of the mono-TIPS Tc, DPT, and rubrene in toluene solution at room temperature, as well as the chemical structure of the monomers in the inset.

The absorption of mono-TIPS Tc (Fig. 6.1 a) displays a vibronic progression linked to the lowest energy transition, $S_1 \leftarrow S_0$, characterized by pronounced absorption bands in the UV-visible region. The anticipated absorption peaks between 420-485 nm result from electronic transitions within the conjugated system. With respect to the emission spectra, this monomer emits fluorescence in the region between 490-565 nm when excited in the UV-visible band. The photo-

[†]Mono-TIPS Tc molecule was synthesized by John Anthony (University of Kentucky) and characterized by Daniel Polak at the University of Leicester, including absorption, photoluminescence, and transient absorption spectroscopy.

[‡]DPT monomer was synthesized by Wataru Ishii at Kyushu University in Japan

luminescence spectrum exhibits minimal change from the ideal mirror image of the absorbance, with a notably small Stokes shift of 37 meV.

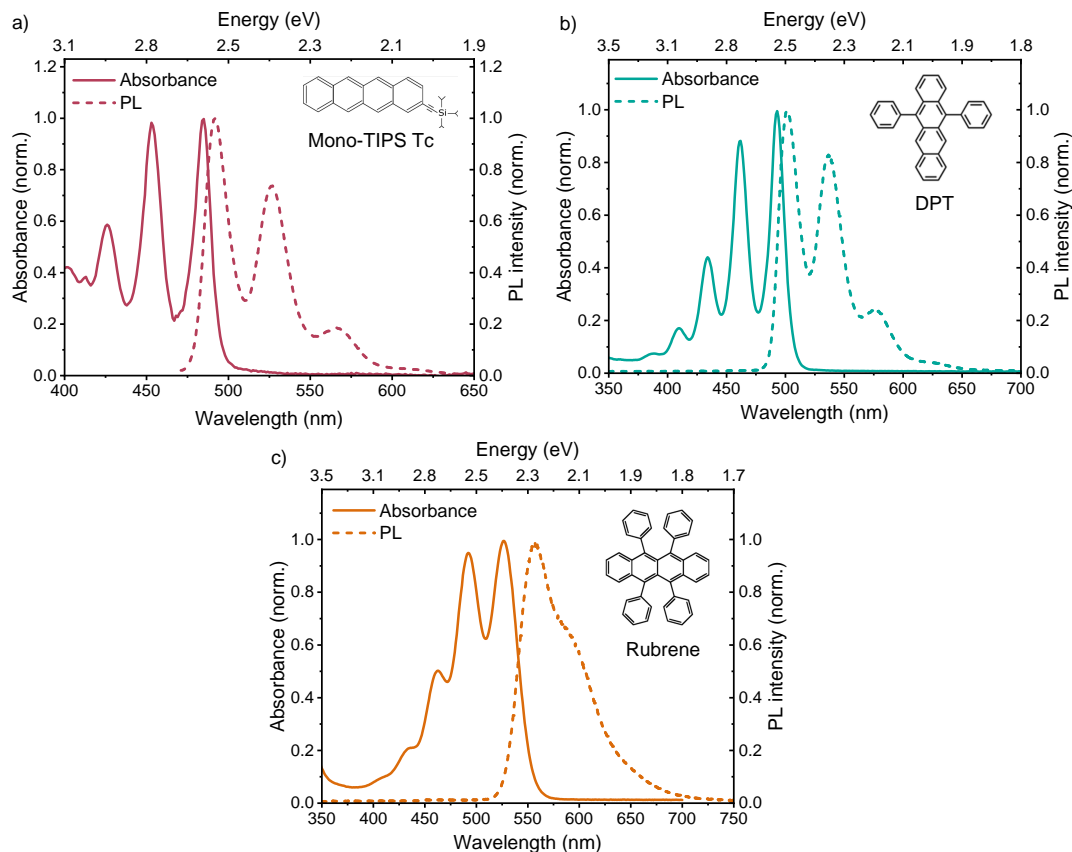


Figure 6.1 – Steady-state absorption and fluorescence. Normalized absorption (solid line) and fluorescence (dotted line) spectra of (a) Mono-TIPS tetracene, (b) Diphenyltetracene (DPT), and (c) Tetraphenyltetracene (rubrene) in toluene solutions at room temperature. The chemical structure of the monomers is shown in the inset.

Figure 6.1 b displays the absorption and emission spectra of DPT, which reveal a prominent vibrational progression associated with a symmetric structural mode. The spectra obtained for the DPT solutions exhibit a vibronic progression similar to that of the mono-TIPS tetracene, yet the peak values are shifted to lower energies by 8 nm and 10 nm for absorption and emission, respectively, as illustrated in Figure 6.2. The slight shifts suggest that the substitution of phenyl only causes a minor change in the electronic structure of the tetracene base of DPT.¹⁵⁴ The emission spectra of DPT exhibit a small reduction in the ratio of

the amplitudes of the first and second emission peaks in the vibronic progression relative to mono-TIPS tetracene. The excitonic interactions between tetracene chromophores in the DPT structure were investigated from the absorption spectra of DPT monomer at room temperature.

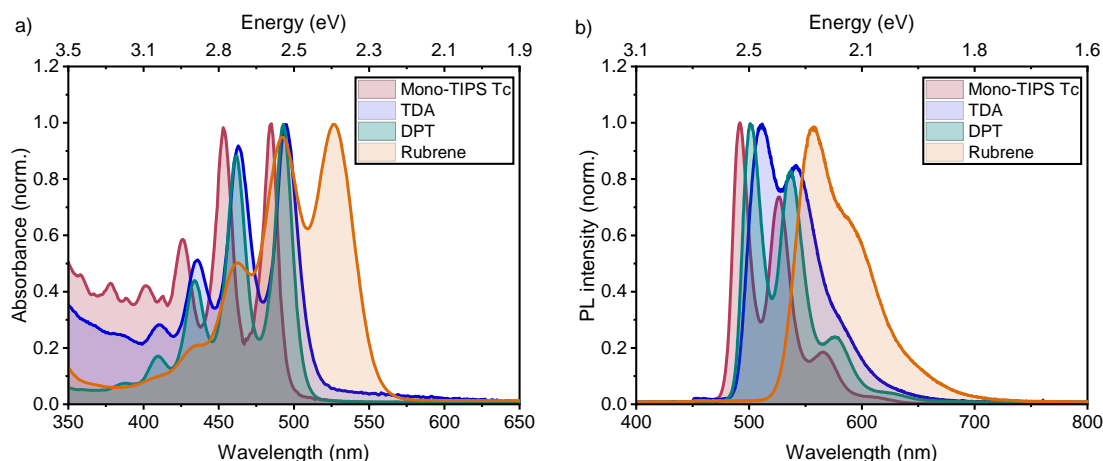


Figure 6.2 – Merged absorption and photoluminescence spectra of tetracene monomers. Comparison of (a) absorption and (b) photoluminescence (PL) spectra for mono-TIPS Tc (red), TDA (blue), DPT (green), and rubrene (orange). The overlap and differences between the absorption and PL spectra are shown, highlighting vibronic progression and Stokes shifts across the molecules.

Beer-Lambert plots of DPT monomer in toluene (Figure 6.3) show that it is in the molecularly dispersed state up to 2000 μM . The normalized spectra in Fig. 6.3b demonstrate variation in the vibronic peaks at concentrations of 2000 μM and 2127 μM . This indicates potential molecular aggregation/dimerization at these concentrations, but not before. Further investigation of DPT molecular aggregation is provided below in the DOSY-NMR analysis, section 6.2.4.

In the case of rubrene, Figure 6.1c presents the absorption and emission spectra of the rubrene monomers in the toluene solution. The absorption spectrum shows a dominance of three peaks, while the emission spectrum shows a dominance of two. The absorption peaks occur between 460–525 nm, whilst the emission spectrum of this monomer emits fluorescence in the 455–590 nm range. This res-

ults in an increased Stokes shift of approximately 135 meV, in contrast to mono-TIPS Tc and DPT. The spectra of rubrene exhibit a notable red shift relative to mono-TIPS Tc, by 67 nm in emission and approximately 40 nm in absorption, as illustrated in Figure 6.2. The absorption and photoluminescence spectra of the TDA monomer are also illustrated in Figure 6.2 for comparative analysis. It exhibits a comparable absorption spectrum to DPT. Conversely, the PL spectrum exhibits only two peaks with a slight red shift in the emission, displacing it to longer wavelengths relative to DPT.

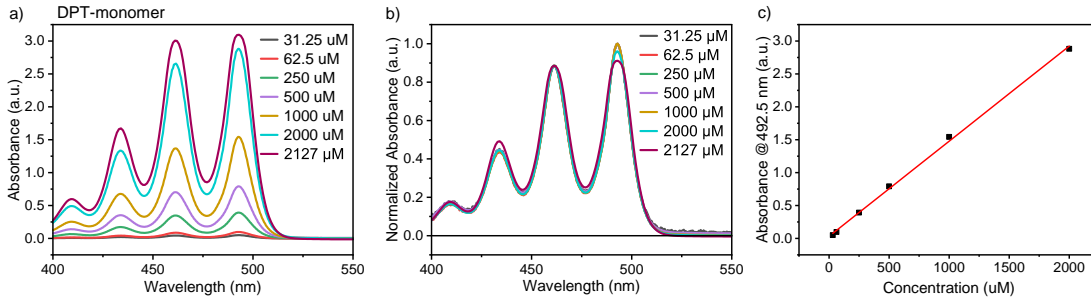


Figure 6.3 – Concentration-dependent absorption spectra of DPT-monomer.[†](a) Absorption and (b) Normalized absorption spectra of DPT-monomer in toluene solution at different concentrations ranging from 31.25 μM to 2127 μM . (c) Calibration curve of DPT-monomer in toluene at 492.5 nm.

6.2.2 Photoluminescence quantum yield (PLQY)

Photoluminescence quantum yield in rubrene, TDA, and DPT was investigated next to evaluate the efficiency of this material in converting absorbed photons into emitted photons in order to understand their emissive properties. Rubrene, recognized for its outstanding emissive characteristics, demonstrated a PLQY of $\sim 98 - 100\%$ in solution,^{261,263} acting as a reference for our calculation. PLQY measurements were performed using 405 nm excitation wavelength, and calculated for TDA and DPT monomers using the equation:²⁶⁴

$$\text{PLQY}_{\text{sample}} = \text{PLQY}_{\text{reference}} \times \left(\frac{I_{\text{sample}}}{I_{\text{reference}}} \right) \times \left(\frac{A_{\text{reference}}}{A_{\text{sample}}} \right) \times \left(\frac{n_{\text{sample}}}{n_{\text{reference}}} \right)^2,$$

[†]This figure was measured by me and Wataru Ishii at Kyushu University in Japan.

where (I) is the integrated PL intensity of the emission, (A) is the absorbance of the solution, and (n) is the solvent's refractive index. Given that toluene was employed as a solvent for all monomers, the refractive index of the solvents is uniform, so we omitted the last component of the equation. The PL quantum yields of TDA were found to be 60% and DPT to be 67% according to this standard. Details of the PLQY calculations are presented in the Appendix B.2.2. These findings show that although TDA and DPT have less emissiveness than rubrene, they yet show notable PL efficiencies, which could be explained by variations in their electronic and molecular structures. The photoluminescence quantum yield of the mono-TIPS Tc monomer could not be determined in this work due to the unavailability of the material and the lack of this specific measurement in the data supplied by the synthesising researcher. Nonetheless, according to the calculated outcomes and the anticipated photophysical characteristics, the PLQY is expected to correlate closely with the TDA and DPT values.

6.2.3 Excitation wavelength dependence in mono-TIPS tetracene monomer

Transient absorption spectra of the mono-TIPS tetracene monomer excited at 500 nm and 400 nm in toluene solution are shown in Figure 6.4 a and 6.4 b, respectively. At $\lambda_{\text{exc}} = 500$ nm, the excited state absorption features appear at 400-650 nm and at 1200 nm. All of these features decay with the same time constants (kinetics match in the right panel), with very little evolution in the temporal range within the transient absorption signal. Random change in intensity in the 500 nm region originates from the excitation pulse, which is scattered into the detector and cannot be fully removed by data processing. The peak in the NIR region matches the singlet peak from the literature study on tetracene in solution,²¹⁹ where the data was taken at 300 fs delay. As the peak in the visible region (400 nm) matches the decay, we can also assign the visible peak to the excited singlet state.

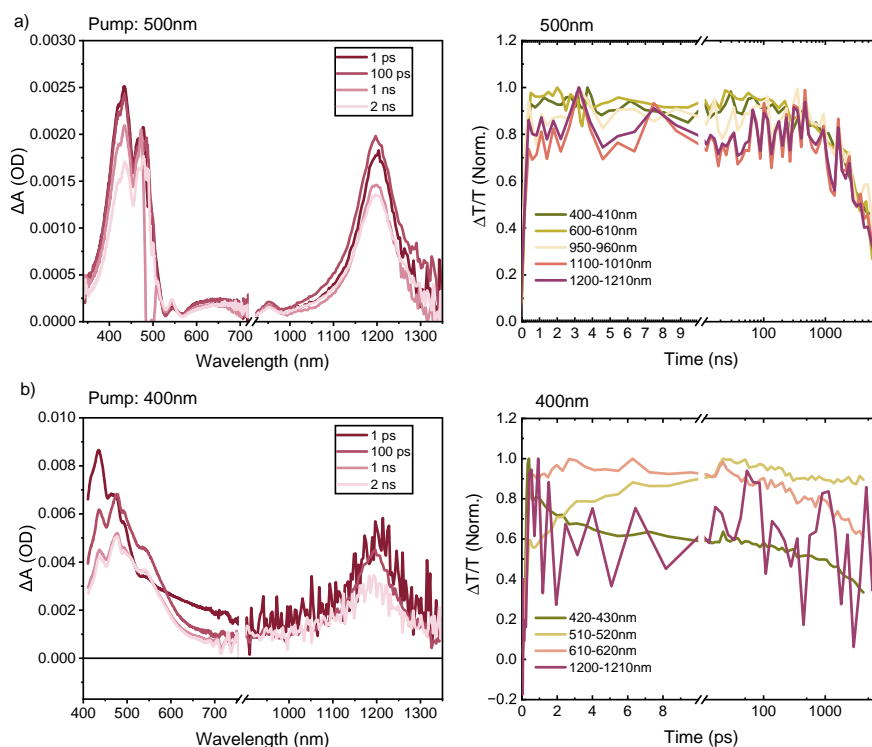


Figure 6.4 – Excitation wavelength dependence of transient absorption spectroscopy for mono-TIPS Tc.[†] Transient absorption spectra (left) and normalized dynamics of the main species (right) of mono-TIPS Tc in toluene solution at excitation wavelengths (a) 500 nm and (b) 400 nm.

The spectral shape is different for $\lambda_{\text{exc}} = 400$ nm excitation, but the same general peaks are visible. The NIR peak is once again present and decays with the same kinetics as the 400 nm singlet peak. However, we now have a peak rising slower than the others around 500-650 nm. The late-rising peaks are similar to the proposed triplet TA features in the monomer in ref.²¹⁹ While it would appear we have an interconversion between two states, the singlet signal remains for several nanoseconds. This suggests that a significant singlet population does not convert to triplets on fast time scales, suggesting a slower process such as inter-system crossing rather than singlet fission. These results confirm the observation that similar to TDA monomer, mono-TIPS Tc exhibits an excitation-dependent behaviour.

[†]This measurement was conducted by Daniel Polak at the University of Leicester.

6.2.4 Excitation wavelength dependence in DPT

Transient absorption measurements were then utilised in diphenyltetracene (DPT) to characterize its excited state dynamics on femtosecond time scales (Figure 6.5). The TA spectra of DPT in a toluene solution at 2×10^{-4} M, measured using an on-resonance pump wavelength of 500 nm at room temperature, are shown in Figure 6.5 a. The UV-visible region was measured with an average pump power of 250 μ W, whereas the near-infrared (NIR) region was measured using 1 mW pump power. The normalized kinetics of the main species are shown in Figure 6.5 b. When DPT is excited at 500 nm, ground-state bleach (GSB) is shown at 460 and 496 nm, which correspond to the vibronic progression of DPT's ground-state absorption spectrum (the solid grey line). A third negative feature appears at 537 nm, caused by stimulated emission (SE) from DPT's S_1 state. The strong photo-induced absorption band at 415 nm that arises right after photoexcitation is the most noticeable characteristic in the spectra, and we thus attribute it to $S_1 \rightarrow S_n$ transition.²²⁸ The excited state absorption features appear at 890 nm and 1176 nm decay with the same time constants as the 415 nm peak (kinetics match in Figure 6.5 b), indicating that the NIR peaks also correspond to the excited singlet state.

A small photo-induced absorption band is seen at 476 nm. This feature occurs on a 100 fs time scale and becomes more intense on a nanosecond time scale, suggesting an extended lifetime. As mentioned in the TDA and mono-TIPS Tc monomers, the presence of an induced absorption band between 400 and 500 nm strongly implies the generation of triplet excitons.^{219,231–233} This rapid triplet state population suggests an ultrafast ISC process in DPT, as explained earlier in the TDA monomer using Birech's proposed model (Fig 5.10)²²⁸. In the inset of Figure 6.5, we compare the feature obtained at 476 nm with a sensitized triplet absorption spectrum of DPT solution in Ref.²³¹ While the position of the triplet feature is well-aligned with the sensitized triplet absorption, the sensitized triplet is broader than the feature shown in our data. This could be due to overlapping GSB/SE.

It is worth mentioning that we conducted sensitization measurements, using anthracene and fullerene-C60. Unfortunately, both experiments were unsuccessful, resulting in similar TA spectra and kinetics for the mixed solution and single sensitizer (see Appendix B.3). This implies no transfer of triplet energy to the triplet acceptor. This might be due to the higher triplet state energy gap between the sensitizer and acceptor. The energy of the lowest triplet state in DPT is ~ 1.203 eV in comparison to anthracene (1.8 eV) and C60 (1.6 eV).^{231,265,266} This could prevent the efficient transfer, as the small energy gap reduces energy losses and improves efficiency.^{121,267}

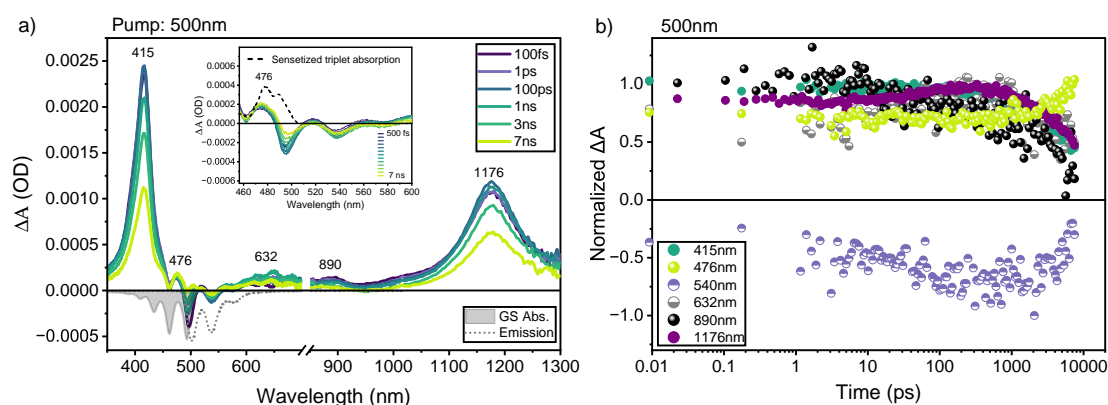


Figure 6.5 – Transient absorption spectroscopy of DPT monomer with visible (left) and NIR (right) probes. (a) Transient absorption spectra of the DPT monomer dissolved in toluene at 2×10^{-4} M obtained following on-resonance 500 nm excitation wavelength with an average pump power of 250 μ W, at room temperature. The inset provides a zoomed-in view of the triplet region at 476 nm, with a sensitized triplet absorption spectrum of DPT extracted from Ref.²³¹ (b) Normalized dynamics of the main species. Ground electronic state absorption and emission spectra are shown in solid and dashed grey lines, respectively, for reference.

Global analysis To achieve a more quantitative comprehension of the DPT excited state spectral characteristics, we conducted a global analysis utilising Surface Xplorer software (Fig 6.6 a) and multivariate curve resolution-alternating least squares (MCR-ALS)^{268,269}(Fig 6.6 b). Upon global fitting, the software provides species-associated spectra (SAS), as seen in Figure 6.6 a, which repres-

ent the contribution of each kinetic component to the overall transient absorption signal. This facilitates the distinction between singlet (black line) and triplet (red line) states in the TA data. Similarly, MCR-ALS analysis was conducted on the TA datasets. Two components with associated spectra were extracted. The orange component in Figure 6.6 b is attributed to the excited singlet absorption, whilst the purple spectral component corresponds to the triplet excited-state spectrum, as they align with the spectra shown in Fig 6.5. The MCR-ALS incorrectly assigned the singlet feature at 630 nm to the triplet state due to the low signal-to-noise ratios, which affect the accurate separation of the overlapped species.

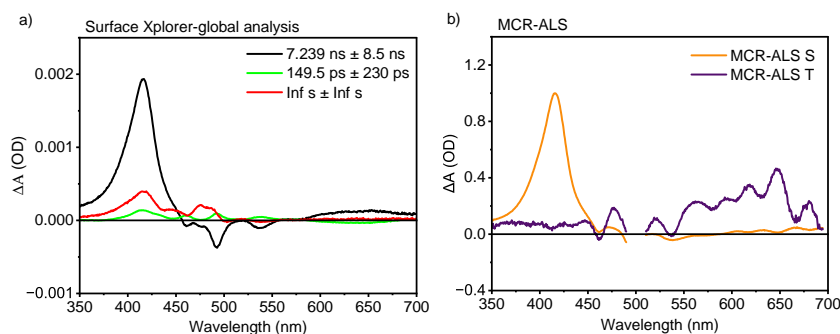


Figure 6.6 – Extraction of the main species from UV-vis-probe transient absorption data in Fig 6.5. (a) Species-Associated Spectra (SAS) obtained via Surface Explorer global analysis. (b) Spectral components were extracted using a global MCR-ALS procedure based on measured reference spectra, giving the DPT singlet (orange) and DPT triplet (purple).

Excitation wavelength dependence The excitation-dependent transient absorption of DPT was conducted next to examine the influence of the excitation pump on triplet behaviour. Figure 6.7 presents TA spectra (upper section) and the normalized dynamics of the main species (lower section) of DPT in toluene solution at a concentration of 2×10^{-4} M for excitation wavelengths $\lambda_{\text{exc}} = 460$ nm (Fig 6.7 a) and 430 nm (Fig 6.7 c). The concentration at $\lambda_{\text{exc}} = 450$ nm is 0.3×10^{-4} M (Fig 6.7 b). None of the TA data was affected by the excitation pump wavelength, confirming the formation of high-level intersystem crossing triplets

at all wavelengths. It is noticeable that the kinetics at $\lambda_{\text{exc}} = 450 \text{ nm}$ (Fig 6.7 b) exhibit noisier data. This is due to our reduction of the concentration to its minimal threshold to guarantee consistent behaviour at the lowest concentration level. Furthermore, we aimed to rule out the potential for aggregation in the solution. As a result, the fact that the fast intersystem crossing triplet formation was seen even at the lowest concentration indicates that the process is not affected by intermolecular interactions such as aggregation or excimer formation.²⁷⁰

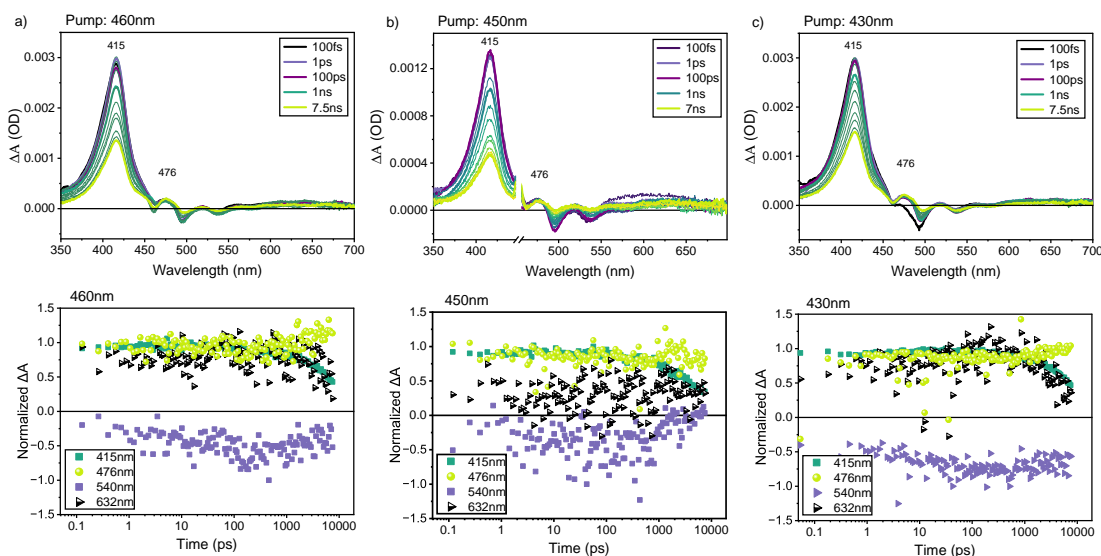


Figure 6.7 – Excitation wavelength dependence of transient absorption spectroscopy for DPT. Transient absorption spectra (up) and normalized dynamics of the main species (down) of DPT at the excitation wavelength of (a) 460 nm, (b) 450 nm, and (c) 340 nm. In toluene solution at $2 \times 10^{-4} \text{ M}$ for (a,c) and at $0.3 \times 10^{-4} \text{ M}$ for (b). No excitation dependency was detected, indicating the creation of high-level intersystem triplets across all wavelengths.

DOSY-NMR [†] To determine whether molecular aggregation occurs under the experimental conditions used in the transient absorption measurements, and to investigate the molecular behaviour in toluene solution, diffusion-ordered spectroscopy nuclear magnetic resonance (DOSY-NMR) analysis was performed. As this technique provides information about the diffusion coefficients of species, we can

[†]Khalid Doudin performed the DOSY-NMR measurement and most of the data analysis

determine whether the molecule exists as monomers or aggregates.^{271–273} There is a strong correlation between the molecular weight (MW) and the diffusion coefficient over many of magnitude. Based on the calculated molecular weight and the overlapping peaks of the dimer and monomer, the obtained diffusion coefficient likely represents an average of the molecular movement in solution. Table 6.1 provides an overview of the three analyzed DPT samples, including the calculated diffusion coefficient and molecular weight. The observed decrease in calculated MW with decreasing concentration suggests a higher proportion of monomers at lower concentrations.

Table 6.1 – DOSY-NMR analysis for different concentrations of DPT in toluene

mg/ml	Cal MW	Diffusion Coefficient	Dimer %
12.00	690	6.9×10^{-10}	81.6%
6.34	640	7.15×10^{-10}	68.4%
1.29	434	8.60×10^{-10}	14.2%

Figure 6.8 demonstrates that at a concentration of 12 mg/ml, approximately 82% of the molecules are dimers, with the remaining as monomers. Reducing the solution concentration to 6.3 mg/ml reduced the proportion of dimers to 68%. When DPT concentration is reduced to 1.29 mg/ml, 14.2% of the molecules are dimers, while the rest are monomers.

The concentrations used in the TA measurements varied from 0.3×10^{-4} M (0.011 mg/ml) to 2×10^{-4} M (0.094 mg/ml). The concentration-dependent data in Figure 6.3 indicate that the variation in the vibronic peaks, attributed to molecular aggregation, begins at a concentration of 20×10^{-4} M, which is tenfold more than the maximum concentration used in TA. Furthermore, DOSY-NMR analysis (Fig. 6.8) showed a significant reduction in the dimer% corresponding to a decrease in concentration.

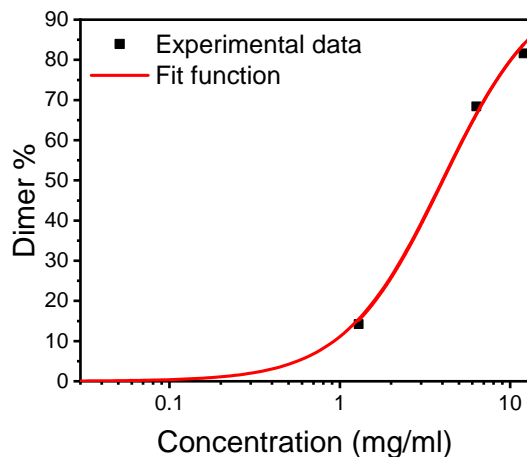


Figure 6.8 – Diffusion-ordered spectroscopy nuclear magnetic resonance data analysis of DPT solution. The data demonstrate that reducing the concentration of the solution leads to a significant reduction in the dimer percentage, highlighting the concentration-dependent nature of dimer formation and molecular self-association behavior. The data is fitted using the Hill-equation: $Dimer\% = \frac{[C]^n}{K^n + [C]^n} \times 100$, where $K=4$ mg/ml and $n=1.5$, which fall within the expected range (Details are provided in the text).

Due to difficulties in measuring DOSY-NMR at very low concentrations, data fitting may provide an estimate of the dimerization percentage for the DPT solution used in the TA. The lowest concentration used in the TA data was 100 times lower than the minimum concentration used in the DOSY-NMR measurements. Consequently, we expect a significant reduction in the dimer %. The data is fitted using the Hill-equation:^{274,275} $Dimer\% = \frac{[C]^n}{K^n + [C]^n} \times 100$, where $[C]$ is the total concentration of the solution, K is the dissociation constant which corresponds to the concentration at which half the maximum dimer population is achieved,^{274,275} and n is the Hill coefficient, which reflects the degree of cooperativity ($n > 1$ in positively cooperative dimer formation²⁷⁶). K and n are fitting parameters, equivalent to 4 mg/ml and 1.5, respectively, which fall within the expected range. Fitting the data shown in Figure 6.8 demonstrates that 0% of dimers are present in the solution used for our TA measurements (see Appendix B.5.5 for the fitting

details). Therefore, we can confirm that the ultrafast intersystem crossing in the transient absorption measurement is attributable to the monomeric DPT. Details of the DOSY-NMR analysis are provided in Appendix B.5.

Excitation wavelength dependence in rubrene

According to Yildiz (1968),²⁶¹ in rubrene solution, the intersystem crossing efficiency is less than 0.05%, which requires specific sensitizers to obtain high triplet concentrations. As a result, the rubrene solution showed only singlet state absorption and no absorption from the triplet state. This aligns with our observations that the rubrene solution exhibits no ISC triplet formation or excitation wavelength dependency. See Appendix B.4 for further details.

The observation of excitation wavelength dependence in TDA with ultrafast ISC triplet production at higher energy (chapter 5), while DPT exhibits ultrafast ISC at all excitation wavelengths, raises an essential question: why do we have excitation dependency in TDA but not DPT? Compared to rubrene and tetracene, rubrene solution exhibits no reliance on excitation wavelength or generation of intersystem crossing triplets. The T_2 state in rubrene is positioned above the S_1 state, with energies of $E_{T_2} = 2.43$ eV and $E_{S_1} = 2.23$ eV.⁸⁹ This diminishes the efficiency of intersystem crossing irrespective of the excitation energy. In tetracene, on the other hand, it is reported that T_2 is located below S_1 state ($E_{S_1} = 2.3$ eV)²¹⁸, and the intersystem crossing between (S_1 - T_2) is very efficient.^{231,259}

The consistent ultrafast ISC in DPT, irrespective of the excitation energy, leads us to hypothesize that the low-lying triplet state T_2 is located below and nearly isoenergetic with S_1 . This will dramatically boost the rate of intersystem crossing. We further suggest that higher-lying singlet states (S_n , $n > 1$) rapidly convert internally to S_1 before the intersystem crossing process, hence limiting any significant impact of excitation wavelength on ISC rates. Such near-degeneracy between S_1 and T_2 has been reported where ultrafast ISC timescales have been

observed.²⁷⁷

In TDA, we hypothesize that T_2 is positioned slightly above S_1 . Therefore, higher excitation energy promotes ultrafast ISC by enhancing the direct population of T_2 , while lower-energy excitation causes slower ISC due to weak coupling between S_1 and T_2 . Figure 6.9 illustrates our hypothesis, presenting the energy level diagram for DPT, TDA, and rubrene.

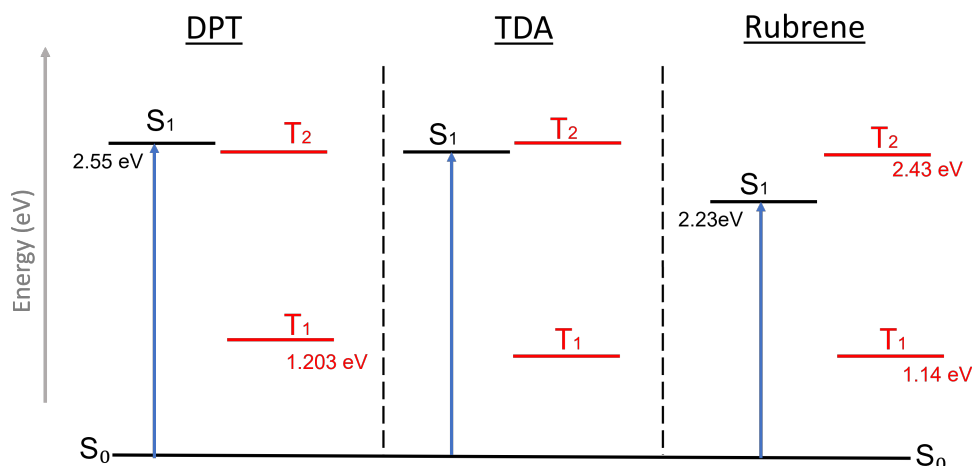


Figure 6.9 – Energy level diagram for DPT, TDA, and rubrene illustrating the proposed intersystem crossing mechanism. The diagram illustrates the relative positions of the singlet (S_1) and triplet (T_1 , T_2) states, emphasizing the significance of a small S_1 – T_2 energy gap in DPT, enabling ultrafast ISC across all excitation wavelengths. The influence of excitation energy on ISC dynamics for TDA is also indicated, where higher-energy excitation promotes ultrafast ISC, whilst lower excitation energy results in slower ISC. Additional spectroscopic analysis of T_1 and T_2 is required to verify this hypothesis.

To explain the continuous S_1 population seen along with triplet formation in the transient absorption spectra, we need to consider a branching process that occurs after photoexcitation. Upon excitation, the system can either undergo rapid intersystem crossing to T_2 or relax vibrationally to the bottom of the S_1 state.²⁷⁸ This vibrational relaxation causes the Stokes shift observed between absorption and emission. This might explain why we still see a singlet signal in

the TA data.

Alternatively, a coherent process may delocalize the excitation across vibronically coupled singlet and triplet states, allowing for rapid ISC. However, this coherence is expected to decohere rapidly, resulting in a branching into ISC or relaxation to the bottom of the S_1 state.²⁷⁹ In DPT, ISC remains efficient regardless of excitation energy, but the presence of S_1 suggests relaxation still competes with ISC. In contrast, TDA shows an excitation dependence; higher energy excitation accesses vibronically coupled regions, facilitating fast ISC, though a fraction of the population still relaxes into the S_1 state, contributing to the observed singlet signal. In comparison, low-energy excitation favors relaxation into the lowest vibrational level of S_1 , leading to slower triplet formation.

The energy of T_1 and T_2 states for TDA and DPT must be determined first to verify our hypothesis, presented in Figure 6.9. The literature only reports the energy of T_1 state for DPT as 1.203 eV,²³¹ while the energy of the T_1 state for TDA remains unreported. This can be quantified using phosphorescence measurement, which has not yet been conducted. The energy of T_2 for both molecules can only be hypothesized, since it is unobservable in the TA data, which is mostly dominated by singlet states. In addition, the sensitization experiment of DPT was unsuccessful. Further spectroscopic investigations are required to definitively confirm this hypothesis, such as nanosecond transient absorption spectroscopy and phosphorescence lifetime measurements, as T_1 and T_2 states remain unreported in the current dataset.

6.3 Conclusion

In this chapter, we have investigated the photophysical properties and the excited state dynamics of several tetracene monomers, with a specific focus on triplet-related aspects. Employing picosecond transient absorption spectroscopy, different excitation-dependent behaviours were observed, revealing distinct triplet formation and intersystem crossing dynamics. Mono-TIPS Tc exhibited slow in-

tersystem crossing at 400 nm excitation, however, no triplet species were seen at 500 nm, indicating a reliance on the excitation wavelength. Conversely, DPT consistently exhibited ultrafast intersystem crossing across all pump wavelengths, demonstrating a robust and inherent intersystem crossing mechanism independent of excitation energy. Ultimately, no triplet state formation or excitation wavelength dependence was seen in the rubrene solution, indicating a lack of significant intersystem crossing or other triplet-generating processes under the examined conditions.

At this point, however, a definite conclusion cannot be achieved due to the need for further spectroscopic investigations, such as nanosecond transient absorption spectroscopy and phosphorescence lifetime measurements, to definitively confirm our hypothesis. Future research is anticipated to provide evidence for it. The complexity and variety of excited-state dynamics in tetracene derivatives are highlighted by these results. The findings provide valuable insights into how structural variations and excitation energies influence intersystem crossing and triplet state formation.

Understanding the excited-state dynamics and the mechanisms governing ultrafast ISC is essential for advancing tetracene-based materials in organic photovoltaics, photodetectors, and light-harvesting systems, thus enhancing energy conversion and device efficiency.

Chapter 7

A Macrocyclic Parallel Dimer Showing Quantum Coherence of Quintet Multiexcitons at Room Temperature

Singlet fission (SF) is a promising approach in quantum information science because it can generate spin-entangled quintet triplet pairs by photoexcitation independent of temperature. However, it is still challenging to rationally achieve quantum coherence at room temperature, which requires precise control of the orientation and dynamics of triplet pairs. Here we show that quantum coherence of quintet multiexcitons can be achieved at room temperature by arranging two pentacene chromophores in parallel and in close proximity within a macrocycle. By making dynamic covalent Schiff-base bonds between aldehyde-modified pentacene derivatives, macrocyclic parallel dimer-1 (**MPD-1**) can be selectively synthesized in a high yield. **MPD-1** exhibits fast subpicosecond SF in poly-

[†]This chapter has been adapted from the following publication³⁴: Ishii *et al.*, *Journal of the American Chemical Society* 146, 37, 25527–25535 (2024). This work was the result of a fruitful collaboration with Wataru Ishii (Kyushu University, Japan). The contributions of myself and other collaborators to the work presented in this chapter are detailed in the acknowledgments.

styrene film and generates spin-polarized quintet multiexcitons. Furthermore, the coherence time T_2 of the **MPD-1** quintet is as long as 648 ns, even at room temperature. This macrocyclic parallel dimer strategy opens up new possibilities for future quantum applications using molecular multilevel qubits.

Acknowledgements: Wataru Ishii and his group carried out the dimer synthesis, ^1H -NMR, MALDI-TOF-MS, high-resolution MS, concentration-dependent absorption spectra, echo detected, PLQY, EPR measurements/analysis, and MD simulation. Eman M. Bu Ali and Samara M. Rivero prepared the solution and polystyrene thin films and carried out the transient absorption measurements and data analysis. Eman M. Bu Ali and Samara M. Rivero also carried out the characterizations of the dimer, including steady-state absorption and photoluminescence, and magnetic field effect measurements.

7.1 Introduction

Quantum information science (QIS), an application of quantum mechanics, is revolutionizing a wide range of fields from computing to communications and sensing.^{280–282} As the fundamental elements of QIS, molecular-based quantum bits (qubits) have the advantage that their structures are uniform at the atomic level and their structures and properties can be precisely controlled by chemical modification.^{216,217,283–285} It is essential for any quantum applications to prepare the initial pure quantum state in the qubit and to have a sufficiently long quantum coherence time. Conventional spin qubits that use thermal equilibrium states require cryogenic temperatures to generate initialized polarized states. Meanwhile, organic molecular spin qubits that use nonthermally equilibrium polarized states generated by photoexcitation can be initialized even under high temperature conditions such as room temperature.^{284–286}

Among photoinitializable molecular qubits, singlet fission (SF) can generate a quintet triplet pair state with four entangled electrons, which should be

useful for future two-qubit gate operation and highly sensitive quantum sensing.^{20,130,166,186,287–293} The singlet excited state S_1 , which is generated by photoexcitation, quickly becomes a singlet-triplet pair state 1TT , which is then converted to a quintet-triplet pair state 5TT by spin evolution. Recent theoretical studies have shown that when the orientations of the chromophores are parallel, it is possible to selectively populate certain sub-levels of the quintet.^{20,215} Although many dimer compounds have been reported in which chromophores are covalently linked, in most cases the linkages contain single bonds and have structural freedom of rotation, which would suffer from decoherence.^{294–298} While dimers linked by rigid linkers have been reported,^{287,288} quantum coherence of quintet multiexcitons at room temperature has not yet been observed.

Recently, quantum coherence of quintet multiexcitons has been observed for the first time at room temperature for pentacene chromophores densely arranged in a metal-organic framework (MOF), indicating that suppressed pentacene motion in the MOF structure is responsible for both the conversion from 1TT to 5TT and the quintet quantum coherence.²⁸⁶ However, the quintet with long coherence time was a minor component due to the poor crystallinity of the MOF. It is desirable to construct a system that can produce quintets with long coherence times in a homogeneous structure. In particular, isolated dimer molecules in an inert host can function as multilevel qubits exhibiting long coherence times, since exciton diffusion-induced spin decoherence, as seen in MOFs and crystals,¹⁶⁶ is suppressed because of the absence of exciton diffusion. Furthermore, it is expected that the combination with microscopy techniques will enable quantum manipulations of electron spins in a single dimer molecule, which is promising for future applications in ultrasensitive and ultrahigh spatial resolution quantum sensing technologies.²⁹⁹

Here we report the synthesis of a macrocyclic parallel dimer (**MPD**) and the observation of quintet quantum coherence even at room temperature. A few macrocyclic compounds exhibiting SF have been synthesized, but in low yields or requiring special reaction systems.^{300,301} By employing the Schiff-base chemistry,

which is commonly used for a dynamic covalent bond formation,^{151,225,226} **MPD-1** with two pentacene chromophores can be selectively synthesized in a good yield (Figure 7.1 a). The relatively rigid bridging structure including benzene ring together with the π - π interaction between pentacene units would suppress the rotational degree of freedom of the pentacene moieties and orient the pentacene units in parallel. This parallel proximity between adjacent pentacene would lead to ultrafast intramolecular SF and selective generation of the quintet states. **MPD-1** dispersed in polystyrene film exhibits the longest room-temperature coherence time T_2 of quintets of 648 ns, indicating that the macrocyclic structure is a promising strategy for generating multilevel qubits that can be driven at room temperature.

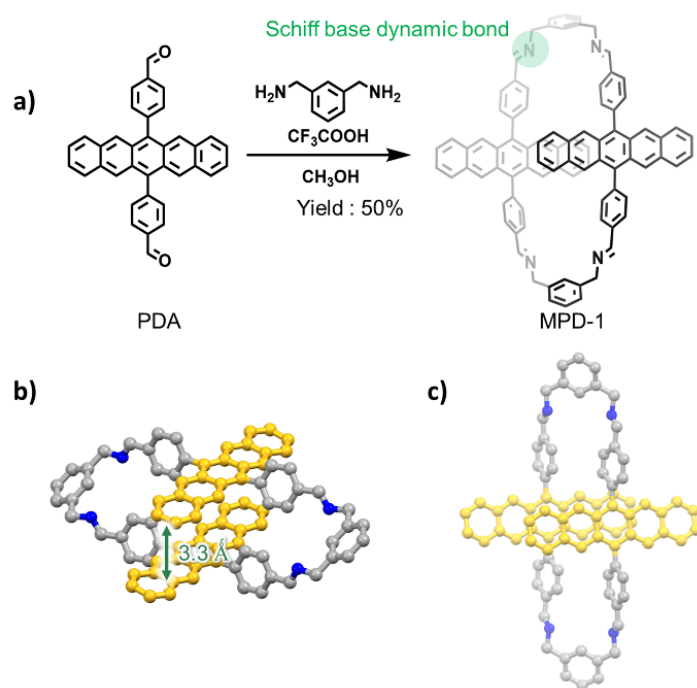


Figure 7.1 – MPD-1 synthetic scheme and crystal structure.(a) Synthetic scheme of MPD-1. (b, c) Single crystal structure of MPD-1. Solvent molecules and hydrogen atoms are omitted for clarity.

7.2 Results and discussion

7.2.1 Model system

The monomeric pentacene dialdehyde, 4,4'-(pentacene-6,13-diyl)dibenzaldehyde (PDA), was synthesized by following the previous report.³⁰² MPD-1 was synthesized using PDA and *m*-xylylenediamine with 5.5 equivalents of trifluoroacetic acid as a catalyst. The dynamic covalent bond chemistry such as Schiff-base formation can selectively produce the thermodynamically most stable compounds.^{151,152} In the current case, MPD-1 was selectively obtained in a high isolated reaction yield of ca. 50%. The purity of MPD-1 was fully confirmed by ¹H NMR spectroscopy (Figure 7.2), MALDI-TOF MS (Figure 7.4), high-resolution MS (Figure 7.5), and elemental analysis. Single-crystal X-ray diffraction (SCXRD) measurements of MPD-1 revealed the parallel orientation between two pentacene units (Figure 7.1 b and 7.1 c). The proximate carbon-carbon distance between the two pentacene units is 3.3 to 3.7 Å, indicating the presence of π - π interactions. NMR measurements were performed to elucidate the dimer structure in CD₂Cl₂ solution at room temperature (Figures 7.3 and 7.2). The significant upfield shift of the pentacene protons in the dimer MPD-1 in comparison with the monomer PDA indicates the π - π interactions between pentacene units are maintained in solution.

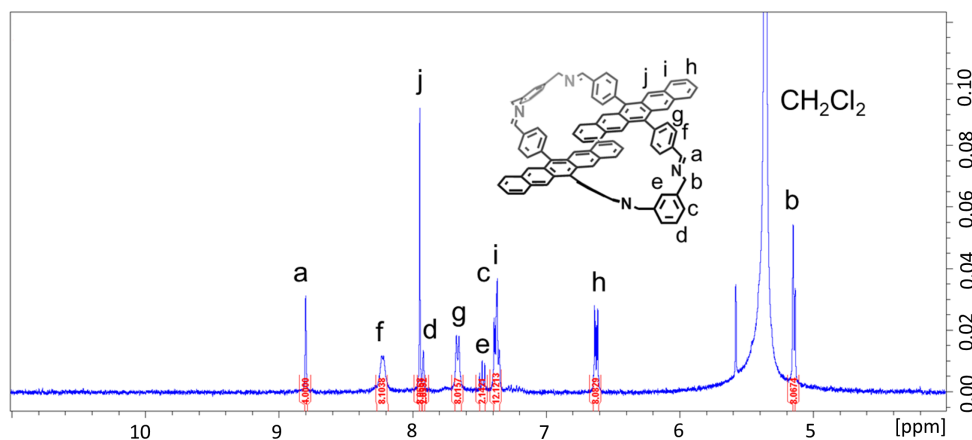


Figure 7.2 – ¹H-NMR spectrum of MPD-1 in CD₂Cl₂

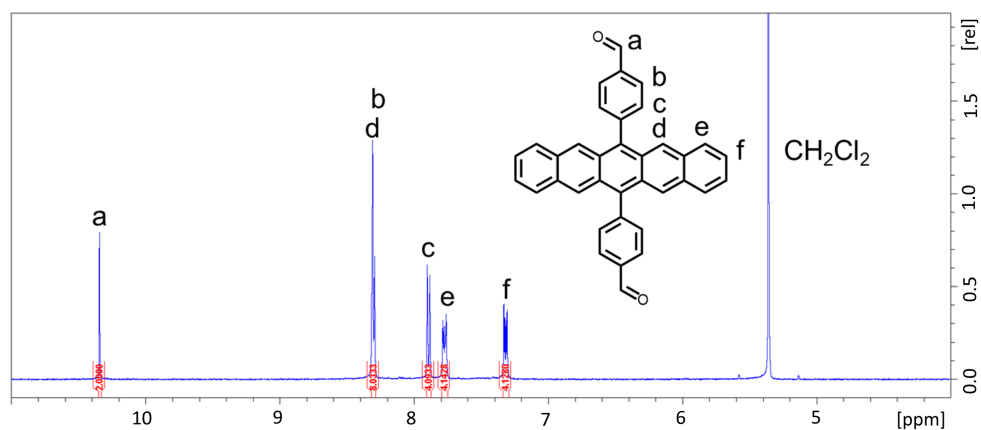


Figure 7.3 – ^1H -NMR spectrum of 4,4'-(pentacene-6,13-diyl)dibenzaldehyde (PDA) in CD_2Cl_2 .

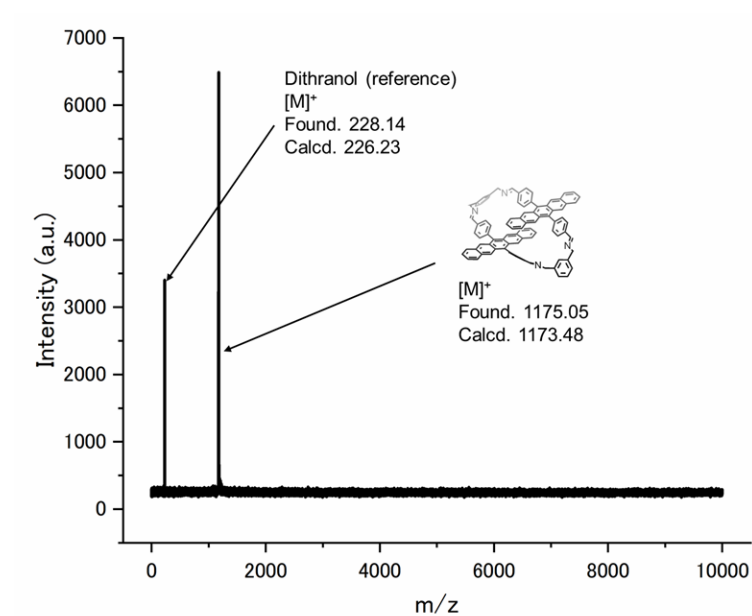


Figure 7.4 – MALDI-TOF-MS spectrum of MPD-1

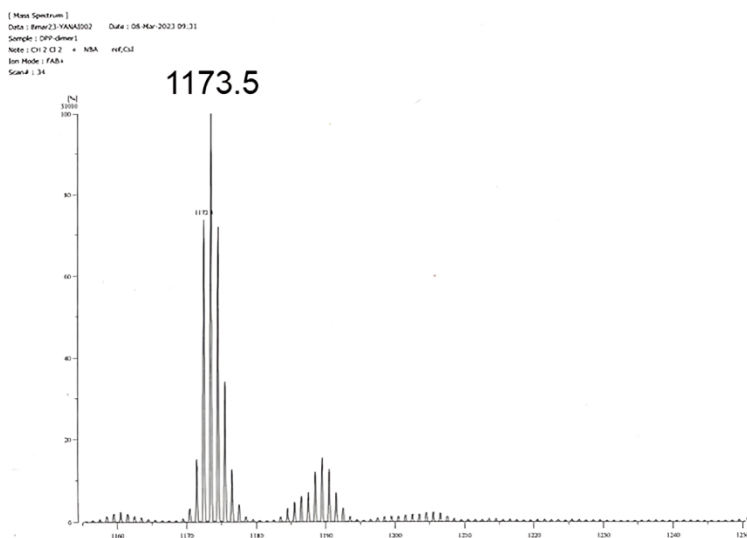


Figure 7.5 – High-resolution MS spectrum of MPD-1 Small peaks around $m/z=1205$ correspond to the oxidized MPD-1 dimer.

Molecular dynamics (MD) simulations were performed to investigate whether the orientation between the pentacene units in MPD-1 can be kept parallel when molecularly dispersed (Figure 7.6 a and 7.6 b). A single molecule of MPD-1 was placed in the center of the cubic MD cell and the remaining space was filled with toluene molecules, which were used as the initial structure for MD simulations. In the system at 300 K, MPD-1 was found to maintain the distance between the centers of the mass of the pentacene units around 5.5 Å for most of the time (Figure 7.6 c), which matches well with the center-to-center distance of 5.5 Å in the DFT-optimized initial structure based on the XRD structure. Two types of angles between the long axis vectors of the pentacene in the plane perpendicular (θ) and parallel (ϕ) to the aromatic ring planes did not take the significant values; the average values during the last 400 ns were $\theta = 9 \pm 9$ degrees and $\phi = 8 \pm 8$ degrees, respectively (Figure 7.6 d and 7.6 e). This indicates that the pentacene units remained parallel for most of the time, while they were occasionally tilted and moved back and forth and from side to side due to thermal fluctuations, as recently demonstrated in the exciton pairs in linked parallel pentacene dimers.

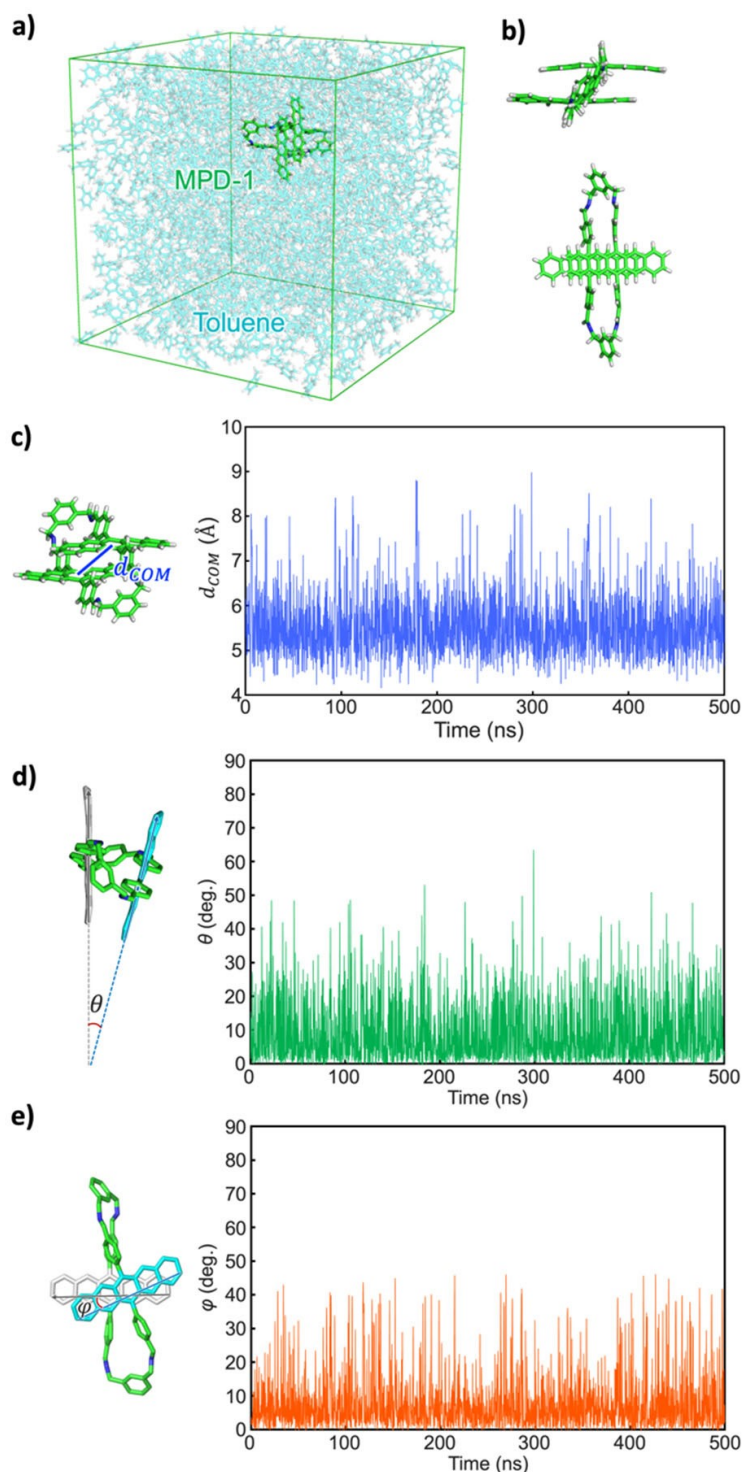


Figure 7.6 – Molecular dynamics simulations. Snapshots of MD simulation at 300 K in equilibrium for (a) the whole system and (b) only MPD-1. Time dependences during the 500 ns of (c) the distance between the centers of the mass of the pentacene units of MPD-1 and two types of angles between the long axis vectors of the pentacene units in the plane (d) perpendicular and (e) parallel to the aromatic ring planes, θ and ϕ , respectively.

In toluene glass at a lower temperature of 80 K, the fluctuations of the distance between the centers of the mass of the adjacent pentacene were smaller and the structure in solution was maintained (Figure 7.7).

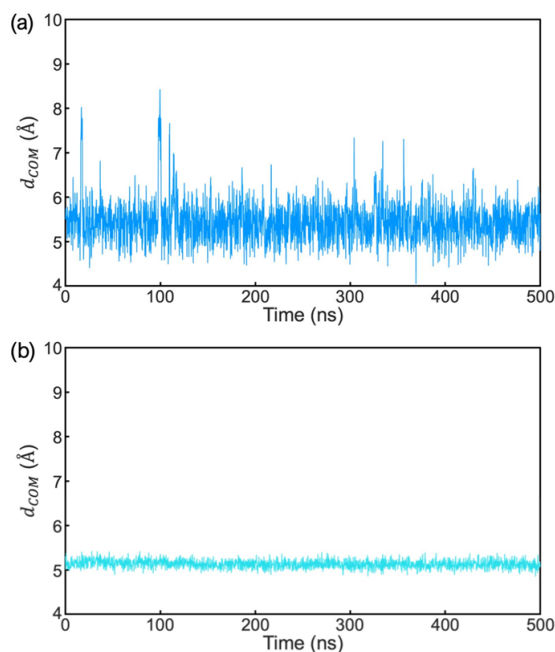


Figure 7.7 – Time dependences of the distance at different temperatures. Time dependences of the distance between the center of the mass of the pentacene units of MPD-1 at (a) 200 K and (b) 80 K.

7.2.2 Optical properties of MPD-1 and PDA

The excitonic interactions between pentacene chromophores in the dimer structure were investigated from the absorption spectra of MPD-1 at room temperature. Beer-Lambert plots of toluene solutions of MPD-1 showed that it is in the molecularly dispersed state up to 200 μ M (Figure 7.8). Absorption spectra of PDA and MPD-1 in toluene at room temperature showed a slight broadening of the spectrum with a redshift of the peak from 601.5 nm to 611.5 nm with an exciton coupling energy of 34 meV for the dimer compared to the monomer (Figure 7.9). This is due to excitonic interactions between neighboring pentacene chromophores, which is consistent with the dimer structure with pentacene

moieties in close proximity observed in NMR measurements and MD simulations.

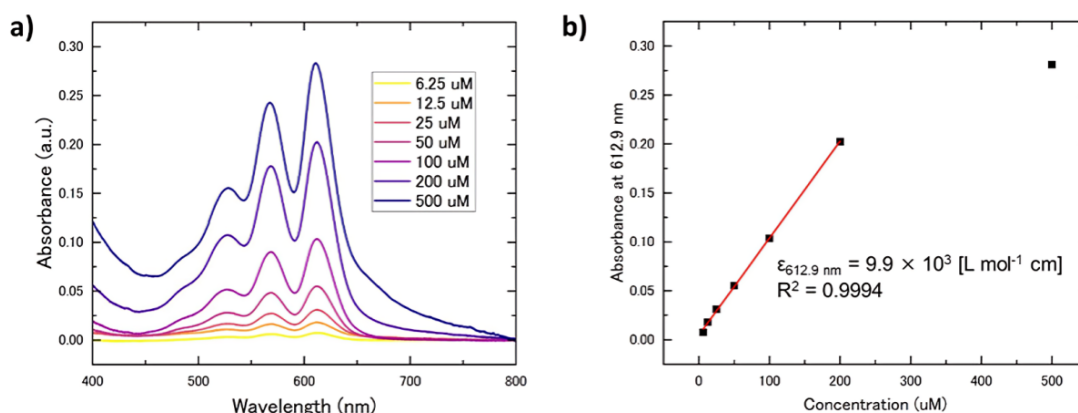


Figure 7.8 – Concentration-dependent absorption spectra of MPD-1.(a) Absorption spectra of MPD-1 at room temperature in toluene at different concentrations. (b) Beer-Lambert plot of MPD-1 in toluene at 612.9 nm. The fitted linear line (red) indicates MPD-1 is molecularly dispersed in toluene up to 200 μM at room temperature.

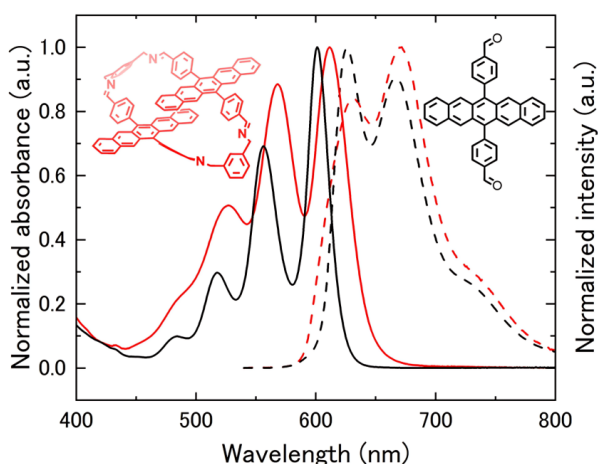


Figure 7.9 – Steady-state absorption and PL spectra. Absorption spectra (solid lines) and fluorescence spectra (dotted lines) of 100 μM of the dimer MPD-1 (red lines) and 200 μM of the monomer PDA (black lines) in toluene at room temperature, respectively.

The emission spectra of the monomer and dimer samples are strikingly similar when taking self-absorption into account (Figure 7.9). This spectral similarity, together with observations from the transient spectroscopy described below, sug-

gests that the 45-fold weaker photoluminescence from the dimer sample is from a minority of emissive monomer ‘impurities’ in the sample, which is supported by a small fraction of oxidized species in HR-MS (Fig. 7.5). As we discuss below, these may originate from photodamage or dissociation of dimers and indicate a need to improve the stability of the dimer in future work. Nevertheless, the dominant photophysics we study in this work originates from the dimers, with monomers contributing a very minor component, as indicated by the absorption and transient absorption spectroscopy described below.

Since it is necessary to evaluate the spin properties in the solid state by EPR measurement, we also measured the optical properties of MPD-1 dispersed in polystyrene film (Figure C.1). The absorption spectrum of MPD-1 in polystyrene indicates its molecular dispersion with no change in peak position and shape up to 5 mol% (Figure 7.10).

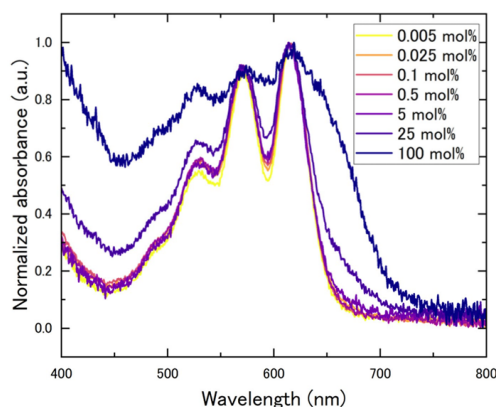


Figure 7.10 – Concentration-dependent absorption spectra of MPD-1 in polystyrene at room temperature The absorption spectrum of MPD-1 indicates its molecular dispersion with no change in peak position and shape up to 5 mol%.

7.2.3 Transient absorption spectroscopy revealed ultra-fast SF in pentacene dimer

Transient absorption spectroscopy (TAS) measures the signature of excited states as a function of time after excitation, allowing us to track their evolution from femtoseconds to milliseconds.

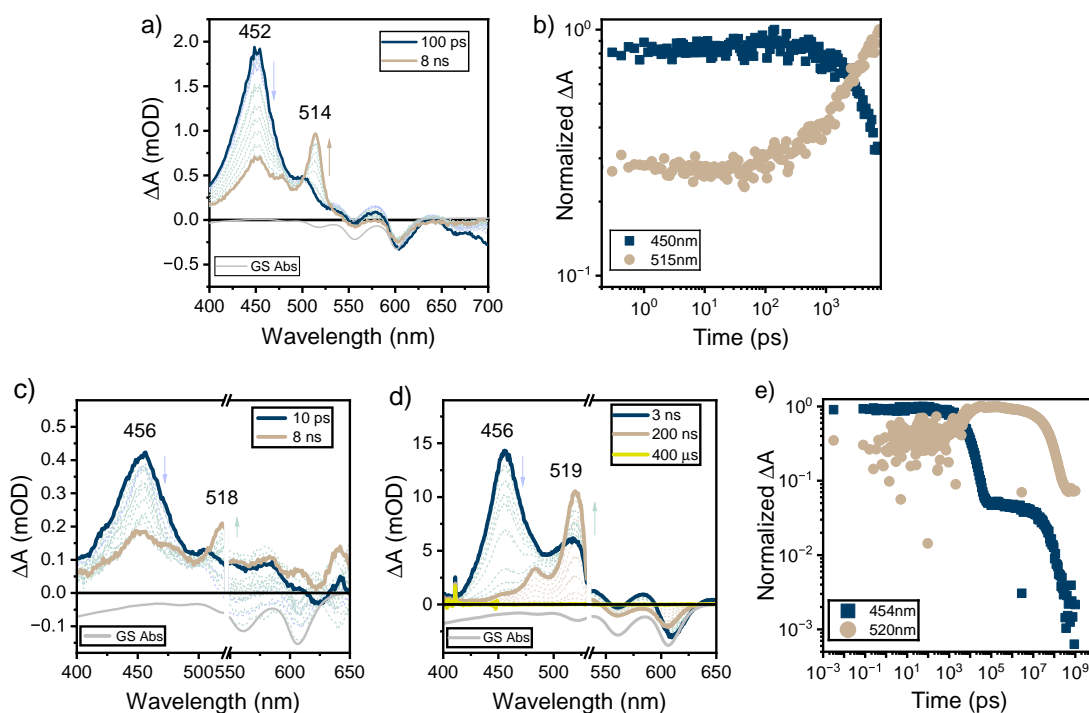


Figure 7.11 – Transient absorption spectroscopy of PDA monomer. Fs-TAS spectra (a, c) and ns-TAS spectra (d) and their corresponding kinetics (b, e) of PDA monomer in (a, b) toluene at 2×10^{-4} M and (c-e) polystyrene film (0.05 mol%) at room temperature. Ground state absorption spectra, in grey, are included for reference.

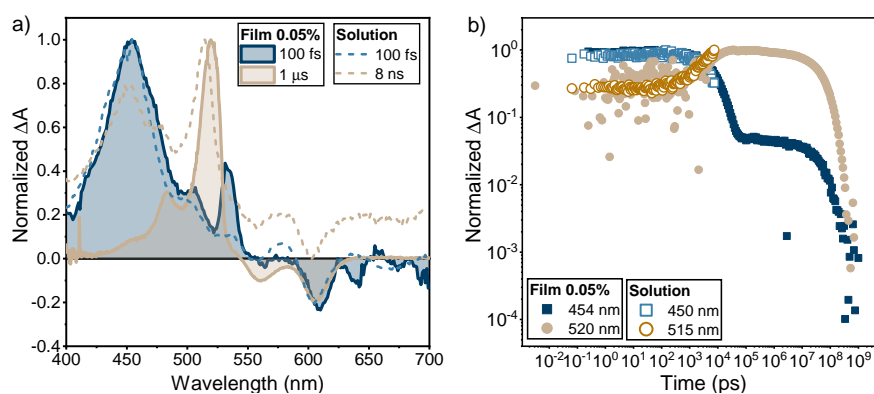


Figure 7.12 – Comparison of TA data for PDA Monomer in solution and film. Selected TAS spectra (a) and their corresponding kinetics (b) of PDA comparing the monomer dispersed in polystyrene film (0.05 mol%) (shaded solid lines/solid markers) and in toluene at 2×10^{-4} M (dashed lines/open markers) at room temperature.

Figure 7.11 shows TA spectra/dynamics of PDA monomer excited at ($\lambda_{\text{exc}} = 532 \text{ nm}$) at room temperature in both toluene solution at $2 \times 10^{-4} \text{ M}$ (Fig 7.11 a, b) and 0.05 mol% polystyrene film (Fig 7.11 c-e). A comparison of TA spectra and their corresponding kinetics of PDA dimer dispersed in polystyrene film (shadowed solid lines/solid markers) and in toluene solution (dashed lines/open markers) are shown in Figure 7.12.

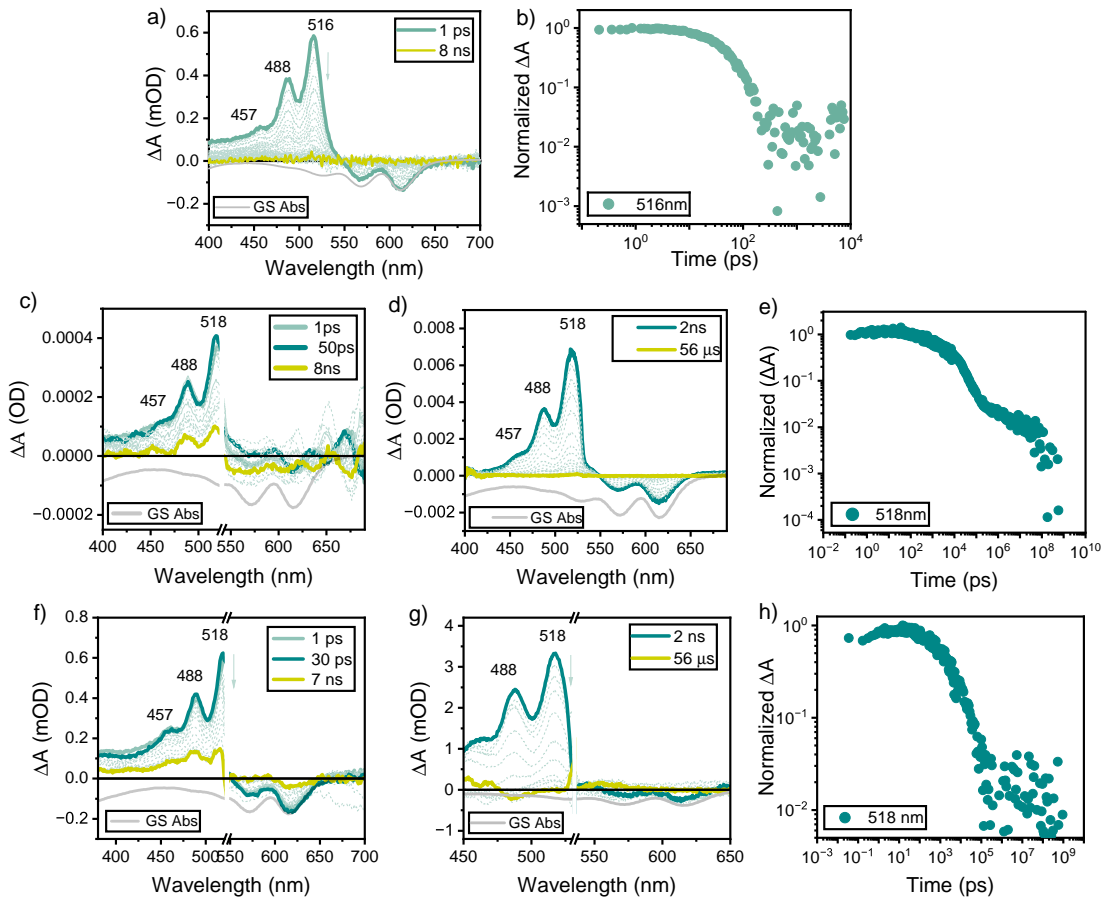


Figure 7.13 – Transient absorption spectroscopy of MPD-1 dimer. fs-TAS spectra (a, c, f) and ns-TAS spectra (d, g) and their corresponding kinetics (b, e, h) of MPD-1 dimer in (a, b) toluene at $1 \times 10^{-4} \text{ M}$ and polystyrene film at (c-e) 0.05 mol% and (f-h) 0.005 mol;% at room temperature. Ground state absorption spectra, in grey, are included for reference.

Furthermore, Figure 7.13 shows TA spectra/dynamics of MPD-1 dimer excited

at ($\lambda_{\text{exc}} = 532 \text{ nm}$) at room temperature in both toluene solution at $1 \times 10^{-4} \text{ M}$ (Fig 7.13 a,b) and polystyrene film at 0.05 mol% (Fig 7.13 c-e) and 0.005 mol% (Fig 7.13 f-h). A comparison of TA spectra and their corresponding kinetics of MPD-1 dimer in polystyrene film at both concentrations (0.05 mol% and 0.005 mol%) and toluene solution is presented in Figure 7.14.

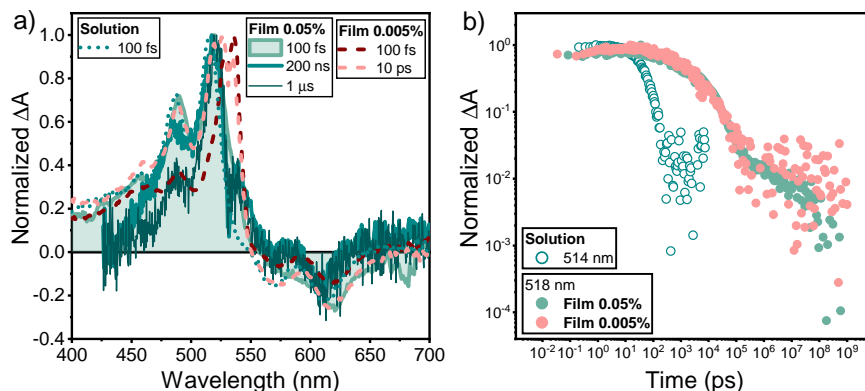


Figure 7.14 – Comparison of TA data for MPD-1 in solution and films. Selected TAS spectra (a) and their corresponding kinetics (b) of MPD-1 dimer in polystyrene film at 0.05 mol% and 0.005 mol% (solid lines and dashed lines, respectively) and in toluene at $1 \times 10^{-4} \text{ M}$ (dotted lines and open markers) at room temperature.

From the full TAS spectra/dynamics above, in Figure 7.15, we present selected TAS spectra and dynamics of the PDA monomer and MPD-1 dimer in polystyrene films at 0.05 mol% with excitation at 532 nm. We chose these conditions for ease of comparison with EPR measurements in Figure 7.16 and 7.20, but find that at these concentrations, the TAS behavior does not depend on concentration (Figure 7.14) between 0.05 mol% and 0.005 mol% (at the limit of our ability to measure TAS), suggesting that the majority of the doped molecules are well isolated from each other and show no signs of inter-dimer aggregation at 0.05 mol%.

Selected TAS spectra and dynamics of the PDA monomer, are shown in Figure 7.15 a and b. Our results reproduce the reported behavior of pentacene monomers in solution: at early times, represented by the 10 ps spectrum (blue) in Figure 7.15 a, the spectra are dominated by singlet S_1 states exhibiting a strong

excited state absorption (ESA) band peaked at ca. 450 nm (452 nm for PDA). Over nanosecond timescales, the spectrum evolves, due to intersystem crossing (ISC) to form triplets.¹³⁰ The triplets are characterized by vibronically structured ESA bands with a dominant peak at ca. 530 nm (514 nm for PDA), represented by the brown spectrum taken at 200 ns pump-probe delay in Figure 7.15. The ISC-generated triplets in this sample decay with a $\sim 50 \mu\text{s}$ time constant (Figure 7.11 e).

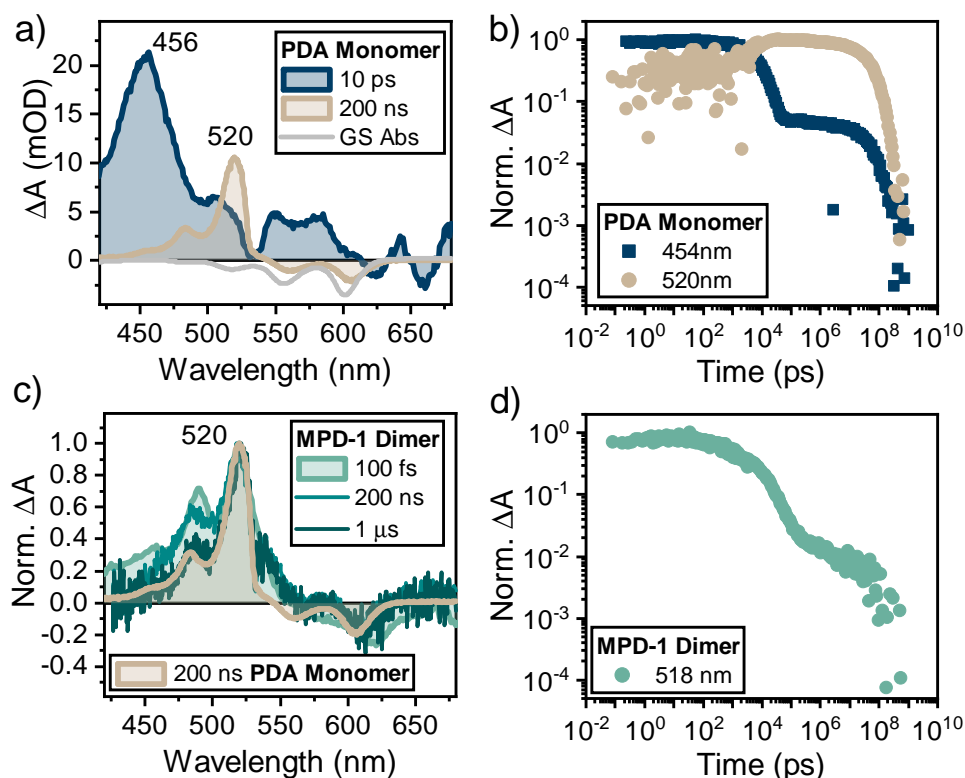


Figure 7.15 – Selected transient absorption data of PDA monomer and MPD-1 dimer. Selected TAS spectra (a, c) and their corresponding kinetics in the full-time window (from ps to ms) (b, d) of (a, b) PDA monomer in polystyrene film (0.05 mol%) at room temperature; and (c, d) MPD-1 dimer in polystyrene film (0.05 mol%) at room temperature. In the monomer (a, b), singlet states (blue) evolve to form triplets by intersystem crossing (brown). In the dimer (c, d), triplet signatures are present from 100 fs (green). Ground state absorption spectra are also shown for reference (grey shadowed lines).

Conversely, selected TAS spectra/dynamics of MPD-1 dimer in Figure 7.15 c

and 7.15 d show the formation of only one excited species on the measured timescales. This species decays with only minor spectral evolution from 100 fs (light green) to beyond 1 μ s (dark green). Given the similarity of this spectrum to the monomer triplet spectrum in Figure 7.15 a (reproduced in brown in Figure 7.15 b for ease of comparison), we assign the MPD-1 TAS spectrum to triplets. The rapid sub-100 fs generation of these triplets in MPD-1 suggests that they are generated by SF within our instrument response time (100 fs). In the dimer, the triplet signatures initially decay rapidly (10s of nanoseconds), orders of magnitude faster than the ISC-generated triplets on isolated molecules (compare figure 7.15 b and 7.15 d), as expected for SF-generated triplets. This rapid decay is associated with the spin-allowed nonradiative decay of the strongly exchange-coupled ^1TT triplet pair state, the initial triplet pair state of SF.⁵²

Following the initial decay, the remaining population decays on a slower timescale. Initially, the spectra are similar to those at the earliest times; compare the spectra at 200 ns and 100 fs in Figure 7.15 c, for example. We assign the triplet signatures on these 10-100s of nanosecond timescales to triplet pairs with quintet character, ^5TT , formed from ^1TT via spin evolution, rather than to isolated triplets. We make this assignment for three reasons: (1) the slower decay implies spin-forbidden decay to the singlet ground state, and therefore it is unlikely to be due to ^1TT population; (2) the ESA spectrum on these timescales (200 ns) is the same as the early-time ^1TT spectrum (100 fs), but different to the monomer ESA triplet spectrum (brown) and therefore is likely to be a triplet pair state on the dimer, rather than isolated triplets; (3) for symmetry reasons, it is most likely that ^1TT converts to ^5TT rather than $^3(\text{TT})$.¹³¹ This assignment is confirmed by TREPR measurements described below.

Before describing the EPR results, we note that the TAS spectral shape in MPD-1 evolves to form the 1 μ s spectrum reported in Figure 7.15 c that is identical to the ISC-generated triplets on the PDA monomer (the differences around 532 nm are artifacts from different pump scatter in the different experiments). These states could be due to ISC-generated triplets on monomer impurities in the di-

mer sample or could indicate uncoupled triplet pairs on dimers. Given the emission spectral features assigned to monomer emission described above and results from the EPR reported below, we conclude that these $\geq 1\text{ }\mu\text{s}$ features are from ISC-generated triplets on monomer impurities in the sample. The TAS signature from these monomers is weak, for example, we see negligible evidence of early-time singlet ESA at 456 nm, and therefore conclude that the proportion of monomers within the dimer sample is small, a conclusion supported by the absorption/emission spectroscopy described above.

We also observe that the strongly exchange coupled triplet pair in the dimer, ^1TT at $\sim 100\text{ fs}$ shows no shift of the main ESA band compared with the monomer triplet ESA; a shift has previously been associated with the triplet pair binding energy.³⁰³ This could suggest that the exchange coupling in this dimer is smaller than in previously measured systems.⁵²

Finally, we note that TAS of MPD-1 in toluene shows identical ESA ^1TT signatures at early times similar to MPD-1 dispersed in polystyrene films (Figure 7.13 a, b), confirming SF in the isolated dimers. However, in solution, where the dimer is unhindered by the polymer matrix, ^1TT decays to the ground state with a $\sim 60\text{ ps}$ time constant, much faster than in the polymer film. We speculate that this short lifetime is due to efficient non-radiative decay, enabled by conformational reorganization in the solution environment. In solution, at room temperature, therefore, ^1TT does not live long enough to form quintets.

7.2.4 Continuous-wave transient electron paramagnetic resonance measurement of MPD-1

Continuous-wave transient electron paramagnetic resonance (CW-TREPR) measurements of MPD-1 in polystyrene film at different concentrations (0.001, 0.0025, 0.005, 0.01, 0.05mol%) were conducted at room temperature (Figure 7.16, C.2, and C.3. All the CW-TREPR spectra at the different concentrations could be fitted using the same quintet and triplet parameters with different quintet/triplet

ratios, confirming that the dimer molecules are well dispersed in polystyrene films at least up to 0.05 mol% (Figure C.3, Tables C.3 and C.5). Highly symmetric spin polarization signals with A/A/E/A/E/E pattern were observed, which is the typical signal of SF-derived quintets. In an outer signal relative to the quintet features, the CW-TREPR data also showed an E/E/E/A/A/A pattern typical of ISC-derived triplets at all concentration conditions, but not the A/E/E/A/A/E pattern characteristic of SF-derived triplets. The fact that the ISC-derived triplet was observed even in the fresh sample suggests that one pentacene units of a small fraction of the dimers were oxidized during synthesis or purification. This result also implies that the dissociated triplets from triplet pairs were not generated due to the strong $\pi - \pi$ interaction by the rigid bridge between the close-contact pentacene units in the macro-cyclic structure (Figure 7.16c).

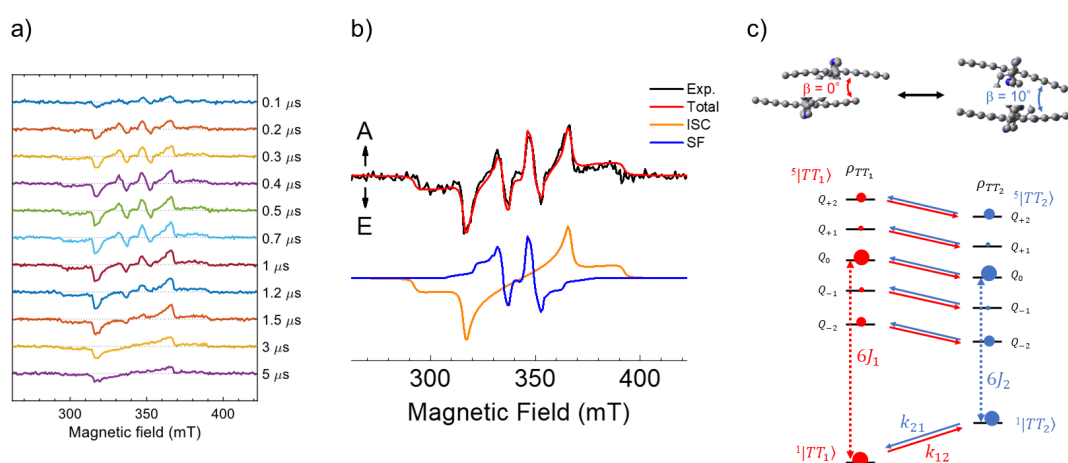


Figure 7.16 – Continuous-wave transient electron paramagnetic resonance.

(a) Time evolution of TREPR spectra of MPD-1 in polystyrene at room temperature with the microwave power of 0.075 mW. (b) Spectrum simulation of TREPR at 200 ns after laser irradiation using the density matrix formalism analysis. (c) Schematic image of quintet polarization generation through the fluctuation of exchange interaction.

Furthermore, only the trivial amounts of the paramagnetic species were observed in the steady-state CW-EPR spectrum on the 0.05 mol% sample both before and after TREPR and pulsed-EPR measurements (Figure 7.17). After pro-

longed laser irradiation, the sample showed only a little color change (Figure 7.18). These results suggest almost no photo-induced decomposition of MPD-1 occurred in polystyrene during EPR measurements.

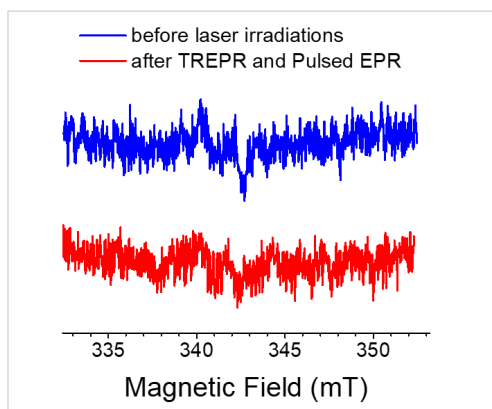


Figure 7.17 – Steady-state CW-EPR spectra of MPD-1. The measurements conducted in polystyrene (0.05 mol%) before (blue) and after (red) CW-TREPR and pulsed EPR. The field modulation frequency and the modulation amplitude were 100 kHz and 0.1 mT, respectively. The microwave power was 0.9464 mW. The microwave frequencies were 9.592550 GHz (blue) and 9.593160 GHz (red).

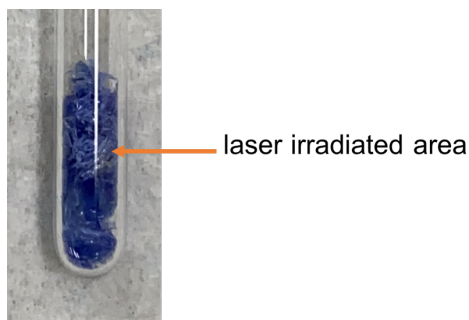


Figure 7.18 – Photograph of the sample of MPD-1 in polystyrene (0.05 mol%) after CW-TREPR and pulsed EPR measurement. After prolonged laser irradiation, the sample showed only a little color change.

The TA spectroscopy described above suggests that after excitation with 532 nm laser, the initially generated ^1TT can be converted to quintet-triplet pair (^5TT). Our calculations suggest this occurs by the modulation of spin-spin exchange interaction J (Figure 7.16 c). In this case, the J modulation would be

induced by the chromophore fluctuation.²¹⁵ Based on this theory, we performed the simulation of TREPR spectrum with two quintet exciton conformations ($^5\text{TT}_1$ and $^5\text{TT}_2$) using the density matrix formalism analysis.

The EPR spectrum was simulated by assuming MPD-1 dimers with two different conformations of the dihedral angle between the aromatic planes, 0° and 10° , as the stable $^5\text{TT}_1$ and the activated $^5\text{TT}_2$ by an energy of 80 cm^{-1} , respectively. We also assumed that the structural fluctuations between them modulate the exchange coupling J to generate quintet triplet pairs (Figure 7.16c). This is in good agreement with the dimer fluctuations observed in the MD simulation for toluene solution, suggesting that the angle of molecular fluctuations in polystyrene film is similar to those in toluene solution.

The negative exchange coupling J represents that ^5TT is more energetically unstable than ^1TT and is responsible for the fast deactivation of the quintets. Transient absorption measurements show that the ^1TT lifetime in toluene solution is very short (60 ps), whereas in polystyrene it is relatively long (10-100 ns). This suggests that the large structural fluctuations of MPD-1, as seen in the MD simulations of toluene solution, should be suppressed in the rigid polystyrene matrix. However, small fluctuations of MPD-1 (10 degree angle change) may result in quintet generation because J would substantially be modulated by the subtle angle changes (Figure 7.16c). The importance of J fluctuations in the transition from ^1TT to ^5TT is well understood by previous studies, and the present results are well explained by that model.^{131,215}

When the principal axes of the pentacene units in the dimer are aligned to be parallel, sublevel-selective transition from ^1TT to ^5TT occurs based on the anisotropic terms in the spin Hamiltonian. In the polystyrene matrix, the parallel orientation of MPD-1 was maintained, resulting in the highly symmetric EPR spectrum (Figure 7.16b). This spectrum shape represents the selective population distribution of quintet sublevels of Q_0 and $Q_{\pm 2}$ thanks to the parallel orientation of MPD-1.

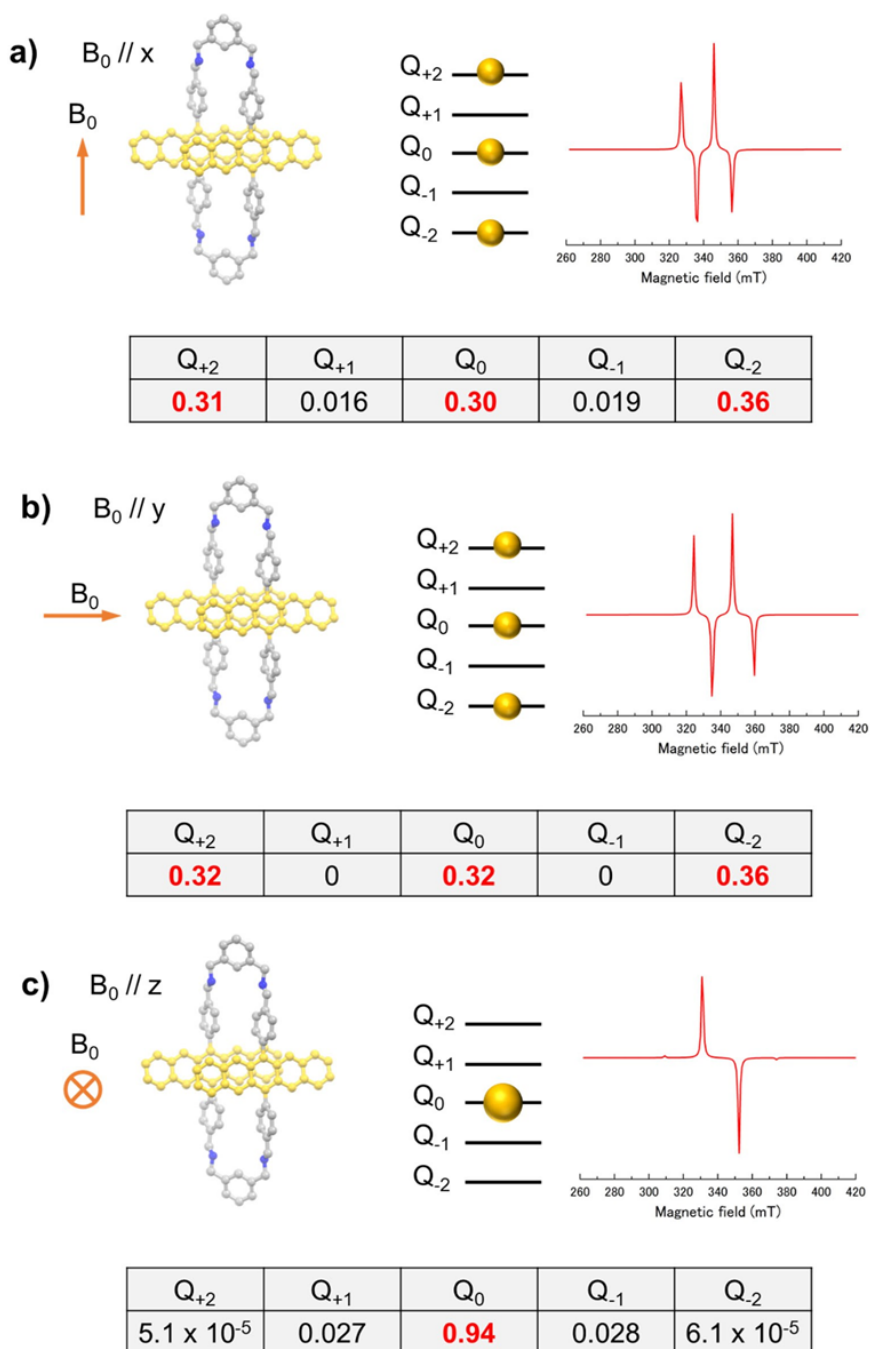


Figure 7.19 – Simulated CW-TREPR spectra and quintet population in the case that the fundamental axes ((a) x, (b) y, and (c) z) of MPD-1 are fixed along the external magnetic field (B_0).

The selectivity would be further enhanced when the dimers take a certain orientation to the external magnetic field. By simulating the case that MPD-1 is

aligned parallel against the external magnetic field ($B_0 \parallel z$), the maximized selective population distribution of quintets was observed (Figure 7.19). This result is in good agreement with the previous theoretical studies,^{20,215} indicating that MPD-1 can work as a high-quality multilevel qubit that produces pure quintet states.

7.2.5 Nutation measurement of MPD-1

In order to assign the spin multiplicities of EPR signals, we performed a nutation measurement of MPD-1 using X-band pulsed EPR (Figure 7.20 b). The nutation signals were obtained under the magnetic fields fixed at the peak tops of the echo-detected EPR spectrum (Figure 7.20 a) and Fourier transformed (Figure 7.20 b). Nutation frequencies of a transition ($\Delta m_S = \pm 1$) are represented as the following equation;

$$\omega = \frac{g\mu_B B_1}{\hbar} \sqrt{S(S+1) - m_S(m_S \pm 1)},$$

where g is the g -value, μ_B is the Bohr magneton, \hbar is the reduced Planck constant and B_1 is the effective magnetic field strength of the microwave pulse. Therefore, the nutation frequency ratio is represented as doublet: triplet: quintet ($Q_{\pm 1} \leftrightarrow Q_{\pm 2}$) : quintet ($Q_0 \leftrightarrow Q_{\pm 1}$) = $1 : \sqrt{2} : 2 : \sqrt{6}$. In the spin nutation measurements, the nutation frequency ratio of 1.00: 1.47: 2.13: 2.58 was obtained, which approximately coincides with the theoretical values. Furthermore, we measured the delay time (t_{delay}) dependence between the microwave pulses and the laser flash on the echo signal (Figure 7.20 c). The quick rise in the quintet echo originates from deactivation rate constant in the singlet TT with $k_{Rec}=2.0 \times 10^7 \text{ s}^{-1}$ (Table C.3 in the Appendix). This is due to the quick deactivation of ^1TT , the source of quintet generation. This singlet TT deactivation kinetics is in good agreement with the initial rapid decay (10s of nanoseconds) observed in the TA signal.

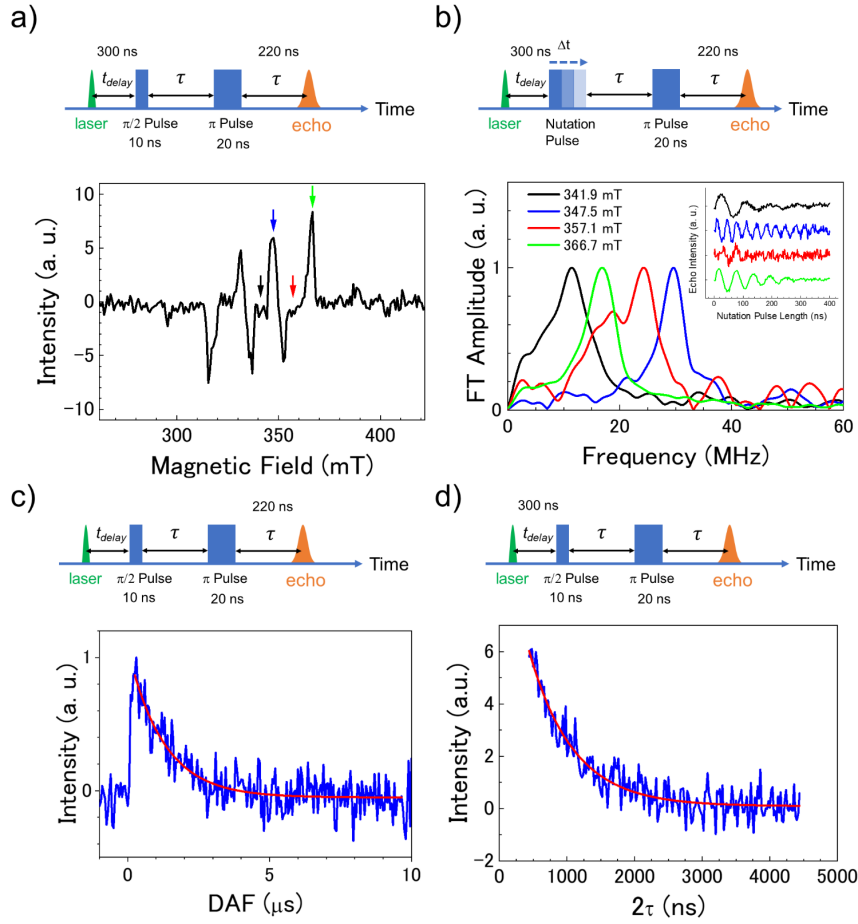


Figure 7.20 – An echo detected spectrum (bottom) of MPD-1 in polystyrene obtained by 532 nm laser irradiations at room temperature and its pulse sequence (top). The pulse sequence was employed as laser- t_{delay} - t_1 - t_{echo} - t_2 - t_{echo} -echo. The durations of the first pulse (t_1) and the second pulse (t_2) are 10 ns and 20 ns, respectively. The delay time of t_{delay} and t_{echo} are 300 ns and 220 ns, respectively. Spin nutation measurements were carried out at the magnetic field indicated by the arrows. (b) Fourier transformed spin nutation signals. The inset shows time profiles of spin nutation signals with baseline corrections. The peaks of the nutation frequencies at the magnetic field, indicated by the arrows in (a), were 11.47, 16.85, 24.41, and 29.54 MHz, respectively. (c) Dependence of t_{delay} of the echo intensity at 347.5 mT (blue line) employing $\pi/2 = 10$ ns, $\pi = 20$ ns and $t_{\text{echo}} = 220$ ns with a fitting line (red line). The $^5\text{TT}_0$ spin relaxation time obtained from the echo signal decay was $1.27 \mu\text{s}$. (d) Coherence time (T_2) of the quintet triplet pairs. A pulse sequence of the Hahn echo detection (laser- t_{delay} - t_1 - t_{echo} - t_2 - t_{echo} -echo) used in the measurement with $t_1 = 10$ ns, $t_2 = 20$ ns and $t_{\text{echo}} = 220$ ns. $T_2 = 648$ ns was obtained by plotting the echo signal with varying t_{echo} at $B_0 = 347.5$ mT with $t_{\text{delay}} = 300$ ns.

The $^1\text{TT} \rightarrow ^5\text{TT}_0$ spin relaxation time constant is thus obtained to be $1.24\ \mu\text{s}$ from the echo signal decay in Figure 7.20 c. This is almost the same as the decay time constant ($1.17\ \mu\text{s}$) of the quintet signal obtained by CW-TREPR (Figure 7.21). This means that the components observed in the spin echoes are the major components in the system, i.e., the dimers are well dispersed in the polystyrene matrix and in a uniform environment. The slight difference in the two time constants is probably due to the fact that the decay time of CW-TREPR is influenced by the high power intensity of the irradiated continuous microwave in the dielectric resonator.¹⁶⁶

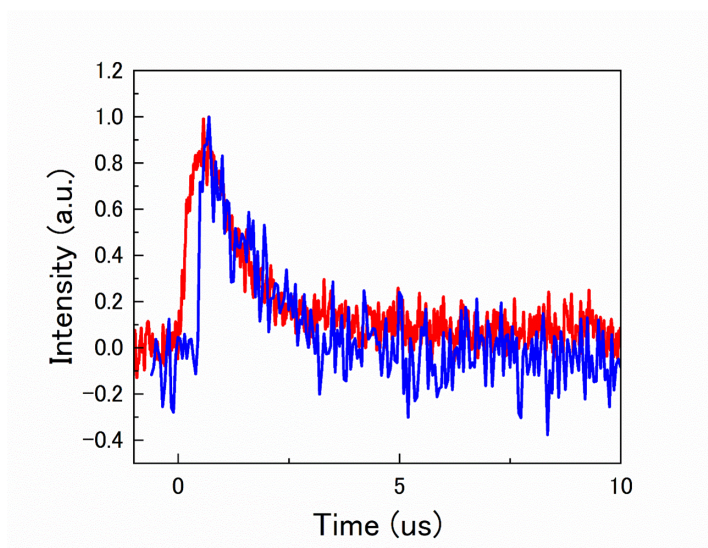


Figure 7.21 – The decay of echo and TREPR signals. Dependence of t_{delay} of the echo intensity by pulsed EPR (blue) and TREPR decay signal (red) of MPD-1 at 347.5 mT. The decay constants of the echo signal and TREPR signal were $1.24\ \mu\text{s}$ and $1.17\ \mu\text{s}$, respectively.

While previous reports on Pn-MOF concluded that the quintets observed in CW-TREPR and pulsed EPR comes from different components due to low crystallinity,²⁸⁶ in this study, the dimers are uniformly dispersed in polystyrene and the signals observed in CW-TREPR and pulsed EPR should be derived from the same component. In addition, overlapping the kinetics of TA signal at 518 nm and the kinetics of the echo signal obtained by pulsed EPR shows relatively good

agreement on the 100-1000s of nanosecond timescales, indicating good consistency between TA and EPR regarding the quintet dynamics (Figure 7.22).

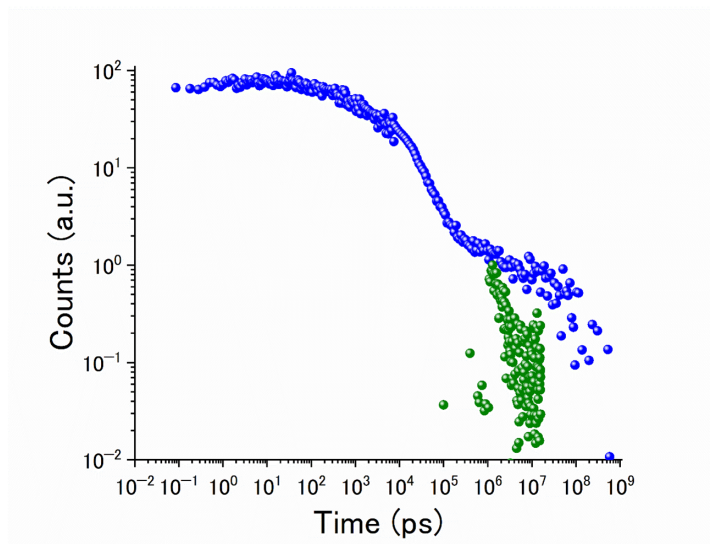


Figure 7.22 – Comparison between TA kinetics and echo signal decay. The overlap of TA kinetics at 518 nm (blue dots) and echo signal decay of the quintet ($Q_0 \leftrightarrow Q_{\pm 1}$, 347.5 mT) was obtained by pulsed EPR (green dots) of MPD-1 in polystyrene (0.05 mol%) at room temperature.

In the spin coherence time (T_2) measurements of MPD-1 by the Hahn echo detection (Figure 7.20 d), notably long T_2 of 648 ns was observed even at room temperature. The quintet is generated by J modulation with slight conformation change (Figure 7.16 c), and the large and random fluctuation of anisotropic zero-field splitting interactions should not dominate in this system. This relatively long coherence time opens the possibility of quintet spins as multilevel qubits that can be driven even at room temperature.²⁸⁶ The T_2 obtained in the present study is about 5 times longer than that in the MOF (120 - 150 ns). The reason for longer T_2 may be due to the absence of phonon effect by the molecular aggregation in the present dispersed dimer system, reflecting the suppressive fluctuations of the solid polystyrene environment at room temperature. This is very different from the kinetic behavior in toluene shown in Figure 7.6, and an ideal environment for generating spin quantum nature. As pointed out previously, there is a trade-

off between quintet generation efficiency and spin coherence time.²⁸⁷ The quintet generation efficiency in MPD-1 dimer was low ($< 1\%$). This is consistent with long coherence time due to the lack of decoherence through mixing of ^1TT and ^5TT . On the contrary, when the quintet generation efficiency is high, the fast spin evolution from ^5TT to ^1TT leads to a shorter quintet spin coherence time.

7.3 Conclusion

In conclusion, we have shown that the macrocyclic parallel dimer is an appropriate molecular design for exhibiting a long coherence time T_2 of quintet state even at room temperature. The use of dynamic covalent Schiff base chemistry allowed us to easily synthesize the MPD-1 dimer in high yield, and the macrocyclic structure keeps the pentacene units oriented parallel to each other in close proximity in solution or polymer matrix, leading to ultrafast SF of less than 100 fs and allowing the selective population of specific quintet sublevels. The structural fluctuations of the pentacene units in the MPD-1 dimer were kept small, and the longest room-temperature quintet coherence time to date of 648 ns was achieved. Unlike previous MOF systems, the homogeneously dispersed dimers have the advantage that the component with the long coherence time is major. Further fine tuning of linker and chromophore structures would provide a wide range of attractive MPDs from a viewpoint of flexibility, distance, orientation, and stability. In addition to the potential of precise structural control, optically-detected magnetic resonance at the single-molecule level will be possible by using chromophores that exhibit delayed fluorescence due to triplet-triplet annihilation, the reverse process of SF. The multilevel qubits, whose structure can be strictly defined at the atomic level, and which have long coherence time, would be very powerful in elucidating a wide range of biological and physical phenomena in the future.

Chapter 8

Conclusions

This chapter summarises the primary findings of the work described in this thesis, and highlights the most critical areas that need further investigation.

8.1 Summary

In this thesis, we investigated the fundamental mechanisms that contribute to triplet exciton generation in organic molecular systems, such as singlet fission, triplet-triplet annihilation, and intersystem crossing. We examined the effects of external conditions such as magnetic fields and temperature, as well as internal factors like molecular structure, on these processes. By focusing on diF-TES-ADT, tetracene, and pentacene-based materials, this work sheds light on how changes in experimental conditions and molecular structures can lead to significant differences in exciton behaviours and triplet generation mechanisms.

In Chapter 4, we study the temperature and magnetic field dependence on photoluminescence of a diF-TES-ADT singlet fission system. Previous studies based on transient absorption and photoluminescence spectroscopy have suggested that the first step of singlet fission, the generation of $^1(\text{TT})$, is temperature-independent in polycrystalline films of this material. However, in this chapter, we show that magnetic field-dependent photoluminescence spectroscopy reveals that singlet fission to form $(\text{T}..\text{T})$ is highly temperature-dependent in this material.

Our study further highlights the importance of combining a range of different optical and magnetic resonance spectroscopic techniques to obtain a full picture of the photophysical processes in materials for singlet fission and triplet-triplet annihilation.

In Chapter 5, we investigate the photophysical properties of new macrocyclic parallel tetracene dimers, and illustrate the mechanism of triplet formation using excitation wavelength-dependent transient absorption spectroscopy. Utilizing picosecond transient absorption spectroscopy in solution, the tetracene dimer 1 and its monomer display ultrafast intersystem crossing triplet production at higher excitation energy, whereas exciting the molecule with lower energy reveals a slow intersystem crossing process. These results suggest that intersystem crossing is influenced by the excitation wavelength in this system, and the triplet yield increases at higher excitation energy. Furthermore, this finding shows that the tetracene dimer can be considered a structural unit accountable for both rapid intersystem crossing and singlet fission processes.

In Chapter 6, we broaden our excitation wavelength-dependent study to include more monomeric tetracene compounds. Through picosecond transient absorption spectroscopy, we investigate the photophysical properties of different tetracene derivatives in solution. By providing a comprehensive analysis of the excited state dynamics, we showed excitation-dependent behaviour in some monomers, displaying unique characteristics, along with the detection of ultrafast intersystem crossing triplet formation.

These findings demonstrate the complexity of excited-state dynamics in tetracene derivatives. We showed that molecular structure and excitation conditions influence triplet-state formation, affecting excited-state relaxation pathways and photophysical behaviour. Understanding these dynamics, particularly the mechanisms governing ultrafast ISC, is essential for advancing tetracene-based materials in organic photovoltaics, photodetectors, and light-harvesting systems, ultimately contributing to improved energy conversion and device performance.

Finally, in Chapter 7, we investigated the photophysical properties of a newly

synthesized macrocyclic parallel pentacene dimer. This dimer demonstrated an ultrafast intramolecular singlet fission process and selective generation of the quintet states. It also exhibits the longest room-temperature coherence time of a quintet state, to our knowledge at the time of publication, of ca. 648 ns. This indicates that the macrocyclic structure is a promising strategy for generating multilevel quantum bits (qubits) at room temperature, which would be very powerful in elucidating a wide range of biological and physical phenomena in the future.

8.2 Open Questions and Future Work

The findings presented in this thesis open up some important questions and suggest potential directions for future research to address them. For example, in Chapter 4, using magnetic field effect and trESR experiments our results indicate direct intersystem crossing (ISC) from bound triplet pairs to individual triplet states, $^1(\text{TT}) \rightarrow \text{T}_1$, takes place at low temperatures, whereas at higher temperatures, singlet fission becomes dominant. This raises a general question that remains unanswered: how does morphology influence singlet fission and intersystem crossing, and therefore, triplet-triplet annihilation in this molecular system? Are the observed temperature-dependent transitions between SF and ISC specific to the current sample preparation, or do they represent a more general behavior across morphology?

According to Merrifield’s original theory, magnetic field effects are influenced by sample morphology, since the zero-field splitting terms in the spin Hamiltonian rely on relative molecule orientation.¹²⁹ The spin physics of strongly coupled triplet pairs can also be influenced by molecular orientation.⁶⁹ Additionally, morphology has a significant impact on the rate of triplet-pair separation.³⁰⁴ For instance, $^1(\text{TT})$ may stay bound for tens of microseconds in a polycrystalline TIPS-tetracene sample, yet quickly separates into free triplets in an amorphous sample.⁸⁵

Therefore, we suggest further temperature-dependent magnetic field effects

experiments on diF-TES-ADT samples with various morphologies in order to obtain a clear dataset for investigating the impact of morphology on singlet fission and triplet fusion.

Moreover, in Chapter 5, the first tetracene monomer (TDA) demonstrated excitation wavelength dependence and ultrafast ISC triplet generation at higher energy. However, the second tetracene monomer (DPT) exhibited ultrafast ISC across all excitation wavelengths, as presented in Chapter 6. This raises an essential question: why do we have excitation dependence in TDA but not DPT?

The consistent ultrafast ISC in DPT, irrespective of the excitation energy, leads us to hypothesize that the low-lying triplet state T_2 is located below and nearly isoenergetic with S_1 . This will dramatically boost the rate of intersystem crossing. In TDA, we hypothesize that T_2 is positioned slightly above S_1 . Therefore, higher excitation energy promotes ultrafast ISC by enhancing the direct population of T_2 , while lower-energy excitation causes slower ISC due to weak coupling between S_1 and T_2 .

Further spectroscopic investigations are required to definitively confirm this hypothesis, such as nanosecond transient absorption spectroscopy and phosphorescence lifetime measurements, as T_1 and T_2 states remain unreported in the current dataset.

In Chapter 7, transient electron paramagnetic resonance (trEPR) data indicated the existence of a quintet state, characterized by a long coherence time. Nevertheless, this quintet state could not be directly observed via optical techniques. An alternative technique, such as optically detected magnetic resonance (ODMR), facilitates an optical readout by integrating optical measurements, such as fluorescence, with electron paramagnetic resonance (EPR). It studies the spin properties of materials by monitoring changes in their optical response, such as fluorescence intensity, during exposure to microwaves.³⁰⁵ However, the ODMR technique was unsuccessful in pentacene, since the quintet state couldn't be detected, resulting in the inability to provide optical readout. It is also ineffective in tetracene, where singlet fission was not detected under the examined circum-

stances. Subsequently, other candidate materials, such as rubrene, may be examined, since they have shown the ability to produce efficient singlet fission,⁸⁹ and could therefore be a better starting point for combining magnetic and optical detection.

Another issue we encountered in this chapter was the limited stability of pentacene. Although it has attractive photophysical properties, it degrades when exposed to air, light, or moisture, making it challenging to work with over time. To make pentacene more practical for future studies or applications, it is important to understand what causes this instability and how we may enhance it, whether through molecular modifications or encapsulation techniques.

In conclusion, this thesis enhanced our understanding of singlet fission and intersystem crossing in organic semiconductor systems. particularly, how external factors such as temperature, magnetic field, and excitation conditions, together with internal conditions like molecular structures, influence these spin-state formation processes. These studies can serve in the development of new solar materials that use sunlight more effectively and might exceed the Shockley-Queisser limit, by clarifying how singlet fission competes with, or dominates over, intersystem crossing in different systems. This research also contributes to the quantum information science field, by showing how molecular systems can be tuned to form spin-correlated multiexciton states. These states have the potential to serve as a foundation for molecular qubit systems, contributing to the advancement of quantum technologies.

Appendix A

Supplementary information for Chapter 4

A.1 Morphological Characterization of diF-TES-ADT Films

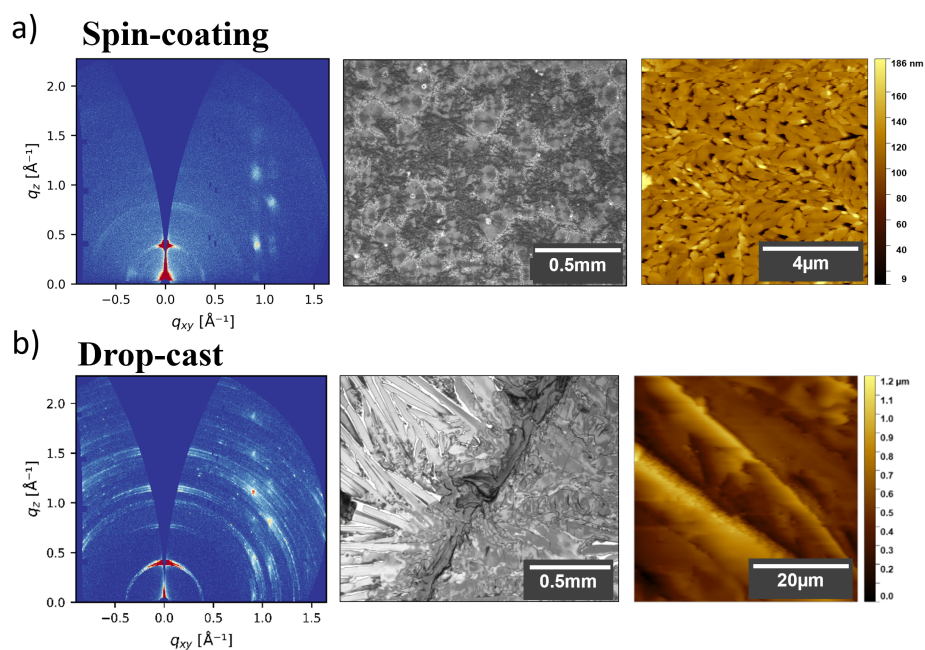


Figure A.1 – GIWAXS pattern (left), polarized microscope images (middle), and AFM scan (right) of (a) spin-coated and (b) drop-cast diF-TES-ADT films.

Figure A.1 shows grazing incidence wide-angle X-ray scattering GIWAXS (left), polarized microscope (middle), and atomic force microscopy AFM (right) images of (a) spin-coated and (b) drop-cast diF-TES- ADT films. Spin-coated thin film displays micron-scale crystalline texture (Fig. A.1a). The distinct grains apparent in the AFM are significantly smaller in the spin-coated film and show stronger preferential orientation with respect to the substrate, as evidenced by the appearance of Bragg spots (in comparison to the broader arc/ ring like features seen in the drop-cast sample). On the other hand, diF-TES- ADT drop-cast film crystallizes into large domains that are dispersed across the substrate (Fig. A.1b). We see that these crystalline domains are hundreds of micrometers in size.

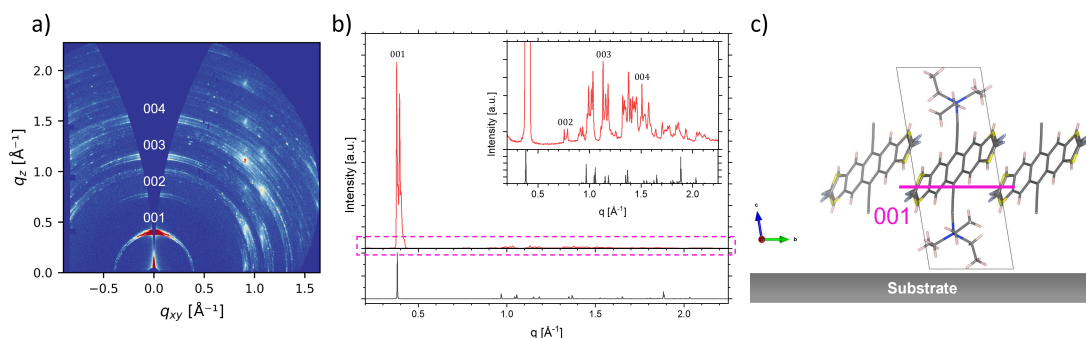


Figure A.2 – (a) 2D GIWAXS pattern of a drop-cast diF-TES- ADT film (repeated from Figure 1b) with the 001 and higher order reflections labeled. (b) Corresponding 1D GIWAXS intensity profile and simulated powder XRD of the reported crystal structure,³⁰⁶ simulated using VESTA software.³⁰⁷ The inset shows the region highlighted by the pink dashed rectangle. 1D GIWAXS intensity profiles were generated by azimuthally integrating the 2D pattern across the full q and azimuthal ranges. Here $q = 4\pi \sin \theta / \lambda$, where 2θ is the angle between the incident and scattered X-ray of wavelength λ and the azimuthal angle is the angle normal to the beam incidence at the detector. The out-of-plane scattering is dominated by a feature corresponding to the (001) plane, indicating a predominantly lamellar textured film (edge-on motif) with (001) planes aligned parallel to the substrate, as illustrated in (c).

Several distinct scattering peaks are observed corresponding to the diffraction from highly crystalline domains within the diF-TES- ADT film. The structure

of these crystalline regions is consistent with the previously reported brickwork packing with a predominantly edge-on lamellar motif as confirmed by GIWAXS (Figure A.2).³⁰⁶

A.2 Steady-State Absorption and Emission

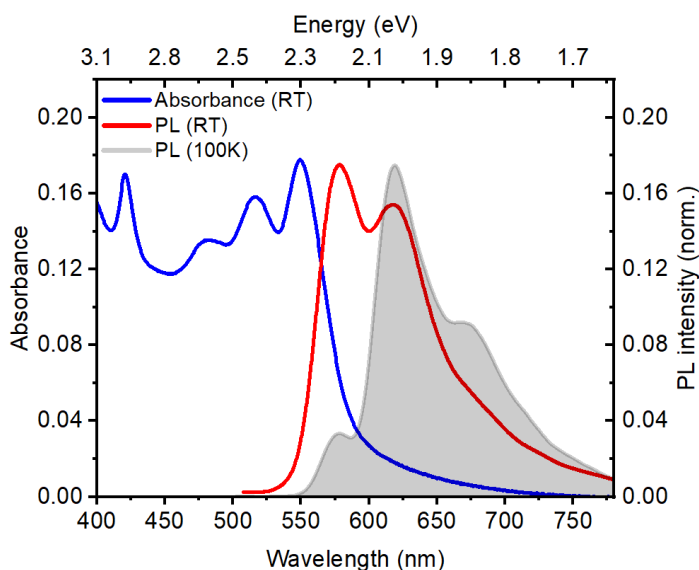


Figure A.3 – diF-TES-ADT thin film steady-state room temperature absorption spectrum (blue) and photoluminescence (PL) spectra at room temperature (red) and 100 K (gray shaded).

Temperature-dependent steady-state PL of the diF-TES-ADT film excited at 532 nm in Figure A.4 exhibits an increase of a strongly coupled triplet pair state $^1(\text{TT})$ emission at low temperatures.³⁷ This emission is shifted towards slightly longer wavelengths compared to the original emission peak at RT. The contribution from singlet states decreases as the temperature decreases from room temperature to 100 K.

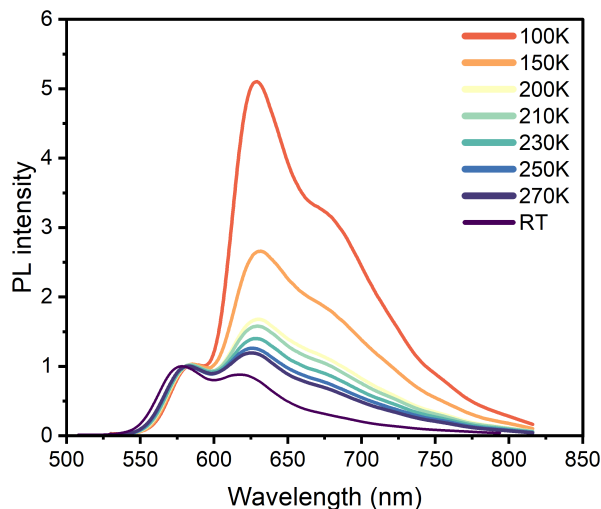


Figure A.4 – Temperature-dependent steady-state PL of a diF-TES-ADT, excited at 532 nm, exhibits an increase of the $^1(\text{TT})$ emission at low temperatures along with a decrease in the contribution from singlet states.

A.3 Temperature-Dependent Time-Resolved Photoluminescence Dynamics

TrPL dynamics exhibit minimal temperature dependence within the time constants range from ~ 10 to 30 ns, while changing the temperature from 20 K to RT, as illustrated in Figure A.5. As previously observed, the PL intensity initially decreases exponentially, characterized by a single time constant of ~ 25 ns, which is the lifetime of the emissive $^1(\text{TT})$ states. These $^1(\text{TT})$ states, created by singlet fission SF, may either return to the ground state or transform into long-lived triplets.⁸⁶ More intense emission on longer timescales indicates bimolecular triplet-triplet annihilation TTA, as reported in reference.³⁷

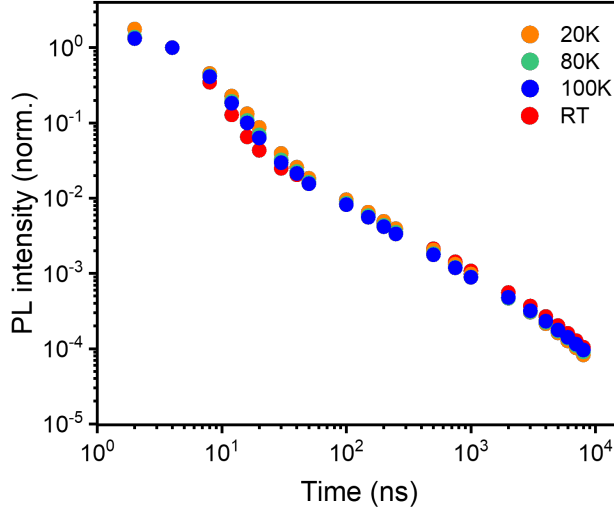


Figure A.5 – Temperature-dependent time-resolved photoluminescence dynamics of the diF-TES-ADT film, excited at 532 nm. TrPL dynamics exhibit minimal temperature dependence within the time constants range from ~ 10 to 30 ns, while changing the temperature from 20 K to RT.

A.4 Temperature-Dependent MFE measurements

The impact of the magnetic field was evaluated by measuring PL spectra at varied magnetic field strengths ranging from 0 mT to 280 mT, and at various delay times ranging from 5 ns to 1 μ s. The PL spectra were recorded while repeatedly changing the magnetic field strength in both upward and downward directions to ensure that the PL spectra obtained in both cases have the exact shape and magnitude. This was done to exclude any potential impacts of sample photo-degradation or laser power fluctuations and to reinforce our confidence in the reliability of the noted effects of the magnetic field. Figure A.6 shows some of the recorded PL spectra at RT (Fig. A.6a) and 100 K (Fig. A.6b), while repeatedly changing the magnetic field strength in both upward (black dots) and downward (lines) directions. At different delay times, the recorded spectra remained consistent in

terms of shape and magnitude while increasing and then decreasing the magnetic field strength.

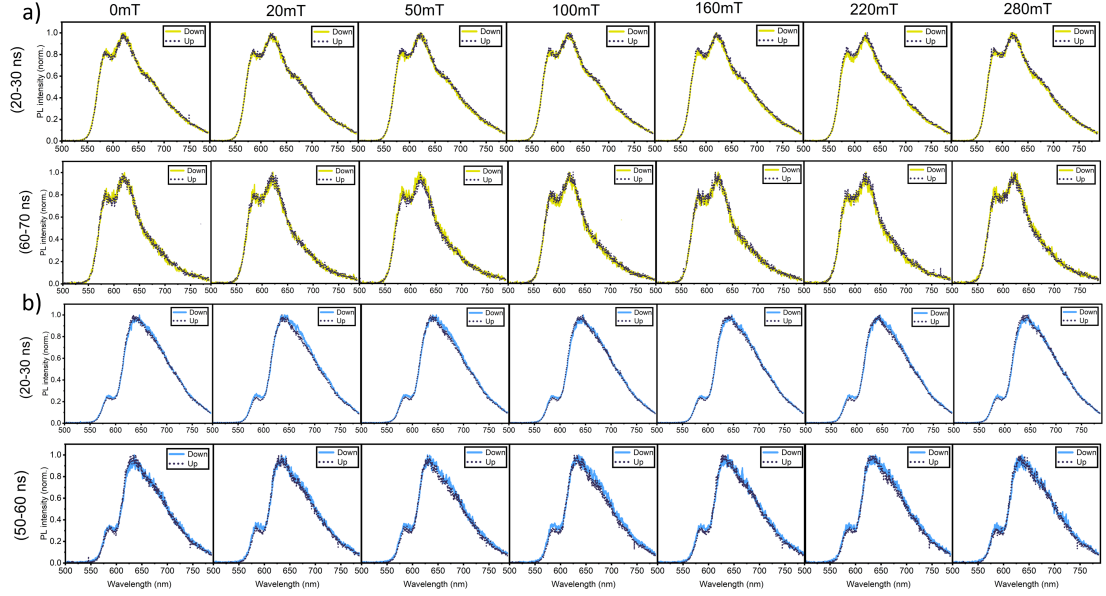


Figure A.6 – The recorded PL spectra at (a) Room temperature and (b) 100 K while repeatedly changing the magnetic field strength in both upward (black dots) and downward (lines) directions, showing the exact shape and magnitude of the PL spectra in both cases.

The laser power level was monitored using a power meter to evaluate laser stability and record any power fluctuations. This allowed the integration of the whole range of wavelengths and to calculate the MFE using the relevant equation:

$$\frac{\Delta \text{PL}}{\text{PL}} (\text{B}) = \frac{\text{PL}(\text{B}) - \text{PL}(0)}{\text{PL}(0)}$$

Figure A.7 illustrates the impact of magnetic field on the PL spectra of the diF-TES- ADT crystal at room temperature and 100 K. By recording PL spectra at different magnetic field strengths, Figure A.7(a,b) demonstrates an inverse pattern of PL intensity measured at RT. This variation is observed between early and later delay times, 10-20 ns and 350-500 ns, respectively. In contrast, at 100 K, although there is a variation in the magnetic field strength, we observe no corresponding change in the emission intensity throughout the earliest delay time

(Fig. A.7c). However, at a later time, 350-500 nm, changing the magnetic field strength caused a noticeable change in the emission intensity (Fig. A.7d), which is consistent with the recorded data at room temperature. The resulting MFE at various delay times ranging from 5 ns to 1 μ s is shown in Figure A.8, representing $\Delta\text{PL}/\text{PL}(\%)$ as a function of magnetic field strength at room temperature (Fig. A.8a) and 100 K (Fig. A.8b).

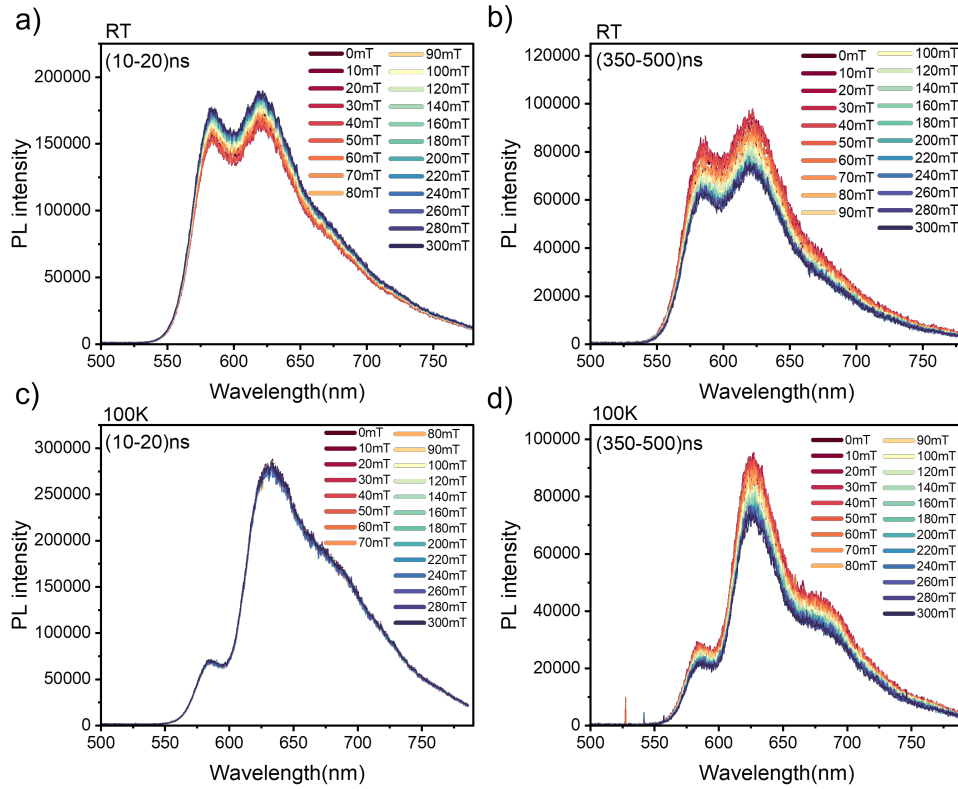


Figure A.7 – Temperature-dependent Photoluminescence spectra of the diF-TES-ADT drop-cast film as a function of magnetic field strengths measured at (a,b) room temperature, and (c,d) 100 K, at 10-20 ns and 350-500 ns, respectively.

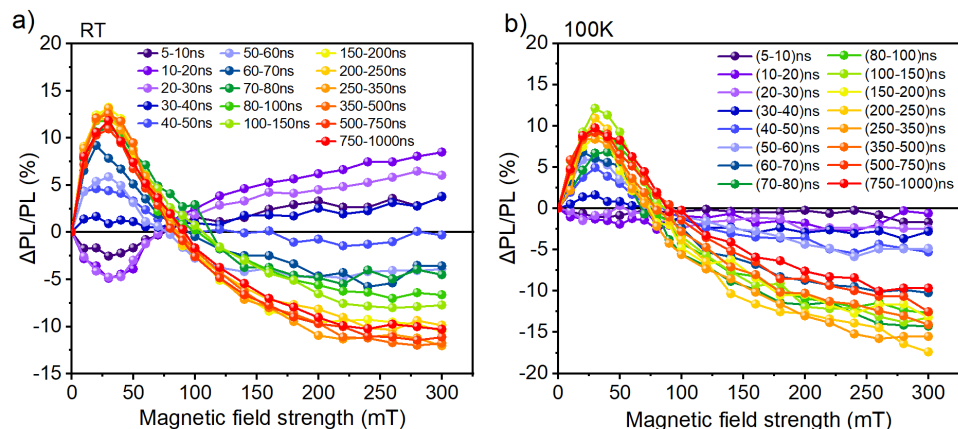


Figure A.8 – MFE of the diF-TES-ADT drop-cast film measured at 532nm across different delay times, from 5 ns to 1 μ s, exhibiting $\Delta\text{PL}/\text{PL}(\%)$ as a function of magnetic field strength at (a) Room temperature, and (b) 100 K.

A.5 Simulation and modeling of MFEs

A.5.1 Kinetic Modeling of Room Temperature MFE

The initial purpose of Merrifield's model was to describe the magnetic field-dependent fluorescence.³¹ Merrifield's kinetic model was recently modified³⁷ to simulate the emission dynamics at room temperature, see Ref.³⁷ for details. The rate model, in this modification, explicitly included two separate populations of triplet-pairs, exchange coupled triplet-pairs $^1(\text{TT})$ and weakly interacting triplet-pairs $(\text{T}\cdot\cdot\text{T})^l$. This model includes Merrifield's nine states denoted as $(\text{T}\cdot\cdot\text{T})^l$ where $l=1, 2, \dots, 9$, and their degree of overlap with the singlet is determined by the coefficients $|C_S^l|^2$, which are calculated from the spin Hamiltonian¹⁷⁹. Hence, the $|C_S^l|^2$ coefficients change with the magnetic field in accordance with the spin Hamiltonian. The molecule orientation was determined from the crystal structure in Ref.¹⁹⁵ and the zero-field splitting parameters, D and E , were taken from Ref.⁸⁶ In addition, it includes spin-lattice relaxation and non-radiative triplet decay from $(\text{T}\cdot\cdot\text{T})^l$ to $2\times\text{T}_1$. This kinetic model is represented

as $S_1 \rightleftharpoons {}^1(TT) \rightleftharpoons (T..T) \rightleftharpoons T_1 + T_1$ and shown in Figure A.9. In the original publication³⁷, this kinetic model and associated rate equations were used to simulate MFE data recorded at two delay times, 20-30 ns and 100-200 ns, using a custom-made Python code. The governing rate equations are as follows:

$$\begin{aligned} \frac{d[S_1]}{dt} &= - (k_{sf} + k_{snr}) [S_1] + k_{-sf}[{}^1(TT)] \\ \frac{d[{}^1(TT)]}{dt} &= k_{sf}[S_1] - \left(k_{-sf} + k_{hop} \sum_{l=1}^9 |C_S^l|^2 + k_{ttnr} \right) [{}^1(TT)] + k_{-hop} \sum_{l=1}^9 |C_S^l|^2 [(T..T)^l] \\ \frac{d[(T..T)^l]}{dt} &= k_{hop} |C_S^l|^2 [{}^1(TT)] - (k_{-hop} |C_S^l|^2 + k_{hop2} + k_{tnr} + k_{relax}) [(T..T)^l] \\ &\quad + \frac{1}{8} k_{relax} \sum_{j \neq l} [(T..T)^j] + \frac{1}{9} k_{tta} [T_1]^2 \\ \frac{d[T_1]}{dt} &= (k_{tnr} + 2k_{hop2}) \sum_{l=1}^9 [(T..T)^l] - 2k_{tta} [T_1]^2 - k_{tnr} [T_1] \end{aligned}$$

The square brackets in these equations represent the concentrations of the states, which are expressed in units of cm^{-3} . The definitions of all rate constants are shown in Figure A.9.

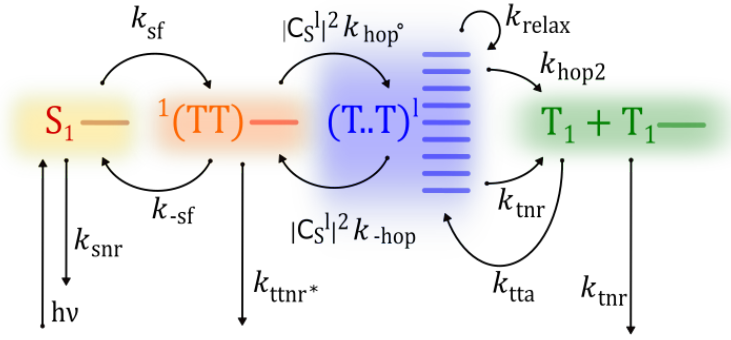


Figure A.9 – Kinetic scheme of the first modification of Merrifield model which presents SF and TTA behaviors at room temperature.

For our modeling, described below, the initial rate constants k_{SF} , k_{-SF} , k_{hop} , k_{hop} , k_{relax} , k_{hop2} , k_{tta} , k_{snr} , k_{ssa} , k_{ttnr} and k_{tnr} were taken from the fitting performed in Bossanyi *et al.*,³⁷ and used with minimal changes that were well within the constrained values (see supplementary information of Ref.³⁷).

In that study, the rate constants (k_{sf} , k_{-sf} , k_{snr}) were obtained by fitting the

diF-TES-ADT thin film transient absorption data. The remaining seven rate constants were optimized to provide a global fit for a large dataset comprising transient photoluminescence as a function of excitation density and temperature. Uncertainty analysis of this fitting is shown in the supplementary information of Ref.³⁷

The first step of singlet fission is shorter than the time resolution of the transient PL measurements on which this fitting was based, hence, the parameters k_{sf} , k_{-sf} , and k_{snr} have an insignificant impact on the model's output (but are constrained by the transient absorption data). Furthermore, k_{relax} has no lower bound for temperatures above 100 K, so it only has a significant role at low temperature. Conversely, k_{hop} , k_{-hop} , k_{hop2} , k_{tta} , k_{ttnr} , and k_{tnr} are generally tightly constrained.

Using these rate constants (fitted to and constrained by the transient PL and transient absorption data), we can *simulate* the room temperature time-resolved magnetic field effect without any fitting. This was our starting point and works reasonably well. Then, with only minor changes to the room temperature rate constants reported below in Table A.1 for k_{hop} , k_{-hop} , k_{hop2} , and k_{ttnr} (that are well within the bounds described in the uncertainty graphs in³⁷), we more accurately fit the magnetic field effects over all the time ranges measured in the current work.

A.5.2 Kinetic Modeling of Temperature-Dependent MFE

Here we have further modified the Merrifield kinetic model to include intersystem crossing from $^1(TT)$ and explicitly include temperature-dependence of the triplet-pair separation. Figure A.10 presents the kinetic scheme of this newly modified model. This modification involves including an Arrhenius term in the calculation of k_{hop} within the same rate equations used in the kinetic model based on Ref.³⁷. With fixed parameters from literature,³⁷ $k_{hop*} = k_{hop^\circ} \cdot e^{(\frac{-\Delta E}{k_B T})}$, where k_B is the Boltzmann constant, and ΔE is the activation energy of $\Delta E=20$ meV.⁸⁶ k_{hop° was initially calculated using the value of k_{hop} reported in Ref.³⁷, which is equal

to 0.0493 ns^{-1} , divided by the factor $e^{(\frac{-\Delta E}{k_B T})}$ at RT.

The second modification of the rate equations involves including intersystem crossing rate constant k_{ISC} to take into account ISC from the $^1(\text{TT})$ state to the T_1 state. The value of this constant was determined by inputting it into the code starting from zero and gradually increasing it until our simulations closely matched the actual data, as illustrated in Figure A.11 and A.12. Lastly, here we use k_{tnr^*} to distinguish it from the rate used by Ref.³⁷ who implicitly included k_{ISC} within the non-radiative decay of $^1(\text{TT})$, which they called k_{tnr} .

The governing modified rate equations used in this model are as follows (where $k_{\text{tnr}^*} = k_{\text{tnr}} - k_{\text{ISC}}$ when using k_{tnr} from Ref.³⁷):

$$\begin{aligned}
\frac{d[\text{S}_1]}{dt} &= -(k_{\text{sf}} + k_{\text{snr}}) [\text{S}_1] + k_{-\text{sf}} [^1(\text{TT})] \\
\frac{d[^1(\text{TT})]}{dt} &= k_{\text{sf}} [\text{S}_1] - \left(k_{-\text{sf}} + k_{\text{ISC}} + k_{\text{hop}^*} \sum_{l=1}^9 |C_{\text{S}}^l|^2 + k_{\text{tnr}^*} \right) [^1(\text{TT})] + \\
&\quad k_{-\text{hop}} \sum_{l=1}^9 |C_{\text{S}}^l|^2 [(\text{T}..\text{T})^l] \\
\frac{d[(\text{T}..\text{T})^l]}{dt} &= k_{\text{hop}^*} |C_{\text{S}}^l|^2 [^1(\text{TT})] - (k_{-\text{hop}} |C_{\text{S}}^l|^2 + k_{\text{hop}2} + k_{\text{tnr}} + k_{\text{relax}}) [(\text{T}..\text{T})^l] \\
&\quad + \frac{1}{9} k_{\text{tta}} [\text{T}_1]^2 + \frac{1}{8} k_{\text{relax}} \sum_{j \neq l} [(\text{T}..\text{T})^j] \\
\frac{d[\text{T}_1]}{dt} &= (k_{\text{tnr}} + 2k_{\text{hop}2}) \sum_{l=1}^9 [(\text{T}..\text{T})^l] + k_{\text{ISC}} [^1(\text{TT})] - 2k_{\text{tta}} [\text{T}_1]^2 - k_{\text{tnr}} [\text{T}_1]
\end{aligned}$$

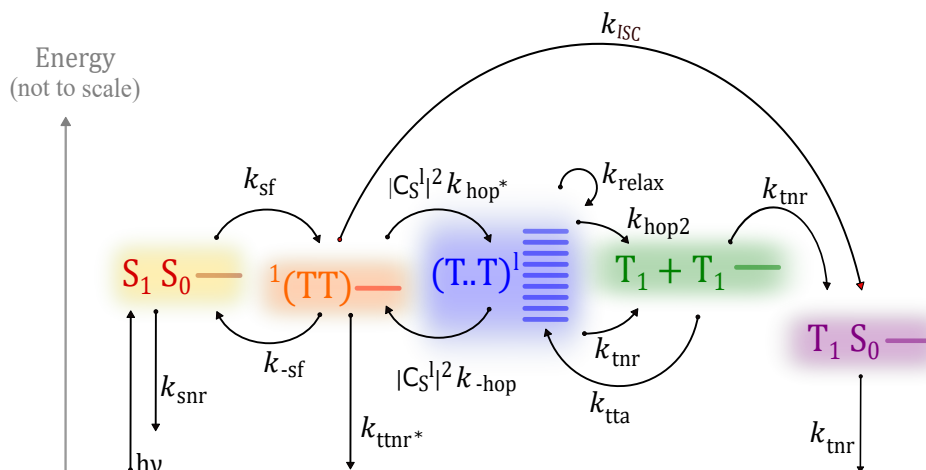


Figure A.10 – The updated kinetic scheme involving singlet fission at temperatures ranging from 270 K to RT and intersystem crossing at temperatures below 270 K. The rates used in our model are marked in the figure. Here k_{snr} , k_{ttnr*} and k_{tnr} include both radiative and non-radiative decay to the ground-state. The relative energies are NOT to scale (separation between T..T levels is on the order of $1\text{-}10\mu\text{eV}$, and exchange energy $2J$ between S_0S_1/S_0T_1 is on the order of 1 eV , while the difference between $^1(\text{TT})$ and T_1+T_1 is $\sim 30\text{ meV}$).

By applying the updated kinetic model and its associated rate equations, we initiated our simulation with the initial rate constant values from reference³⁷ (Table A.1). By raising the intersystem crossing rate constant value gradually and observing its impact on the curves across the entire time range, we obtain the results presented in Figure A.11 and A.12. The simulation of the MFE at RT (Fig.A.11) and 100 K (Fig.A.12) demonstrates that when the intersystem crossing rate constant k_{ISC} is 0.17 ns^{-1} , we see similar MFE behavior as in the experimental data. Increasing k_{ISC} further improves the MFE shapes until they reach a saturation point at higher values. The rate constants were adjusted to fine-tune the intensity of the curves to closely match the actual data. The final result of the optimized MFE simulation is shown in Figure A.13, which is based on the optimized numbers provided in Table A.1.

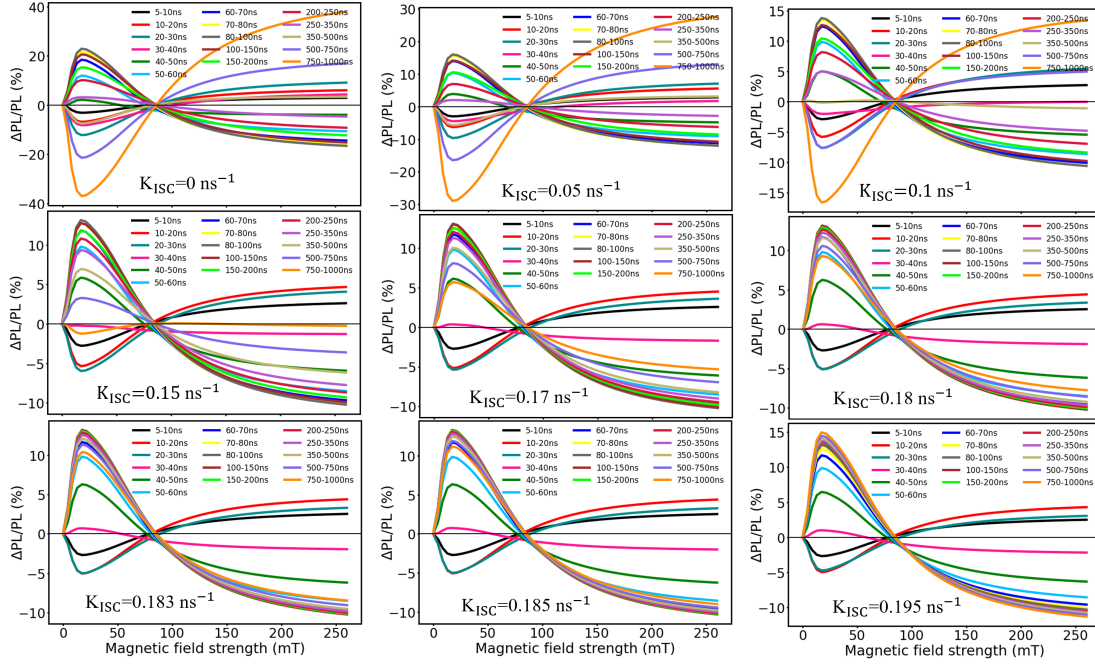


Figure A.11 – MFE simulation at RT illustrating the impact of a rising intersystem crossing rate constant (k_{ISC}) value on the behavior of the curves across the entire time range.

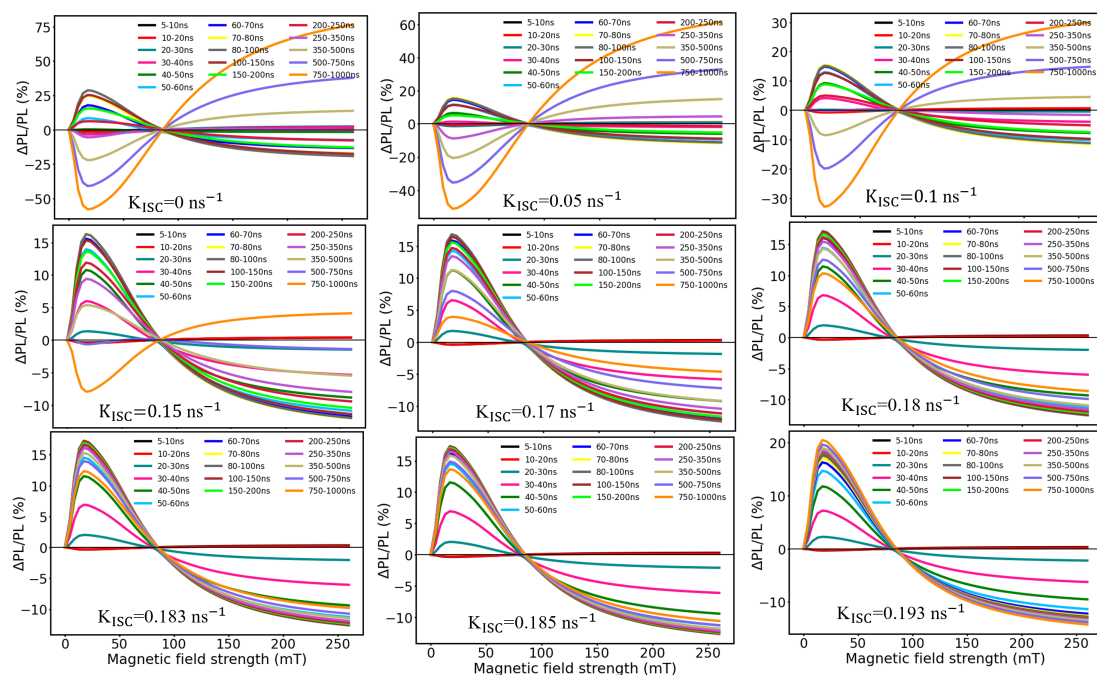


Figure A.12 – MFE simulation at 100 K illustrating the impact of a rising intersystem crossing rate constant (k_{ISC}) value on the behavior of the curves across the entire time range.

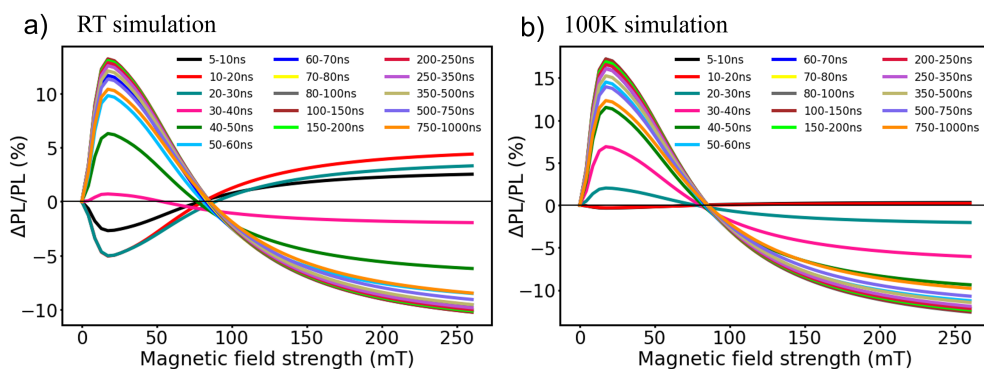


Figure A.13 – The final result of the MFE simulation at (a) RT and (b) 100 K using the optimized rate constants in Table A.1.

Table A.1 – The initial rate constant values from Ref.³⁷ based on fitting time-, fluence- and temperature-dependent PL of diF-TES-ADT films (left column) and the optimized rate values used in this work to simulate MFE data at RT, 100 K, and power-dependent data. The rate constants are as described in Fig. 4.10 in the main text. Note that in our rate model, the temperature-dependent k_{hop} rate is replaced by a thermally-activated rate $k_{\text{hop}}^* = k_{\text{hop}}^0 \exp(-E_A/k_B T)$ using $E_A = 20$ meV from Ref.⁸⁶

Rate	Initial values (ns ⁻¹)	Optimized values (ns ⁻¹)
k_{gen}	1.8	1.8
k_{sf}	10	10
$k_{\text{-sf}}$	0.083	0.083
$k_{\text{hop}}/k_{\text{hop}}^*$	0.0493	0.0493
$k_{\text{-hop}}$	0.0906	0.1106
k_{relax}	0	0
k_{hop2}	0.0644	0.0701
k_{tta}	5.43×10^{-20}	5.43×10^{-20}
k_{snr}	0.083	0.083
k_{ssa}	0	0
k_{ttnr}	0.0948	0.0948
k_{tnr}	1.68×10^{-6}	1.68×10^{-6}
k_{ISC}	-	0.183

Figure A.14 displays the derived MFE data and the simulation of diF-TES-ADT drop-cast film at room temperature (A.14 a, b), and 100 K (A.14 c, d). As presented in this Figure, across all measured delay times, we find that the simulation and the experimental data are in good agreement in terms of shape, intensity, and zero-crossing.

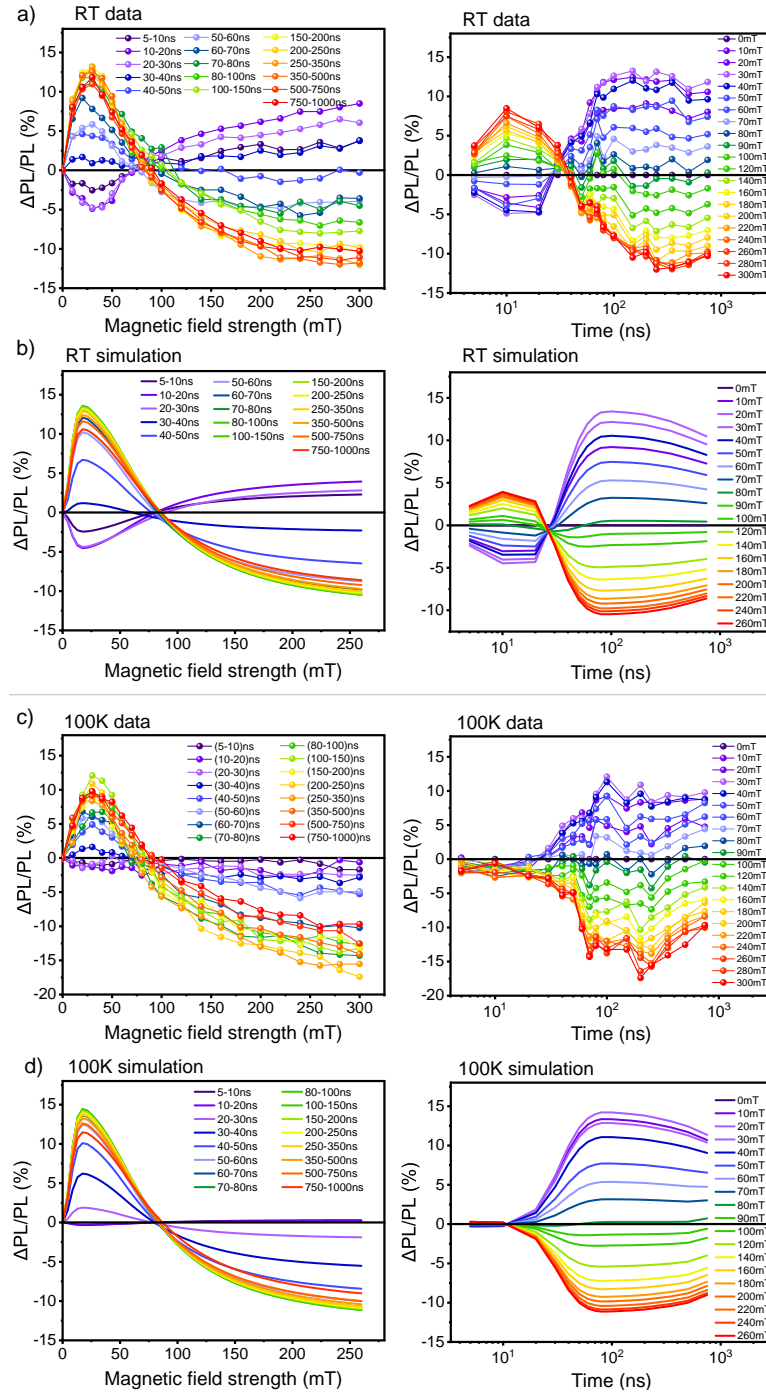


Figure A.14 – Comparison of experimental results (a,c) and simulations (b,d) of MFEs on the photoluminescence of the diF-TES-ADT drop-cast film measured at 532 nm across different delay times at (a,b) room temperature and (c,d) 100 K, respectively. The simulation and the data of the MFE at RT and 100 K are in reasonably good agreement.

A.5.3 Fluence-dependent simulation

To simulate the power-dependent MFE results at 100 K, the reported laser power, measured in μW , had to be converted to the exciton density, measured in cm^{-3} , before being applied to our updated code. Using the following equation, the values of the average exciton density N were calculated from the measured laser power P , where P was set to 11, 33, 100, 300, 900, and 2300 μW :

$$N = F_A(1 - F_S)R_P \frac{P\lambda}{f\pi r_x r_y d h c}$$

Here F_S and F_A represent the fractions of incident light scattered and absorbed by the sample respectively, which were determined from the UV–Vis transmission spectrum. For drop-cast diF-TES-ADT film, the sample thickness varies from 100 nm to 15 μm . Therefore, these fractions ranged from 0.2 to 0.45 for F_S , and from 0.21 to 0.34 for F_A . R_P is the ratio of measured power between the sample position and power meter position, which was determined to be 0.58 in our setup. The repetition rate of the laser, f , was set at 1 kHz for internally triggered power measurements. The radii of the excitation beam spot, r_x and r_y , are measured as 158.6 μm and 99.8 μm , respectively, using a CCD beam profiler from Thorlabs. The excitation wavelength is 532 nm, and h and c are Planck’s constant and the speed of light, respectively. However, the potential excitation densities vary by approximately three orders of magnitude due to the non-uniform thickness of the drop-cast film. Accurately determining the excitation densities for this specific sample is somewhat challenging. Consequently, we’ll be phenomenological and use the thin film’s excitation densities in our simulation since we possess precise measurements of the film’s thickness. Using these data to simulate our findings exhibits similar behaviour to the experimental fluence-dependent MFE data presented in the main text, as shown in Figure A.15.

Figure A.15 shows the resulting fluence-dependent simulation exhibiting a drop in the TTA-MFE as the excitation density rises, which is consistent with the experimental data presented in the main text (Fig. 4.6). It is important to observe that exceeding an exciton density of 5×10^{18} results in signal saturation,

whilst decreasing the exciton density below 2.3×10^{16} yields an even greater signal. Thus, our data is likely within this range of exciton densities.

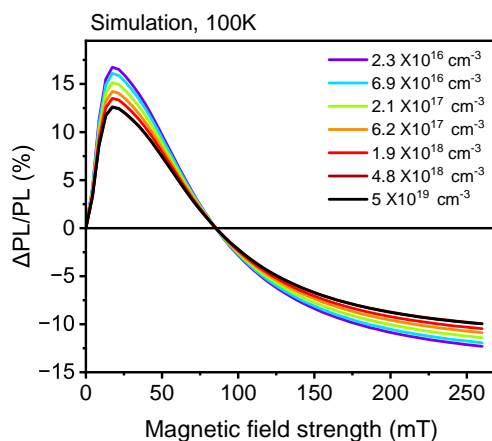


Figure A.15 – Simulation of the fluence- dependent magnetic field effect of diF-TES-ADT drop-cast film measured at 523 nm at 100 K. The simulation shows the drop in the TTA-MFE as the exciton density rises and broadly shows good agreement with the experimental MFE behavior.

A.6 Transient Electron Spin Resonance

A.6.1 trESR measurements on diF-TES-ADT in frozen solution

In order to clearly identify and assign features in ESR spectra attributable to singlet fission or triplet-triplet annihilation, reference measurements were performed on dilute frozen solutions of diF-TES-ADT in toluene, where these processes do not occur. The corresponding trESR spectra are shown in Fig. A.16 and show the presence of an intersystem crossing (ISC)-polarized triplet excited state at all temperatures probed. The triplet state ESR signal decays over time while maintaining the initial spin polarization pattern. These results are compared to the results obtained for drop-cast diF-TES-ADT films in Fig. 4.7 of the main text in Chapter 4.

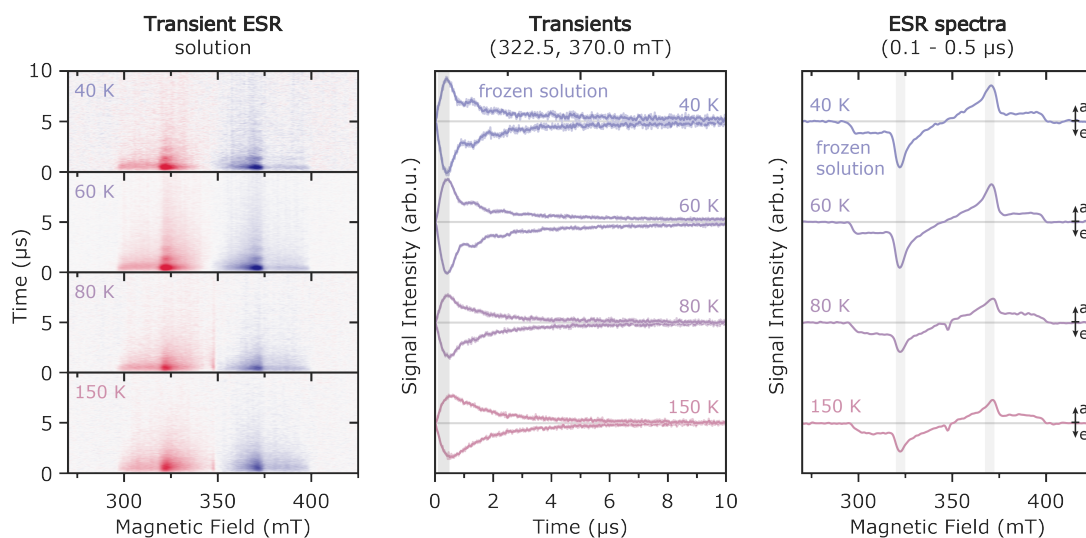


Figure A.16 – Transient ESR measurements on diF-TES-ADT in frozen solution at a series of temperatures. Time-dependent evolution of the ESR spectra as a function of time after laser excitation (*left*, red = emissive, blue = absorptive), transients extracted at the field positions corresponding to the X canonical field positions (322.5 mT and 370.0 mT, *center*) and spectra extracted at early times after laser excitation (0.1 - 0.5 μ s, *right*).

A.6.2 Spectral signatures for photoinduced paramagnetic states for different formation mechanisms

The spectral signature of the triplet state in diF-TES-ADT resulting from ISC is compared to the expected signatures for triplet and quintet states resulting from singlet fission in Fig. A.17. The differences in spin polarization pattern and position of the main spectral features between the ISC and singlet-fission born triplet and quintet states allow unequivocal interpretation of the experimental results in terms of ISC-born triplet states.

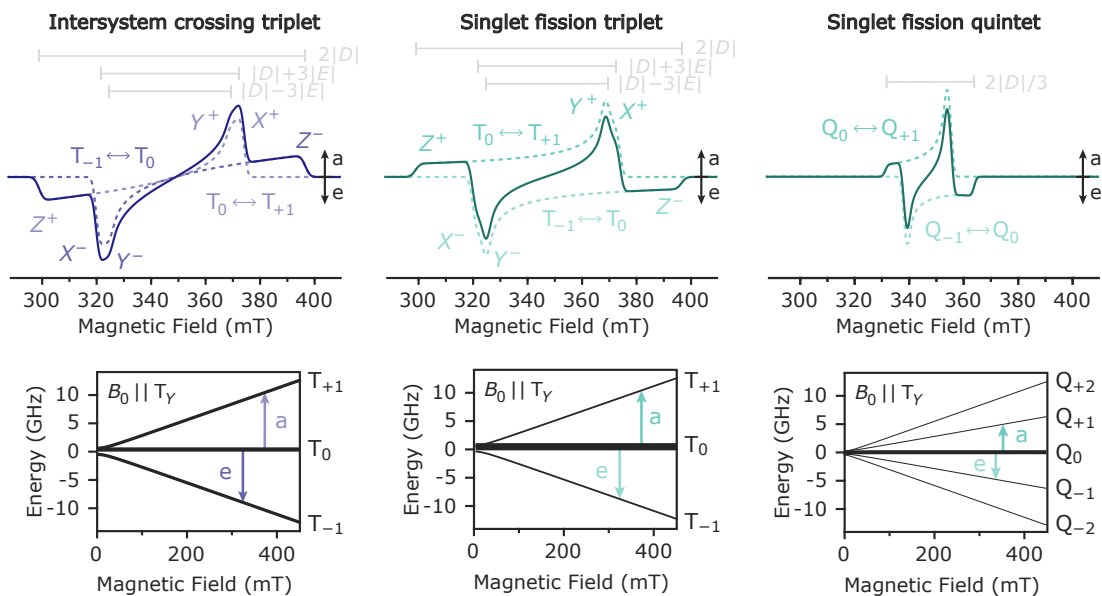


Figure A.17 – Calculated spectral signatures expected for triplet and quintet states in diF-TES-ADT resulting from different mechanisms: spin-selective population of zero-field populations by intersystem crossing (ISC) and selective population of the $m_S = 0$ sublevel by singlet fission. The contributions of the different transitions are shown as dashed lines and the overall spectrum resulting from their sum is shown as a solid line. The energy level diagrams with line thickness representing relative sublevel populations are shown for a magnetic field aligned with the Y -axis of the zero-field interaction.

A.6.3 Partial ordering in diF-TES- ADT films

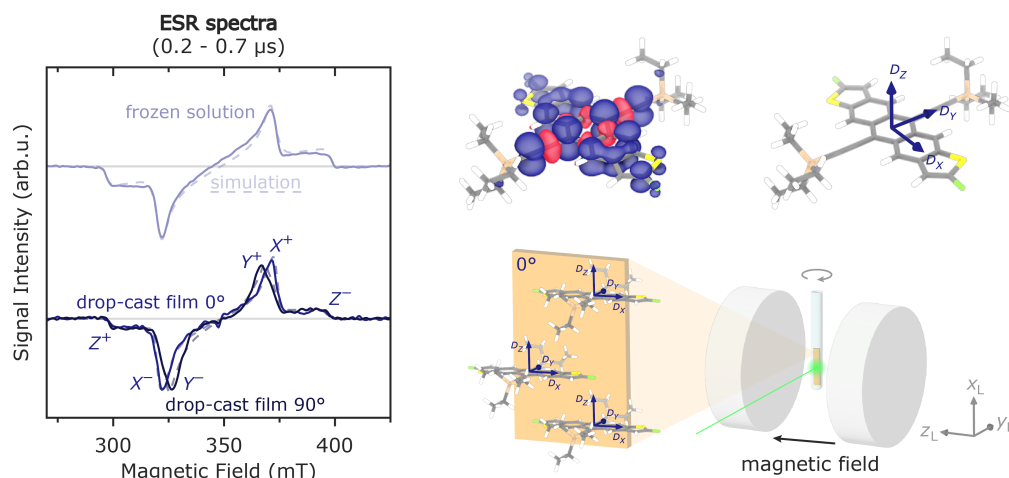


Figure A.18 – Transient EPR spectra for diF-TES- ADT in frozen solution and in a drop-cast film recorded at 20 K and extracted at early times after photoexcitation (0.2 - 0.7 μ s). The spectra are displayed for two different orientations of the film in the spectrometer, 0° corresponds to a magnetic field parallel to the substrate and 90° to the magnetic field along the substrate normal (see drawing on the bottom right). The spin density distribution predicted by DFT for the photoexcited triplet state of diF-TES- ADT and the orientation of the principal axes of the zero-field interaction within the molecular structure are displayed on the top right. The experimental spectra are compared to simulations shown as dashed lines, which for the drop-cast films take a probability distribution of molecular orientations in the film into account.

Transient ESR measurements performed on freshly prepared drop-cast diF-TES-ADT films at 20 K show evidence for partial ordering of the diF-TES-ADT molecules in the film as revealed by differences in the ESR spectra recorded with the magnetic field aligned with the substrate plane and with the substrate normal (Fig. A.18). Simulation of both the frozen solution and the drop-cast film measurements at the two substrate orientations, combined with information on the orientation of the principal axis frame of the zero-field interaction from DFT, indicates a preferential orientation of diF-TES-ADT molecules with the axis of maximum dipolar coupling (Z), the out-of-plane axis, parallel to the substrate

plane and the zero-field Y axis, lying along the TES sidechains, aligned with the substrate normal. The orientational dependence of the film ESR spectra is in agreement with the preferential edge-on orientation of the diF-TES- ADT molecules determined by GIWAXS, confirming a common morphology between films used for the optical and ESR measurements.

A.6.4 Contributions to the trESR spectra

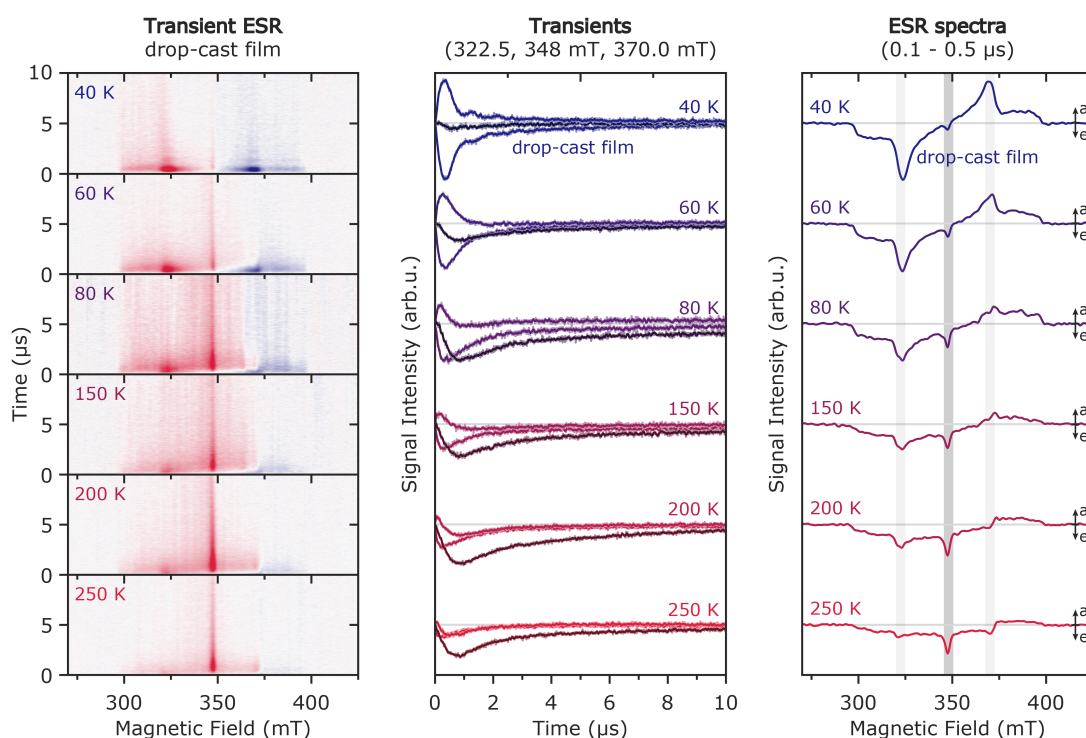


Figure A.19 – Transient ESR measurements on diF-TES- ADT drop-cast films at a series of temperatures. Time-dependent evolution of the ESR spectra as a function of time after laser excitation (*left*, red = emissive, blue = absorptive), transients extracted at the field positions corresponding to the X canonical field positions (322.5 mT and 370.0 mT) and to the field position of the narrow emissive signal contribution (348 mT, *center*) and spectra extracted at early times after laser excitation (0.1 - 0.5 μ s, *right*).

The trESR spectra exhibit a sharp emissive signal at $g \approx 2.004$ (347.6 mT), in addition to the broad signal of the photoexcited triplet state. This signal has an approximately Lorentzian lineshape with a FWHM of ca. 1.7 mT and its con-

tribution is more pronounced in the films and increases in intensity for higher temperatures. The rise time of this signal contribution is slower compared to that of the main triplet ESR signal (see Fig. A.19). Potential origins for this signal contribution are a spin-correlated radical pair formed by charge transfer, highly mobile triplets with averaged out dipolar interaction^{182,200} or a polarized radical state formed following photodegradation. The absence of a signal at the corresponding field position by continuous-wave ESR rules out the third option. Attempts at clearly discriminating between a radical and a triplet state origin through pulse or transient nutations were unfortunately not successful.

For a very mobile triplet state, the anisotropic zero-field interaction, which leads to the line splitting at the origin of the broad triplet signals, could be averaged out, leading to a reduced linewidth of the signal and resulting in a narrower line.^{200,291} In addition, hyperfine interactions between the electron spin and surrounding nuclear spins can contribute to line broadening in the rigid or low-mobility regime. When molecular motion is sufficiently fast, these hyperfine couplings are dynamically averaged, leading to further narrowing of the EPR signal. If the signal were due to motionally averaged triplets, the width would depend on the mobility and therefore, we would have expected contributions from a distribution of widths, for triplets with different mobility across regions of the sample with different local order and crystallinity. We would also have expected increased narrowing at higher temperatures, where the increased contribution of triplet-triplet annihilation evidenced by the increasingly emissive triplet polarization clearly indicates an increase in mobility.

In a radical pair/charge-transfer state, the weak coupling in a charge-transfer state leads to narrow signals typically falling in the region of $g \approx 2$. For a singlet-born radical pair, a spin polarization pattern with emissive and absorptive contributions is typically expected due to spin conservation. Triplet-born radical pairs can exhibit a wider range of different polarization patterns, depending on the exact nature of the triplet state and of the resulting radical pair. Comparison of the rise times of the broad triplet signal and the narrow central resonance across

different temperatures in Figure A.19 shows a delayed rise of the narrow central signal: it rises as the broad triplet signal starts to decay. In combination with the previous arguments, this led us to a charge-transfer state with the observed triplet state as a precursor as the most likely explanation for the observed signal.

A.6.5 Modeling of the trESR time evolution

The time evolution of the spin-polarized ESR signal was simulated to confirm assignment of the observed change in spin polarization pattern to triplet-triplet annihilation and extract the characteristic kinetic parameters describing this process. The kinetic model used for the simulation was adapted from Ref.²⁰³ and is shown schematically in Fig. A.20. The evolution of the triplet state sublevel populations, N_{+1} , N_0 and N_{-1} , was determined from the solution of the following set of differential equations taking into account spin relaxation, spin-selective unimolecular triplet decay kinetics and bimolecular triplet-triplet annihilation:

$$\begin{aligned}\frac{dN_{+1}}{dt} &= -w_{0\leftrightarrow+}N_{+1} - w_{-\leftrightarrow+}N_{+1} + w_{0\leftrightarrow+}p_{0\leftrightarrow+}N_0 + w_{-\leftrightarrow+}p_{-\leftrightarrow+}N_{-1} \\ &\quad - k_{+1}N_{+1} - k_{\text{TTA},+1}N_{+1}N_{-1} \\ \frac{dN_0}{dt} &= -w_{0\leftrightarrow+}p_{0\leftrightarrow+}N_0 - w_{-\leftrightarrow 0}N_0 + w_{0\leftrightarrow+}N_{+1} + w_{-\leftrightarrow 0}p_{-\leftrightarrow 0}N_{-1} \\ &\quad - k_0N_0 - k_{\text{TTA},0}N_0N_0 \\ \frac{dN_{-1}}{dt} &= -w_{-1\leftrightarrow 0}p_{-1\leftrightarrow 0}N_{-1} - w_{-\leftrightarrow+}p_{-\leftrightarrow+}N_{-1} + w_{-\leftrightarrow 0}N_0 + w_{-\leftrightarrow+}N_{+1} \\ &\quad - k_{-1}N_{-1} - k_{\text{TTA},-1}N_{+1}N_{-1}\end{aligned}$$

$w_{i\leftrightarrow j}$ are the relaxation rates for the different level pairs and the factors $p_{i\leftrightarrow j}$

$$p_{i\leftrightarrow j} = \exp(-(E_j - E_i)/k_{\text{B}}T)$$

ensure return to the Boltzmann equilibrium populations.

k_{+1} , k_0 and k_{-1} are the unimolecular triplet decay rates for each high-field triplet sublevel, which are determined from the selective decay rates k_X , k_Y and k_Z in the molecular (zero-field) frame for each molecular orientation as

$$k_i = \sum_l c_i^2 k_l \quad i = -1, 0, +1 \quad l = X, Y, Z$$

$k_{\text{TTA},+1}$, $k_{\text{TTA},0}$ and $k_{\text{TTA},-1}$ are the decay rates for the triplet-triplet annihilation process corresponding to each high-field triplet sublevel.

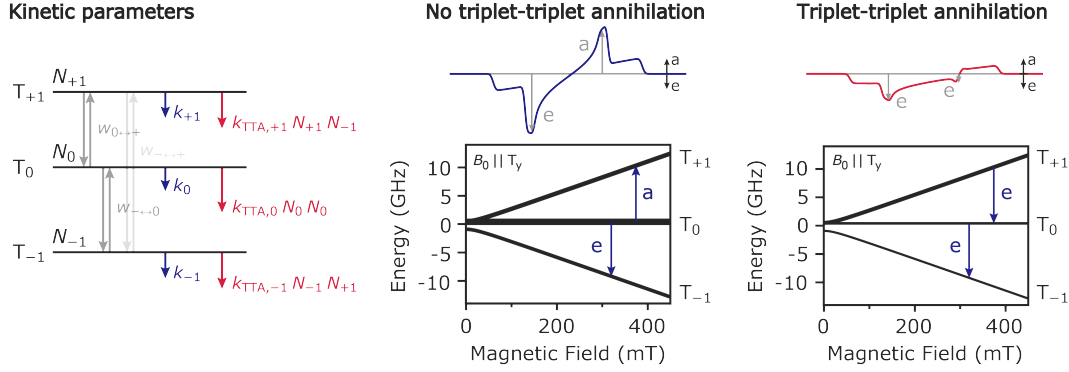


Figure A.20 – Schematic drawing of the kinetic model used for the trESR simulations (*left*) and illustration of the effect of triplet-triplet annihilation on the triplet sublevel populations and therefore the spin polarization of the ESR spectrum (*right*). The energy level diagrams are shown for a magnetic field aligned with the Y -axis of the zero-field interaction, the orientation most sensitive to the effects of triplet-triplet annihilation for this system.

This kinetic model was implemented in a modified version of the EasySpin `resfields` function,^{164,308} which calculates the triplet sublevel populations for each time point and each orientation in the powder average by solution of the differential equations using Matlab's built-in ODE solver and constructs the ESR spectrum at different times after photoexcitation. The finite rise time of the signal was modeled by multiplication of the calculated transients with a response function determined by the resonator bandwidth for a given resonator Q -value.

In order to reduce the number of variable fitting parameters, and therefore minimize the risk of overfitting, we made a series of approximations. The relaxation rates for the level pairs corresponding to a $\Delta m_S = \pm 1$ transition were set to be equal ($w_{- \leftrightarrow 0} = w_{0 \leftrightarrow +}$) and the relaxation rate for level pairs with $\Delta m_S = \pm 2$ was set to be negligible. The unimolecular decay rates k_X , k_Y and k_Z were assumed to be the same for diF-TES-ADT in frozen solution and in drop-cast films and independent of temperature.

The unimolecular decay rates and the temperature-dependent relaxation rates were determined from a global fit of the frozen solution trESR spectra and transients recorded at 40 K, 60 K, 80 K and 150 K. The simulation parameters are reported in Fig. A.2. An excellent agreement with the experimental results could be obtained as shown in Fig. A.21. The presence of Torrey oscillations in trESR datasets recorded at low temperatures indicates that the measurement conditions, with the microwave power necessary to acquire data with sufficient signal-to-noise ratio, correspond to the underdamped regime.³⁰⁹ As the relaxation times decrease for higher temperature, a transition to the overdamped regime is observed. In both regimes, the decay of the signal is not purely determined by T_1 , with T_2 significantly influencing the decay in the underdamped regime and the decay constant only approaching T_1 when $\nu_1^2 T_1 T_2 \ll 1$.³⁰⁹ Therefore relaxation rate constants determined from the fit cannot be interpreted in terms of specific relaxation times. However, the purpose of modeling the frozen solution trESR data was to determine the rate constants of all processes except triplet-triplet annihilation, so that these could then be kept fixed for the simulation of the data recorded for the drop-cast films to better isolate the contribution of triplet-triplet annihilation.

For the simulation of the trESR data recorded for diF-TES- ADT in drop-cast films, the bimolecular decay rates for the T_{-1} and T_{+1} sublevels were kept equal ($k_{\text{TTA},-1} = k_{\text{TTA},+1}$) and the ratio $k_{\text{TTA},+1/-1}/k_{\text{TTA},0}$ was kept fixed for all temperatures and laser fluences. The ratio $k_{\text{TTA},+1/-1}/k_{\text{TTA},0}$ and the magnitude of TTA decay were determined from a global fit of the trESR spectra and transients recorded at different temperatures and different laser fluences. The resulting simulations are shown in Fig. A.21 and the corresponding simulation parameters are summarized in Fig. A.2. The simulations based on this kinetic model including bimolecular triplet-triplet annihilation are clearly able to reproduce the evolution from a symmetric ISC-populated triplet state spectrum at very early times after photoexcitation to the mostly emissive spectrum with a net polarization within the first 1-4 μs . The transition is most clearly visible at the field position

corresponding to the high-field Y canonical transition (ca. 370 mT) and results from an inversion of the relative population of the T_{+1} and T_0 levels due to the spin-selectivity of triplet-triplet annihilation (see Fig. A.20). Agreement between experiment and simulation is obtained for increased triplet-triplet annihilation at higher temperatures and higher laser fluences.

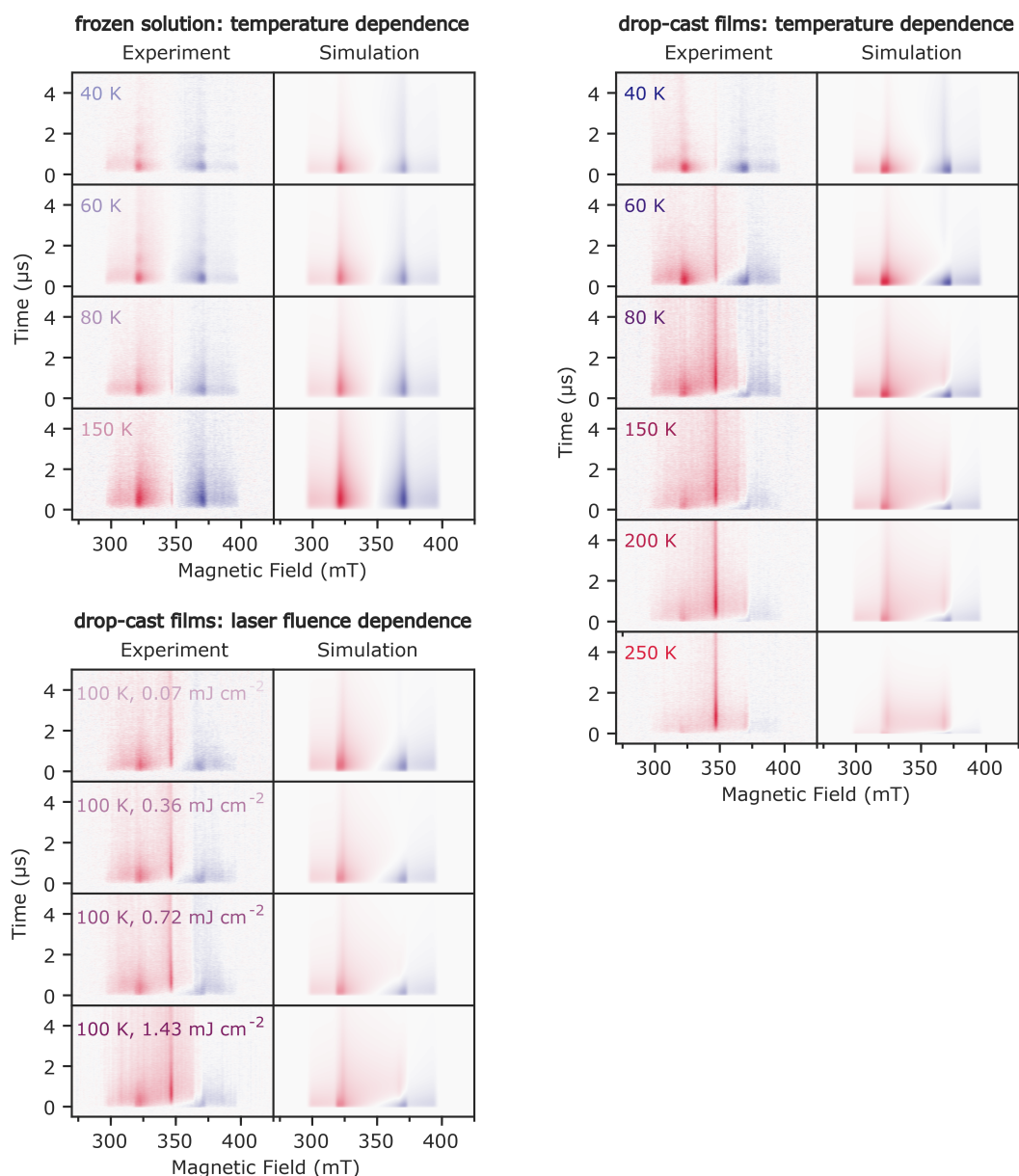


Figure A.21 – Comparison of the results of the trESR experiments performed as a function of temperature for diF-TES-ADT in frozen solution and as a function of temperature and laser fluence for diF-TES-ADT in drop-cast films with simulations based on a kinetic model taking relaxation, spin-selective unimolecular triplet decay and bimolecular triplet-triplet annihilation into account, performed as described in the text. The simulation parameters are reported in table A.2.

Spin system parameters

	frozen solution	drop-cast film
g	2.0059 ± 0.0005	2.0059 ± 0.0005
D	1420 ± 5 MHz	1370 ± 5 MHz
E	-32 ± 2 MHz	-50 ± 5 MHz
D strain	[100 120] MHz	[79 20] MHz
H strain	50 MHz	50 MHz

Spin-selective triplet population and decay

$$p_X : p_Y : p_Z \quad 0.45:0.36:0.19 \quad (\pm 0.02)$$

$$k_X : k_Y : k_Z \quad 0.32:0.26:0.41 \quad (\pm 0.02) \text{ } \mu\text{s}^{-1}$$

Relaxation

	40 K	60 K	80 K	100 K	150 K	200 K	250 K
$w_{-\leftrightarrow 0} = w_{0\leftrightarrow +} \text{ (}\mu\text{s}^{-1}\text{)}$	0.92	0.60	0.33	0.22	0.22	0.50	0.65
$w_{-\leftrightarrow +} = 10^{-4} \text{ } \mu\text{s}^{-1}$	$\delta w = 0.05 \text{ } \mu\text{s}^{-1}$						

Triplet-triplet annihilation*

Temperature	40 K	60 K	80 K	150 K	200 K	250 K
$k_{\text{TTA},+1} = k_{\text{TTA},-1} \text{ (}\mu\text{s}^{-1}\text{)}$	0.42	3.0	7.4	11.0	19.2	38.5
$k_{\text{TTA},0} \text{ (}\mu\text{s}^{-1}\text{)}$	0.47	3.4	8.3	12.3	21.6	43.2

$T = 100 \text{ K}$

Laser fluence (mJ cm^{-2})	0.07	0.36	0.72	1.43
$k_{\text{TTA},+1} = k_{\text{TTA},-1} \text{ (}\mu\text{s}^{-1}\text{)}$	2.7	3.8	5.5	8.8
$k_{\text{TTA},0} \text{ (}\mu\text{s}^{-1}\text{)}$	3.1	4.3	6.2	9.9

* The ratio $k_{\text{TTA},+1/-1} : k_{\text{TTA},0} (= 0.89 : 1)$ is fixed across all temperatures and laser fluences.

Table A.2 – Parameters for the simulation of ESR spectra and their time dependence.

A.6.6 Experimental Procedures and Data Analysis Conducted by Collaborators at the University of Oxford

Transient Electron Spin Resonance

Transient ESR experiments were performed on a Bruker Elexsys E680 X-band spectrometer equipped with a Bruker ER- 4118X-MD5-W1 dielectric resonator with an optical window. Measurements at a series of temperatures in the range from 20 K to 250 K were performed using liquid helium or liquid nitrogen cooling with an Oxford Instruments CF935 cryostat and temperature-control system. Laser excitation at 532 nm was provided by an EKSPLA NT230 diode pumped Q-switched Nd:YAG laser and optical parametric oscillator (OPO) with 5 ns pulses and a 50 Hz repetition rate. After the last laser turning mirror, the light was depolarized using an achromatic depolarizer. A Stanford Research System digital delay generator (DG645) was used for synchronization of the laser and EPR spectrometer. The laser energy incident on the sample was estimated based on laser energy measurements within the resonator and cryostat using a ThorLabs TD2X thermal detector placed at the position of the sample (after calibration outside the resonator). Transient EPR experiments were performed by direct detection with the transient recorder (Video Amplifier III, 1 GHz bandwidth) without lock-in amplification using a microwave power of 2 mW. The laser background signal was removed by 2D baseline-correction determined based on low- and high-field off-resonance transients.

Density Functional Theory calculations

DFT calculations were performed to predict the orientation of the principal axes of the zero-field interaction with respect to the molecular structure. Geometry optimizations for the ground and triplet state were performed in ORCA (v.5.0.4)³¹⁰ with the BP86 basis set and the def2-SVP basis set, including a dispersion correction,^{311–314} EPR parameters were calculated for the optimized geometry with the PBE0 basis set and EPR-II basis for H, C and N and the IGLO-III basis set for

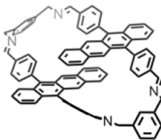
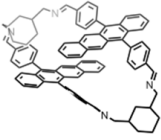
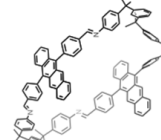
S.³¹⁵⁻³¹⁸ The calculated spin density distribution and principal axis orientations are depicted in A.18. DFT predicts a positive zero-field splitting D value with the Z principal axis along the out-of-plane direction, in agreement with other polyacene-based molecules.

Appendix B

Supplementary information for Chapter 5 and 6

B.1 Tetracene dimers

B.1.1 Molecular weight of DPT-dimers

Molecule	Molecular structure	Molecular weight (g/mol)
DPT-dimer1		1073.36
DPT-dimer2		1084.54
DPT-dimer3		1488.70

B.1.2 Absorbance spectra of the dimers

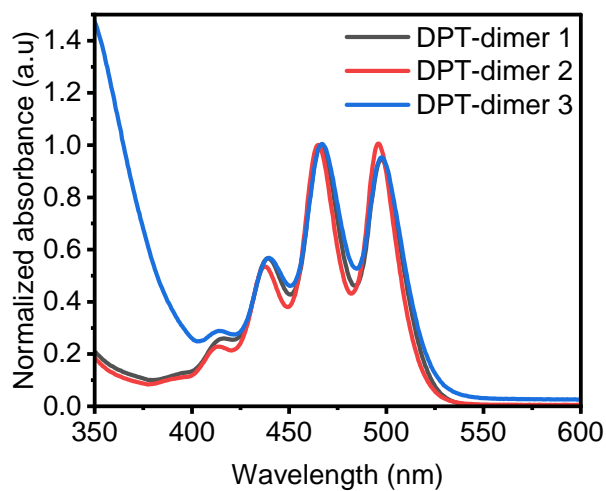


Figure B.1 – Steady-state absorption spectra of DPT-dimers. Normalized absorption spectra of DPT-dimer 1 (black), DPT-dimer 2 (red line), and DPT-dimer 3 (blue line) in toluene solutions at room temperature. The absorption spectra of tetra-cene dimers exhibit similar spectral features regarding peak positions and intensities, indicating comparable electrical and structural properties.

B.1.3 Absorption spectra of DPT-dimer1: solvent dependency

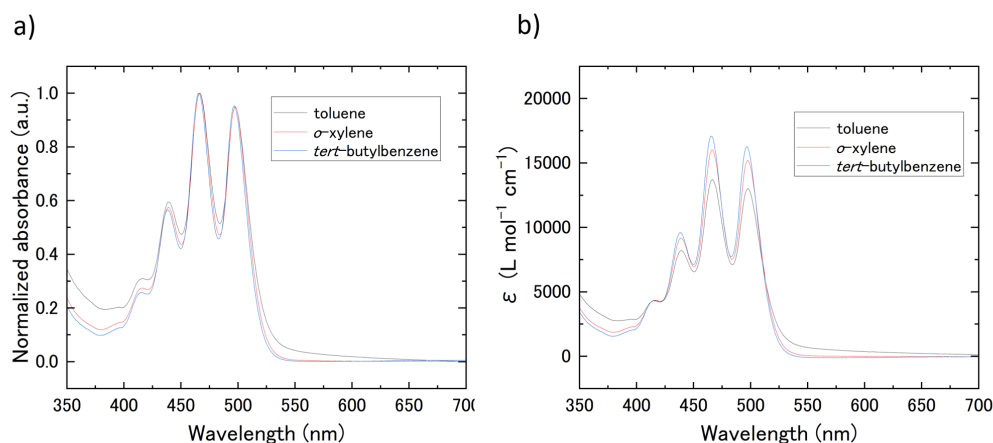


Figure B.2 – Solvent dependence of DPT-dimer1. (a) Normalized absorbance spectra of the of DPT-dimer 1 in toluene (black line), o-xylene (red line), and tert-butylbenzene (blue line), presenting comparable spectral features and consistent peak positions across all solvents. (b) Absorption coefficient spectra of the DPT- dimer 1 in the same solvents, showing identical peak positions but different intensities, reflecting differences in solvent-dependent absorption strength. Note: This figure was measured by Wataru Ishii at Kyushu University in Japan.

B.1.4 calibration curves of DPT-dimer1 in different solvents at different wavelengths

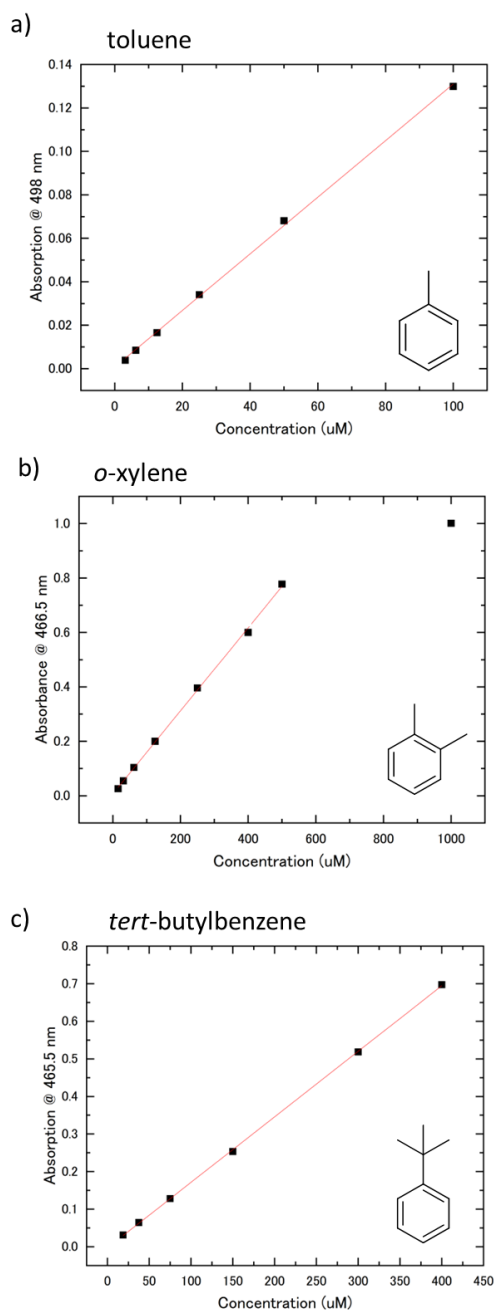
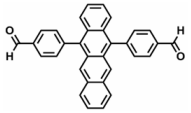
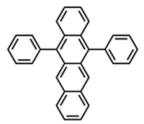
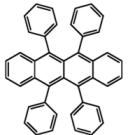


Figure B.3 – Calibration curves of DPT-dimer1 in different solvents. Calibration curve of DPT-dimer 1 in (a) Toluene at $\lambda = 498$ nm, (b) *O*-xylene at $\lambda = 466.5$ nm, and (c) *Tert*-butylbenzene at $\lambda = 465.5$ nm. Note: This figure was measured by Wataru Ishii at Kyushu University in Japan.

B.2 Tetracene monomers and rubrene

B.2.1 Molecular weight of the monomers

Molecule	Molecular structure	Molecular weight (g/mol)
Tetracene-2,6-dicarboxaldehyde, TDA		436.51
5,12-diphenyltetracene, DPT		380.49
5,6,11,12-tetraphenyltetracene Rubrene		532.7

B.2.2 Photoluminescence quantum yield (PLQY) of the monomers

The PLQY for TDA and DPT monomers was calculated using the equation provided below.²⁶⁴

$$\text{PLQY}_{\text{sample}} = \text{PLQY}_{\text{reference}} \times \left(\frac{I_{\text{sample}}}{I_{\text{reference}}} \right) \times \left(\frac{A_{\text{reference}}}{A_{\text{sample}}} \right) \times \left(\frac{n_{\text{sample}}}{n_{\text{reference}}} \right)^2$$

Where (I) is the integrated PL intensity of the emission, (A) is the absorbance of the solution, and (n) is the solvent's refractive index. Given that toluene was employed as a solvent for all monomers, the refractive index of the solvents is uniform, so we omitted the last component of the equation. Rubrene, recognized for its outstanding emissive characteristics, demonstrated a PLQY of ~98 - 100% in solution,^{261,263} acting as a reference for our calculation. The PL quantum yields of DPT were found to be 67% and TDA to be 60% according to this standard. The absorbance and photoluminescence values used in these calculations are shown below.

Concentration-dependent steady-state absorption and PL of rubrene and DPT-monomer

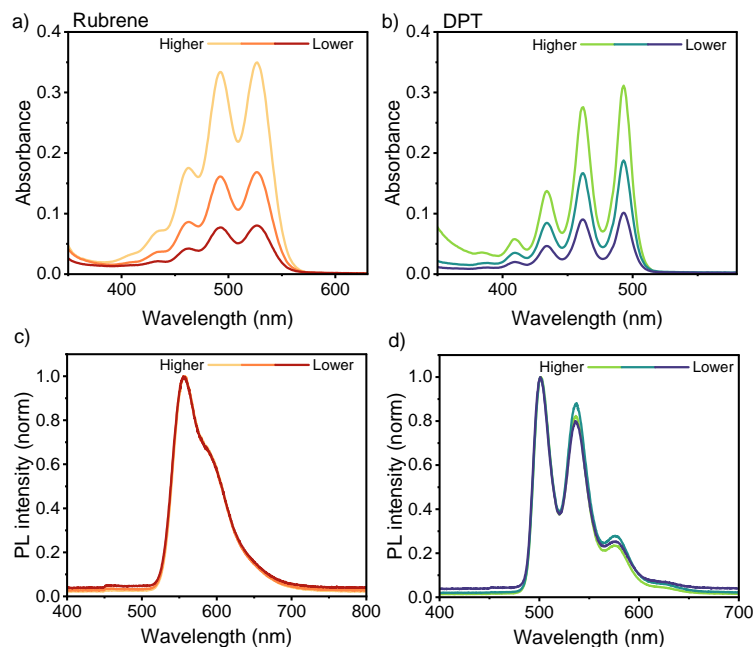


Figure B.4 – Concentration-dependent steady-state absorption and photoluminescence of rubrene and DPT. Steady-state UV-vis absorption and normalized photoluminescence spectra of (a, c) Rubrene and (b, d) DPT, respectively, in toluene solution at different concentrations.

Table A1: Absorbance and integrated normalized PL values from Figure B.4 for PLQY calculation of DPT-monomer using rubrene as reference

Molecule	Rubrene	DPT
Absorbance	0.075	0.086
Normalized emission-1	82.88415	59.83714
Normalized emission-2	85.52662	66.92747
Normalized emission-3	92.68647	74.2586
PLQY _{DPT1}	63%	
PLQY _{DPT2}	68%	
PLQY _{DPT3}	69%	
PLQY _{DPT} (average)	67%	
stdev	3.61	
Error	2.08	

Concentration-dependent steady-state absorption and PL of rubrene and TDA-monomer

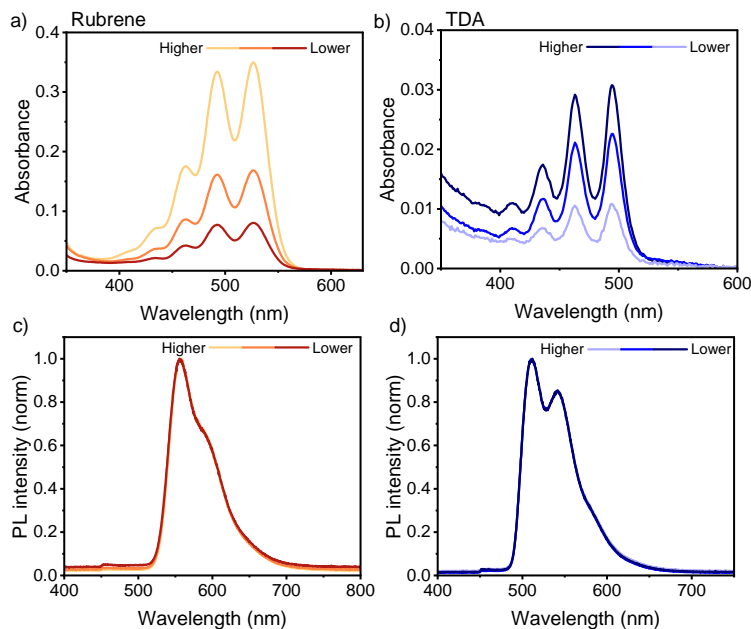


Figure B.5 – Concentration-dependent steady-state absorption and photoluminescence of rubrene and TDA. Steady-state UV-vis absorption and normalized photoluminescence spectra of (a, c) Rubrene and (b, d) TDA, respectively, in toluene solution at different concentrations

Table A2: Absorbance and integrated normalized PL values from Figure B.5 for PLQY calculation of TDA-monomer using rubrene as reference

Molecule	Rubrene	TDA
Absorbance	0.019	0.029
Normalized emission-1	83.53656	81.85706
Normalized emission-2	81.76456	76.72465
Normalized emission-3	93.82167	78.80298
PLQY _{TDA1}	55%	
PLQY _{TDA2}	61.5%	
PLQY _{TDA3}	64.2%	
PLQY _{TDA} (average)	60.23%	
stdev	4.7	
Error	2.72	

B.3 DPT sensitization measurement using different sensitizers.

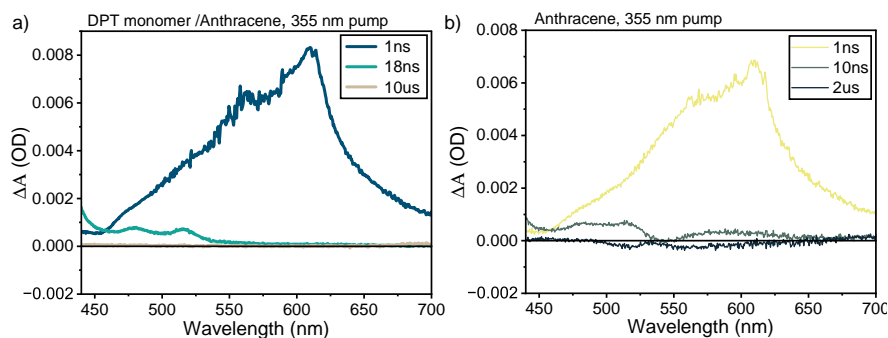


Figure B.6 – Nanosecond-millisecond transient absorption spectra of anthracene-sensitized DPT monomer in toluene with pump wavelength 355nm with a visible probe. The solution is a 10:1 molar ratio of anthracene (500 μ M) and DPT (50 μ M) in toluene. The spectra for (a) anthracene: DPT mixture and (b) anthracene solution are identical due to the absence of energy transfer to DPT monomer.

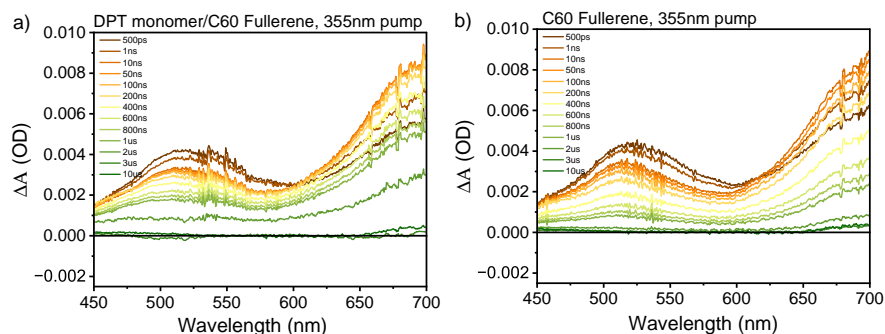


Figure B.7 – Nanosecond-millisecond transient absorption spectra of Fullerene-C60-sensitized DPT monomer in toluene with pump wavelength 355nm with a visible probe. The solution is a 1:1 molar ratio of C60 (50 μ M) and DPT (50 μ M) in toluene. The spectra for (a) C60: DPT mixture and (b) C60 solution are identical due to the absence of energy transfer to DPT monomer.

[†]James Pidgeon and I measured the sensitization data using nanosecond-millisecond transient absorption spectroscopy.

B.4 Excitation wavelength dependence in rubrene

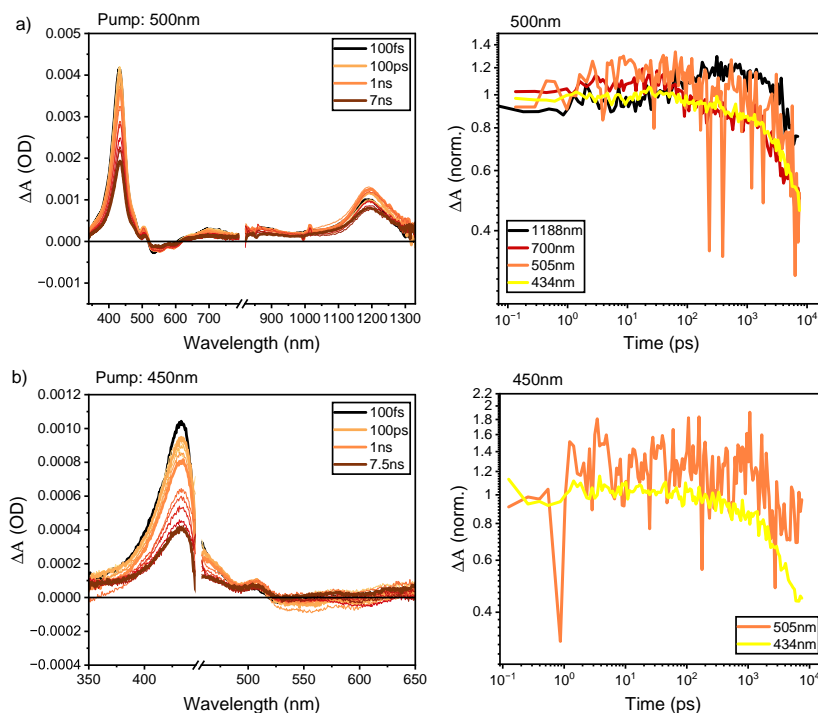


Figure B.8 – Excitation wavelength dependence of transient absorption spectroscopy for rubrene monomer Transient absorption spectra (left) and normalized dynamics of the main species (right) of rubrene in toluene solution at the excitation wavelength (a) 500 nm and (b) 450 nm, with an average pump power of 1 mW.

Figure B.8 presents transient absorption spectra of rubrene in toluene solution, excited at 500 nm (Fig B.8 a) and at 450 nm (Fig B.8 b). The TA spectra exhibit a photoinduced absorption band at 434 nm that decays mono-exponentially on a rapid timescale. This was attributed to the absorption of the excited singlet state ($S_1 \rightarrow S_N$).^{156,262} The small positive feature at 505 nm decays as singlets, indicating no triplet formation in this region. According to Yildiz (1968),²⁶¹ in rubrene solution, the intersystem crossing efficiency is less than 0.05, which requires specific sensitizers to obtain high triplet concentrations. As a result, the rubrene solution showed only singlet state absorption and no absorption in the triplet state. The broad PIA features at around 700 and 1188 nm exhibit kinetic decays

similar to the 434 nm band (Fig B.8 a), leading us to attribute them to $S_1 \rightarrow S_N$ transitions, as reported in Ref.³¹⁹ These findings provide conclusive evidence that the rubrene solution does not show any excitation wavelength dependency.

B.5 Diffusion-ordered spectroscopy nuclear magnetic resonance (DOSY-NMR) analysis

B.5.1 DiPhenyltetracene 7.2 mg in 0.6 ml of toluene

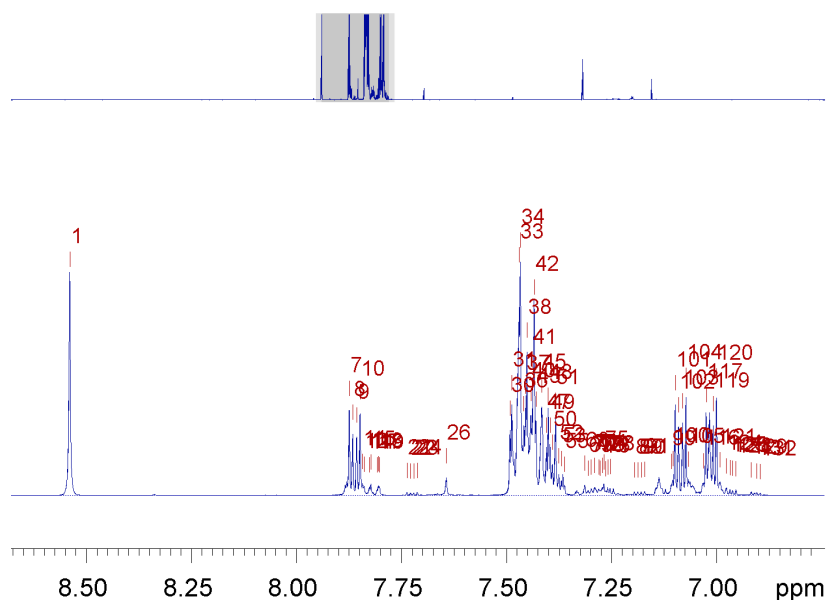


Figure B.9 – 2D diffusion ordered spectroscopy (DOSY) NMR spectra of 7.2 mg of DPT in 0.6 ml of toluene.

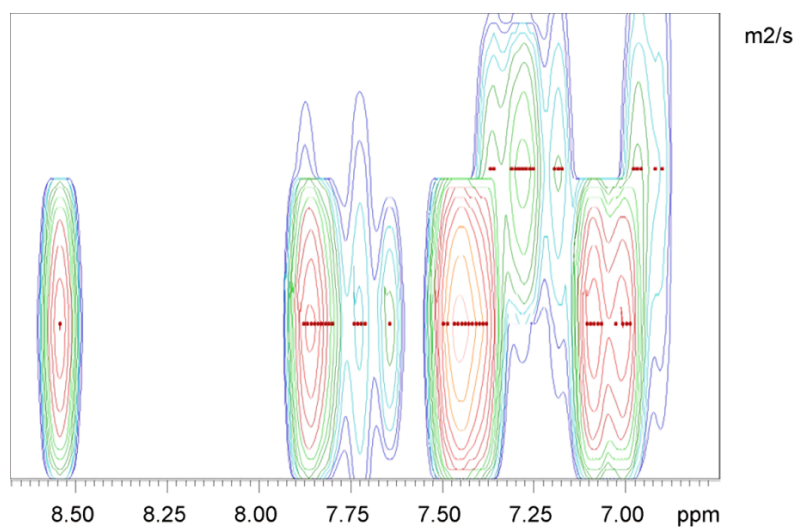


Figure B.10 – DOSY-NMR contour plot. Peak positions are represented by the red dots, showing where significant diffusion signals are detected.

Fitted function:	$f(x) = I_0 \cdot \exp(-D \cdot x^2 \cdot \gamma^2 \cdot \Delta^2 \cdot (\Delta_{\text{big}} - \Delta_{\text{small}}/3) \cdot 10^4)$
used gamma:	26752 rad/(s*Gauss)
used little delta:	0.0032000 s
used big delta:	0.039900 s
used gradient strength:	variable
Random error estimation of data:	RMS per spectrum (or trace/plane)
Systematic error estimation of data:	worst case per peak scenario
Fit parameter Error estimation method:	from fit using arbitrary y uncertainties
Confidence level:	95%
Used peaks:	automatically picked peaks
Used integrals:	peak intensities
Used Gradient strength:	all values (including replicates) used

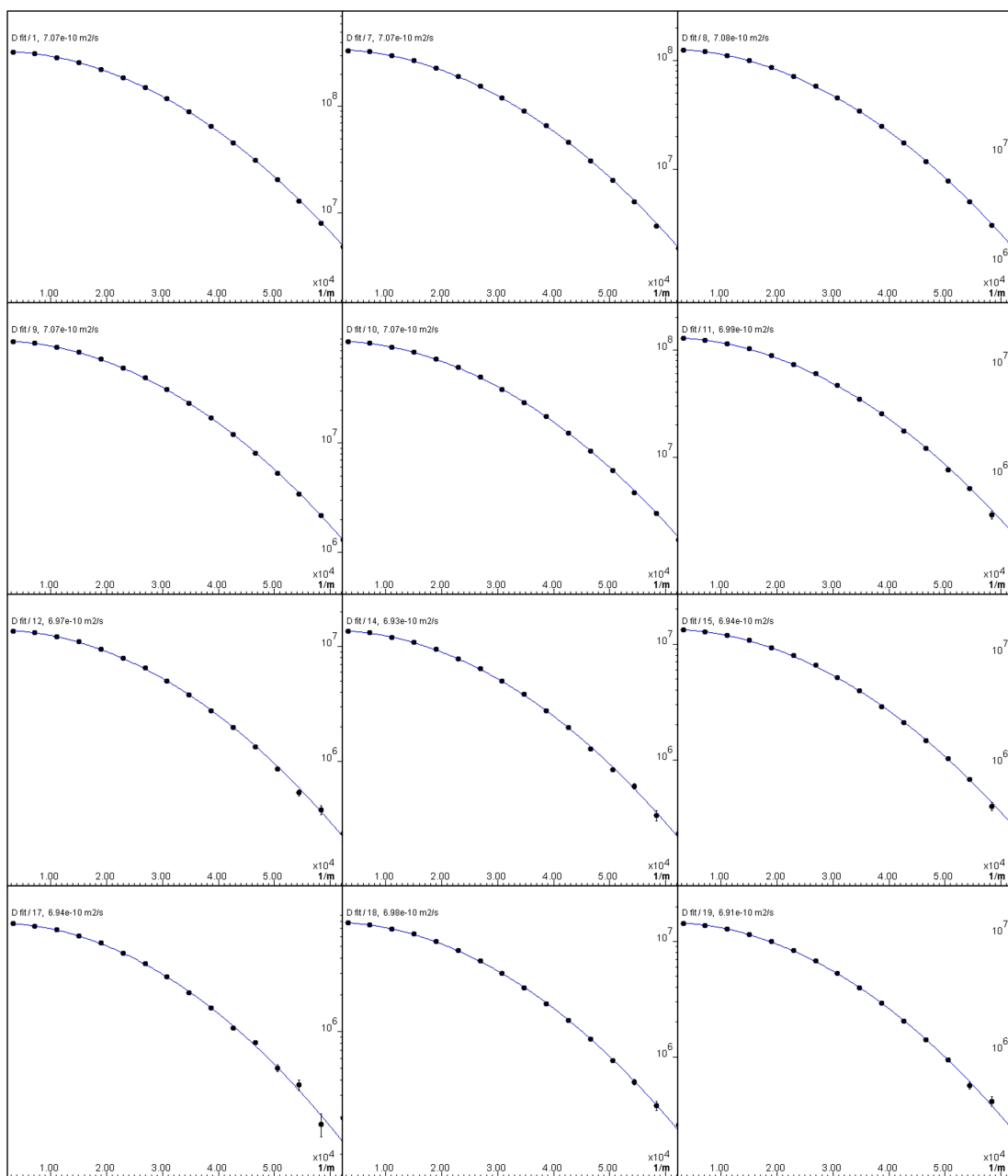


Figure B.11 – Non-linear fit of some diffusion peaks intensities.

B.5.2 DiPhenyltetracene 3.8 mg in 0.6 ml of toluene

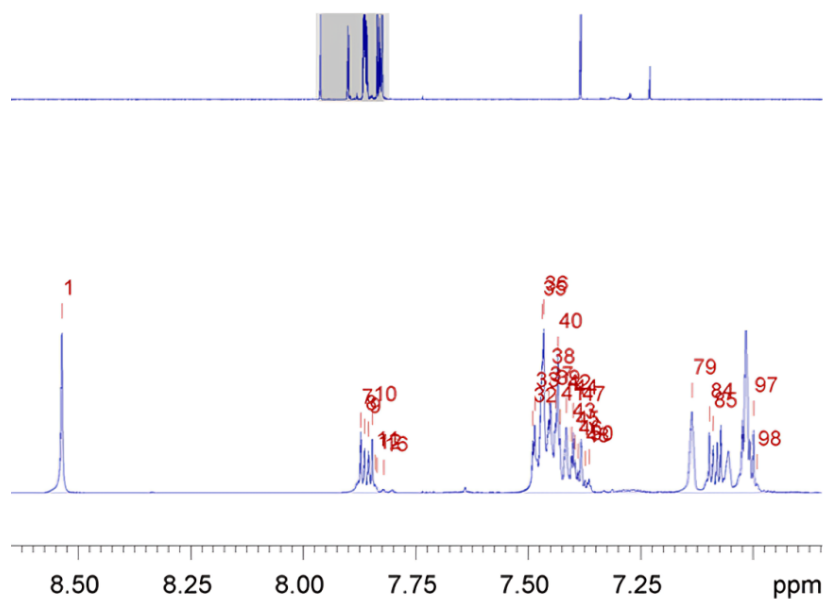


Figure B.12 – 2D diffusion ordered spectroscopy (DOSY) NMR spectra of 3.8 mg of DPT in 0.6 ml of toluene.

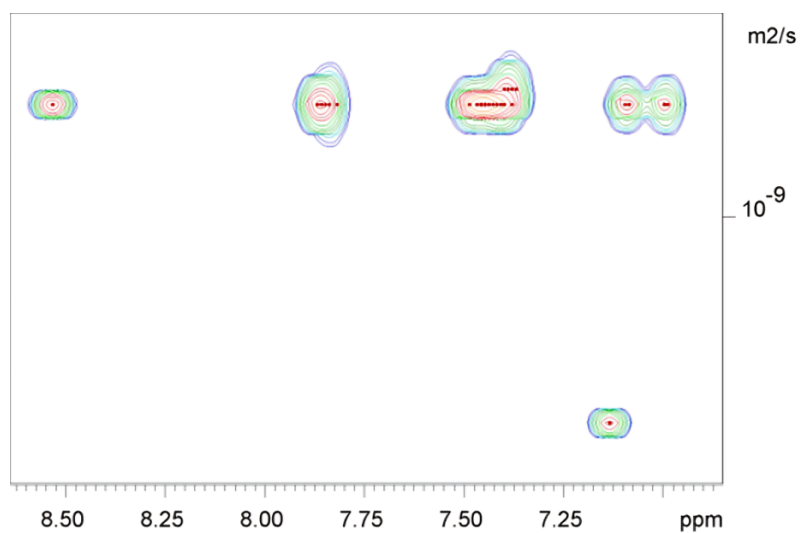


Figure B.13 – DOSY-NMR contour plot. Peak positions are represented by the red dots, showing where significant diffusion signals are detected.

Fitted function:	$f(x) = I_0 \cdot \exp(-D \cdot x^2 \cdot \gamma^2 \cdot \text{littleDelta}^2 / (\text{bigDelta} - \text{littleDelta}/3) \cdot 10^4)$
used gamma:	26752 rad/(s*Gauss)
used little delta:	0.0024000 s
used big delta:	0.039900 s
used gradient strength:	variable
Random error estimation of data:	RMS per spectrum (or trace/plane)
Systematic error estimation of data:	worst case per peak scenario
Fit parameter Error estimation method:	from fit using arbitrary y uncertainties
Confidence level:	95%
Used peaks:	automatically picked peaks
Used integrals:	peak intensities
Used Gradient strength:	all values (including replicates) used

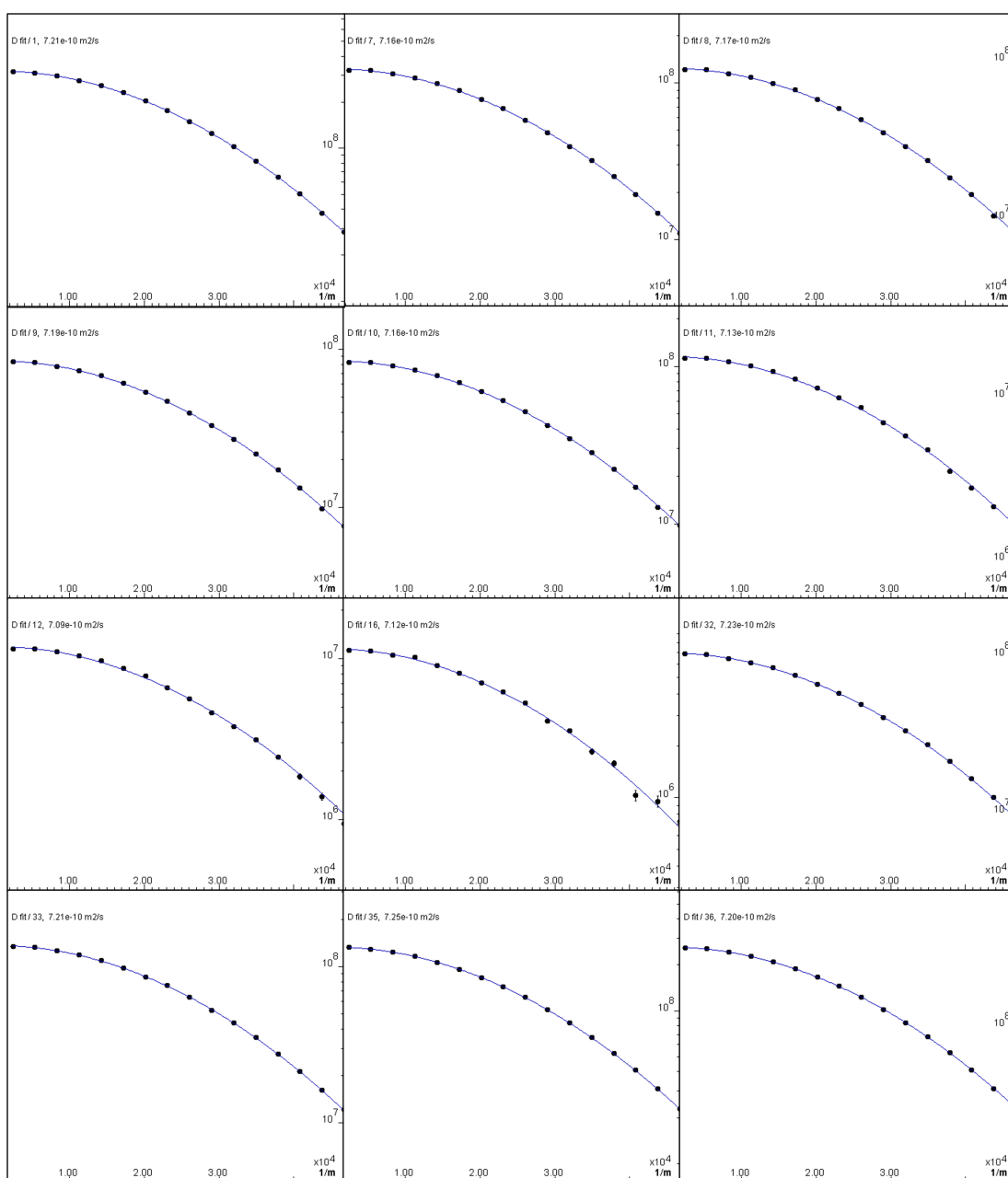


Figure B.14 – Non-linear fit of some diffusion peaks intensities.

B.5.3 DiPhenyltetracene 2.2 mg in 0.62 ml of CDCl_3

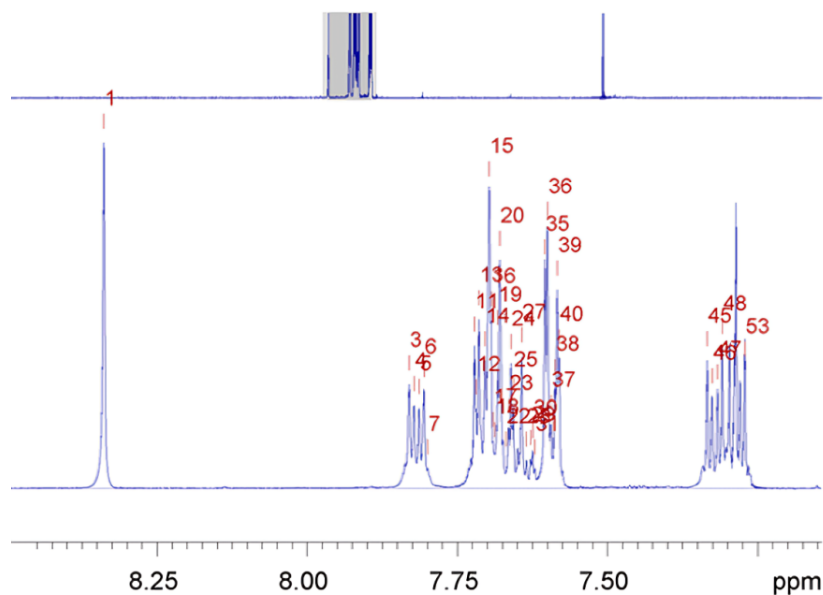


Figure B.15 – 2D diffusion ordered spectroscopy (DOSY) NMR spectra of 2.2 mg of DPT in 0.62 ml of CDCl_3 .

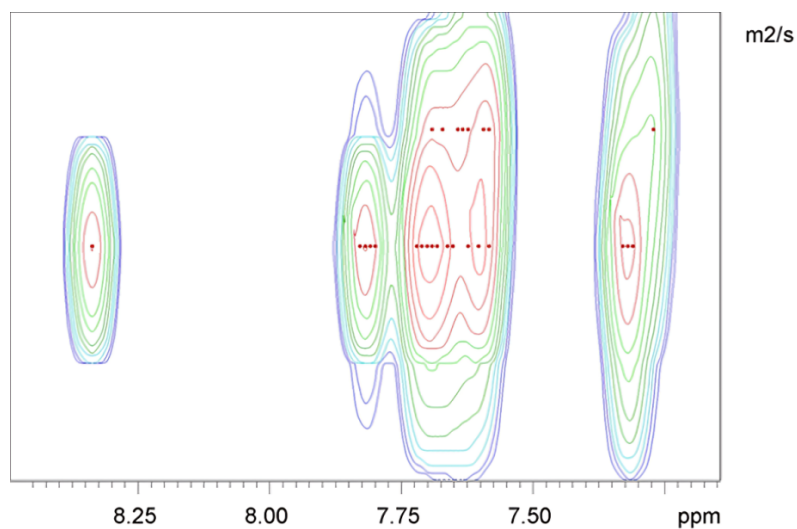


Figure B.16 – DOSY-NMR contour plot. Peak positions are represented by the red dots, showing where significant diffusion signals are detected.

Fitted function:	$f(x) = I_0 \cdot \exp(-D \cdot x^2 \cdot \gamma^2 \cdot \text{littleDelta}^2 / (\text{bigDelta} - \text{littleDelta}/3) \cdot 10^4)$
used gamma:	26752 rad/(s*Gauss)
used little delta:	0.0032000 s
used big delta:	0.039900 s
used gradient strength:	variable
Random error estimation of data:	RMS per spectrum (or trace/plane)
Systematic error estimation of data:	worst case per peak scenario
Fit parameter Error estimation method:	from fit using arbitrary y uncertainties
Confidence level:	95%
Used peaks:	automatically picked peaks
Used integrals:	peak intensities
Used Gradient strength:	all values (including replicates) used

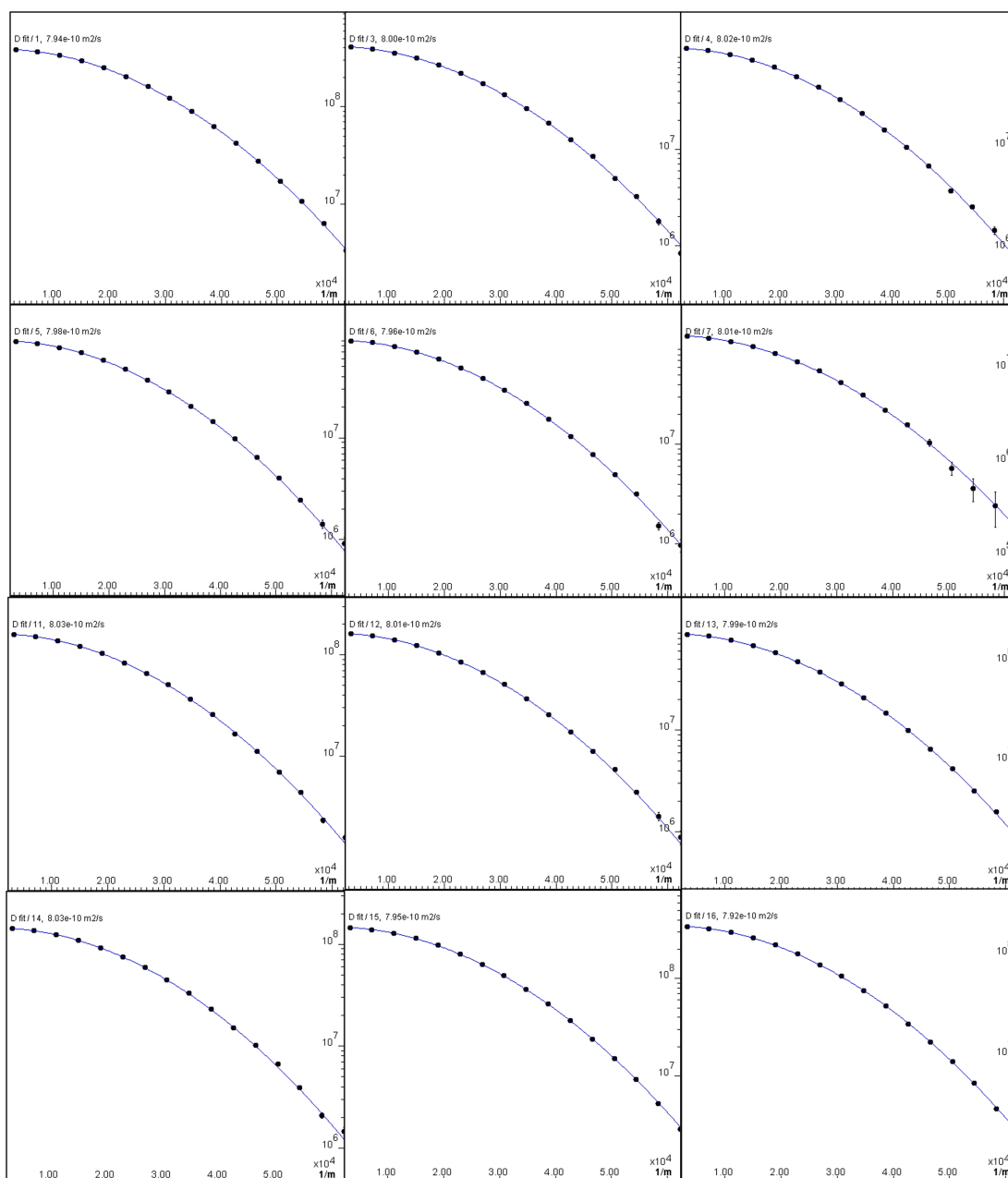


Figure B.17 – Non-linear fit of some diffusion peaks intensities.

B.5.4 DiPhenyltetracene 0.82 mg in 0.55 ml of toluene

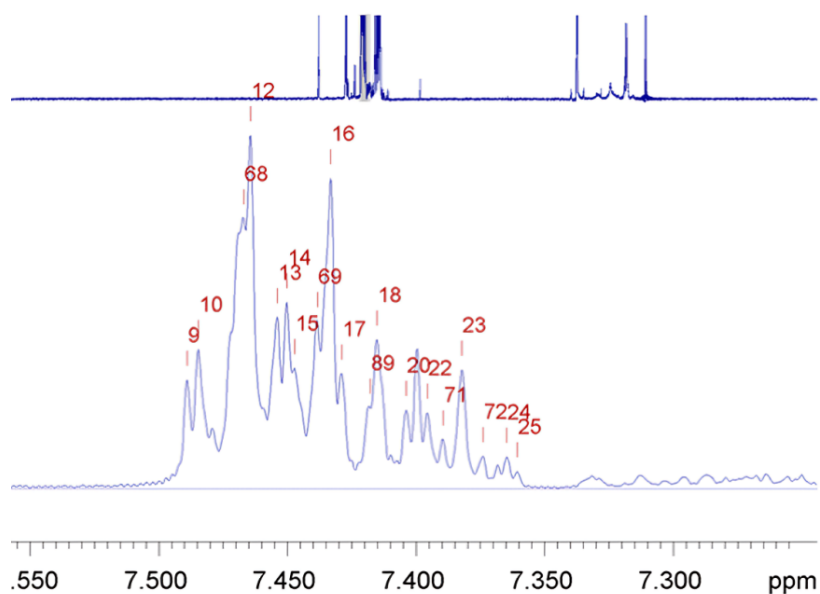


Figure B.18 – 2D diffusion ordered spectroscopy (DOSY) NMR spectra of 0.82 mg of DPT in 0.55 ml of toluene.

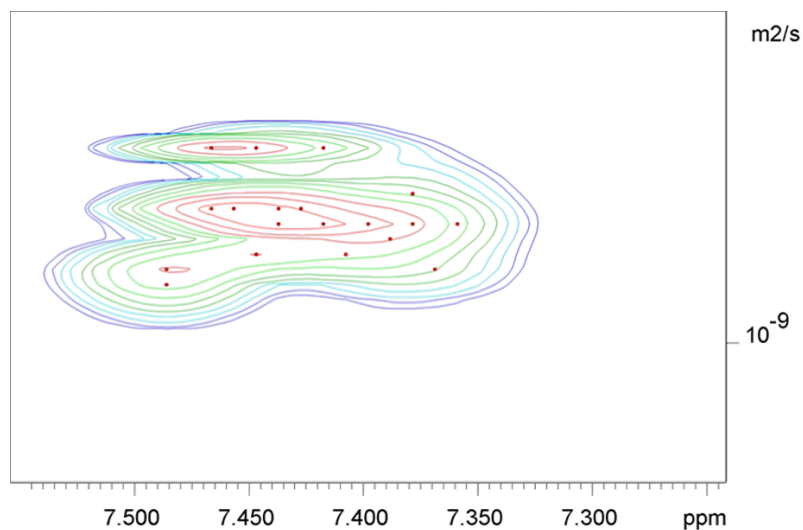


Figure B.19 – DOSY-NMR contour plot. Peak positions are represented by the red dots, showing where significant diffusion signals are detected.

Fitted function:	$f(x) = I_0 \cdot \exp(-D \cdot x^2 \cdot \gamma^2 \cdot \text{littleDelta}^2 \cdot (\text{bigDelta} - \text{littleDelta}/3) \cdot 10^4)$
used gamma:	26752 rad/(s*Gauss)
used little delta:	0.0024000 s
used big delta:	0.039900 s
used gradient strength:	variable
Random error estimation of data:	RMS per spectrum (or trace/plane)
Systematic error estimation of data:	worst case per peak scenario
Fit parameter Error estimation method:	from fit using arbitrary y uncertainties
Confidence level:	95%
Used peaks:	automatically picked peaks
Used integrals:	peak intensities
Used Gradient strength:	all values (including replicates) used

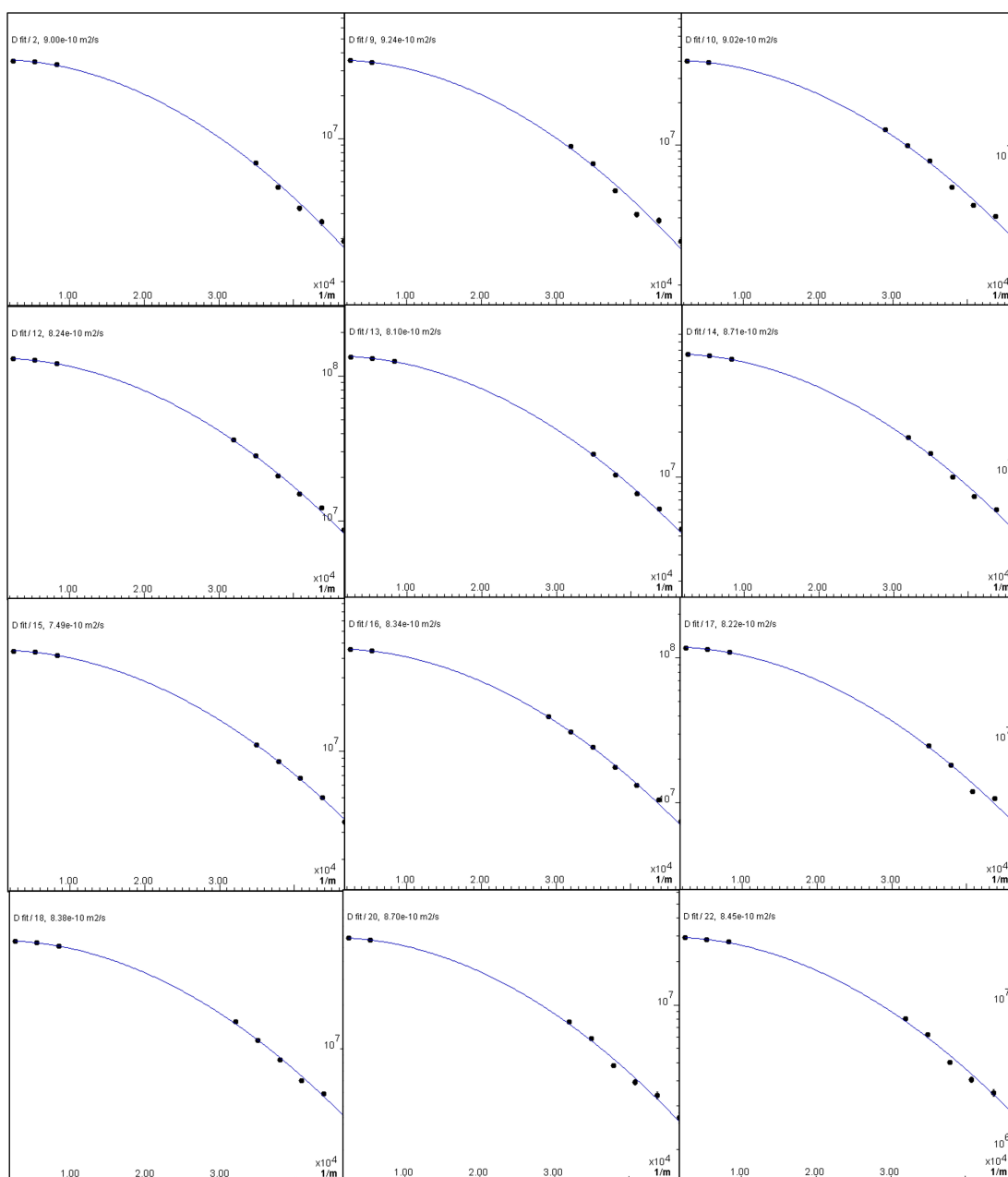


Figure B.20 – Non-linear fit of some diffusion peaks intensities.

B.5.5 Monomer-dimer fitting using Hill equation

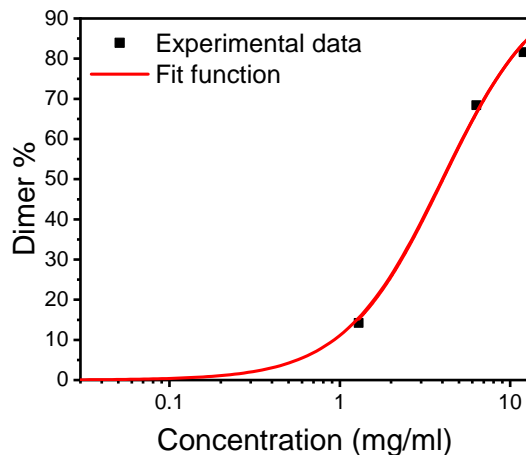


Figure B.21 – Diffusion-ordered spectroscopy nuclear magnetic resonance data analysis of DPT solution. The data demonstrate that reducing the concentration of the solution leads to a significant reduction in the dimer percentage, highlighting the concentration-dependent nature of dimer formation and molecular self-association behavior. The data is fitted using Hill-equation as described below.

The Hill equation was first introduced by Archibald V. Hill in 1910 to characterise the cooperative binding of oxygen to haemoglobin.^{275,320} Although it was originally developed for ligand–protein interactions, it has now been extensively used to describe many cooperative systems, including self-assembly processes such as dimerization and aggregation.^{274,275,321,322} This approach is useful when the mechanistic modeling is more difficult due to limited data, as in our case. The use of the Hill equation is therefore allowing for a quantitative analysis of the dimer formation trends in solution.

Here, we used the Hill equation to fit the experimental data presented in Figure B.21, which describes the concentration-dependent formation of dimers. The general Form of the Hill equation is^{275,276}

$$\theta = \frac{[L^n]}{K_d^n + [L^n]} \quad (\text{B.1})$$

Where, θ is the fraction of occupied binding sites (or, analogously, dimer fraction), $[L]$ is the ligand (or the solution concentration), K_d is the dissociation constant, and n is Hill coefficient. To express this in terms of percentage dimerization, the equation is scaled by 100

$$Dimer\% = \frac{[C^n]}{K^n + [C^n]} \times 100 \quad (B.2)$$

Where $[C]$ is the total concentration of the solution, K is the dissociation constant which corresponds to the concentration at which half the maximum dimer population is achieved,^{274,275} and n is the Hill coefficient, which reflects the degree of cooperativity ($n > 1$ in positively cooperative dimer formation).²⁷⁶ K and n are fitting parameters, equivalent to 4 mg/ml and 1.5, respectively, which fall within the expected range.

In the context of dimerization, where two identical units associate, the use of the Hill model provides a simplified description of the system's sigmoidal behavior. As shown in Figure B.21, the fitted curve matches the experimental data well.

Appendix C

Supplementary information for Chapter 7

C.1 General characterizations conducted at Kyushu University by collaborators

^1H NMR (400 MHz) spectra were measured on a Bruker Ascend NMR 400 MHz with TMS as the internal standard. High-resolution MS were measured on a JEOL JMS-700 at the Evaluation Center of Materials Properties and Function, Institute for Materials Chemistry and Engineering, Kyushu University. MALDI-TOF MS was measured on Bruker Auto lex max MALDI-TOF MS mass spectrometer. Elemental analysis was carried out using a Tanaco CHN Corder MT-5 at the Elemental Analysis Center, Kyushu University. Single crystal X-ray data were collected on a CCD diffractometer (Rigaku Saturn VariMax) with graphite-monochromate Mo K α radiation ($\lambda_{\text{ex}} = 0.7170 \text{ \AA}$). UV-vis absorption spectra were obtained on a JASCO V-780 spectrophotometer. Photoluminescence (PL) spectra were obtained using a JASCO FP-8300.

C.2 Crystallography

The crystallographic data and refinement for MPD-1 is shown in Table C.1. Crystal of suitable size was selected from the mother liquor and immersed in paratone oil and then mounted for data collection. Single crystal X-ray data for MPD-1 was collected at 150 K using a Rigaku Saturn VariMax CCD diffractometer with graphite-monochromatized Mo-K α radiation ($\lambda = 0.71069 \text{ \AA}$). The data integration and reduction were processed using CrysAlisPro 1.171.39.43c (Rigaku OD, 2018) software. The structure was solved by the direct method using SHELXT 2014/5 and was refined on F² by a full-matrix least-squares technique using the SHELXL-2018/3 program package. CCDC number 2315019 corresponds to MPD-1 reported in this manuscript and this data can be obtained free of charge from The Cambridge crystallographic Data Center via www.ccdc.cam.ac.uk/data_request/cif

Table C.1 – Crystal Data and Refinement Parameters for MPD-1

Identification code	MPD-1
Chemical formula	$C_{11.5}H_8Cl_{1.5}N_{0.5}$
Formula weight (g/mol)	206.36
Crystal Color	Purple
Crystal Size (mm)	$0.048 \times 0.04 \times 0.026$
Temperature (K)	150(2)
Crystal System	Triclinic
Space Group	$\bar{P}1$
a (Å)	9.9829(5)
b (Å)	11.0695(7)
c (Å)	18.0357(10)
α (°)	86.617(5)
β (°)	77.604(4)
γ (°)	81.837(4)
Z	8
V (Å ³)	1926.02(19)
Density (g/cm ³)	1.423
μ (mm ⁻¹)	0.484
$F(000)$	848
Reflections Collected	27496
Independent Reflections	9542
R_{int}	0.0604
Number of parameters	487
GOF on F^2	1.109
Final R_1/wR_2 ($I \geq 2\sigma(I)$)	0.392
Weighted R_1/wR_2 (all data)	0.466
CCDC number	2315019

C.3 MD simulations

All-atom MD simulations in this study were performed using the MD program GROMACS 2016.6. In the initial structure of the simulated system, a single molecule of MPD-1 from the SCXRD structure, optimized by DFT calculations mentioned below, was placed in the center of the cubic MD cell with 6 nm on a side and the remaining space was filled with 1200 toluene molecules. The generalized Amber force field³²³ parameters were used for the force field parameters in the present MD simulations. The atomic charges of both MPD-1 and toluene molecules were calculated using the restrained electrostatic potential (RESP)³²⁴ methodology based on DFT calculations (B3LYP/6-31G(d,p) with the GAUSSIAN 16 revision C01 program (Gaussian, Inc., Wallingford CT, 2016).

After the steepest energy minimization, the 5 ns pre-equilibration and the 500 ns equilibration runs were performed in sequence at 300 K, 250 K, 200 K, 150 K, and 80 K to realize the cooling process. For each temperature, the system reached the equilibration state after at least 100 ns. The pressure of all the systems was maintained at 1 bar. The temperature and pressure of the pre-equilibration runs were kept constant using the Berendsen thermostat and barostat³²⁵ with relaxation times of 0.2 and 2.0 ps, respectively. For the equilibration runs, the NoseHoover thermostat³²⁶ and the Parrinello-Rahman barostat³²⁷ with relaxation times of 1.0 and 5.0 ps, respectively, were selected for temperature and pressure coupling. All bonds connected to hydrogen atoms were constrained with LINCS³²⁸ algorithm. The time step of both pre-equilibration and equilibration was set to 2 fs. The long-range Coulomb interactions were calculated with the smooth particle-mesh Ewald method³²⁹ with a grid spacing of 0.30 nm. The real space cutoff for both Coulomb and van der Waals interactions was 1.2 nm.

The time dependence of the distance between the centers of the mass of the pentacene units of MPD-1 in the 500 ns equilibration run at 300 K was shown in Fig. 7.6c and its average value from 100 ns to 500 ns was 5.5 ± 0.7 Å. Two types of angles between the long axis vectors of the pentacene units in the plane

perpendicular and parallel to the aromatic ring planes, defined as θ and ϕ in Figs. 7.6 d and 7.6 e, respectively, were analyzed. The average values of these two angles during the 400 ns were 9 ± 9 degree and 8 ± 8 degree, respectively.

For the cooling process simulations, the time dependences of the distance between the centers of the mass of the pentacene units at 200 K and 80 K were analyzed as shown in Figure 7.7. At lower temperatures than the room temperature, the pentacene units were more stable and large fluctuations were not observed.

C.4 Steady-state absorption and fluorescence spectra of pentacene dimer and monomer in polystyrene film

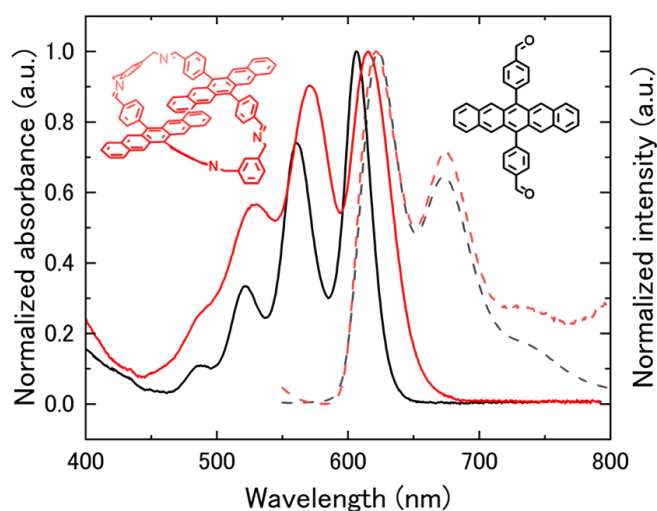


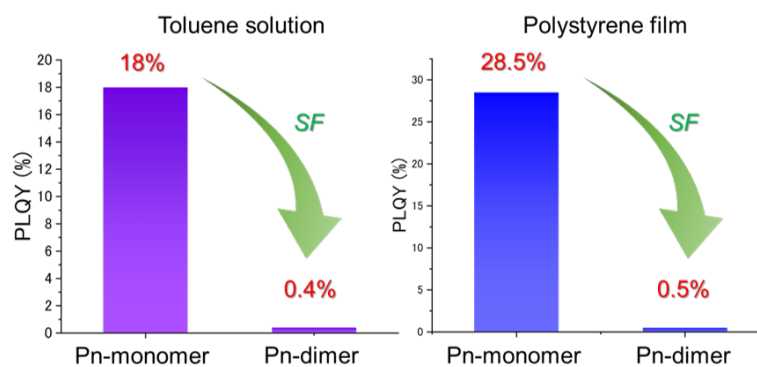
Figure C.1 – Absorption spectra (solid lines) and fluorescence spectra (dotted lines) of 0.05 mol% of the dimer MPD-1 (red lines) and 0.1 mol% of the monomer PDA (black lines) in polystyrene film at room temperature, respectively.

C.5 Photoluminescence quantum yield (PLQY)

Photoluminescence quantum yields of MPD-1 and PDA were measured in toluene solution and polystyrene film at room temperature. In both solution and film samples, PLQY of Pn-dimer was much lower than that of Pn-monomer, indicating highly efficient intramolecular SF occurs in MPD-1 in both toluene solution and polystyrene film.

Table C.2 – Photoluminescence Quantum Yields of MPD-1 and PDA in toluene solution (100 μ M) and polystyrene film (0.005 mol%) at room temperature.

Sample	PLQY (%)
MPD-1 in toluene	0.4
PDA in toluene	18
MPD-1 in polystyrene	0.5
PDA in polystyrene	28.5



C.6 Time-resolved CW-EPR and pulsed EPR measurements

Time-resolved EPR measurements were performed at room temperature using an X-band (9.682 GHz in the CW-EPR and 9.589 GHz in the pulsed EPR) CW/pulsed EPR spectrometer (ELEXSYS II E580) with a dielectric resonator using a quadrature detection. Samples were photoexcited by the second harmonics (532 nm) of a Nd:YAG laser (Continuum, Minilite II; full width at half maximum of about 5 ns). A laser depolarizer (SIGMA KOKI, DEQ 1N) was placed between the laser exit and the microwave cavity. The repetition rate and the pulse energy were 10 Hz and 1 mJ, respectively. The CW-TREPR experiments were performed using a transient mode in the Bruker Xepr software by using a home-written python script through the XeprAPI. The TREPR signals were amplified by a video amplifier for a digitizer of SpecJet-III. The TREPR data were smoothed for denoising using a binomial-weighted moving average to time course with a window of 200 ns for the spectra. The pulsed EPR measurements were performed by using PatternJet-II controlled by the Xepr program. Pulse sequences of the Hahn echo detection (laser- t_{delay} - $\pi/2$ - t_{echo} - π - t_{echo} -echo) was used in the pulsed EPR measurements. The power of microwave pulse was set to maximize the intensity of the spin echo signal of quintet transition ($Q_0 \leftrightarrow Q_{+1}$) observed in the CW-TREPR measurement. In this, the pulse durations were $\pi/2 = 10$ ns and $\pi = 20$ ns, respectively. In spin nutation measurements, pulse durations of $x = 0$ -440 ns and $t_2 = 20$ ns were used in place of the $\pi/2$ and π pulses.

Table C.3 – Parameters of quintet applied for computations of the CW-TREPR spectrum at room temperature.²¹⁵

	J /MHz	D /MHz a)	E /MHz a)	D_{ss} /MHz	Euler angles ^{b)} /degrees (α, β, γ)	Dipolar angles ^{c)} /degrees (θ, ϕ)	$\bar{\nu}_{\text{vib}}$ /cm ⁻¹	ΔE_{12} / cm ⁻¹ d)	$k_{\text{Rec}}/\text{s}^{-1}$ (Singlet recombination)
TT ₁	-2.0 $\times 10^5$	1200	-5	-240	$\alpha = 90$ $\beta = 180$ $\gamma = -90$	$\theta = 45$ $\phi = 90$	44	80	2×10^7
TT ₂	-7.0 $\times 10^4$	1200	-5	-240	$\alpha = 90$ $\beta = 170$ $\gamma = -90$	$\theta = 0$ $\phi = 90$			-

a) Zero-field splitting parameters in $\hat{H}_{\text{ZFS}} = D(S_z^2 - S(S+1)/3) + E(S_x^2 - S_y^2)$ for each triplet in multiexciton.

b) Conformation of the principal axes in \hat{H}_{ZFS} of the T_B component with respect to the principal axes of T_A component in the T_AT_B multiexciton with the x-convention.

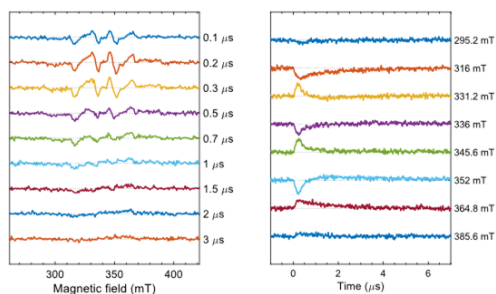
c) Direction for the T_B component was set by the polar angles (θ_2, ϕ_2) with respect to the (X₁, Y₁, Z₁) principal axes in T_A.

d) The energy gap between TT₁ and TT₂ states represented by $\Delta E_{12} = E(\text{TT}_2) - E(\text{TT}_1)$.

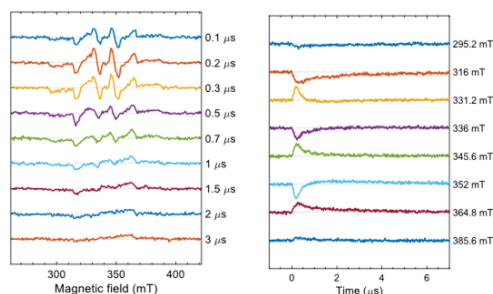
Table C.4 – Parameters of triplet applied for computations of the CW-TREPR spectrum at room temperature.

D /mT	E /mT	p_x	p_y	p_z
140	1.5	0.5	0.5	0

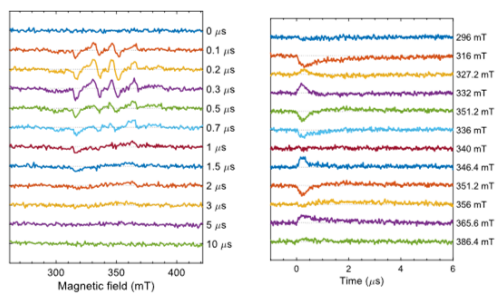
(a) 0.001 mol%



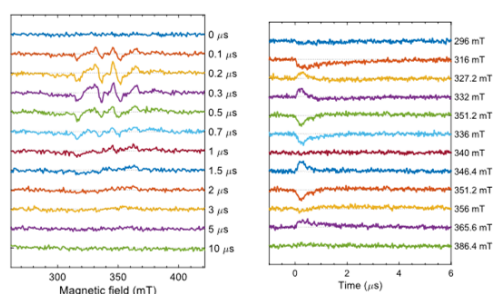
(b) 0.0025 mol%



(c) 0.005 mol%



(d) 0.01 mol%



(e) 0.05 mol%

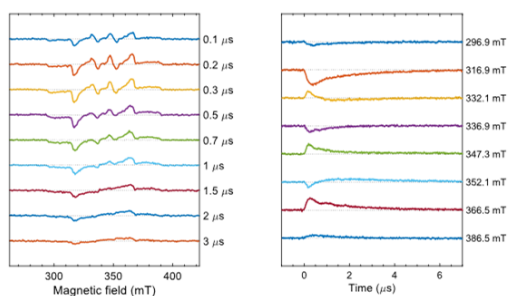


Figure C.2 – CW-TREPR spectrum of MPD-1 in polystyrene at room temperature on different concentrations ((a) 0.001 mol%, (b) 0.0025 mol%, (c) 0.005 mol%, (d) 0.01 mol%, (e) 0.05 mol%) with the microwave power of 4.7 mW.

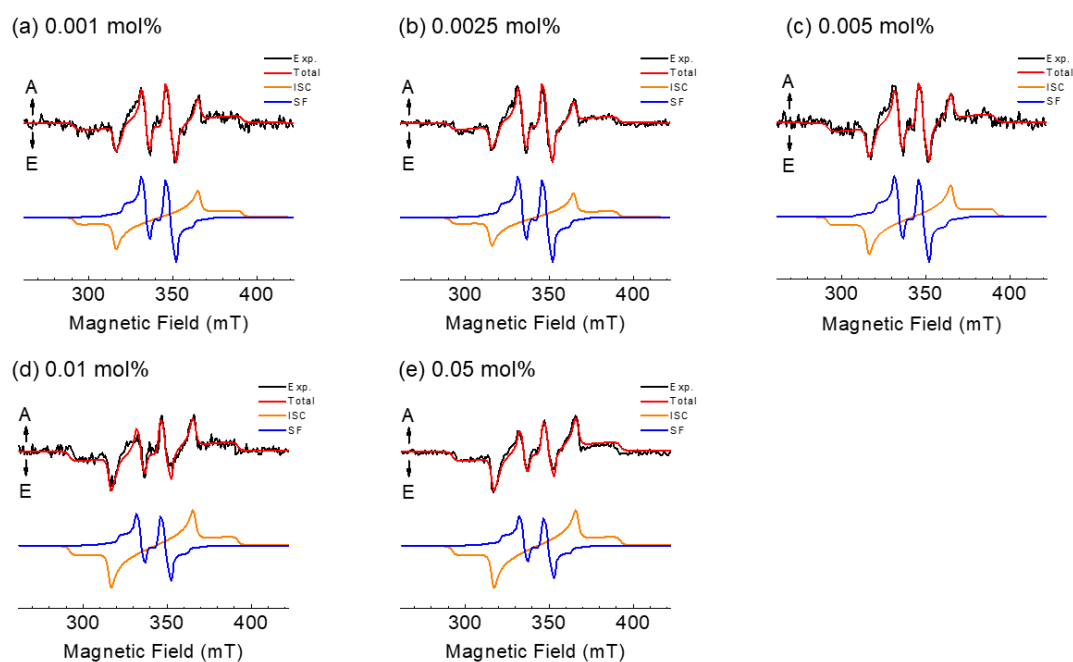


Figure C.3 – CW-TREPR spectrum simulation (200 ns) of MPD-1 in polystyrene at room temperature at different concentrations ((a) 0.001 mol%, (b) 0.0025 mol%, (c) 0.005 mol%, (d) 0.01 mol%, (e) 0.05 mol%)

Table C.5 – Ratios of the signal intensities of the quintet produced by singlet fission to the triplet produced by intersystem crossing in TREPR simulations.

	Quintet	Triplet
0.001 mol%	0.58	0.42
0.0025 mol%	0.61	0.39
0.005 mol%	0.54	0.46
0.01 mol%	0.49	0.51
0.05 mol%	0.44	0.56

C.7 Magnetic field effect measurement

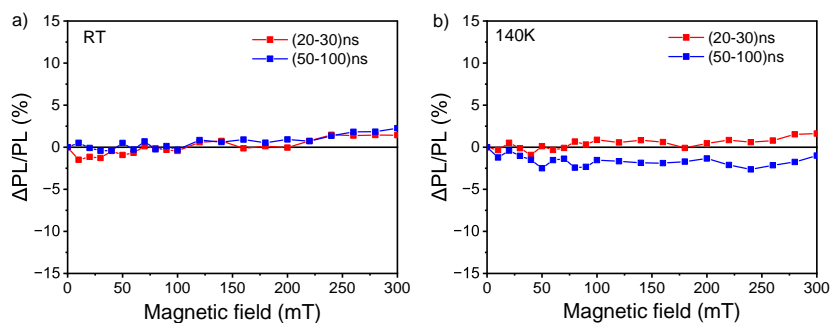


Figure C.4 – Magnetic field effects on photoluminescence for MPD-1 in polystyrene film measured at 532 nm across different delay times at (a) room temperature and (b) 140 K. $\Delta PL/PL(\%)$ is reported as a function of magnetic field strength. No MFE on the PL signal was observed because the PL intensity was very low due to the very low concentration of pentacene in polystyrene film. The weakened PL intensity likely limited the measurement's sensitivity, preventing any influences of the magnetic field.

References

- [1] M. H. Futscher, A. Rao, and B. Ehrler, ‘The potential of singlet fission photon multipliers as an alternative to silicon-based tandem solar cells’, *ACS Energy Letters* **3**, 2587–2592 (2018).
- [2] S. W. Tabernig, B. Daiber, T. Wang, and B. Ehrler, ‘Enhancing silicon solar cells with singlet fission: the case for Förster resonant energy transfer using a quantum dot intermediate’, *Journal of Photonics for Energy* **8**, 022008–022008 (2018).
- [3] B. Daiber, K. van den Hoven, M. H. Futscher, and B. Ehrler, ‘Realistic efficiency limits for singlet-fission silicon solar cells’, *ACS Energy Letters* **6**, 2800–2808 (2021).
- [4] A. Rao and R. H. Friend, ‘Harnessing singlet exciton fission to break the Shockley–Queisser limit’, *Nature Reviews Materials* **2**, 1–12 (2017).
- [5] B. Ehrler, ‘Singlet fission solar cells’, in *Emerging Strategies to Reduce Transmission and Thermalization Losses in Solar Cells* (Springer, 2022), pages 313–339.
- [6] B. Ehrler, M. W. Wilson, A. Rao, R. H. Friend, and N. C. Greenham, ‘Singlet exciton fission-sensitized infrared quantum dot solar cells’, *Nano Letters* **12**, 1053–1057 (2012).
- [7] B. Ehrler, E. Alarcón-Lladó, S. W. Tabernig, T. Veeken, E. C. Garnett, and A. Polman, *Photovoltaics reaching for the Shockley–Queisser limit*, 2020.

- [8] A. Polman, M. Knight, E. C. Garnett, B. Ehrler, and W. C. Sinke, ‘Photovoltaic materials: Present efficiencies and future challenges’, *Science* **352**, aad4424 (2016).
- [9] M. B. Smith and J. Michl, ‘Singlet fission’, *Chemical Reviews* **110**, 6891–6936 (2010).
- [10] D. Dexter, ‘Two ideas on energy transfer phenomena: Ion-pair effects involving the OH stretching mode, and sensitization of photovoltaic cells’, *Journal of Luminescence* **18**, 779–784 (1979).
- [11] Y. Jiang, M. P. Nielsen, A. J. Baldacchino, M. A. Green, D. R. McCamey, M. J. Tayebjee, T. W. Schmidt, and N. J. Ekins-Daukes, ‘Singlet fission and tandem solar cells reduce thermal degradation and enhance lifespan’, *Progress in Photovoltaics: Research and Applications* **29**, 899–906 (2021).
- [12] M. Hanna and A. Nozik, ‘Solar conversion efficiency of photovoltaic and photoelectrolysis cells with carrier multiplication absorbers’, *Journal of Applied Physics* **100**, 074510 (2006).
- [13] A. Rao and R. H. Friend, ‘Harnessing singlet exciton fission to break the Shockley–Queisser limit’, *Nature Reviews Materials* **2**, 1–12 (2017).
- [14] M. W. Wilson, A. Rao, B. Ehrler, and R. H. Friend, ‘Singlet exciton fission in polycrystalline pentacene: from photophysics toward devices’, *Accounts of Chemical Research* **46**, 1330–1338 (2013).
- [15] H. Liu, V. M. Nichols, L. Shen, S. Jahansou, Y. Chen, K. M. Hanson, C. J. Bardeen, and X. Li, ‘Synthesis and photophysical properties of a “face-to-face” stacked tetracene dimer’, *Physical Chemistry Chemical Physics* **17**, 6523–6531 (2015).
- [16] X. Tang, R. Pan, X. Zhao, H. Zhu, and Z. Xiong, ‘Achievement of High-Level Reverse Intersystem Crossing in Rubrene-Doped Organic Light-Emitting Diodes’, *The Journal of Physical Chemistry Letters* **11**, 2804–2811 (2020).

-
- [17] R. Nagata, H. Nakanotani, W. J. Potscavage Jr, and C. Adachi, ‘Exploiting singlet fission in organic light-emitting diodes’, *Advanced Materials* **30**, 1801484 (2018).
- [18] P. E. Teichen and J. D. Eaves, ‘Collective aspects of singlet fission in molecular crystals’, *The Journal of Chemical Physics* **143**, 044118 (2015).
- [19] C. J. Bardeen, ‘Time dependent correlations of entangled states with nondegenerate branches and possible experimental realization using singlet fission’, *The Journal of Chemical Physics* **151**, 124503 (2019).
- [20] K. E. Smyser and J. D. Eaves, ‘Singlet fission for quantum information and quantum computing: the parallel JDE model’, *Scientific Reports* **10**, 1–10 (2020).
- [21] M. Einzinger, T. Wu, J. F. Kompalla, H. L. Smith, C. F. Perkinson, L. Nienhaus, S. Wieghold, D. N. Congreve, A. Kahn, M. G. Bawendi, et al., ‘Sensitization of silicon by singlet exciton fission in tetracene’, *Nature* **571**, 90–94 (2019).
- [22] D. Y. Kondakov, ‘Triplet–triplet annihilation in highly efficient fluorescent organic light-emitting diodes: current state and future outlook’, *Philosophical Transactions of the Royal Society A: Mathematical, Physical and Engineering Sciences* **373**, 20140321 (2015).
- [23] Z. Yang, Z. Mao, Z. Xie, Y. Zhang, S. Liu, J. Zhao, J. Xu, Z. Chi, and M. P. Aldred, ‘Recent advances in organic thermally activated delayed fluorescence materials’, *Chemical Society Reviews* **46**, 915–1016 (2017).
- [24] J. Day, S. Senthilarasu, and T. K. Mallick, ‘Improving spectral modification for applications in solar cells: A review’, *Renewable Energy* **132**, 186–205 (2019).
- [25] M. J. Tayebjee, D. R. McCamey, and T. W. Schmidt, ‘Beyond Shockley–Queisser: molecular approaches to high-efficiency photovoltaics’, *The Journal of Physical Chemistry Letters* **6**, 2367–2378 (2015).

- [26] J. Zhou, Q. Liu, W. Feng, Y. Sun, and F. Li, ‘Upconversion luminescent materials: advances and applications’, *Chemical Reviews* **115**, 395–465 (2015).
- [27] W. Wang, Q. Liu, C. Zhan, A. Barhoumi, T. Yang, R. G. Wylie, P. A. Armstrong, and D. S. Kohane, ‘Efficient triplet–triplet annihilation-based upconversion for nanoparticle phototargeting’, *Nano Letters* **15**, 6332–6338 (2015).
- [28] Y. Sasaki, M. Oshikawa, P. Bharmoria, H. Kouno, A. Hayashi-Takagi, M. Sato, I. Ajioka, N. Yanai, and N. Kimizuka, ‘Near-infrared optogenetic genome engineering based on photon-upconversion hydrogels’, *Angewandte Chemie* **131**, 17991–17997 (2019).
- [29] R. Merrifield, P. Avakian, and R. Groff, ‘Fission of singlet excitons into pairs of triplet excitons in tetracene crystals’, *Chemical Physics Letters* **3**, 386–388 (1969).
- [30] R. C. Johnson, R. E. Merrifield, P. Avakian, and R. B. Flippen, ‘Effects of magnetic fields on the mutual annihilation of triplet excitons in molecular crystals’, *Phys. Rev. Lett.* **19**, 285–288 (1967).
- [31] R. Johnson and R. Merrifield, ‘Effects of magnetic fields on the mutual annihilation of triplet excitons in anthracene crystals’, *Phys. Rev. B* **1**, 896 (1970).
- [32] N. Geacintov, M. Pope, and F. Vogel, ‘Effect of magnetic field on the fluorescence of tetracene crystals: exciton fission’, *Physical Review Letters* **22**, 593 (1969).
- [33] R. Johnson, R. Merrifield, P. Avakian, and R. Flippen, ‘Effects of magnetic fields on the mutual annihilation of triplet excitons in molecular crystals’, *Physical Review Letters* **19**, 285 (1967).

-
- [34] W. Ishii, M. Fuki, E. M. B. Ali, S. Sato, B. Parmar, A. Yamauchi, C. H. Mulyadi, M. Uji, S. M. Rivero, G. Watanabe, et al., ‘A Macrocyclic Parallel Dimer Showing Quantum Coherence of Quintet Multiexcitons at Room Temperature’, (2024).
- [35] T. Wu, W. Ni, G. G. Gurzadyan, and L. Sun, ‘Singlet fission from upper excited singlet states and polaron formation in rubrene film’, *RSC Advances* **11**, 4639–4645 (2021).
- [36] M. B. Smith and J. Michl, ‘Recent advances in singlet fission’, *Annual Review of Physical Chemistry* **64**, 361–386 (2013).
- [37] D. G. Bossanyi, M. Matthiesen, S. Wang, J. A. Smith, R. C. Kilbride, J. D. Shipp, D. Chekulaev, E. Holland, J. E. Anthony, J. Zaumseil, A. J. Musser, and J. Clark, ‘Emissive spin-0 triplet-pairs are a direct product of triplet–triplet annihilation in pentacene single crystals and anthradithiophene films’, *Nature Chemistry* **13**, 163–171 (2021).
- [38] L. Wang, T. S. Zhang, L. Fu, S. Xie, Y. Wu, G. Cui, W. H. Fang, J. Yao, and H. Fu, ‘High-Lying 31Ag Dark-State-Mediated Singlet Fission’, *J. Am. Chem. Soc.* **143**, 5691–5697 (2021).
- [39] H. Kim and P. M. Zimmerman, ‘Coupled double triplet state in singlet fission’, *Phys. Chem. Chem. Phys.* **20**, 30083–30094 (2018).
- [40] R. Merrifield, ‘Magnetic effects on triplet exciton interactions’, *Pure and Applied Chemistry* **27**, 481–498 (1971).
- [41] R. Xu, C. Zhang, and M. Xiao, ‘Magnetic field effects on singlet fission dynamics’, *Trends in Chemistry* (2022).
- [42] J. J. Burdett, G. B. Piland, and C. J. Bardeen, ‘Magnetic field effects and the role of spin states in singlet fission’, *Chemical Physics Letters* **585**, 1–10 (2013).

- [43] T. Yago, K. Ishikawa, R. Katoh, and M. Wakasa, ‘Magnetic field effects on triplet pair generated by singlet fission in an organic crystal: Application of radical pair model to triplet pair’, *J. Phys. Chem. C* **120**, 27858–27870 (2016).
- [44] G. D. Scholes, ‘Correlated pair states formed by singlet fission and exciton–exciton annihilation’, *J. Phys. Chem. A* **119**, 12699–12705 (2015).
- [45] C. K. Yong, A. J. Musser, S. L. Bayliss, S. Lukman, H. Tamura, O. Bubnova, R. K. Hallani, A. Meneau, R. Resel, M. Maruyama, et al., ‘The entangled triplet pair state in acene and heteroacene materials’, *Nature Communications* **8**, 15953 (2017).
- [46] M. Lee, O.-K. Song, J.-C. Seo, D. Kim, Y. D. Suh, S. M. Jin, and S. K. Kim, ‘Low-lying electronically excited states of C60 and C70 and measurement of their picosecond transient absorption in solution’, *Chemical Physics Letters* **196**, 325–329 (1992).
- [47] R. Morales-Cueto, M. Esquivelzeta-Rabell, J. Saucedo-Zugazagoitia, and J. Peon, ‘Singlet excited-state dynamics of nitropolycyclic aromatic hydrocarbons: Direct measurements by femtosecond fluorescence up-conversion’, *The Journal of Physical Chemistry A* **111**, 552–557 (2007).
- [48] M. B. Smith and J. Michl, ‘Singlet fission’, *Chemical Reviews* **110**, 6891–6936 (2010).
- [49] J. J. Burdett and C. J. Bardeen, ‘Quantum beats in crystalline tetracene delayed fluorescence due to triplet pair coherences produced by direct singlet fission’, *Journal of the American Chemical Society* **134**, 8597–8607 (2012).
- [50] A. Köhler and H. Bässler, *Electronic processes in organic semiconductors: An introduction* (John Wiley & Sons, 2015).
- [51] A. Köhler and H. Bässler, ‘Triplet states in organic semiconductors’, *Materials Science and Engineering: R: Reports* **66**, 71–109 (2009).

-
- [52] A. J. Musser and J. Clark, ‘Triplet-Pair States in Organic Semiconductors’, *Annual Review of Physical Chemistry* **70**, 323–351 (2019).
- [53] P. W. Atkins and R. S. Friedman, *Molecular quantum mechanics* (Oxford University Press, USA, 2011).
- [54] S. Morab, M. M. Sundaram, and A. Pivrikas, ‘Review on charge carrier transport in inorganic and organic semiconductors’, *Coatings* **13**, 1657 (2023).
- [55] M. H. Boratto, ‘Semiconducting and Insulating oxides applied to electronic devices’, (2018).
- [56] J. Knoester and V. M. Agranovich, ‘Frenkel and charge-transfer excitons in organic solids’, *Thin Films and Nanostructures* **31**, 1–96 (2003).
- [57] M. Pope and C. E. Swenberg, *Electronic processes in organic crystals and polymers* (Oxford University Press, 1999).
- [58] A. Sugie, K. Nakano, K. Tajima, I. Osaka, and H. Yoshida, ‘Dependence of exciton binding energy on bandgap of organic semiconductors’, *The Journal of Physical Chemistry Letters* **14**, 11412–11420 (2023).
- [59] J. M. Brown, *Molecular Spectroscopy*, Oxford Chemistry Primers 55 (Oxford University Press, Oxford; New York, 1998).
- [60] W. Barford, *Electronic and optical properties of conjugated polymers*, Vol. 129 (OUP Oxford, 2013).
- [61] A. Köhler and D. Beljonne, ‘The singlet–triplet exchange energy in conjugated polymers’, *Advanced Functional Materials* **14**, 11–18 (2004).
- [62] A. Pazur, C. Schimek, and P. Galland, ‘Magnetoreception in microorganisms and fungi’, *Open Life Sciences* **2**, 597–659 (2007).
- [63] P. J. Hore and H. Mouritsen, ‘The radical-pair mechanism of magnetoreception’, *Annual Review of Biophysics* **45**, 299–344 (2016).

- [64] M. Zarea, R. Carmieli, M. A. Ratner, and M. R. Wasielewski, ‘Spin dynamics of radical pairs with restricted geometries and strong exchange coupling: The role of hyperfine coupling’, *The Journal of Physical Chemistry A* **118**, 4249–4255 (2014).
- [65] J. Lloyd and G. Pake, ‘Spin relaxation in free radical solutions exhibiting hyperfine structure’, *Physical Review* **94**, 579 (1954).
- [66] G. Mamin, F. Murzakhonov, I. Gracheva, M. Gafurov, and V. Soltamov, ‘Influence of Second-Order Effects due to Hyperfine Interaction on the Magnitude of the Larmor Frequency 14N’, *Applied Magnetic Resonance* **56**, 285–295 (2025).
- [67] J. M. Hollas, *Basic atomic and molecular spectroscopy*, Vol. 11 (Royal Society of Chemistry, 2002).
- [68] J. H. Denschlag, ‘Powered by symmetry’, *Nature* **448**, 422–423 (2007).
- [69] S. L. Bayliss, L. R. Weiss, A. Rao, R. H. Friend, A. D. Chepelianskii, and N. C. Greenham, ‘Spin signatures of exchange-coupled triplet pairs formed by singlet fission’, *Phys. Rev. B* **94**, 045204 (2016).
- [70] M. Pope and C. E. Swenberg, ‘Electronic processes in organic solids’, *Annual Review of Physical Chemistry* **35**, 613–655 (1984).
- [71] S. Richert, C. E. Tait, and C. R. Timmel, ‘Delocalisation of photoexcited triplet states probed by transient EPR and hyperfine spectroscopy’, *Journal of Magnetic Resonance* **280**, 103–116 (2017).
- [72] C. P. Poole, H. A. Farach, and W. K. Jackson, ‘Standardization of convention for zero field splitting parameters’, *Journal of Chemical Physics* **61**, 2220–2221 (1974).
- [73] S. Stoll and A. Schweiger, ‘EasySpin, a comprehensive software package for spectral simulation and analysis in EPR’, *Journal of Magnetic Resonance* **178**, 42–55 (2006).

-
- [74] C. Kollmar, ‘Electronic structure of diradical and dicarbene intermediates in short-chain polydiacetylene oligomers’, *The Journal of Chemical Physics* **98**, 7210–7228 (1993).
- [75] A. J. Musser, M. Maiuri, D. Brida, G. Cerullo, R. H. Friend, and J. Clark, ‘The nature of singlet exciton fission in carotenoid aggregates’, *Journal of the American Chemical Society* **137**, 5130–5139 (2015).
- [76] A. A. Bakulin, C. Silva, and E. Vella, ‘Ultrafast spectroscopy with photocurrent detection: watching excitonic optoelectronic systems at work’, *The Journal of Physical Chemistry Letters* **7**, 250–258 (2016).
- [77] S. L. Bayliss, L. R. Weiss, A. Mitioglu, K. Galkowski, Z. Yang, K. Yunusova, A. Surrente, K. J. Thorley, J. Behrends, R. Bittl, et al., ‘Site-selective measurement of coupled spin pairs in an organic semiconductor’, *Proceedings of the National Academy of Sciences* **115**, 5077–5082 (2018).
- [78] K. Yunusova, S. Bayliss, T. Chanelière, V. Derkach, J. Anthony, A. Chepelianskii, and L. Weiss, ‘Spin fine structure reveals biexciton geometry in an organic semiconductor’, *Physical Review Letters* **125**, 097402 (2020).
- [79] A. J. Musser and J. Clark, ‘Triplet-pair states in organic semiconductors’, *Annual Review of Physical Chemistry* **70**, 323–351 (2019).
- [80] H. L. Stern, A. J. Musser, S. Gelinas, P. Parkinson, L. M. Herz, M. J. Bruzek, J. Anthony, R. H. Friend, and B. J. Walker, ‘Identification of a triplet pair intermediate in singlet exciton fission in solution’, *Proceedings of the National Academy of Sciences* **112**, 7656–7661 (2015).
- [81] H. L. Stern, A. Cheminal, S. R. Yost, K. Broch, S. L. Bayliss, K. Chen, M. Tabachnyk, K. Thorley, N. Greenham, J. M. Hodgkiss, et al., ‘Vibronically coherent ultrafast triplet-pair formation and subsequent thermally activated dissociation control efficient endothermic singlet fission’, *Nature Chemistry* **9**, 1205–1212 (2017).

- [82] J. J. Burdett, D. Gosztola, and C. J. Bardeen, ‘The dependence of singlet exciton relaxation on excitation density and temperature in polycrystalline tetracene thin films: Kinetic evidence for a dark intermediate state and implications for singlet fission’, *The Journal of Chemical Physics* **135** (2011).
- [83] M. J. Tayebjee, R. G. Clady, and T. W. Schmidt, ‘The exciton dynamics in tetracene thin films’, *Physical Chemistry Chemical Physics* **15**, 14797–14805 (2013).
- [84] D. G. Bossanyi, M. Matthiesen, S. Wang, J. A. Smith, R. C. Kilbride, J. D. Shipp, D. Chekulaev, E. Holland, J. E. Anthony, J. Zaumseil, et al., ‘Emissive spin-0 triplet-pairs are a direct product of triplet–triplet annihilation in pentacene single crystals and anthradithiophene films’, *Nature Chemistry* **13**, 163–171 (2021).
- [85] H. L. Stern, A. Cheminal, S. R. Yost, K. Broch, S. L. Bayliss, K. Chen, M. Tabachnyk, K. Thorley, N. Greenham, J. M. Hodgkiss, J. Anthony, M. Head-Gordon, A. J. Musser, A. Rao, and R. H. Friend, ‘Vibronically coherent ultrafast triplet-pair formation and subsequent thermally activated dissociation control efficient endothermic singlet fission’, *Nature Chemistry* **9**, 1205–1212 (2017).
- [86] C. K. Yong, A. J. Musser, S. L. Bayliss, S. Lukman, H. Tamura, O. Bubnova, R. K. Hallani, A. Meneau, R. Resel, and M. Maruyama, ‘The entangled triplet pair state in acene and heteroacene materials’, *Nature Comm.* **8**, 15953 (2017).
- [87] E. J. Taffet, D. Beljonne, and G. D. Scholes, ‘Overlap-driven splitting of triplet pairs in singlet fission’, *Journal of the American Chemical Society* **142**, 20040–20047 (2020).
- [88] J. Walton, ‘Modulated Magnetic Field Effects, Molecular Design, and Indigoids: A Mechanistic Study of Singlet Fission’, PhD thesis (University of Cambridge, 2024).

-
- [89] D. G. Bossanyi, Y. Sasaki, S. Wang, D. Chekulaev, N. Kimizuka, N. Yanai, and J. Clark, ‘Spin statistics for triplet–triplet annihilation upconversion: Exchange coupling, intermolecular orientation, and reverse intersystem crossing’, *JACS Au* **1**, 2188–2201 (2021).
- [90] D. Bossanyi, ‘Triplet-pair states in exciton fission and fusion’, PhD thesis (University of Sheffield, 2022).
- [91] F. Wilkinson and A. Abdel-Shafi, ‘Mechanism of quenching of triplet states by oxygen: Biphenyl derivatives in acetonitrile’, *The Journal of Physical Chemistry A* **101**, 5509–5516 (1997).
- [92] L. R. Weiss, S. L. Bayliss, F. Kraffert, K. J. Thorley, J. E. Anthony, R. Bittl, R. H. Friend, A. Rao, N. C. Greenham, and J. Behrends, ‘Strongly exchange-coupled triplet pairs in an organic semiconductor’, *Nature Physics* **13**, 176–181 (2017).
- [93] Y.-J. Chen, M. Hoffmann, B. Zimmermann, G. Bihlmayer, S. Blügel, C. M. Schneider, and C. Tusche, ‘Quantum spin mixing in Dirac materials’, *Communications Physics* **4**, 179 (2021).
- [94] L. Kan, F. Zhao, J. Zhang, J. Hu, Y. Xie, J. Li, X. Zhu, X. Ma, H. Yu, J. Li, et al., ‘Coherent spin mixing at charge transfer states for spin polaron pair dissociation and energy loss in organic bulk heterojunction solar cells’, *Communications Physics* **8**, 47 (2025).
- [95] T. Miura, K. Maeda, and T. Arai, ‘The spin mixing process of a radical pair in low magnetic field observed by transient absorption detected nanosecond pulsed magnetic field effect’, *The Journal of Physical Chemistry A* **110**, 4151–4156 (2006).
- [96] J. M. Shaw, R. Knut, A. Armstrong, S. Bhandary, Y. Kvashnin, D. Thonig, E. K. Delczeg-Czirjak, O. Karis, T. Silva, E. Weschke, et al., ‘Quantifying spin-mixed states in ferromagnets’, *Physical Review Letters* **127**, 207201 (2021).

- [97] M. Glazov and E. Ivchenko, ‘Effect of electron-electron interaction on spin relaxation of charge carriers in semiconductors’, *Journal of Experimental and Theoretical Physics* **99**, 1279–1290 (2004).
- [98] Z. Wang, C. Zhang, R. Wang, G. Wang, X. Wang, and M. Xiao, ‘Weakly coupled triplet pair states probed by quantum beating in delayed fluorescence in tetracene crystals’, *J. Chem. Phys.* **151** (2019).
- [99] M. Chabr, U. Wild, J. Fünfschilling, and I. Zschokke-Gränacher, ‘Quantum beats of prompt fluorescence in tetracene crystals’, *Chemical Physics* **57**, 425–430 (1981).
- [100] R. Holzinger, N. S. Bassler, H. Ritsch, and C. Genes, ‘Scaling Law for Kasha’s Rule in Photoexcited Molecular Aggregates’, *The Journal of Physical Chemistry A* **128**, 3910–3915 (2024).
- [101] J. R. Lakowicz and B. R. Masters, ‘Principles of fluorescence spectroscopy’, *Journal of Biomedical Optics* **13**, 029901 (2008).
- [102] S. Karabunarliev, M. Baumgarten, E. R. Bittner, and K. Müllen, ‘Rigorous Franck–Condon absorption and emission spectra of conjugated oligomers from quantum chemistry’, *The Journal of Chemical Physics* **113**, 11372–11381 (2000).
- [103] J. Hermann, R. A. DiStasio Jr, and A. Tkatchenko, ‘First-principles models for van der Waals interactions in molecules and materials: Concepts, theory, and applications’, *Chemical Reviews* **117**, 4714–4758 (2017).
- [104] F. C. Spano, ‘The spectral signatures of Frenkel polarons in H-and J-aggregates’, *Accounts of Chemical Research* **43**, 429–439 (2010).
- [105] F. C. Spano and C. Silva, ‘H-and J-aggregate behavior in polymeric semiconductors’, *Annual Review of Physical Chemistry* **65**, 477–500 (2014).
- [106] A. S. Klymchenko, ‘Emerging field of self-assembled fluorescent organic dye nanoparticles’, *J. Nanosci. Lett* **3**, 21 (2013).

-
- [107] A. Stoneham, ‘Non-radiative transitions in semiconductors’, *Reports on Progress in Physics* **44**, 1251 (1981).
- [108] L. Shen, B. Xie, Z. Li, L. Liu, G. Cui, and W.-H. Fang, ‘Role of multistate intersections in photochemistry’, *The Journal of Physical Chemistry Letters* **11**, 8490–8501 (2020).
- [109] Y. Boeije and M. Olivucci, ‘From a one-mode to a multi-mode understanding of conical intersection mediated ultrafast organic photochemical reactions’, *Chemical Society Reviews* **52**, 2643–2687 (2023).
- [110] D. Beljonne, Z. Shuai, G. Pourtois, and J. Bredas, ‘Spin-orbit coupling and intersystem crossing in conjugated polymers: a configuration interaction description’, *The Journal of Physical Chemistry A* **105**, 3899–3907 (2001).
- [111] M. El-Sayed, ‘Spin—orbit coupling and the radiationless processes in nitrogen heterocyclics’, *The Journal of Chemical Physics* **38**, 2834–2838 (1963).
- [112] M. A. El-Sayed, ‘Triplet state. Its radiative and nonradiative properties’, *Accounts of Chemical Research* **1**, 8–16 (1968).
- [113] T. J. Penfold, E. Gindensperger, C. Daniel, and C. M. Marian, ‘Spin-vibronic mechanism for intersystem crossing’, *Chemical Reviews* **118**, 6975–7025 (2018).
- [114] C. M. Marian, ‘Spin-orbit coupling and intersystem crossing in molecules’, *Wiley Interdisciplinary Reviews: Computational Molecular Science* **2**, 187–203 (2012).
- [115] A. C. Albrecht, ‘Vibronic—Spin-Orbit Perturbations and the Assignment of the Lowest Triplet State of Benzene’, *The Journal of Chemical Physics* **38**, 354–365 (1963).
- [116] F. Tanaka, M. Okamoto, and S. Hirayama, ‘Pressure and temperature dependences of the rate constant for S1-T2 intersystem crossing of anthracene compounds in solution’, *The Journal of Physical Chemistry* **99**, 525–530 (1995).

- [117] W. Stacy and C. Swenberg, ‘Temperature dependence of intersystem crossing in crystalline anthracene’, *The Journal of Chemical Physics* **52**, 1962–1965 (1970).
- [118] R. Kellogg, ‘Second triplet state of anthracene’, *The Journal of Chemical Physics* **44**, 411–412 (1966).
- [119] G. J. Hedley, A. Ruseckas, and I. D. Samuel, ‘Light harvesting for organic photovoltaics’, *Chemical Reviews* **117**, 796–837 (2017).
- [120] O. V. Mikhnenko, P. W. Blom, and T.-Q. Nguyen, ‘Exciton diffusion in organic semiconductors’, *Energy & Environmental Science* **8**, 1867–1888 (2015).
- [121] P. Bharmoria, H. Bildirir, and K. Moth-Poulsen, ‘Triplet–triplet annihilation based near infrared to visible molecular photon upconversion’, *Chemical Society Reviews* **49**, 6529–6554 (2020).
- [122] S. Liu, X. Wang, H. Liu, L. Shen, D. Zhao, and X. Li, ‘Enhancing triplet sensitization ability of donor–acceptor dyads via intramolecular triplet energy transfer’, *Journal of Materials Chemistry C* **8**, 3536–3544 (2020).
- [123] Y. Huang, I. A. Buyanova, C. Phansa, M. E. Sandoval-Salinas, D. Casanova, W. K. Myers, N. C. Greenham, A. Rao, W. M. Chen, and Y. Puttisong, ‘Competition between triplet pair formation and excimer-like recombination controls singlet fission yield’, *Cell Reports Physical Science* **2** (2021).
- [124] C. B. Dover, J. K. Gallaher, L. Frazer, P. C. Tapping, A. J. Petty, M. J. Crossley, J. E. Anthony, T. W. Kee, and T. W. Schmidt, ‘Endothermic singlet fission is hindered by excimer formation’, *Nature Chemistry* **10**, 305–310 (2018).
- [125] J. J. Burdett, G. B. Piland, and C. J. Bardeen, ‘Magnetic field effects and the role of spin states in singlet fission’, *Chem. Phys. Lett.* **585**, 1–10 (2013).

-
- [126] X. Qiao and D. Ma, *Nonlinear optoelectronic processes in organic optoelectronic devices: Triplet-triplet annihilation and singlet fission*, 2021.
- [127] S. Singh, W. Jones, W. Siebrand, B. Stoicheff, and W. Schneider, ‘Laser generation of excitons and fluorescence in anthracene crystals’, *The Journal of Chemical Physics* **42**, 330–342 (1965).
- [128] R. Groff, P. Avakian, and R. Merrifield, ‘Coexistence of exciton fission and fusion in tetracene crystals’, *Physical Review B* **1**, 815 (1970).
- [129] R. E. Merrifield, P. Avakian, and R. P. Groff, ‘Fission of singlet excitons into pairs of triplet excitons in tetracene crystals’, *Chem. Phys. Lett.* **3**, 386–388 (1969).
- [130] M. I. Collins, D. R. McCamey, and M. J. Tayebjee, ‘Fluctuating exchange interactions enable quintet multiexciton formation in singlet fission’, *The Journal of Chemical Physics* **151** (2019).
- [131] M. I. Collins, F. Campaioli, M. J. Tayebjee, J. H. Cole, and D. R. McCamey, ‘Quintet formation, exchange fluctuations, and the role of stochastic resonance in singlet fission’, *Communications Physics* **6**, 64 (2023).
- [132] N. Monahan and X.-Y. Zhu, ‘Charge transfer-mediated singlet fission’, *Annual Review of Physical Chemistry* **66**, 601–618 (2015).
- [133] J. C. Johnson, A. J. Nozik, and J. Michl, ‘The role of chromophore coupling in singlet fission’, *Accounts of Chemical Research* **46**, 1290–1299 (2013).
- [134] D. a. Howe, T. J. Millar, S. Uniforme, a. Goddard, I. R. Sims, I. W. M. Smith, K. M. Hickson, N. Daugey, P. Caubet, M. Costes, E. a. Bergin, C. J. Lada, D. W. a. Stewart, C. F. Williams, D. C. Clary, P. Honvault, P. Halvick, C. Xie, D. Xie, H. Guo, R. Dynamics, a. Lagana, G. Lendvay, D. H. Zhang, a. F. J. Wagner, J. J. Schwab, and J. G. Anderson, ‘Observing the Multiexciton State in’, *Science*, 1541–1545 (2011).

- [135] P. M. Zimmerman, Z. Zhang, and C. B. Musgrave, ‘Singlet fission in pentacene through multi-exciton quantum states’, *Nature Chemistry* **2**, 648–652 (2010).
- [136] N. Nagaya, K. Lee, C. F. Perkinson, A. Li, Y. Lee, X. Zhong, S. Lee, L. P. Weisburn, T. K. Baikie, M. G. Bawendi, et al., ‘Exciton Fission Enhanced Silicon Solar Cell’, *ArXiv Preprint ArXiv:2407.21093* (2024).
- [137] P. C. Tapping and D. M. Huang, ‘Comment on “magnetic field effects on singlet fission and fluorescence decay dynamics in amorphous rubrene”’, *The Journal of Physical Chemistry C* **120**, 25151–25157 (2016).
- [138] R. Forecast, E. M. Gholizadeh, S. K. Prasad, S. Blacket, P. C. Tapping, D. R. McCamey, M. J. Tayebjee, D. M. Huang, J. H. Cole, and T. W. Schmidt, ‘Power Dependence of the Magnetic Field Effect on Triplet Fusion: A Quantitative Model’, *J. Phys. Chem. Lett.* **14**, 4742–4747 (2023).
- [139] J. Feng, P. Hosseinabadi, D. M. de Clercq, B. P. Carwithen, M. P. Nielsen, M. W. Brett, S. K. Prasad, A. A. Farahani, H. L. Li, S. N. Sanders, et al., ‘Magnetic fields reveal signatures of triplet-pair multi-exciton photoluminescence in singlet fission’, *Nature Chemistry*, 1–7 (2024).
- [140] Y. Pan, J. Huang, Z. Wang, D. Yu, B. Yang, and Y. Ma, ‘Computational investigation on the large energy gap between the triplet excited-states in acenes’, *RSC Advances* **7**, 26697–26703 (2017).
- [141] M. Wakasa, M. Kaise, T. Yago, R. Katoh, Y. Wakikawa, and T. Ikoma, ‘What can be learned from magnetic field effects on singlet fission: Role of exchange interaction in excited triplet pairs’, *The Journal of Physical Chemistry C* **119**, 25840–25844 (2015).
- [142] M. W. Wilson, A. Rao, J. Clark, R. S. S. Kumar, D. Brida, G. Cerullo, and R. H. Friend, ‘Ultrafast dynamics of exciton fission in polycrystalline pentacene’, *Journal of the American Chemical Society* **133**, 11830–11833 (2011).

-
- [143] A. R. Reddy and M. Bendikov, ‘Diels–Alder reaction of acenes with singlet and triplet oxygen—theoretical study of two-state reactivity’, *Chemical Communications*, 1179–1181 (2006).
- [144] S. S. Zade, N. Zamoshchik, A. R. Reddy, G. Fridman-Marueli, D. Sheberla, and M. Bendikov, ‘Products and mechanism of acene dimerization. A computational study’, *Journal of the American Chemical Society* **133**, 10803–10816 (2011).
- [145] C. Swenberg and W. Stacy, ‘Bimolecular radiationless transitions in crystalline tetracene’, *Chemical Physics Letters* **2**, 327–328 (1968).
- [146] J. Burgos, M. Pope, C. E. Swenberg, and R. Alfano, ‘Heterofission in pentacene-doped tetracene single crystals’, *Phys. Status Solidi B* **83**, 249–256 (1977).
- [147] M. W. Wilson, A. Rao, K. Johnson, S. Gélinas, R. Di Pietro, J. Clark, and R. H. Friend, ‘Temperature-independent singlet exciton fission in tetracene’, *Journal of the American Chemical Society* **135**, 16680–16688 (2013).
- [148] R. K. Hallani, K. J. Thorley, Y. Mei, S. R. Parkin, O. D. Jurchescu, and J. E. Anthony, ‘Structural and electronic properties of crystalline, isomerically pure anthradithiophene derivatives’, *Advanced Functional Materials* **26**, 2341–2348 (2016).
- [149] S. Subramanian, S. K. Park, S. R. Parkin, V. Podzorov, T. N. Jackson, and J. E. Anthony, ‘Chromophore fluorination enhances crystallization and stability of soluble anthradithiophene semiconductors’, *Journal of the American Chemical Society* **130**, 2706–2707 (2008).
- [150] C. K. Yong, A. J. Musser, S. L. Bayliss, S. Lukman, H. Tamura, O. Bubnova, R. K. Hallani, A. Meneau, R. Resel, M. Maruyama, et al., ‘The entangled triplet pair state in acene and heteroacene materials’, *Nature Communications* **8**, 1–12 (2017).

- [151] S. J. Rowan, S. J. Cantrill, G. R. Cousins, J. K. Sanders, and J. F. Stoddart, 'Dynamic covalent chemistry', *Angewandte Chemie International Edition* **41**, 898–952 (2002).
- [152] Y. Jin, C. Yu, R. J. Denman, and W. Zhang, 'Recent advances in dynamic covalent chemistry', *Chemical Society Reviews* **42**, 6634–6654 (2013).
- [153] N. J. Thompson, E. Hontz, W. Chang, T. Van Voorhis, and M. Baldo, 'Magnetic field dependence of singlet fission in solutions of diphenyl tetracene', *Philosophical Transactions of the Royal Society A: Mathematical, Physical and Engineering Sciences* **373**, 20140323 (2015).
- [154] M. R. Eric et al., 'Efficient Singlet Fission Discovered in a Disordered Acene Film', (2012).
- [155] V. C. Sundar, J. Zaumseil, V. Podzorov, E. Menard, R. L. Willett, T. Someya, M. E. Gershenson, and J. A. Rogers, 'Elastomeric transistor stamps: reversible probing of charge transport in organic crystals', *Science* **303**, 1644–1646 (2004).
- [156] L. Ma, K. Zhang, C. Kloc, H. Sun, M. E. Michel-Beyerle, and G. G. Gurzadyan, 'Singlet fission in rubrene single crystal: direct observation by femtosecond pump–probe spectroscopy', *Physical Chemistry Chemical Physics* **14**, 8307–8312 (2012).
- [157] I. Biaggio and P. Irkhin, 'Extremely efficient exciton fission and fusion and its dominant contribution to the photoluminescence yield in rubrene single crystals', *Applied Physics Letters* **103** (2013).
- [158] G. Ashiotis, A. Deschildre, Z. Nawaz, J. P. Wright, D. Karkoulis, F. E. Picca, and J. Kieffer, 'The fast azimuthal integration Python library: pyFAI', *Journal of Applied Crystallography* **48**, 510–519 (2015).
- [159] D. Agrawal, A. Pathan, P. Bhatt, B. Dave, and N. Bora, 'A Portable Experimental set-up for AFM to work at cryogenic temperature', in National Conference on Recent Trends in Engineering & Technology (2011), pages 1–4.

-
- [160] D. Necas, ‘Gwyddion: an open-source software for SPM data analysis’, *Cent Eur J Phys* **10**, 181 (2012).
- [161] R. Berera, R. van Grondelle, and J. T. Kennis, ‘Ultrafast transient absorption spectroscopy: principles and application to photosynthetic systems’, *Photosynthesis Research* **101**, 105–118 (2009).
- [162] Y. Tamai, Y. Murata, S.-i. Natsuda, and Y. Sakamoto, ‘How to interpret transient absorption data?: an overview of case studies for application to organic solar cells’, *Advanced Energy Materials* **14**, 2301890 (2024).
- [163] S. Weber, ‘Transient epr’, *EPR Spectroscopy: Fundamentals and Methods* **195** (2018).
- [164] C. E. Tait, M. D. Krzyaniak, and S. Stoll, ‘Computational tools for the simulation and analysis of spin-polarized EPR spectra’, *J. Magn. Reson.* **349**, 107410–1–16 (2023).
- [165] S. Stoll, G. Jeschke, M. Willer, and A. Schweiger, ‘Nutation-frequency correlated EPR spectroscopy: the PEANUT experiment’, *Journal of Magnetic Resonance* **130**, 86–96 (1998).
- [166] R. M. Jacobberger, Y. Qiu, M. L. Williams, M. D. Krzyaniak, and M. R. Wasielewski, ‘Using molecular design to enhance the coherence time of quintet multiexcitons generated by singlet fission in single crystals’, *Journal of the American Chemical Society* **144**, 2276–2283 (2022).
- [167] E. M. Bu Ali, A. Bertran, G. Moise, S. Wang, R. C. Kilbride, J. E. Anthony, C. E. Tait, and J. Clark, ‘Intersystem crossing outcompetes triplet-pair separation from 1 (TT) below 270 K in anthradithiophene films’, *Journal of the American Chemical Society* (2025).
- [168] R. R. Tykwinski and D. M. Guldi, ‘Singlet Fission’, *ChemPhotoChem* **5**, 392 (2021).

- [169] M. C. Hanna and A. J. Nozik, ‘Solar conversion efficiency of photovoltaic and photoelectrolysis cells with carrier multiplication absorbers’, *Journal of Applied Physics* **100**, [10.1063/1.2356795](#) (2006).
- [170] M. W. B. Wilson, A. Rao, B. Ehrler, and R. H. Friend, ‘Singlet exciton fission in polycrystalline pentacene: from photophysics toward devices’, *Accounts of Chemical Research* **46**, 1330–1338 (2013).
- [171] B. Ehrler, ‘Singlet fission solar cells’, *Emerging Strategies to Reduce Transmission and Thermalization Losses in Solar Cells: Redefining the Limits of Solar Power Conversion Efficiency*, 313–339 (2022).
- [172] M. J. Y. Tayebjee, A. A. Gray-Weale, and T. W. Schmidt, ‘Thermodynamic limit of exciton fission solar cell efficiency’, *J. Phys. Chem. Lett.* **3**, 2749–2754 (2012).
- [173] M. J. Y. Tayebjee, D. R. McCamey, and T. W. Schmidt, ‘Beyond Shockley-Queisser: Molecular Approaches to High-Efficiency Photovoltaics’, *J. Phys. Chem. Lett.* **6**, 5 (2015).
- [174] P. Bharmoria, H. Bildirir, and K. Moth-Poulsen, ‘Triplet-triplet annihilation based near infrared to visible molecular photon upconversion’, *Chemical Society Reviews* **49**, 6529–6554 (2020).
- [175] S. N. Sanders, T. H. Schloemer, M. K. Gangishetty, D. Anderson, M. Seitz, A. O. Gallegos, R. C. Stokes, and D. N. Congreve, ‘Triplet fusion upconversion nanocapsules for volumetric 3D printing’, *Nature* **604**, 474–478 (2022).
- [176] M. J. Tayebjee, S. N. Sanders, E. Kumarasamy, L. M. Campos, M. Y. Sfeir, and D. R. McCamey, ‘Quintet multiexciton dynamics in singlet fission’, *Nature Physics* **13**, 182–188 (2017).
- [177] A. Neef, S. Beaulieu, S. Hammer, S. Dong, J. Maklar, T. Pincelli, R. P. Xian, M. Wolf, L. Rettig, J. Pflaum, et al., ‘Orbital-resolved observation of singlet fission’, *Nature* **616**, 275–279 (2023).

-
- [178] M. Wakasa, T. Yago, Y. Sonoda, and R. Katoh, ‘Structure and dynamics of triplet-exciton pairs generated from singlet fission studied via magnetic field effects’, *Communications Chemistry* **1**, 9 (2018).
- [179] G. B. Piland, J. J. Burdett, D. Kurunthu, and C. J. Bardeen, ‘Magnetic field effects on singlet fission and fluorescence decay dynamics in amorphous rubrene’, *J. Phys. Chem. C* **117**, 1224–1236 (2013).
- [180] B. S. Basel, J. Zirzmeier, C. Hetzer, B. T. Phelan, M. D. Krzyaniak, S. R. Reddy, P. B. Coto, N. E. Horwitz, R. M. Young, F. J. White, F. Hampel, T. Clark, M. Thoss, R. R. Tykwinski, M. R. Wasielewski, and D. M. Guldi, ‘Unified model for singlet fission within a non-conjugated covalent pentacene dimer’, *Nat. Commun.* **8**, 15171–1–8 (2017).
- [181] B. S. Basel, J. Zirzmeier, C. Hetzer, S. R. Reddy, B. T. Phelan, M. D. Krzyaniak, M. K. Volland, P. B. Coto, R. M. Young, T. Clark, M. Thoss, R. R. Tykwinski, M. R. Wasielewski, and D. M. Guldi, ‘Evidence for Charge-Transfer Mediation in the Primary Events of Singlet Fission in a Weakly Coupled Pentacene Dimer Evidence for Charge-Transfer Mediation in the Primary Events of Singlet Fission in a Weakly Coupled Pentacene Dimer’, *Chem* **4**, 1092–1111 (2018).
- [182] S. Matsuda, S. Oyama, and Y. Kobori, ‘Electron spin polarization generated by transport of singlet and quintet multiexcitons to spin-correlated triplet pairs during singlet fissions’, *Chem. Sci.* **11**, 2934–2942 (2020).
- [183] Y. Kobori, M. Fuki, S. Nakamura, and T. Hasobe, ‘Geometries and terahertz motions driving quintet multiexcitons and ultimate triplet-triplet dissociations via the intramolecular singlet fissions’, *J. Phys. Chem. B* **124**, 9411–9419 (2020).
- [184] Y. Kawashima, T. Hamachi, A. Yamauchi, K. Nishimura, Y. Nakashima, S. Fujiwara, N. Kimizuka, T. Ryu, T. Tamura, M. Saigo, K. Onda, S. Sato, Y. Kobori, K. Tateishi, T. Uesaka, G. Watanabe, K. Miyata, and

- N. Yanai, ‘Singlet fission as a polarized spin generator for dynamic nuclear polarization’, *Nat. Commun.* **14**, 1056–1–12 (2023).
- [185] K. Majumder, S. Mukherjee, N. A. Panjwani, J. Lee, R. Bittl, W. Kim, S. Patil, and A. J. Musser, ‘Controlling Intramolecular Singlet Fission Dynamics via Torsional Modulation of Through-Bond versus Through-Space Couplings’, *J. Am. Chem. Soc.* **145**, 20883–20896 (2023).
- [186] S. Bayliss, L. Weiss, F. Krafft, D. Granger, J. Anthony, J. Behrends, and R. Bittl, ‘Probing the wave function and dynamics of the quintet multiexciton state with coherent control in a singlet fission material’, *Physical Review X* **10**, 021070 (2020).
- [187] M. Chen, M. D. Krzyaniak, J. N. Nelson, Y. J. Bae, S. M. Harvey, R. D. Schaller, R. M. Young, and M. R. Wasielewski, ‘Quintet-triplet mixing determines the fate of the multiexciton state produced by singlet fission in a terrylenediimide dimer at room temperature’, *Proc. Natl. Acad. Sci.* **116**, 8178–8183 (2019).
- [188] Y. J. Bae, X. Zhao, M. D. Kryzaniak, H. Nagashima, J. Strzalka, Q. Zhang, and M. R. Wasielewski, ‘Spin dynamics of quintet and triplet states resulting from singlet fission in oriented terrylenediimide and quaterrylenediimide films’, *J. Phys. Chem. C* **124**, 9822–9833 (2020).
- [189] B. K. Rugg, K. E. Smyser, B. Fluegel, C. H. Chang, K. J. Thorley, S. Parkin, J. E. Anthony, J. D. Eaves, and J. C. Johnson, ‘Triplet-pair spin signatures from macroscopically aligned heteroacenes in an oriented single crystal’, *Proc. Natl. Acad. Sci.* **119**, e2201879119–1–10 (2022).
- [190] G. He, K. R. Parenti, P. J. Budden, J. Niklas, T. Macdonald, E. Kumarasamy, X. Chen, X. Yin, D. R. McCamey, O. G. Poluektov, L. M. Campos, and M. Y. Sfeir, ‘Unraveling Triplet Formation Mechanisms in Acenothiophene Chromophores’, *J. Am. Chem. Soc.* **145**, 22058–22068 (2023).

-
- [191] K. E. S. W. Ilson and C. Y. Athy, ‘Broadband single-shot transient absorption spectroscopy’, **28**, 11339–11355 (2020).
- [192] N. Hofeditz, J. Hausch, K. Broch, W. Heimbrod, F. Schreiber, and M. Gerhard, ‘Efficient Energy Transfer and Singlet Fission in Co-Deposited Thin Films of Pentacene and Anthradithiophene’, *Advanced Materials Interfaces*, 2300922 (2024).
- [193] I. Nasrallah, M. K. Ravva, K. Broch, J. Novak, J. Armitage, G. Schweicher, A. Sadhanala, J. E. Anthony, J.-L. Bredas, and H. Sirringhaus, ‘A Novel Mitigation Mechanism for Photo-Induced Trapping in an Anthradithiophene Derivative Using Additives’, *Advanced Electronic Materials* **6**, 2000250 (2020).
- [194] N. Nishimura, J. R. Allardice, J. Xiao, Q. Gu, V. Gray, and A. Rao, ‘Photon upconversion utilizing energy beyond the band gap of crystalline silicon with a hybrid TES-ADT/PbS quantum dots system’, *Chemical Science* **10**, 4750–4760 (2019).
- [195] S. Subramanian, S. K. Park, S. R. Parkin, V. Podzorov, T. N. Jackson, and J. E. Anthony, ‘Chromophore fluorination enhances crystallization and stability of soluble anthradithiophene semiconductors’, *J. Am. Chem. Soc.* **130**, 2706–2707 (2008).
- [196] G. Mayonado, K. T. Vogt, J. D. Van Schenck, L. Zhu, G. Fregoso, J. Anthony, O. Ostroverkhova, and M. W. Graham, ‘High-symmetry anthradithiophene molecular packing motifs promote thermally activated singlet fission’, *The Journal of Physical Chemistry C* **126**, 4433–4445 (2022).
- [197] Z. Jagoo, Z. A. Lamport, O. D. Jurchescu, and L. E. McNeil, ‘Efficiency enhancement of organic thin-film phototransistors due to photoassisted charge injection’, *Applied Physics Letters* **119**, 10 . 1063 / 5 . 0047570 (2021).

- [198] D. A. Anthéunis, J. Schmidt, and J. H. van der Waals, ‘Spin-forbidden radiationless processes in isoelectronic molecules: Anthracene, acridine and phenazine’, *Mol. Phys.* **27**, 1521–1541 (1974).
- [199] R. H. Clarke and H. A. Frank, ‘Triplet state radiationless transitions in polycyclic hydrocarbons’, *J. Chem. Phys.* **65**, 39–47 (1976).
- [200] T. Okamoto, S. Izawa, M. Hiramoto, and Y. Kobori, ‘Efficient Spin Interconversion by Molecular Conformation Dynamics of a Triplet Pair for Photon Up-Conversion in an Amorphous Solid’, *J. Phys. Chem. Lett.* **15**, 2966–2975 (2024).
- [201] S. K. Wong, D. A. Hutchinson, and J. K. S. Wan, ‘Chemically induced dynamic electron polarization. II. A general theory for radicals produced by photochemical reactions of excited triplet carbonyl compounds’, *J. Chem. Phys.* **58**, 985–989 (1973).
- [202] K. M. Salikhov, ‘Mechanism of the Electron Spin Polarization of Excited Triplet States Caused by the Mutual Annihilation of Triplet States’, *Appl. Magn. Reson.* **26**, 135–144 (2004).
- [203] C. Corvaja, L. Franco, K. Salikhov, and V. Voronkova, ‘The first observation of electron spin polarization in the excited triplet states caused by the triplet-triplet annihilation’, *Appl. Magn. Reson.* **28**, 181–193 (2005).
- [204] B. R. Nielsen, A. Mortensen, K. Jørgensen, and L. H. Skibsted, ‘Singlet versus triplet reactivity in photodegradation of C40 carotenoids’, *Journal of Agricultural and Food Chemistry* **44**, 2106–2113 (1996).
- [205] M. Andrzejak and P. Petelenz, ‘Vibronic relaxation energies of acene-related molecules upon excitation or ionization’, *Physical Chemistry Chemical Physics* **20**, 14061–14071 (2018).
- [206] B. Hajgató, D. Szieberth, P. Geerlings, F. De Proft, and M. Deleuze, ‘A benchmark theoretical study of the electronic ground state and of the singlet-triplet split of benzene and linear acenes’, *The Journal of Chemical Physics* **131** (2009).

-
- [207] S. L. Bayliss, F. Kraffert, R. Wang, C. Zhang, R. Bittl, and J. Behrends, ‘Tuning spin dynamics in crystalline tetracene’, *J. Phys. Chem. Lett.* **10**, 1908–1913 (2019).
- [208] Y. Jue Bae, M. D. Krzyaniak, M. B. Majewski, M. Desroches, J.-F. Morin, Y.-L. Wu, and M. R. Wasielewski, ‘Competition between singlet fission and spin-orbit-induced intersystem crossing in anthanthrene and anthanthrone derivatives’, *ChemPlusChem* **84**, 1432–1438 (2019).
- [209] N. Maity, W. Kim, N. A. Panjwani, A. Kundu, K. Majumder, P. Kasetty, D. Mishra, R. Bittl, J. Nagesh, J. Dasgupta, et al., ‘Parallel triplet formation pathways in a singlet fission material’, *Nature Communications* **13**, 5244 (2022).
- [210] C. Lin, Y. Qi, P. J. Brown, M. L. Williams, J. R. Palmer, M. Myong, X. Zhao, R. M. Young, and M. R. Wasielewski, ‘Singlet fission in perylene monoimide single crystals and polycrystalline films’, *The Journal of Physical Chemistry Letters* **14**, 2573–2579 (2023).
- [211] C. M. Marian, ‘Understanding and controlling intersystem crossing in molecules’, *Annual Review of Physical Chemistry* **72**, 617–640 (2021).
- [212] G. N. Lewis and M. Kasha, ‘Phosphorescence and the triplet state’, *Journal of the American Chemical Society* **66**, 2100–2116 (1944).
- [213] M. Pope, ‘Charge-transfer exciton state, ionic energy levels, and delayed fluorescence in anthracene’, *Molecular Crystals* **4**, 183–190 (1968).
- [214] M. Schwoerer and H. C. Wolf, *Organic molecular solids* (John Wiley & Sons, 2007).
- [215] Y. Kobori, M. Fuki, S. Nakamura, and T. Hasobe, ‘Geometries and Terahertz Motions Driving Quintet Multiexcitons and Ultimate Triplet–Triplet Dissociations via the Intramolecular Singlet Fissions’, *The Journal of Physical Chemistry B* **124**, 9411–9419 (2020).

- [216] M. R. Wasielewski, M. D. Forbes, N. L. Frank, K. Kowalski, G. D. Scholes, J. Yuen-Zhou, M. A. Baldo, D. E. Freedman, R. H. Goldsmith, T. Goodson III, et al., ‘Exploiting chemistry and molecular systems for quantum information science’, *Nature Reviews Chemistry* **4**, 490–504 (2020).
- [217] S. Bayliss, D. Laorenza, P. Mintun, B. Kovos, D. E. Freedman, and D. Awschalom, ‘Optically addressable molecular spins for quantum information processing’, *Science* **370**, 1309–1312 (2020).
- [218] V. K. Thorsmølle, R. D. Averitt, J. Demsar, D. Smith, S. Tretiak, R. Martin, X. Chi, B. K. Crone, A. Ramirez, and A. J. Taylor, ‘Morphology effectively controls singlet-triplet exciton relaxation and charge transport in organic semiconductors’, *Physical Review Letters* **102**, 017401 (2009).
- [219] J. J. Burdett, A. M. Müller, D. Gosztola, and C. J. Bardeen, ‘Excited state dynamics in solid and monomeric tetracene: The roles of superradiance and exciton fission’, *The Journal of Chemical Physics* **133** (2010).
- [220] S.-H. Lim, T. G. Bjorklund, F. C. Spano, and C. J. Bardeen, ‘Exciton delocalization and superradiance in tetracene thin films and nanoaggregates’, *Physical Review Letters* **92**, 107402 (2004).
- [221] A. M. Müller, Y. S. Avlasevich, K. Müllen, and C. J. Bardeen, ‘Evidence for exciton fission and fusion in a covalently linked tetracene dimer’, *Chemical Physics Letters* **421**, 518–522 (2006).
- [222] A. M. Müller, Y. S. Avlasevich, W. W. Schoeller, K. Müllen, and C. J. Bardeen, ‘Exciton fission and fusion in bis (tetracene) molecules with different covalent linker structures’, *Journal of the American Chemical Society* **129**, 14240–14250 (2007).
- [223] J. C. Johnson, A. Akdag, M. Zamadar, X. Chen, A. F. Schwerin, I. Paci, M. B. Smith, Z. Havlas, J. R. Miller, M. A. Ratner, et al., ‘Toward designed singlet fission: solution photophysics of two indirectly coupled covalent dimers of 1, 3-diphenylisobenzofuran’, *The Journal of Physical Chemistry B* **117**, 4680–4695 (2013).

-
- [224] E. C. Greyson, B. R. Stepp, X. Chen, A. F. Schwerin, I. Paci, M. B. Smith, A. Akdag, J. C. Johnson, A. J. Nozik, J. Michl, et al., ‘Singlet exciton fission for solar cell applications: energy aspects of interchromophore coupling’, *The Journal of Physical Chemistry B* **114**, 14223–14232 (2010).
- [225] T. Hasell, X. Wu, J. T. Jones, J. Bacsá, A. Steiner, T. Mitra, A. Trewin, D. J. Adams, and A. I. Cooper, ‘Triply interlocked covalent organic cages’, *Nature Chemistry* **2**, 750–755 (2010).
- [226] T. Tozawa, J. T. Jones, S. I. Swamy, S. Jiang, D. J. Adams, S. Shakespeare, R. Clowes, D. Bradshaw, T. Hasell, S. Y. Chong, et al., ‘Porous organic cages’, *Nature materials* **8**, 973–978 (2009).
- [227] A. S. Bogomolov, V. M. Rogoveshko, and A. V. Baklanov, ‘Fast intersystem crossing in the tetracene dimers as a source of “dark” state’, *AIP Advances* **13** (2023).
- [228] Z. Birech, M. Schwoerer, T. Schmeiler, J. Pflaum, and H. Schwoerer, ‘Ultrafast dynamics of excitons in tetracene single crystals’, *The Journal of Chemical Physics* **140** (2014).
- [229] J.-P. Yang, W. Paa, and S. Rentsch, ‘Femtosecond investigations of photophysics of ultrafast intersystem crossing in terthiophene by wavelength dependent excitation’, *Chemical Physics Letters* **320**, 665–672 (2000).
- [230] N. Wollscheid, B. Günther, V. J. Rao, F. J. Berger, J. L. P. Lustres, M. Motzkus, J. Zaumseil, L. H. Gade, S. Höfener, and T. Buckup, ‘Ultrafast singlet fission and intersystem crossing in halogenated tetraazaperopyrenes’, *The Journal of Physical Chemistry A* **124**, 7857–7868 (2020).
- [231] C. Burgdorff, T. Kircher, and H.-G. Löhmannsröben, ‘Photophysical properties of tetracene derivatives in solution’, *Spectrochimica Acta Part A: Molecular Spectroscopy* **44**, 1137–1141 (1988).
- [232] R. Bensasson and E. Land, ‘Triplet-triplet extinction coefficients via energy transfer’, *Transactions of the Faraday Society* **67**, 1904–1915 (1971).

- [233] C. Burgdorff and H.-G. Löhmansröben, ‘Photophysical properties of tetracene derivatives in solution III. Thermally activated nonradiative processes and triplet state properties’, *Journal of Luminescence* **59**, 201–208 (1994).
- [234] K. H. Park, W. Kim, J. Yang, and D. Kim, ‘Excited-state structural relaxation and exciton delocalization dynamics in linear and cyclic π -conjugated oligothiophenes’, *Chemical Society Reviews* **47**, 4279–4294 (2018).
- [235] Y. Meyer, R. Astier, and J. Leclercq, ‘Triplet-Triplet Spectroscopy of Polyacenes’, *The Journal of Chemical Physics* **56**, 801–815 (1972).
- [236] Z. Khan and B. Khanna, ‘Formation of the Radical Cations of Some Tetracyclic Aromatic Hydrocarbons in Boric Acid Glass’, *Canadian Journal of Chemistry* **52**, 827–828 (1974).
- [237] K. Kimura, T. Yamazaki, and S. Katsumata, ‘Dimerization of the perylene and tetracene radical cations and electronic absorption spectra of their dimers’, *The Journal of Physical Chemistry* **75**, 1768–1774 (1971).
- [238] X. Chen, X. Zhang, X. Xiao, Z. Wang, and J. Zhao, ‘Recent Developments on Understanding Charge Transfer in Molecular Electron Donor-Acceptor Systems’, *Angewandte Chemie International Edition* **62**, e202216010 (2023).
- [239] R. M. Young and M. R. Wasielewski, ‘Mixed Electronic States in Molecular Dimers: Connecting Singlet Fission, Excimer Formation, and Symmetry-Breaking Charge Transfer’, *Accounts of Chemical Research* **53**, 1957–1968 (2020).
- [240] Z. Huang, H. Xie, J. Miao, Y. Wei, Y. Zou, T. Hua, X. Cao, and C. Yang, ‘Charge transfer excited state promoted multiple resonance delayed fluorescence emitter for high-performance narrowband electroluminescence’, *Journal of the American Chemical Society* **145**, 12550–12560 (2023).

-
- [241] A. A. Bakulin, A. Rao, V. G. Pavelyev, P. H. van Loosdrecht, M. S. Pshenichnikov, D. Niedzialek, J. Cornil, D. Beljonne, and R. H. Friend, ‘The role of driving energy and delocalized states for charge separation in organic semiconductors’, *Science* **335**, 1340–1344 (2012).
- [242] O. F. Mohammed and E. Vauthey, ‘Excited-state dynamics of nitroperylene in solution: solvent and excitation wavelength dependence’, *The Journal of Physical Chemistry A* **112**, 3823–3830 (2008).
- [243] T. Nikkonen, M. M. Oliva, A. Kahnt, M. Muuronen, J. Helaja, and D. M. Guldi, ‘Photoinduced Charge Transfer in a Conformational Switching Chlorin Dimer–Azafulleroid in Polar and Nonpolar Media’, *Chemistry–A European Journal* **21**, 590–600 (2015).
- [244] M. Chen, Y. J. Bae, C. M. Mauck, A. Mandal, R. M. Young, and M. R. Wasielewski, ‘Singlet fission in covalent terrylenediimide dimers: Probing the nature of the multiexciton state using femtosecond mid-infrared spectroscopy’, *Journal of the American Chemical Society* **140**, 9184–9192 (2018).
- [245] T. Takahashi, T. Takenobu, J. Takeya, and Y. Iwasa, ‘Ambipolar light-emitting transistors of a tetracene single crystal’, *Advanced Functional Materials* **17**, 1623–1628 (2007).
- [246] C.-T. Chien, C.-C. Lin, M. Watanabe, Y.-D. Lin, T.-H. Chao, T.-c. Chiang, X.-H. Huang, Y.-S. Wen, C.-H. Tu, C.-H. Sun, et al., ‘Tetracene-based field-effect transistors using solution processes’, *Journal of Materials Chemistry* **22**, 13070–13075 (2012).
- [247] R. De Boer, T. Klapwijk, and A. Morpurgo, ‘Field-effect transistors on tetracene single crystals’, *Applied Physics Letters* **83**, 4345–4347 (2003).
- [248] L. Jiang, H. Dong, and W. Hu, ‘Organic single crystal field-effect transistors: advances and perspectives’, *Journal of Materials Chemistry* **20**, 4994–5007 (2010).

- [249] C.-W. Chu, Y. Shao, V. Shrotriya, and Y. Yang, ‘Efficient photovoltaic energy conversion in tetracene-C60 based heterojunctions’, *Applied Physics Letters* **86** (2005).
- [250] J.-L. Brédas, J. E. Norton, J. Cornil, and V. Coropceanu, ‘Molecular understanding of organic solar cells: the challenges’, *Accounts of Chemical Research* **42**, 1691–1699 (2009).
- [251] N. Chuchvaga, K. Zholdybayev, K. Aimaganbetov, S. Zhantuarov, and A. Serikkanov, ‘Development of hetero-junction silicon solar cells with intrinsic thin layer: a review’, *Coatings* **13**, 796 (2023).
- [252] S. Yoo, B. Domercq, and B. Kippelen, ‘Efficient thin-film organic solar cells based on pentacene/C60 heterojunctions’, *Applied Physics Letters* **85**, 5427–5429 (2004).
- [253] Y. Shao, S. Sista, C.-W. Chu, D. Sievers, and Y. Yang, ‘Enhancement of tetracene photovoltaic devices with heat treatment’, *Applied Physics Letters* **90** (2007).
- [254] Z. Hong, R. Lessmann, B. Maennig, Q. Huang, K. Harada, M. Riede, and K. Leo, ‘Antenna effects and improved efficiency in multiple heterojunction photovoltaic cells based on pentacene, zinc phthalocyanine, and C60’, *Journal of Applied Physics* **106** (2009).
- [255] H. Shpaisman, O. Niitsoo, I. Lubomirsky, and D. Cahen, ‘Can up-and down-conversion and multi-exciton generation improve photovoltaics?’, *Solar Energy Materials and Solar Cells* **92**, 1541–1546 (2008).
- [256] H. Marciniak, I. Pugliesi, B. Nickel, and S. Lochbrunner, ‘Ultrafast singlet and triplet dynamics in microcrystalline pentacene films’, *Physical Review B—Condensed Matter and Materials Physics* **79**, 235318 (2009).
- [257] A. Rao, M. W. Wilson, J. M. Hodgkiss, S. Albert-Seifried, H. Bassler, and R. H. Friend, ‘Exciton fission and charge generation via triplet excitons in pentacene/C60 bilayers’, *Journal of the American Chemical Society* **132**, 12698–12703 (2010).

-
- [258] C. Wang and M. J. Tauber, ‘High-yield singlet fission in a zeaxanthin aggregate observed by picosecond resonance Raman spectroscopy’, *Journal of the American Chemical Society* **132**, 13988–13991 (2010).
- [259] S. T. Roberts, C. W. Schlenker, V. Barlier, R. E. McAnally, Y. Zhang, J. N. Mastron, M. E. Thompson, and S. E. Bradforth, ‘Observation of triplet exciton formation in a platinum-sensitized organic photovoltaic device’, *The Journal of Physical Chemistry Letters* **2**, 48–54 (2011).
- [260] N. J. Turro, *Modern molecular photochemistry* (University science books, 1991).
- [261] A. Yildiz, P. T. Kissinger, and C. N. Reilley, ‘Triplet→Triplet Fluorescence of Rubrene in Solution’, *The Journal of Chemical Physics* **49**, 1403–1406 (1968).
- [262] D. G. Bossanyi, Y. Sasaki, S. Wang, D. Chekulaev, N. Kimizuka, N. Yanai, and J. Clark, ‘In optimized rubrene-based nanoparticle blends for photon upconversion, singlet energy collection outcompetes triplet-pair separation, not singlet fission’, *Journal of Materials Chemistry C* **10**, 4684–4696 (2022).
- [263] M. Mahboub, H. Maghsoudiganjeh, A. M. Pham, Z. Huang, and M. L. Tang, ‘Triplet energy transfer from PbS (Se) nanocrystals to rubrene: the relationship between the upconversion quantum yield and size’, *Advanced Functional Materials* **26**, 6091–6097 (2016).
- [264] K. Lawson-Wood, S. Upstone, and K. Evans, ‘Determination of Relative Fluorescence Quantum Yields using the FL6500 Fluorescence Spectrometer’, *Fluoresc. Spectrosc* **4**, 1–5 (2018).
- [265] M. Kállay, K. Németh, and P. R. Surján, ‘Triplet state characteristics of higher fullerenes’, *The Journal of Physical Chemistry A* **102**, 1261–1273 (1998).

- [266] T. Lazarides, M. A. Alamiry, H. Adams, S. J. Pope, S. Faulkner, J. A. Weinstein, and M. D. Ward, ‘Anthracene as a sensitiser for near-infrared luminescence in complexes of Nd (III), Er (III) and Yb (III): an unexpected sensitisation mechanism based on electron transfer’, *Dalton Transactions*, 1484–1491 (2007).
- [267] Y. V. Aulin, M. Van Seville, M. Moes, and F. C. Grozema, ‘Photochemical upconversion in metal-based octaethyl porphyrin–diphenylanthracene systems’, *RSC Advances* **5**, 107896–107903 (2015).
- [268] J. Jaumot, R. Gargallo, A. De Juan, and R. Tauler, ‘A graphical user-friendly interface for MCR-ALS: a new tool for multivariate curve resolution in MATLAB’, *Chemometrics and Intelligent Laboratory Systems* **76**, 101–110 (2005).
- [269] J. Jaumot, A. de Juan, and R. Tauler, ‘MCR-ALS GUI 2.0: New features and applications’, *Chemometrics and Intelligent Laboratory Systems* **140**, 1–12 (2015).
- [270] N. F. Pompetti, K. E. Smyser, B. Feingold, R. Owens, B. Lama, S. Sharma, N. H. Damrauer, and J. C. Johnson, ‘Tetracene Diacid Aggregates for Directing Energy Flow toward Triplet Pairs’, *Journal of the American Chemical Society* **146**, 11473–11485 (2024).
- [271] D. Li, I. Keresztes, R. Hopson, and P. G. Williard, ‘Characterization of reactive intermediates by multinuclear diffusion-ordered NMR spectroscopy (DOSY)’, *Accounts of Chemical Research* **42**, 270–280 (2009).
- [272] R. Huo, R. Wehrens, J. Van Duynhoven, and L. Buydens, ‘Assessment of techniques for DOSY NMR data processing’, *Analytica Chimica Acta* **490**, 231–251 (2003).
- [273] E. Durand, M. Clemancey, A.-A. Quoineaud, J. Verstraete, D. Espinat, and J.-M. Lancelin, ‘¹H diffusion-ordered spectroscopy (DOSY) nuclear magnetic resonance (NMR) as a powerful tool for the analysis of hydrocarbon mixtures and asphaltenes’, *Energy & Fuels* **22**, 2604–2610 (2008).

-
- [274] M. Bouhaddou and M. R. Birtwistle, ‘Dimerization-based control of cooperativity’, *Molecular BioSystems* **10**, 1824–1832 (2014).
- [275] R. Gesztelyi, J. Zsuga, A. Kemeny-Beke, B. Varga, B. Juhasz, and A. Tosaki, ‘The Hill equation and the origin of quantitative pharmacology’, *Archive For History of Exact Sciences* **66**, 427–438 (2012).
- [276] M. Niello, R. Gradisch, C. J. Loland, T. Stockner, and H. H. Sitte, ‘Allosteric modulation of neurotransmitter transporters as a therapeutic strategy’, *Trends in Pharmacological Sciences* **41**, 446–463 (2020).
- [277] J. Sunny, E. Sebastian, S. Sujilkumar, F. Würthner, B. Engels, and M. Hariharan, ‘Unveiling the intersystem crossing dynamics in N-annulated perylene bisimides’, *Physical Chemistry Chemical Physics* **25**, 28428–28436 (2023).
- [278] D. Valverde, S. J. Hoehn, E. D. Koyanagui, S. E. Krul, C. E. Crespo-Hernández, and A. C. Borin, ‘Theoretical and Experimental Evaluation of the Electronic Relaxation Mechanisms of 2-Pyrimidinone: The Primary UVA Absorbing Moiety of the DNA and RNA (6–4) Photolesion’, *ChemPhotoChem* **8**, e202400070 (2024).
- [279] D. Vörös and S. Mai, ‘Role of ultrafast internal conversion and intersystem crossing in the nonadiabatic relaxation dynamics of ortho-nitrobenzaldehyde’, *The Journal of Physical Chemistry A* **127**, 5872–5886 (2023).
- [280] D. P. DiVincenzo, ‘The physical implementation of quantum computation’, *Fortschritte der Physik: Progress of Physics* **48**, 771–783 (2000).
- [281] M. K. Bhaskar, R. Riedinger, B. Machielse, D. S. Levonian, C. T. Nguyen, E. N. Knall, H. Park, D. Englund, M. Lončar, D. D. Sukachev, et al., ‘Experimental demonstration of memory-enhanced quantum communication’, *Nature* **580**, 60–64 (2020).
- [282] C. L. Degen, F. Reinhard, and P. Cappellaro, ‘Quantum sensing’, *Reviews of Modern Physics* **89**, 035002 (2017).

- [283] B. W. Stein, C. R. Tichnell, J. Chen, D. A. Shultz, and M. L. Kirk, ‘Excited state magnetic exchange interactions enable large spin polarization effects’, *Journal of the American Chemical Society* **140**, 2221–2228 (2018).
- [284] M. Mayländer, P. Thielert, T. Quintes, A. Vargas Jentzsch, and S. Richert, ‘Room temperature electron spin coherence in photogenerated molecular spin qubit candidates’, *Journal of the American Chemical Society* **145**, 14064–14069 (2023).
- [285] S. Gorgon, K. Lv, J. Grüne, B. H. Drummond, W. K. Myers, G. Londi, G. Ricci, D. Valverde, C. Tonnelé, P. Murto, et al., ‘Reversible spin-optical interface in luminescent organic radicals’, *Nature* **620**, 538–544 (2023).
- [286] A. Yamauchi, K. Tanaka, M. Fuki, S. Fujiwara, N. Kimizuka, T. Ryu, M. Saigo, K. Onda, R. Kusumoto, N. Ueno, et al., ‘Room-temperature quantum coherence of entangled multiexcitons in a metal-organic framework’, *Science Advances* **10**, eadi3147 (2024).
- [287] R. D. Dill, K. E. Smyser, B. K. Rugg, N. H. Damrauer, and J. D. Eaves, ‘Entangled spin-polarized excitons from singlet fission in a rigid dimer’, *Nature Communications* **14**, 1180 (2023).
- [288] L.-C. Lin, T. Smith, Q. Ai, B. K. Rugg, C. Risko, J. E. Anthony, N. H. Damrauer, and J. C. Johnson, ‘Multiexciton quintet state populations in a rigid pyrene-bridged parallel tetracene dimer’, *Chemical Science* **14**, 11554–11565 (2023).
- [289] D. Lubert-Perquel, E. Salvadori, M. Dyson, P. N. Stavrinou, R. Montis, H. Nagashima, Y. Kobori, S. Heutz, and C. W. Kay, ‘Identifying triplet pathways in dilute pentacene films’, *Nature Communications* **9**, 4222 (2018).
- [290] T. S. MacDonald, M. J. Tayebjee, M. I. Collins, E. Kumarasamy, S. N. Sanders, M. Y. Sfeir, L. M. Campos, and D. R. McCamey, ‘Anisotropic multiexciton quintet and triplet dynamics in singlet fission via pulsed electron spin resonance’, *Journal of the American Chemical Society* **145**, 15275–15283 (2023).

-
- [291] S. Matsuda, S. Oyama, and Y. Kobori, ‘Electron spin polarization generated by transport of singlet and quintet multiexcitons to spin-correlated triplet pairs during singlet fissions’, *Chemical Science* **11**, 2934–2942 (2020).
- [292] S. R. Orsborne, J. Gorman, L. R. Weiss, A. Sridhar, N. A. Panjwani, G. Divitini, P. Budden, D. Palecek, S. T. Ryan, A. Rao, et al., ‘Photogeneration of spin quintet triplet–triplet excitations in DNA-assembled pentacene stacks’, *Journal of the American Chemical Society* **145**, 5431–5438 (2023).
- [293] B. K. Rugg, K. E. Smyser, B. Fluegel, C. H. Chang, K. J. Thorley, S. Parkin, J. E. Anthony, J. D. Eaves, and J. C. Johnson, ‘Triplet-pair spin signatures from macroscopically aligned heteroacenes in an oriented single crystal’, *Proceedings of the National Academy of Sciences* **119**, e2201879119 (2022).
- [294] S. N. Sanders, E. Kumarasamy, A. B. Pun, M. T. Trinh, B. Choi, J. Xia, E. J. Taffet, J. Z. Low, J. R. Miller, X. Roy, et al., ‘Quantitative intramolecular singlet fission in bipentacenes’, *Journal of the American Chemical Society* **137**, 8965–8972 (2015).
- [295] J. Zirzmeier, D. Lehnher, P. B. Coto, E. T. Chernick, R. Casillas, B. S. Basel, M. Thoss, R. R. Tykwinski, and D. M. Guldi, ‘Singlet fission in pentacene dimers’, *Proceedings of the National Academy of Sciences* **112**, 5325–5330 (2015).
- [296] H. Sakai, R. Inaya, H. Nagashima, S. Nakamura, Y. Kobori, N. V. Tkachenko, and T. Hasobe, ‘Multiexciton dynamics depending on intramolecular orientations in pentacene dimers: Recombination and dissociation of correlated triplet pairs’, *The Journal of Physical Chemistry Letters* **9**, 3354–3360 (2018).
- [297] S. Lukman, A. J. Musser, K. Chen, S. Athanasopoulos, C. K. Yong, Z. Zeng, Q. Ye, C. Chi, J. M. Hodgkiss, J. Wu, et al., ‘Tuneable singlet exciton

- fission and triplet–triplet annihilation in an orthogonal pentacene dimer’, *Advanced Functional Materials* **25**, 5452–5461 (2015).
- [298] K. Majumder, S. Mukherjee, N. A. Panjwani, J. Lee, R. Bittl, W. Kim, S. Patil, and A. J. Musser, ‘Controlling Intramolecular Singlet Fission Dynamics via Torsional Modulation of Through-Bond versus Through-Space Couplings’, *Journal of the American Chemical Society* **145**, 20883–20896 (2023).
- [299] O. G. Reid, J. C. Johnson, J. D. Eaves, N. H. Damrauer, and J. E. Anthony, ‘Molecular Control of Triplet-Pair Spin Polarization and Its Optoelectronic Magnetic Resonance Probes’, *Accounts of Chemical Research* **57**, 59–69 (2023).
- [300] K. Kuroda, K. Yazaki, Y. Tanaka, M. Akita, H. Sakai, T. Hasobe, N. V. Tkachenko, and M. Yoshizawa, ‘A Pentacene-based Nanotube Displaying Enriched Electrochemical and Photochemical Activities’, *Angewandte Chemie* **131**, 1127–1131 (2019).
- [301] H. M. Bergman, G. R. Kiel, R. J. Witzke, D. P. Nenon, A. M. Schwartzberg, Y. Liu, and T. D. Tilley, ‘Shape-selective synthesis of pentacene macrocycles and the effect of geometry on singlet fission’, *Journal of the American Chemical Society* **142**, 19850–19855 (2020).
- [302] S. Fujiwara, M. Hosoyamada, K. Tateishi, T. Uesaka, K. Ideta, N. Kimizuka, and N. Yanai, ‘Dynamic nuclear polarization of metal–organic frameworks using photoexcited triplet electrons’, *Journal of the American Chemical Society* **140**, 15606–15610 (2018).
- [303] S. Lukman, J. M. Richter, L. Yang, P. Hu, J. Wu, N. C. Greenham, and A. J. Musser, ‘Efficient singlet fission and triplet-pair emission in a family of zethrene diradicaloids’, *Journal of the American Chemical Society* **139**, 18376–18385 (2017).

-
- [304] C. Grieco, G. S. Doucette, J. M. Munro, E. R. Kennehan, Y. Lee, A. Rimshaw, M. M. Payne, N. Wonderling, J. E. Anthony, I. Dabo, et al., ‘Triplet Transfer Mediates Triplet Pair Separation during Singlet Fission in 6, 13-Bis (triisopropylsilylethynyl)-Pentacene’, *Advanced Functional Materials* **27**, 1703929 (2017).
- [305] D. Carbonera, ‘Optically detected magnetic resonance (ODMR) of photo-excited triplet states’, *Photosynthesis Research* **102**, 403–414 (2009).
- [306] R. K. Hallani, K. J. Thorley, Y. Mei, S. R. Parkin, O. D. Jurchescu, and J. E. Anthony, ‘Structural and electronic properties of crystalline, isomerically pure anthradithiophene derivatives’, *Advanced Functional Materials* **26**, 2341–2348 (2016).
- [307] K. Momma and F. Izumi, ‘VESTA: a three-dimensional visualization system for electronic and structural analysis’, *Journal of Applied Crystallography* **41**, 653–658 (2008).
- [308] S. Stoll and A. Schweiger, ‘EasySpin, a comprehensive software package for spectral simulation and analysis in EPR.’, *J. Magn. Reson.* **178**, 42–55 (2006).
- [309] R. Furrer, F. Fujara, C. Lange, D. Stehlik, H. M. Vieth, and W. Vollmann, ‘Transient ESR nutation signals in excited aromatic triplet states’, *Chem. Phys. Lett.* **75**, 332–339 (1980).
- [310] F. Neese, F. Wennmohs, U. Becker, and C. Riplinger, ‘The ORCA quantum chemistry program package’, *J. Chem. Phys.* **152**, 224108–1–18 (2020).
- [311] F. Weigend and R. Ahlrichs, ‘Balanced basis sets of split valence, triple zeta valence and quadruple zeta valence quality for H to Rn: Design and assessment of accuracy.’, *Phys. Chem. Chem. Phys.* **7**, 3297–3305 (2005).
- [312] F. Weigend, ‘Accurate Coulomb-fitting basis sets for H to Rn w’, *Phys. Chem. Chem. Phys.* **8**, 1057–1065 (2006).

- [313] S. Grimme, J. Antony, S. Ehrlich, and H. Krieg, ‘A consistent and accurate ab initio parametrization of density functional dispersion correction (DFT-D) for the 94 elements H-Pu’, *J. Chem. Phys.* **132**, 154104–1–19 (2010).
- [314] S. Grimme, S. Ehrlich, and L. Goerigk, ‘Effect of the Damping Function in Dispersion Corrected Density Functional Theory’, *J. Comput. Chem.* **32**, 1456–1465 (2011).
- [315] V. Barone, ‘Structure, Magnetic Properties and Reactivities of Open-Shell Species From Density Functional and Self-Consistent Hybrid Methods’, in *Recent Advances in Density Functional Methods*, Vol. 1, edited by D. P. Chong (World Scientific Publ. Co., Singapore, 1995) Chap. 8, pages 287–334.
- [316] N. Rega, M. Cossi, and V. Barone, ‘Development and validation of reliable quantum mechanical approaches for the study of free radicals in solution’, *J. Chem. Phys.* **105**, 11060–11067 (1996).
- [317] S. Huzinaga, ‘Gaussian-Type Functions for Polyatomic Systems. I’, *J. Chem. Phys.* **42**, 1293–1302 (1965).
- [318] W. Kutzelnigg, U. Fleischer, and M. Schindler, ‘The IGLO-Method: Ab initio Calculation and Interpretation of NMR Chemical Shifts and Magnetic Susceptibilities’, in *NMR Basic Principles and Progress Vol. 23*, edited by P. Diehl, E. Fluck, H. Günther, R. Kosfeld, and J. Seelig (Springer, Heidelberg, 1990), page 165.
- [319] K. Miyata, Y. Kurashige, K. Watanabe, T. Sugimoto, S. Takahashi, S. Tanaka, J. Takeya, T. Yanai, and Y. Matsumoto, ‘Coherent singlet fission activated by symmetry breaking’, *Nature Chemistry* **9**, 983–989 (2017).
- [320] A. V. Hill, ‘The possible effects of the aggregation of the molecules of hemoglobin on its dissociation curves’, *The Journal of Physiology* **40**, iv–vii (1910).

-
- [321] M. Faller, M. Matsunaga, S. Yin, J. A. Loo, and F. Guo, ‘Heme is involved in microRNA processing’, *Nature Structural & Molecular Biology* **14**, 23–29 (2007).
- [322] L. Silvestrini, N. Belhaj, L. Comez, Y. Gerelli, A. Lauria, V. Libera, P. Mariani, P. Marzullo, M. G. Ortore, A. Palumbo Piccionello, et al., ‘The dimer-monomer equilibrium of SARS-CoV-2 main protease is affected by small molecule inhibitors’, *Scientific Reports* **11**, 9283 (2021).
- [323] J. Wang, R. M. Wolf, J. W. Caldwell, P. A. Kollman, and D. A. Case, ‘Development and testing of a general amber force field’, *Journal of Computational Chemistry* **25**, 1157–1174 (2004).
- [324] C. I. Bayly, P. Cieplak, W. Cornell, and P. A. Kollman, ‘A well-behaved electrostatic potential based method using charge restraints for deriving atomic charges: the RESP model’, *The Journal of Physical Chemistry* **97**, 10269–10280 (1993).
- [325] H. J. Berendsen, J. v. Postma, W. F. Van Gunsteren, A. DiNola, and J. R. Haak, ‘Molecular dynamics with coupling to an external bath’, *The Journal of Chemical Physics* **81**, 3684–3690 (1984).
- [326] S. Nosé, ‘A molecular dynamics method for simulations in the canonical ensemble’, *Molecular Physics* **52**, 255–268 (1984).
- [327] M. Parrinello and A. Rahman, ‘Polymorphic transitions in single crystals: A new molecular dynamics method’, *Journal of Applied Physics* **52**, 7182–7190 (1981).
- [328] B. Hess, H. Bekker, H. J. Berendsen, and J. G. Fraaije, ‘LINCS: a linear constraint solver for molecular simulations’, *Journal of Computational chemistry* **18**, 1463–1472 (1997).
- [329] T. Darden, D. York, and L. Pedersen, ‘Particle mesh Ewald: An $N \log(N)$ method for Ewald sums in large systems’, *The Journal of Chemical Physics* **98**, 10089–10092 (1993).

